The Dissertation Committee for Paul Montgomery Robertson
certifies that this is the approved version of the following dissertation:

Discovering New Solar Systems: Jupiter Analogs and the Quest to Find Another Earth

Committee:

Sarah E. Dodson-Robinson, Supervisor

Michael Endl, Supervisor

William D. Cochran

Edward L. Robinson

Gregory A. Shields

Jason T. Wright

Discovering New Solar Systems: Jupiter Analogs and the Quest to Find Another Earth

by

Paul Montgomery Robertson, B.A., M.A.

DISSERTATION

Presented to the Faculty of the Graduate School of

The University of Texas at Austin

in Partial Fulfillment

of the Requirements

for the Degree of

DOCTOR OF PHILOSOPHY

THE UNIVERSITY OF TEXAS AT AUSTIN

August 2013

Dedicated to my wife, Emily, without whom this would most certainly have never been possible.

Acknowledgments

If it takes a village to raise a child, I often feel like it took the entire city of Austin to raise this PhD student. While I will certainly fail to remember some very important people in this space, I would nevertheless like to express my gratitude to a number of family, friends and colleagues who made this dissertation both academically rewarding and thoroughly enjoyable.

First and foremost, I must thank my lovely wife Emily. Your love, dedication, and support are essential to everything I do, and anything positive arising from the work herein is a tribute to you. It is my greatest joy to share my life with you, and I am humbled by your unwavering support.

The Astronomy Department at the University of Texas has been a wonderfully supportive environment, and I am thankful every day to have had the opportunity to study here. Before I attempt a semi-comprehensive list of everyone I want to acknowledge there, I wish to highlight two men in particular who have gone above and beyond the call of duty in shaping my evolution as an astronomer. The first is my advisor, Mike Endl. Mike, you have done a fantastic job of teaching me the science, literature, and technique of our field. More importantly, though, you have guided and advised me while still allowing me the independence and creative freedom to follow my own lead and pursue the problems that compel me. As a result, I have both the competence

and the confidence necessary to succeed going forward. I would also like to acknowledge the tremendous support I have received from Greg Shields, who in addition to broadening and strengthening my academic work has been an invaluable confidant and friend. As with Mike, Greg has always put my best interests first, and encourages me to follow my passions. Greg, I appreciate your guidance and dedication much more than you probably realize; while the bulk of this dissertation research is not in your field, your contributions were essential to making it a reality.

I have been extraordinarily fortunate in that the rest of my committee is truly outstanding. To Bill Cochran, Sally Dodson-Robinson, Jason Wright, and Rob Robinson: I can honestly say that if someone asked me to create the ideal PhD committee from scratch, whatever I came up with would pale in comparison to you. Both individually and collectively, you have supported, guided, encouraged, and challenged me in exactly the right way. When I have students of my own, I will do my very best to follow your example.

There is an enormous number of faculty, research and administrative staff members at UT who were not members of my committee, yet still went out of their way to help me out in some way personally or professionally. While the following list is assuredly incomplete, I would like to thank in particular Dan Jaffe, Rachel Walker, Terry Bruegging, Anita Cochran, Don Winget, Barbara Castanheira-Endl, Gordon Orris, Kelly Quinney, Rupert Ruiz, Barbara McArthur, Judit Ries, Michel Breger, Lana Beranek, Karl Gebhardt, Cloud Mason, and Craig Wheeler. I will not attempt to list every time

one of these people did some little (or, more often, huge) thing to make my day/semester/life better, because I would sell them short. To each of you: please know that I remember all of those things, and I really appreciate it.

The work contained herein would have but a fraction of its scientific weight and interest if not for the brilliant minds with whom I have had the pleasure of collaborating. In addition to my committee members, all of whom have also been wonderful collaborators, I must acknowledge in particular Phillip MacQueen, Rob Wittenmyer, and Jonti Horner. Just taking advantage of your scientific results is a tremendous benefit to me, but our conversations and brainstorms have been of even greater value. I furthermore extend my heartfelt thanks to *all* my coauthors, of which there are too many to list here, but especially Guillermo Blanc, Romeel Davé, Joel Green, and Erik Brugamyer.

On that note, it is important to mention that the work presented in this dissertation has previously been published in the Astrophysical Journal, and includes contributions from many people. In particular, in Chapters 2 and 3, I am indebted to Erik Brugamyer for the stellar parameter lists, Attila Simon for his line bisector analysis, and Rob Wittenmyer and Jonti Horner for running their dynamical stability code on my orbital fits. In Appendix C, I thank Romeel Davé for his cosmological hydrodynamic modeling. Furthermore, none of the work in Chapters 2-5 would be possible without access to over a decade's worth of data from the McDonald Observatory exoplanet survey, kindly provided by PIs Mike Endl, Bill Cochran, and Phillip MacQueen. For a complete list of coauthors whose contributions were included in this

work, please see references [188–193].

My research would likewise have been impossible without an enormous amount of *new* data from McDonald Observatory. I am therefore indebted to the entire McDonald Observatory mountain staff, especially Dave Doss, Kevin Meyer, and the HET resident astronomers. I also send my thanks to the staff at the Astronomer's Lodge, who never hesitated to do everything possible to make me enormously comfortable out in West Texas. To Tom Montemayor: thanks for making McDonald Observatory, Lake Travis, and Pflugerville all more fun! Finally, a salute to the local and federal firefighters who risked their lives to protect both myself and the telescopes during the wildfires of April, 2011. That was one of the scariest experiences of my life, and your efforts were truly heroic.

I would like to send a lot of love to my family, who have always been there for me throughout my growth as a student and a man. To my grandmother, Billie Rose Robertson, who supported my education both financially and emotionally, and never placed any restrictions on what I could pursue, or asked anything in return. Billie Rose passed away just a year before I completed my PhD studies, and I regret tremendously that she could not be here to see me receive my doctorate, but I am confident she knew her investment paid off. To my father, William Robertson: this journey really started 20 years ago with the two of us getting up at 3AM to spot Neptune in the backyard telescope. Your willingness to embrace and encourage my curiosity is the catalyst that set everything I do now into motion. To my mother, Blair

Robertson: you always say you hope I'm happy with the life I've made for myself. I am very much so, and this work reflects that. During my time in Austin, I have been blessed to gain a new family in the form of my in-laws, the Haughee-Bartletts. John, Judy, Claire, and Anna, thank you for embracing me so thoroughly. I love you all. And of course, to my Austin family: Jim, Melinda, Nick, and Julie. It has been wonderful to spend more time with you while I've been in Austin. Thanks so much for making the transition easier.

Finally, I would like to thank all my fellow students in the UT Astronomy program for making these years such a fun, memorable experience. I have always felt at home with you all, and coming in to work has never felt like a chore with you around. Many of you have had a direct hand in the work presented here, and for that you have my thanks. The rest of you have left your mark on it all the same–I hope it shows!

Discovering New Solar Systems: Jupiter Analogs and the Quest to Find Another Earth

Paul Montgomery Robertson, Ph.D.
The University of Texas at Austin, 2013

Supervisors: Sarah E. Dodson-Robinson
Michael Endl

Exoplanets are now known to be ubiquitous throughout the Galaxy. From the *Kepler* survey, we expect nearly every main-sequence star to form planetary systems during its formation phase. However, the detection limits of *Kepler* are confined to planets with short orbital periods, comparable to those in the inner solar system. Thanks to the long observational time baseline of the McDonald Observatory Radial Velocity (RV) Survey, we can identify gas giant planets in the outer regions of extrasolar planetary systems. The statistics of such planets are not well known, and are important for understanding the physics behind planet formation and migration. In this dissertation, I detail the discovery of five giant exoplanets on long-period orbits–so-called "Jupiter analogs." For two systems of giant planets discovered through our survey, pairs of planets follow closely-packed orbits, creating the possibility for dynamical instability. I therefore examine the orbital resonances that allow these planets to avoid gravitational disruption.

Because we see an abundance of small, potentially habitable exoplanets in the *Kepler* data set, current and upcoming exoplanet surveys concentrate on finding Earth-mass planets orbiting stars near enough to facilitate detailed follow-up observations. Particularly attractive targets are cool, low-mass "M dwarf" stars. Their low masses (and thus higher RV amplitudes from exoplanets) and close-in habitable zones allow for relatively quick detection of low-mass planets in the habitable zone. However, the RV signals of such planets will be obscured by stellar magnetic activity, which is poorly understood for M stars. In an effort to improve the planet detection capabilities of our M dwarf planet survey, I have conducted a detailed investigation of the magnetic behavior of our target stars. I show that, while stellar activity does not appear to systematically influence RV measurements above a precision level of ~ 5 m/s, activity cycles can occasionally produce RV signals in excess of 10 m/s. Additionally, I show that long-term, solar-type stellar activity cycles are common amongst our M dwarf targets, although they are significantly less frequent than for FGK stars. In the case of GJ 328, I have discovered a magnetic activity cycle that appears in the RV data, causing the giant planet around the star to appear to be on a more circular orbit than indicated by the activity-corrected data. Such corrections are essential for the discovery of Earthlike exoplanets.

Table of Contents

List of Tables

List of Figures

Chapter 1

Introduction

Beginning with the first discoveries of planets orbiting nearby main-sequence stars [136, 156], the identification and characterization of exoplanets has relied on the radial velocity (RV) method of detection, which involves the measurement of Doppler shifts in stellar absorption lines caused by the gravitational influence of an orbiting planet. Although the RV technique was initially limited in precision to only the most massive, close-in exoplanets (the so-called "hot Jupiters"), the implementation of wavelength calibration data taken simultaneously with stellar spectra (e.g. [34, 71, 220]) soon allowed for extremely precise velocity determination. While these advances have allowed for the discovery of much less massive planets (the GJ 581 system, for example, [157]), there remain two categories of planets whose frequencies and properties are vital data for understanding exoplanet formation and distribution, yet remain underrepresented in the know planet population. The first is the "Jupiter analog" family–gas giant planets whose orbits have not migrated significantly inward from their formation locations in the protoplanetary disk [233]. The second category, considered the "holy grail" of exoplanet discovery, is terrestrial planets in the circumstellar habitable zone (HZ; [119]), sometimes referred to as "Earth analogs."

1

While current RV precision allows for the discovery of giant planets at practically any orbital distance, confidently determining the orbit of a Jupiter analog requires semi-constant observational coverage over at least one full period, thus requiring continuous data over a decade or more. With an abundance of available time year-round on the 2.7 m Harlan J. Smith (HJST) and 9.2 m Hobby-Eberly (HET) Telescopes, the McDonald Observatory Planet Search Program is one of only a few RV programs worldwide capable of detecting long-period gas giants. As the program's time baseline has just reached 12 years, approximately the orbital period of Jupiter, we see evidence of a large population of giant planets at periods $P \geq 10$ years. Determining the occurrence rate of Jupiter analogs and how the properties of their host stars (i.e. mass, temperature, metallicity, etc.) is important in the quest to understand planet formation. For example, giant planets at shorter orbital distances have been shown to exist preferentially around stars with higher masses [115] and greater heavy-element content [76]. These correlations are understood within the model of planet formation via core accretion, in which Jovian planets form by first building a rock/metal core through collisional accretion of heavy elements, and later attracting gaseous material through gravitational attraction. Thus, more massive stars, with correspondingly larger protoplanetary disks, and more metallic stars should prove especially conducive to gas giant formation. Do these rules hold for more distant planets? The disk instability model of planet formation [26], in which giant planets form rapidly via direct collapse of a locally overdense, gravitationally unstable region of the

protoplanetary disk, can be much more efficient at large distances in the disk. Planets formed through disk instability may show differing dependencies on stellar mass or metallicity. Furthermore, it may be the case that some property of the host star or its surrounding environment controls whether planets that form beyond the ice line (where low temperatures allow for the condensation of volatile elements, making those elements available for accretion onto a planet) remain at large radii or migrate inward. Only the identification of a statistically significant number of Jupiter analogs can conclusively answer these questions.

In the following two chapters, I will describe the discovery and characterization of four Jupiter analogs identified through the McDonald RV program. For two of the stars in our survey, we see evidence for two giant planets in each system. The presence of multi-planet systems is not surprising, as the *Kepler* survey has shown systems of multiple planets to be quite common in the Galaxy (e.g. [208]). As for many of the *Kepler* planets, the planets we find in multiple systems follow orbits that cause them to interact gravitationally. In order to remain stable against collisions or orbital decay, these planets must orbit within mean-motion resonances. Similar orbital resonances may have contributed to the architecture of our outer solar system, as a first-order resonance for Jupiter and Saturn could have pushed Uranus and Neptune outward [216]. In the case of exoplanets, demonstrating dynamical stability has become a critical part of validating the discovery of a multi-planet system [98, 104, 105, 235]. I have therefore included detailed modeling of the orbital

dynamics for the planets around HD 155358 and HD 204313, showing that the orbital fits derived from our data are consistent with stable, resonant orbits. HD 204313 represents a particularly interesting case, as the 3:2 mean-motion resonance offers only a very narrow range of parameters where stable orbits are possible.

One of the primary motivations for any exoplanet search is the push to discover Earthlike planets. As of this writing, *Kepler* has shown small, terrestrial planets to be abundant in the Galaxy [7], and has identified a small number of planets tantalizingly close to the "Earth-mass in the habitable zone of a Sun-like star" benchmark [20, 21]. Because the mission of *Kepler* is to provide a statistical estimate of the frequency of terrestrial planets, and not to provide detailed characterization of any individual systems, it is essential for RV programs to locate Earth analogs around nearby stars to facilitate more complete analysis.

For a number of practical and astrophysical reasons, planets around M dwarf stars–the coolest, least massive stars–are particularly attractive targets for RV surveys focusing on Earth analogs. As the most common stars in the Galaxy, M dwarfs very likely represent the most numerous habitable environments. Most of the closest stars to the Sun are also M dwarfs, ensuring Earth analogs found in those systems would be well-suited for space-based imaging or spectroscopic follow-up, or perhaps even robotic missions to visit the planets. From an observational standpoint, the HZ lies much closer to M dwarf stars than their solar-type counterparts. Additionally, their lower mass leads

to a larger reflex velocity from the mass of an orbiting planet. These combined factors means a terrestrial planet in the HZ around an M dwarf would be detectable at the ~ 1 meter per second level (within the limits of current or near-future instruments), whereas a similar planet in the HZ of the Sun would only produce an RV signal of ~ 10 cm/s.

As illustrated by the purported discovery of a $1M_\oplus$ planet around α Cen B [66, 94], the limiting factor for identifying planets with RV amplitudes $K \leq 1$ m/s will not be instrumental precision, but the RV noise (sometimes called "jitter") introduced by magnetic activity on the stellar surface. Stellar magnetic variations may influence RV measurements in a number of ways. Starspot modulation may introduce signals connected to stellar rotation as spots cover red- or blueshifted regions of the star. Granulation on the stellar surface causes a perceived blueshift, as hotter outflowing plasma covers a larger surface area than cooler, inward-flowing gas. A star may also appear redshifted as the presence of more magnetically active regions inhibit convection, reversing the granulation effect (see, e.g. [132]).

Stellar magnetic activity and its effects on RV measurements are particularly poorly understood for M dwarf stars. Traditionally, RV surveys have relied on the Ca II H&K absorption lines to trace stellar activity [6, 111, 189]. However, due to the lack of blue flux from M stars, there is often insufficient S/N to extract meaningful information from the H&K lines. In the case of the High Resolution Spectrograph on HET, we do not even have the spectral coverage to acquire these lines. Fortunately, as shown by [86], the Hα and Na

I D absorption lines are responsive to magnetic activity in M stars, offering alternative tracers for RV work. Using these lines, I have utilized the spectra acquired from the HET M dwarf planet survey to examine the magnetic activity of our targets, and the resulting influence on RV.

The final two chapters of my dissertation detail the results of my M dwarf activity survey. In Chapter 4, I describe the magnetic properties of our targets as traced by the Hα line. We find that at the precision of our RV measurements (approximately 5 m/s for most stars), most M dwarfs do not show activity-induced RV signals reflected in Hα. The Hα data offers a wealth of insight into M dwarf activity, though, with a significant fraction of our targets exhibiting long-term magnetic cycles and trends. Such cycles only occur for stars of mass $M_* \geq 0.4 M_\odot$, though. Since the mass cutoff matches the point at which low-mass stars can no longer maintain a radiative interior, my result suggests M dwarf activity cycles are powered by the dynamo resulting from differential rotation between the radiative and convective layers, which is generally accepted to be the mechanism maintaining the 11-year solar cycle.

More promising for RV work is the Na I D feature. While my investigation of these lines in our M dwarf data is not yet complete, the case of GJ 328 shows an interesting example of their application. Our RV data show evidence for a Jupiter analog planet in a 12-year orbit. Analysis of the sodium feature reveals a magnetic activity cycle with a 5-year period. The RV measurements are correlated with the Na tracer, which is normally a cause for concern when claiming exoplanet detections (e.g. [183]). However, as de-

scribed fully in Chapter 5, the planet and the activity cycle actually create two distinct signals in the RV data, and the removal of the activity signal causes the orbital fit of the planet to become more eccentric. The results of this work suggest it should be possible to use spectral activity tracers to identify and remove activity-induced RV signals in order to detect the low-amplitude RV modulations caused by terrestrial exoplanets.

Chapter 2

Jupiter Analogs and Resonant Giant Planets

2.1 Background

Beginning with the first radial velocity exoplanet detections [136, 156], exoplanet surveys have identified a large number of gas giant planets on very short orbits (see [19, 219, 238] for complete details). However, to answer the fundamental question "how common are planetary systems analogous to our solar system?" requires years of data from dedicated exoplanet surveys to achieve the observational time baseline necessary to detect the true Jupiter analogs–those giant planets which do not undergo significant inward migration after the dissipation of the protoplanetary disk. Planets with periods greater than approximately 2 years are particularly valuable, as they are outside the detection limits of space-based transit searches such as *Kepler* [18] and CoRoT [3], whose mission timescales are too short to confirm such detections.

Identifying long-period Jovian planets is essential to constraining theoretical and observational results on the true distribution of giant planets versus orbital separation. [48] find approxmiately 10.5% of FGK stars host gas giant planets with periods between 2 and 2000 days, and [233] claim a 3.3% occurrence rate for "Jupiter analogs," which they define as giant planets with

$e < 0.2$ and $P \geq 8$ years. While microlensing surveys (e.g. [89]) derive a higher giant planet fraction, their results are roughly consistent with RV surveys if we consider the differences in sensitivity between the two methods. Microlensing planet searches are particularly sensitive to planets near the Einstein radius (typically 2-4 AU), where core accretion models [11] and extrapolations of RV results [48] agree there should exist a significant population of Jovian planets. The expansion of the time baselines of RV surveys to include these long-period planets is essential to reconcile the statistics of RV and microlensing planet searches.

A more complete census of long-period gas giants also places strong constraints on theories of planet formation and migration. The frequency of Jovian planets offers information on the efficiency of core accretion in proto-planetary disks [27, 62, 151], and the mass-period distribution will test predictions that planets with $m \sin i \geq M_J$ do not migrate as far as Neptune- or Saturn-mass planets [27, 55]. Additionally, enlarging the sample size of giant planets allows for a more robust examination of correlations between the properties of exoplanetary systems (e.g. planet frequency, mass, eccentricity) and those of their stellar hosts, such as metallicity [76], mass [116], and galactic dynamics [67].

The McDonald Observatory Planetary Search [42] has been conducting a high-precision radial velocity survey to identify substellar companions around FGK stars with the Harlan J. Smith 2.7 m telescope since 1987. Since our migration to a cross-dispersed echelle spectrograph in combination with an I_2

9

absorption cell in 1998, and with the addition of the Hobby-Eberly Telescope in 2001, we have successfully monitored hundreds of stars with velocity precision of ~ 3 m/s, giving us a 14 year observational time baseline. As a result, we now see evidence of planets with periods of 5 years or more, a demographic that is still underrepresented in exoplanet discoveries, accounting only 38 of the 518 planets listed in the exoplanets.org database (as of 5 January 2012). In this chapter, we present two such objects–HD 79498b and HD 220773b–a shorter-period Jovian planet around HD 197037, and updated orbital parameters for the two-planet system surrounding HD 155358.

2.2   Sample and Observations

The McDonald Observatory Planet Search Program currently monitors over 250 (mostly FGK) stars with the 2.7 m Harlan J. Smith Telescope for RV variations due to planetary companions. The survey is magnitude limited to $V \sim 10$, and regularly achieves RV precision of 3-6 m/s. The large number of nights provided for our program results in excellent temporal coverage and long observational time baselines for our targets; the objects presented here each have 30-120 data points over 7-10 years. Thus, our sensitivity is more than sufficient to detect RV signatures comparable to that of Jupiter, which would require observations at our level of precision over 12 years.

2.2.1 2.7 m Telescope Observations

The velocities for HD 79498 and HD 197037 were obtained with the Smith Telescope's Tull Coudé Spectrograph [217] using a 1.8 arcsecond slit, giving a resolving power of R = 60,000. Before starlight enters the spectrograph, it passes through an absorption cell containing iodine (I_2) vapor maintained at $50°$ C, resulting in a dense forest of molecular absorption lines over our stellar spectra from 5000-6400 Å. These absorption lines serve as a wavelength metric, allowing us to simultaneously model the instrumental profile (IP) and radial velocity at the time of the observation. For each star, we have at least one high-S/N iodine-free template spectrum, which we have deconvolved from the IP using the Maximum Entropy Method, and against which the shifts due to the star's velocity and the time-variant IP are modeled. Our reported RVs are measured relative to this stellar template, and are further corrected to remove the velocity of the observatory around the solar system barycenter. All radial velocities have been extracted with our pipeline AUSTRAL [71], which handles the modeling of both the IP and stellar velocity shift.

2.2.2 HET Observations

Our RV data for HD 155358 and HD 220773 were taken with the High Resolution Spectrometer (HRS; [218]) on the queue-scheduled 9.2m Hobby-Eberly Telescope (HET; [185]). As with the 2.7 m observations, the HET/HRS spectra are taken at R = 60,000 with an I_2 absorption cell. The fiber-fed HRS

is located below the telescope in a temperature-controlled room. Separate stellar templates were obtained with HRS for these stars. Details of our HET observing procedure are given in [43].

While we use HRS spectra exclusively for obtaining RVs for HD 155358 and HD 220773, we have I_2-free spectra from the 2.7 m telescope for these stars as well. These spectra serve two purposes. First, they allow us to determine the stellar parameters for all five stars using the same instrumental setup. Also, the Tull 2.7 m coudé spectrograph provides Ca H and K indices, which contain information as to the activity levels of the stars.

Tables 2.3-2.6 list the relative velocities and their associated uncertainties for HD 79498, HD 155358, HD 197037 and HD 220773, respectively. Table 2.4 includes observations published in [44], but since all of our spectra have been re-reduced with our most up-to-date methods, the velocities presented here have a higher precision.

2.3 Analysis and Orbit Modeling

2.3.1 Host Star Characterization

We determine the stellar parameters of our targets according to the procedure described in [31]. The method relies on a grid of ATLAS9 model atmospheres [133] in combination with the local thermodynamic (LTE) line analysis and spectral synthesis program MOOG[a] [205]. Using the measured equivalent

---

[a]available at http://www.as.utexas.edu/~chris/moog.html

12

widths of 53 neutral iron lines and 13 singly-ionized iron lines, MOOG force-fits elemental abundances to match the measured equivalent widths according to built-in atomic line behavior. Stellar effective temperature is determined by removing any trends in equivalent widths versus excitation potential, assuming excitation equilibrium. Similarly, we compute the stellar microturbulent velocity ξ by eliminating trends with reduced equivalent width ($\equiv W_\lambda / \lambda$). Finally, by assuming ionization equilibrium, we constrain stellar surface gravity by forcing the abundances derived from Fe I and Fe II lines to match.

We begin our stellar analysis by measuring a solar spectrum taken during daylight (through a solar port) with the same instrumental configuration used to observe our targets. The above procedure yields values of $T_{eff} = 5755 \pm 70$ K, $\log g = 4.48 \pm 0.09$ dex, $\xi = 1.07 \pm 0.06$ km/s, and $\log \epsilon(\mathrm{Fe}) = 7.53 \pm 0.05$ dex. We then repeat this analysis for our target stars, using the I_2-free template spectra. We note that our derived metallicities are, as is conventional, differential to solar. The high S/N and spectral resolution of our stellar templates allow us to make robust estimates of each star's effective temperature, $\log g$, metallicity, and microturbulent velocity, which we include in Table 5.1. We also include photometry, parallax data, and spectral types from the ASCC-2.5 catalog (Version 3, [126], as well as age and mass estimates from [37].

In addition to basic stellar parameters, we use the standard Ca H and K indices to evaluate the hypothesis that our observed RV signals are actually due to stellar activity. For HD 79498 and HD 197037 we have time-series

Star (HD #)	Spec. Type	V^{b}	$B-V^{b}$	M_V	Para-llax (mas)	Dist. (pc)	T_{eff} (K) ±100	$\log g$ ±0.12	[Fe/H] ±0.06	ξ (km/s) ±0.15	Mass^{c} (M$_\odot$)	Age^{c} (Gyr)	S_{HK}	$\log R'_{HK}$
79498	G5	8.03	0.70	4.58	20.4	49	5740	4.37	0.24	1.27	1.06	2.70	0.167	-4.66
155358	G0	7.27	0.55	4.09	23.1	43	5900	4.16	−0.51	0.50	0.92	10.70	0.169	-4.54
197037	F7	6.81	0.52	4.23	30.5	33	6150	4.40	−0.20	1.16	1.11	1.90	0.167	-4.53
220773	F9	7.09	0.63	3.66	20.6	49	5940	4.24	0.09	1.50	1.16	4.40	0.159	-4.98

Table 2.1: Stellar properties.

^{b}[126]
^{c}[37]

measurements of the Mount Wilson S_{HK} index. For each of these stars, we obtain S_{HK} simultaneously with radial velocity, so we include those values in the RV tables. From the average value of these measurements, we derive (via [169]) $\log R'_{HK}$, the ratio of Ca H and K emission to the integrated luminosity of the star, which we include in Table 5.1. The activity indicators are discussed in detail for each star below, but we note here that the sample overall appears to be very quiet, and we have no reason to suspect stellar variability as the cause of the observed signals.

As a second fail-safe against photospheric activity mimicking Keplerian motion, we calculate the bisector velocity spans (BVS) for spectral lines outside the I_2 absorption region. As described in [28], this calculation offers information regarding the shapes of the stellar absorption lines in our spectra. As photospheric activity that might influence RV measurements occurs, it alters the shapes of these lines, causing a corresponding shift in the BVS. Our BVS, then, offer a record of the activity of our target stars. Provided our planetary signals are real, we expect the BVS to be uncorrelated with our RV measurements. For each RV point, we have a corresponding BVS measurement computed from the average of the stellar lines outside the I_2 region.

2.3.2 Orbit Fitting

To determine the orbital parameters of each planetary system, we first analyze each RV set using the fully generalized Lomb-Scargle periodogram [240]. We estimate the significance of each peak in the periodogram by assign-

ing it a preliminary false-alarm probability (FAP) according to the method described in [209]. To conclude our periodogram analysis, we assign a final FAP for each planet using a bootstrap resampling technique. Our bootstrap method, which is analogous to the technique outlined in [131] retains the original time stamps from the RV data set, and selects a velocity from the existing set (with replacement) for each observation. We then run the generalized Lomb-Scargle periodogram for the resampled data. After 10,000 such trials for each data set, the FAP is taken to be the percentage of resampled periodograms that produced higher power than the original RV set. Power in the [240] periodogram is given by $\Delta\chi^2 \equiv \chi_0^2 - \chi_P^2$, or the improvement of fit of an orbit at period P over a linear fit, so a "false positive" result in the bootstrap trial occurs when a random sampling of our measured RVs is better suited to a Keplerian orbit than the actual time series. In Table 2.2, we include both FAP estimates for comparison, but we adopt this bootstrap calculation as our formal confidence estimate.

The periods identified in the periodograms are then used as initial estimates for Keplerian orbital fits, which we perform with the GaussFit program [113]. We list the orbital parameters of each planet in Table 2.2, and describe the individual systems in detail below. As a consistency check, we also fit each orbit using the SYSTEMIC console [160], finding good agreement between our results in every case. An additional advantage of the SYSTEMIC console is that it computes a stellar "jitter" term–a measure of random fluctuations in the stellar photosphere–(e.g. [183]) for each star, which we include in Table

2.2.

2.4 New Planetary Systems

2.4.1 HD 79498

2.4.1.1 RV Data and Orbit Modeling

Our RV data for HD 79498 consist of 65 observations taken over 7 years from the 2.7 m telescope. The data have an RMS scatter of 18.3 m/s and a mean error of 4.15 m/s, indicating significant Doppler motion. Our RVs are listed in Table 2.3, and plotted in Figure 2.1.
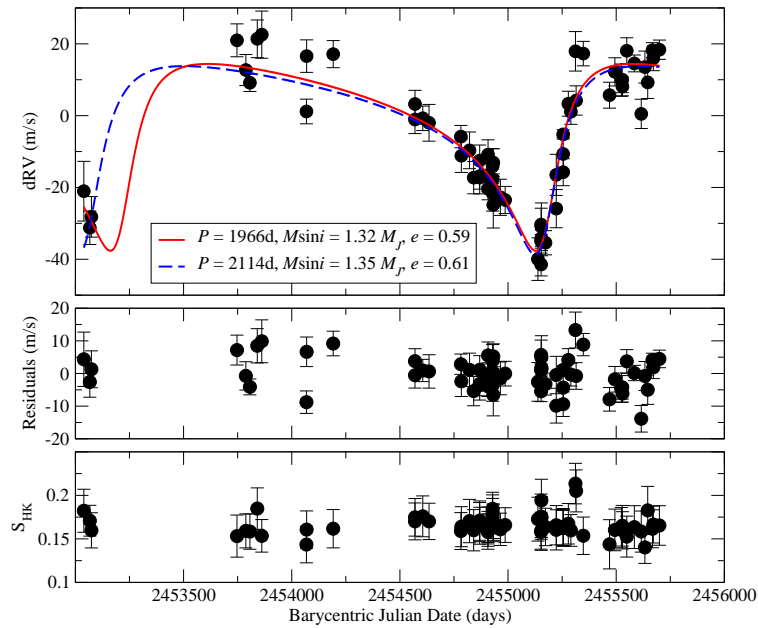
Figure 2.1: *Top*: Radial velocity data for HD 79498. The best-fit orbit model is shown as a solid red line. Our second acceptable fit is also included, shown as a dashed blue line. *Middle*: Residual RVs after subtraction of a one-planet fit. *Bottom*: S_{HK} as measured at each RV point.

17

	HD 79498b	HD 155358		HD 197037b[d]	HD 220773b
		b	c		
Period P (days)	1966.1 ± 41	194.3 ± 0.3	391.9 ± 1	1035.7 ± 13	3724.7 ± 463
Periastron Passage T_0	3210.9 ± 39	1224.8 ± 6	5345.4 ± 28	1353.1 ± 86	3866.4 ± 95
(BJD - 2 450 000)					
RV Amplitude K (m/s)	26.0 ± 1	32.0 ± 2	24.9 ± 1	15.5 ± 1	20.0 ± 3
Mean Anomaly $M_0{}^{\mathrm{e}}$	$329° \pm 11°$	$129° \pm 0.7°$	$233° \pm 0.9°$	$186° \pm 3°$	$226° \pm 13°$
Eccentricity e	0.59 ± 0.02	0.17 ± 0.03	0.16 ± 0.1	0.22 ± 0.07	0.51 ± 0.1
Longitude of Periastron ω	$221° \pm 6°$	$143° \pm 11°$	$180° \pm 26°$	$298° \pm 26°$	$259° \pm 15°$
Semimajor Axis a (AU)	3.13 ± 0.08	0.64 ± 0.01	1.02 ± 0.02	2.07 ± 0.05	4.94 ± 0.2
Minimum Mass $M \sin i$ (M_J)	1.34 ± 0.07	0.85 ± 0.05	0.82 ± 0.07	0.79 ± 0.05	1.45 ± 0.3
RMS (m/s)	5.13	6.14		8.00	6.57
Stellar "jitter" (m/s)	2.76	2.49		2.02	5.10
FAP (from periodogram)	4.09×10^{-9}	1.15×10^{-11}	$< 10^{-14}$	8.53×10^{-8}	$\cdots$
FAP (from bootstrap)	$< 10^{-4}$	$< 10^{-4}$	$< 10^{-4}$	$< 10^{-4}$	$\cdots$

Table 2.2: Derived planet properties.

[d]Parameters include subtraction of linear RV trend in residuals
[e]Evaluated at the time of the first RV point reported for each system

The periodogram for the HD 79498 RVs reveals a large peak around 1815 days, with a preliminary FAP of 4.09×10^{-9}. Performing a Keplerian fit with $P = 1815$ days as an initial guess, we find a single-planet solution with the parameters $P = 1966$ days, $e = 0.59$, and $K = 26.0$ m/s, indicating a planetary companion with $M \sin i = 1.34 M_J$ at $a = 3.13$ AU. Considering the high eccentricity and the width of the periodogram peak, these values are in good agreement with our initial guess. This fit produces a reduced $\chi^2 = 1.77$ with an RMS scatter of 5.13 m/s around the fit. We note that we have not included the stellar "jitter" term in our error analyses, but we have verified that most of the χ^2 excess above unity can be attributed to our fitted value of 2.76 m/s. In a series of 10^4 trials of our bootstrap FAP analysis, we did not find an improvement in $\Delta \chi^2$ for any resampled data set, resulting in an upper limit of 10^{-4} for the FAP of planet b. Figure 2.1 shows our fit, plotted over the time-series RV data. We include the full parameter set for HD 79498b in Table 2.2.

Our analysis of HD 79498b admits a second, slightly different orbital solution of nearly equal significance. This solution converges at $P = 2114$ days, $e = 0.61$, and $K = 26.2$ m/s. The corresponding planetary parameters then become $M \sin i = 1.35 M_J$ and $a = 3.27$ AU. For comparison, we include the plot of this fit in Figure 2.1. Although the shorter-period solution may appear to be driven mainly by the first data point, we note that our fitting routines converge to the 1966-day period regardless of whether that point is included, and that the fitting statistics are still better for the shorter period

with the point excluded. Clearly, the qualitative properties of the planet remain unchanged regardless of the choice of parameters. However, because of the slightly better fitting statistics ($\chi^2 = 1.77$ versus $\chi^2 = 1.84$, RMS = 5.13 m/s versus RMS = 5.50 m/s) for the first model, we adopt it as our formal solution.

We computed the periodogram of the residuals around the fit of HD 79498b to search for additional signals. We see no evidence of additional planets in the system. We note that no additional signals appear in the residuals of the alternate fit for planet b either.

2.4.1.2 Stellar Activity and Line Bisector Analysis

With a $\log R'_{HK} = -4.66$, HD 79498 appears to be a low-activity star, and our indicators corroborate that notion. Our line bisector velocity spans are well behaved, with an RMS scatter of 19 m/s, below the K amplitude of planet b. The BVS are uncorrelated with the measured RVs, and a periodogram reveals no periodicity in the bisector velocities. Likewise, the S_{HK} time series shows no significant signals, and no correlation with the RV series. All measures suggest that HD 79498 is a very quiet star, and should neither mask nor artificially produce large-amplitude RV signals such as the one discussed above.

2.4.1.3 Stellar Companions

HD 79498's location on the sky places it near two faint ($V = 10, 11$) stars, each separated by approximately 60 arcseconds [63]. When examining the proper motions of all three stars, though, we see that only the southern companion, BD+23 2063B, is actually associated with HD 79498, making it a double star system [15]. At a distance of 49 parsecs, the companion star is located at a minimum distance $d \sim 2900$ AU from HD 79498. Given an overly generous mass estimate of $M = 1M_\odot$, the secondary star would impart a gravitational acceleration of just $GM_\odot/d^2 = 0.022$ m s^{-1} yr^{-1}, well below the sensitivity of our instrument. Furthermore, at 2900 AU, the orbital period of the companion would be sufficiently long to appear as a linear slope in our data, not the orbit discussed above. It is possible, however, that the presence of this distant star may excite Kozai cycles [128, 140] in HD 79498b, which serve to maintain its high eccentricity (see, e.g. [120, 231]).

2.4.2 HD 197037
2.4.2.1 RV Data and Orbit Modeling

We have obtained 113 RV points for HD 197037 over 10 years from the 2.7 m telescope. These data have an RMS scatter of 13.1 m/s and a mean error of 7.65 m/s. We report our measured RVs in Table 2.5, and plot them as a time series in Figure 2.2.

Our periodogram analysis of HD 197037, shown in Figure 2.3(a), indicates a strong peak around $P \sim 1030$ days. The power in this peak corresponds
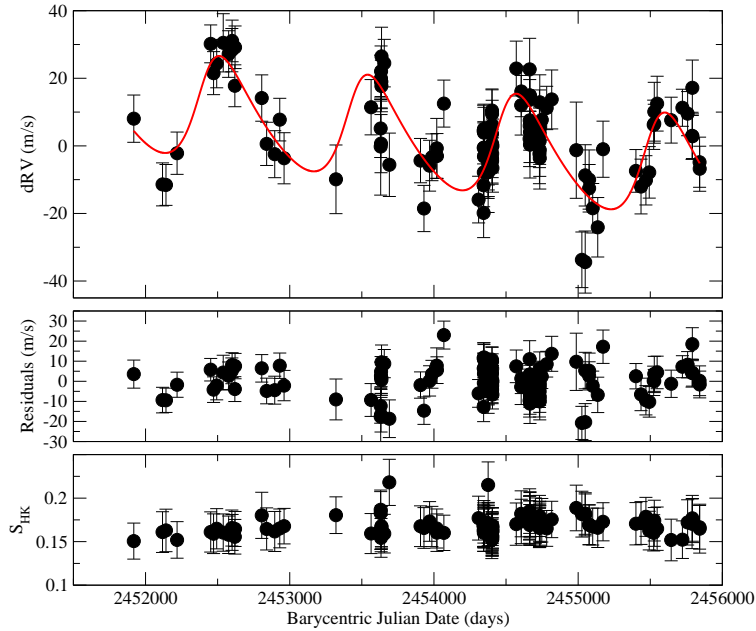
Figure 2.2: *Top*: Radial velocity data for HD 197037. The best-fit orbit model is shown as a solid red line. *Middle*: Residual RVs after subtraction of a one-planet fit and a linear trend. *Bottom*: S_{HK} as measured at each RV point.

to a preliminary FAP of 8.53×10^{-8}. Our one-planet Keplerian model yields parameters of $P = 1036$ days, $e = 0.22$, and $K = 15.5$ m/s, showing excellent agreement with the prediction of our periodogram. The inferred planet has a minimum mass of $0.79 M_J$ and lies at an orbital separation of 2.07 AU. We overplot our model with the RVs in Figure 2.2.

The addition of a single Keplerian orbit only reduces the residual RMS of our RVs to 9.18 m/s, which is nearly a factor of two worse than our other one-planet fits. Furthermore, the periodogram of the residual RVs (Figure 2.3(a)) shows a significant increase in power at long periods. While any addi-

22

tional periods are too far outside our observational time baseline to properly evaluate, we can generate a preliminary two-planet fit with a second $\sim 0.7 M_J$ planet with a period around 4400 days and an eccentricity 0.42. However, our current RV set can also be modeled as a single planet and a linear trend with slope -1.87 ± 0.3 m s^{-1} yr^{-1}. Both fits give a χ^2 of 1.10 and an RMS scatter of 8.00 m/s, so we adopt the more conservative planet-plus-slope model pending further observations. HD 197037 has no known common proper motion companions within 30 arcseconds, so it is very possible that we are seeing evidence for a distant giant planet or brown dwarf companion. The final orbital parameters reported in Table 2.2 are derived from the planet+slope model. We note that we see no additional signals in the residuals of either the two-planet or planet-slope fits.

2.4.2.2   Stellar Activity and Line Bisector Analysis

Even after accounting for the linear trend in the residuals around our fit to planet b, the scatter in our RVs is still higher than we typically expect from our 2.7 m data. Because HD 197037 is an earlier type (F7) than the other stars discussed in this study, we expect a lower precision as a result of fewer spectral lines to determine velocities. Additionally, with $\log R'_{HK} = -4.53$, it is the most active of the stars presented here. With an RMS scatter in the bisector velocity spans of 13 m/s, we must take particular care to ensure we have not mistaken an activity cycle for a planetary signal. In Figure 2.4, we show our measured BVS and S_{HK} indices, which we use to evaluate the

influence of stellar photospheric activity on the signal of HD 197037b. Using both a Pearson correlation test and least-squares fitting, we find no correlation to the RVs for the BVS. While the S_{HK} indices appear somewhat correlated with the RVs to the unaided eye, the Pearson correlation coefficient of -0.26 indicates that the relation is not statistically significant. Periodogram analysis (Figure 2.3(b)) shows no power at the 1030 day peak in the BVS or S_{HK} time series. We do see a modestly (FAP = 0.01) significant peak at 19.1 days in the periodogram of our S_{HK} measurements, which we speculate may be the stellar rotation period. Although we are admittedly unable to completely rule out the possibility of stellar activity as the source of our observed RV signal, the lack of correlation between our activity indicators and the velocities, and the absence of periodicity in S_{HK} and BVS around the fitted period lead us to the conclusion that a planetary orbit is the most likely cause.

While the stellar activity measurements reinforce the planetary nature of the primary RV signal of planet b, the analysis of the long-term trend is not so clear. Our periodograms of the BVS and S_{HK} series both show an increase in power at very long periods, matching the behavior of the trend in the residual RVs, albeit at much lower power. Furthermore, we see a correlation between S_{HK} and the residual RVS around the one-planet fit with a Pearson correlation coefficient of -0.33, which is significant for the size of our data set. The residual RVs are uncorrelated with the BVS, though, so the trends may be coincidental. HD 197037 will need continued monitoring to determine the true nature of this long-period signal.
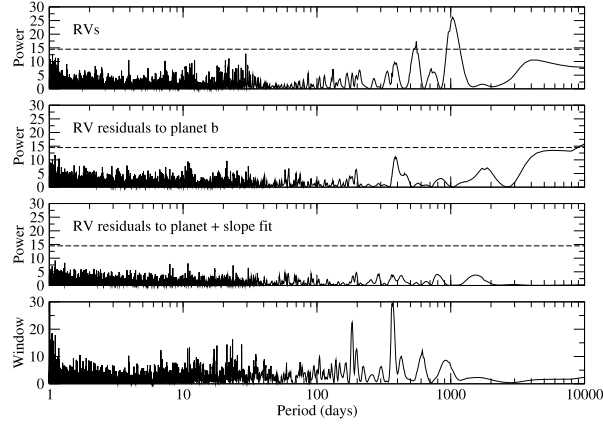
(a)
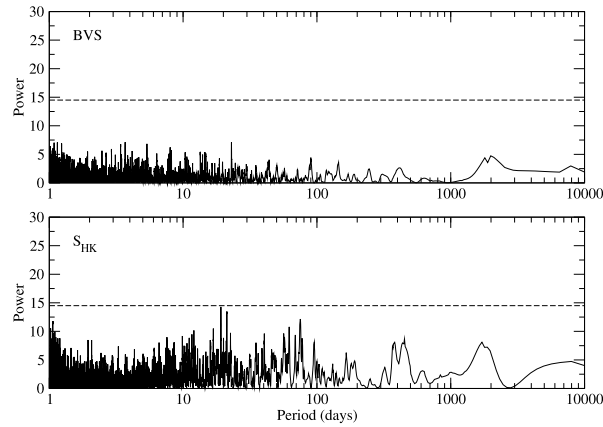
(b)

Figure 2.3: a. *From top*: [*1*] Generalized Lomb-Scargle periodogram for HD 197037 RVs. [*2*] The same periodogram for the residual RVs after subtracting a one-planet fit. [*3*] Periodogram of the residual RVs after subtracting a one-planet fit and a linear trend. [*4*] Periodogram of our time sampling (the window function). b. Generalized Lomb-Scargle periodograms for the BVS (*top*) and S_{HK} indices (*bottom*) of our spectra for HD 197037. The dashed lines indicate the approximate power level for a FAP of 0.01.

25
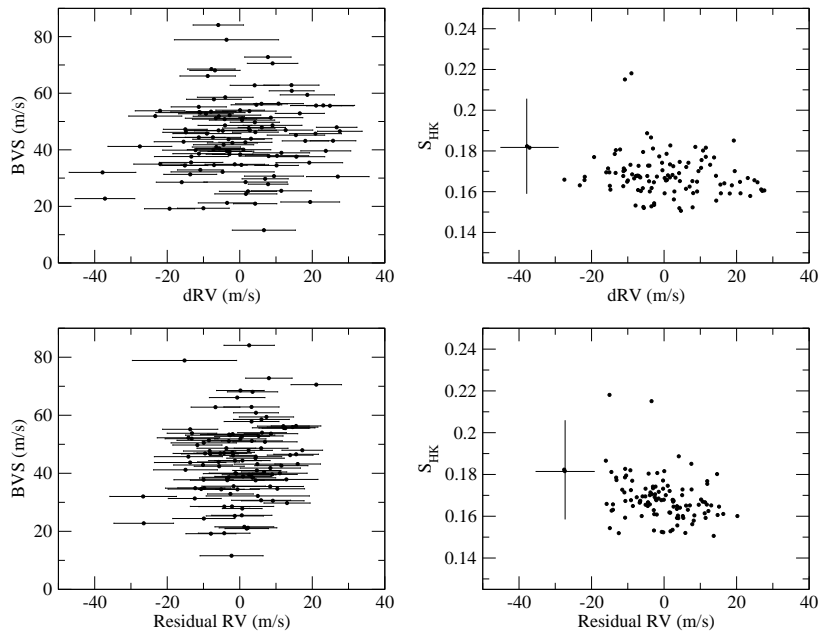
Figure 2.4: *Left*: Bisector velocity spans plotted against our measured RVs (*top*) and residual RVs to a one-planet fit (*bottom*) for HD 197037. *Right*: S_{HK} indices plotted against our measured RVs (*top*) and residual RVs to a one-planet fit (*bottom*) for HD 197037. The error bars shown are representative of the data set.
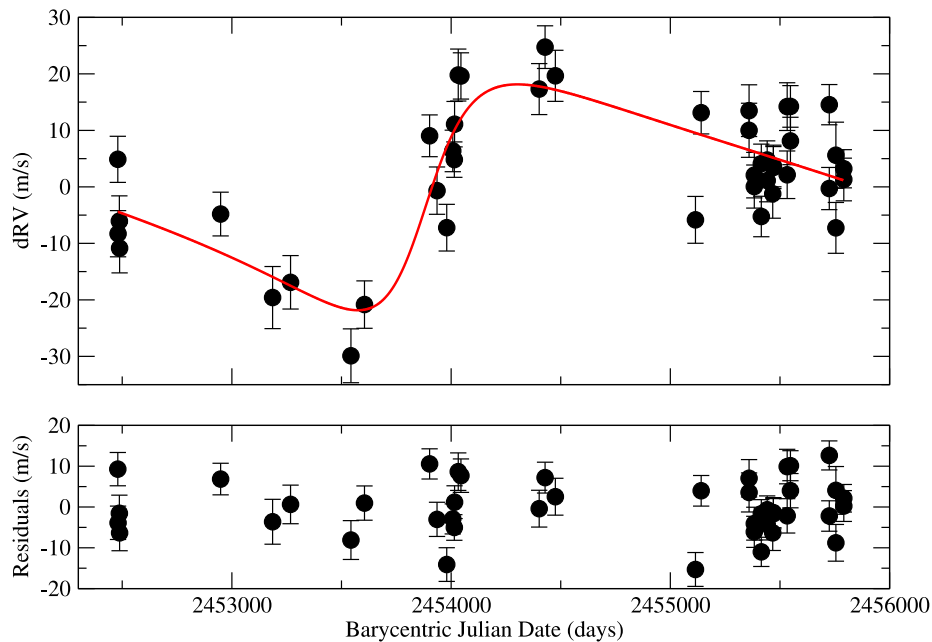
Figure 2.5: *Top*: Radial velocity data for HD 220773. The best-fit orbit model is shown as a red line. *Bottom*: Residuals to a one-planet fit.

2.4.3 HD 220773

2.4.3.1 RV Data and Orbit Modeling

Our RV data set (Table 2.6) for HD 220773 consists of 43 HET/HRS spectra taken over 9 years between July 2002 and August 2011. The data have an RMS of 11.7 m/s and a mean error of 4.11 m/s.

Based on our data, we find evidence for a highly eccentric giant planet on a long-period orbit. Because of its high eccentricity, the period of planet b

27

does not appear at significant power in our periodogram analysis. However, the high RMS of our RV set, combined with the characteristic eccentric turnaround of the velocity time series (Figure 2.5), strongly indicate the presence of a planetary companion. In order to offset the lack of information from the periodogram, we have run GAUSSFIT with a broad range of periods (2500d-4500d) and eccentricities (0.4-0.7). All fits converge unambiguously to a period of 3725 days with an eccentricity of 0.51, indicating a $1.45M_J$ planet at 4.94 AU. We include the plot of this model in Figure 2.5. The final fit gives a reduced χ^2 of 3.14 and an RMS scatter of 6.57 m/s. Because the reduced χ^2 is so high, we have computed the model again after adding the 5.10 m/s "jitter" term in quadrature to the errors listed in Table 2.6. While our fitted parameters and uncertainties do not change significantly from the values given in Table 2.2, the reduced χ^2 drops to 1.18, lending additional confidence to our solution. We do not currently see any evidence for additional signals in the residual RVs.

To confirm the orbital parameters listed in Table 2.2, we use a genetic algorithm to explore the parameter space and evaluate the likelihood of the null hypothesis. The algorithm fits a grid of parameters (number of planets, masses, periods, eccentricities) to the RV set, allowing for a thorough exploration of how χ^2 behaves in response. Areas of parameter space which do not match the data are iteratively rejected, allowing the routine to converge on an optimal solution. We have performed 10,000 iterations of the algorithm with our RV data, considering periods between 3000 and 10,000 days. For this experiment,
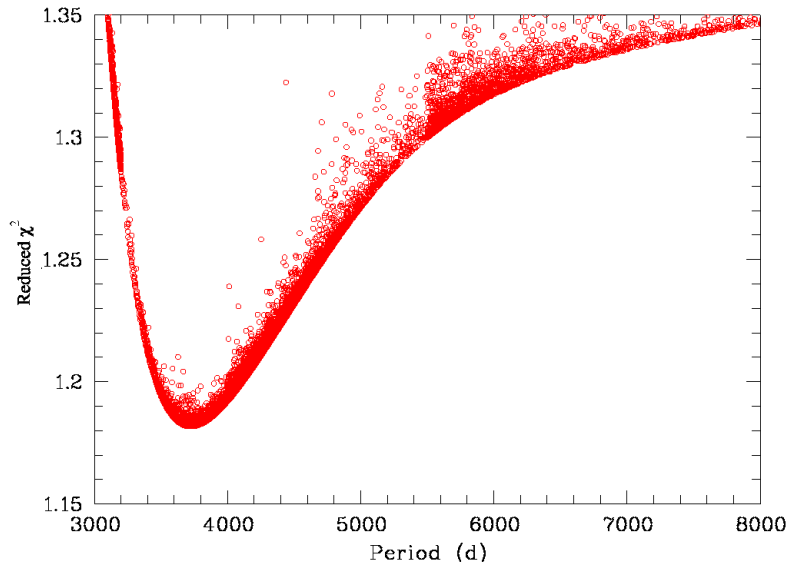
Figure 2.6: Genetic algorithm results for HD 220773. Each circle indicates the minimum χ^2 reached by fitting a one-planet orbit at the given period.

we have again added the stellar "jitter" term to our measurement errors. As shown in Figure 2.6, the genetic algorithm reaches $\chi^2 < 1.20$ for a one-planet model with periods close to our fitted value in Table 2.2. This is a dramatic improvement over a zero-planet model, which yields $\chi^2 = 3.65$.

2.4.3.2 Stellar Activity and Line Bisector Analysis

Our bisector velocity spans for HD 220773, which have an RMS scatter of 24 m/s, show no correlation to our measured RVs, and a periodogram analysis of the BVS shows no power around the period of planet b. While the periodogram signal for the RVs did not meet the criterion for a positive detection, there was a broad peak centered around the ~ 4000 day period of

the planet. The BVS, on the other hand, show no evidence whatsoever for a long-period trend or signal. We conclude, then, that the BVS do not indicate stellar activity which could mimic the behavior of this long-period planet. Likewise, while the HRS does not provide time-series S_{HK} information, our 2.7 m stellar spectrum does offer a "snapshot" value of $\log R'_{HK}$. From this spectrum, we derive $\log R'_{HK} = -4.98$, which is consistent with the low activity level suggested by the BVS analysis.

2.5 Updated Planetary Parameters for HD 155358

HD 155358 has previously been identified as a two-planet system by the McDonald Observatory Planet Search Program [44]. It is a notable system because it hosts two giant planets despite having a measured [Fe/H] among the lowest of any stars with substellar companions of an unambiguously planetary nature (excepting HIP 13044 [200], which apparently originates outside the Galaxy). [82] analyze its chemical abundances in more detail, leading them to claim that the star is actually a member of the thick disk population of the Galaxy, a claim strengthened by the > 10 Gyr age estimate of [37]. While our updated analysis suggests a metallicity of [Fe/H] = -0.51, rather than our original estimate of [Fe/H] = -0.68, the system is still extremely metal-poor relative to the other known exoplanetary systems. Continued monitoring of HD 155358 has caused us to reevaluate our previously reported orbital parameters, resolving the ambiguity in the period of planet c discussed in [44].

2.5.1   RV Data and Orbit Modeling

Since the publication of [44], we have obtained 51 additional RV points
for HD 155358 from HET. We have re-reduced all of our spectra with the latest
version of AUSTRAL for consistency, and include all 122 points in Table 2.4.
The entire set of velocities, shown as a time series in Figure 2.7(a), covers
approximately 10 years from June 2001 until August 2011. These RVs have
an RMS scatter of 30.2 m/s, much higher than we expect from a mean error
of just 5.38 m/s.

We include the periodogram and window function for HD 155358 in
Figure 2.8(a). As expected, we see a significant peak around 196 days, with
a preliminary FAP of 1.15×10^{-11}. Fitting a one-planet orbit from this peak,
we find an RV amplitude $K = 32$ m/s with a period $P = 195$ days and an
eccentricity of $e = 0.23$. Based on this fit, HD 155358b has a minimum mass
of 0.85 Jupiter masses at $a = 0.64$ AU.

[44] note that the periodogram for the residuals around the one-planet
fit to planet b initially showed power around 530 days and 330 days. Compar-
ing fits at both periods produced better results at the longer period for our
data at that time. However, the periodogram of the residuals around planet
b for our current data (Figure 2.8(a)) clearly indicates the shorter period as
the true signal. The peak at 391 days has a preliminary FAP too low for
the precision of our code (approximately 10^{-14}), and we no longer see addi-
tional peaks at longer periods. While the window function for our sampling
does show some power at the one-year alias, the period of this periodogram
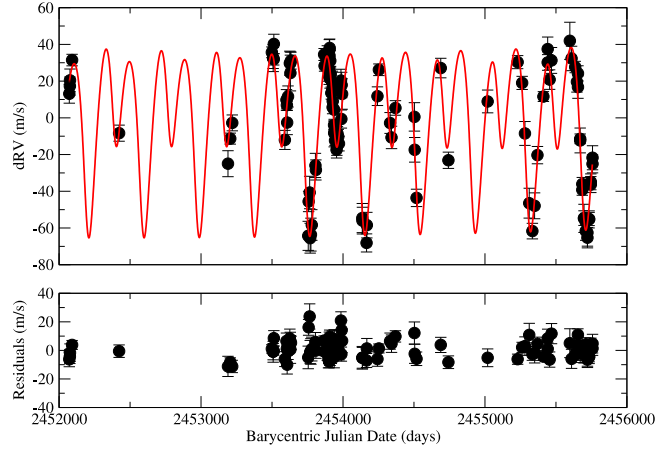
(a)
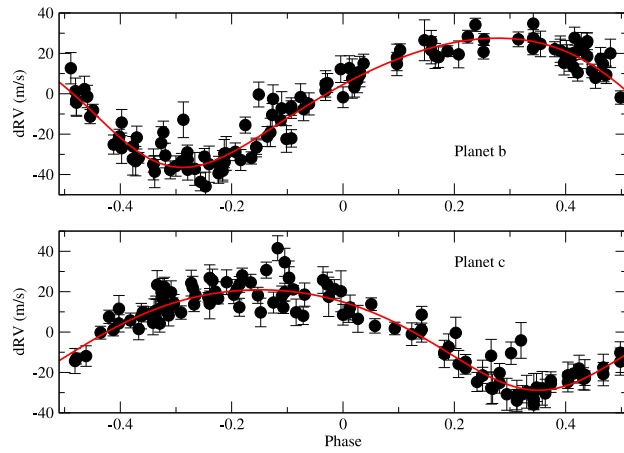
(b)

Figure 2.7: a. *Top*: Radial velocity data for HD 155358. The best-fit orbit model is shown as a red line. *Bottom*: Residuals to a two-planet fit. b. Phase plots for planets b (*top*) and c (*bottom*). In each plot, the signal of the planet not shown has been subtracted from the RVs.
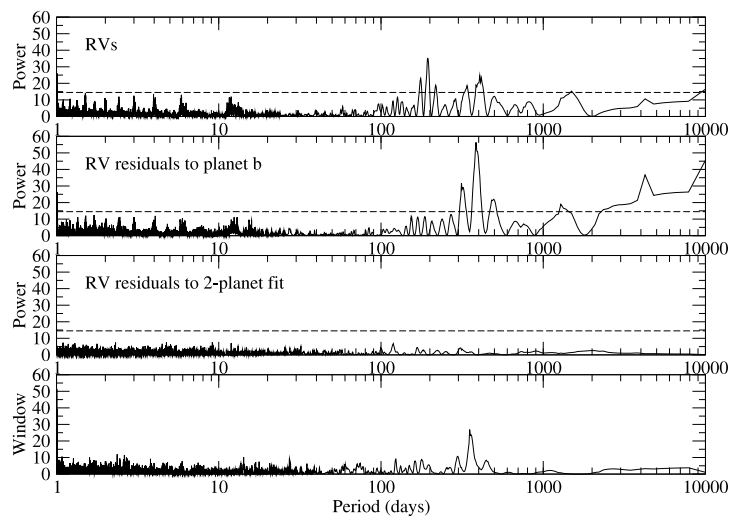
(a)
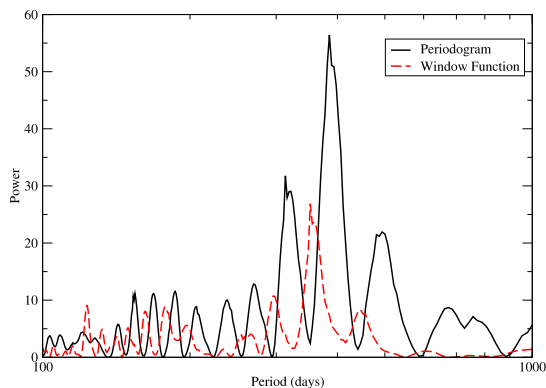
(b)

Figure 2.8: a. *From top*: [*1*] Generalized Lomb-Scargle periodogram for HD 155358 RVs. [*2*] The same periodogram for the residual RVs after subtracting a one-planet fit. [*3*] Periodogram of the residual RVs after subtracting a two-planet fit. [*4*] Periodogram of our time sampling. The dashed lines indicate the approximate power level for a FAP of 0.01. b. Periodogram for planet c (black) with the window function (red).

33

peak is sufficiently separated from the yearly alias (Figure 2.8(b)) that we are confident the signal is not due to our sampling.

Using 391 days as a preliminary guess for the period of planet c, we performed a two-planet fit to our RVs. This updated fit changes the parameters of planet b to $P = 194.3$ days, $M \sin i = 0.85 M_J$, and $e = 0.17$, with the orbital separation remaining at 0.64 AU. Planet c then converges to a period of 391.9 days, with $e = 0.16$ and $K = 25$ m/s. The derived properties for planet c then become $M = 0.82 M_J$ and $a = 1.02$ AU. We plot this orbit over our RV data in Figure 2.7(a). The addition of planet c reduces our RMS to 6.14 m/s with a reduced χ^2 of 1.41. As a consistency check, we test a fit with parameters for planet c more closely matching those from [44], but find no satisfactory solution at this longer period. Holding the parameters for planet c fixed at the values derived in that study result in a reduced χ^2 of 11.2 and a residual RMS of 15.4 m/s.

2.5.2   Stellar Activity and Line Bisector Analysis

The BVS for HD 155358 display an RMS scatter of 25 m/s, and are uncorrelated with both the RVs and the residuals to the 2-planet fit. Additionally, we see no significant peaks in the periodogram of the BVS time series. Also, while we present HET velocities here, we do have some 2.7 m spectra from a preliminary investigation of HD 155358, allowing us to examine the Ca H and K indices. S_{HK} shows very little activity, and we derive a $\log R'_{HK}$ of -4.54. The hypothesis that the two large-amplitude signals observed here are

due to stellar activity can therefore conclusively be ruled out.

2.5.3   Dynamical Analysis of 3-body System

Even at the separation claimed in [44], planets b and c are close enough to interact gravitationally. Our updated orbital model now indicates they are actually much closer together. While their periods suggest the planets are in a 2:1 mean motion resonance, our preliminary orbital simulations showed the system to be unstable for a range of input values. We therefore decided to perform a highly detailed dynamical study of the system to investigate whether the orbits that best fit the data are indeed dynamically feasible. To do this, we performed over 100,000 unique simulations of the HD 155358 system using the Hybrid integrator within the n-body dynamics package MERCURY [39].

To systematically address the stability of the HD 155358 system as a function of the orbits of planets b and c, we followed [104] and [155], and examined test systems in which the initial orbit of the planet with the most tightly constrained orbital parameters (in this case planet b) was held fixed at the nominal best fit values. The initial orbit of the outermost planet was then systematically changed from one simulation to the next, such that scenarios were tested for orbits spanning the full $\pm 3\sigma$ error ranges in semi-major axis, eccentricity, longitude of periastron and mean anomaly. Such tests have already proven critical in confirming or rejecting planets suggested to move on unusual orbits (e.g. [235]), and allow the construction of detailed dynamical maps for the system in orbital element phase space.

Keeping the initial orbit of the innermost planet fixed, we examined 31 unique values of semi-major axis for planet c, ranging from 0.96 AU to 1.08 AU, inclusive, in even steps. For each of these 31 initial semi-major axes, we studied 31 values of orbital eccentricity, ranging from the smallest value possible (0.0) to a maximum of 0.46 (corresponding to the best fit value, 0.16, plus three sigma). For each of the 961 *a-e* pairs, we considered 11 values of initial mean anomaly and initial longitude of periastron (ω), resulting in a total suite of 116281 ($31 \times 31 \times 11 \times 11$) plausible architectures for the HD 155358 system.

In each simulation, the planet masses were set to their minimum ($M \sin i$) values; the mass of the innermost planet was set to $0.85 M_J$, and that of the outermost was set to $0.82 M_J$. As such, the dynamical stability maps obtained show the maximum stability possible (since increasing the masses of the planets would clearly increase the speed at which the system would destabilize for any nominally unstable architecture). The dynamical evolution of the two planets was then followed for a period of 100 million years, or until one of the planets either collided with the central star, was transferred to an orbit that took it to a distance of at least 10 AU from the central star, or collided with the other planet.

The results of our simulations are shown in Figures 2.9-2.10. We present the multi-dimensional grid of orbital parameters over which we ran our simulations as two-dimensional cross sections, indicating the mean and median stability lifetimes over each of the runs at each grid point. So, for example,

each grid point in our plots in a-e space reveals either the mean or the median of 121 unique simulations of an orbit with those particular a-e (i.e. 11 in ω times 11 in mean-anomaly). Similarly, each point in the a-ω plots corresponds to the mean (or median) of 341 separate trials (31 in e times 11 in ω).

The first thing that is apparent from Figure 3.5(a), which shows the mean lifetime of the system as a function of semi-major axis and eccentricity, is that the stability of the system is a strong function of eccentricity. Solutions with low orbital eccentricity are typically far more dynamically stable than those with high eccentricity. In addition, the stabilizing effect of the 2:1 mean-motion resonance between planets b and c can be clearly seen as offering a region of some stability to even high eccentricities between $a \sim 1.05$ and 1.25 AU. However, it is apparent when one examines the median lifetime plot (Figure 2.9(b)) that a significant fraction of eccentric orbits in that region are dynamically unstable (the reason for the apparently low median lifetimes in that region). The reason for this is that the dynamical stability of orbits in this region, particularly for high eccentricities, is also a strong function of the initial longitude of periastron for planet c's orbit. Indeed, comparison of this figure to those showing the influence of the longitude of periastron for planet c reveals that the most stable regions therein lie beyond the 1σ error bars for the nominal orbit. For low eccentricities ($e < 0.1$), in the vicinity of the 2:1 resonance, then the orbit is stable regardless of the initial longitude of periastron, but for high eccentricities ($e > 0.15$), the stable regions lie towards the edge of the allowed parameter space, making such a solution seem relatively

37
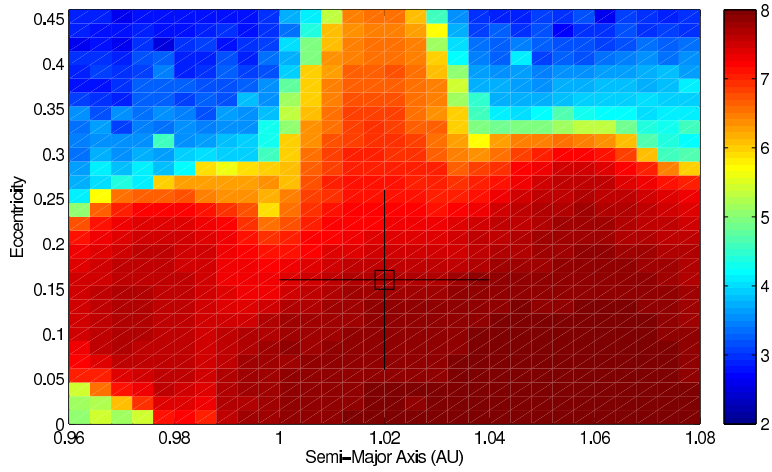
(a)
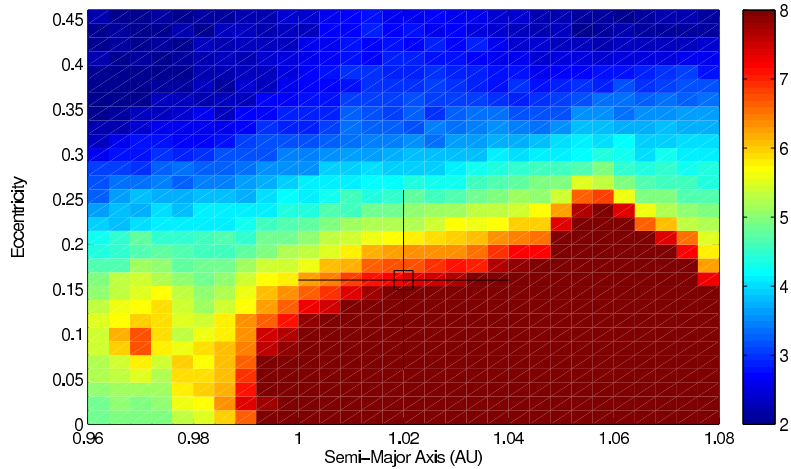
(b)

Figure 2.9: Results of our stability analysis for the HD 155358 planetary system in $a - e$ space. At each grid point, we have run 25 dynamic simulations with planet c at that point, with planet b remaining fixed at the configuration given in Table 2.2. The resulting intensity indicates the mean (a) or median (b) lifetime of the planet over those 25 runs in log years. Longer lifetimes indicate a more stable configuration. The crosshairs indicate our best-fit parameters as derived from the RV data (Table 2.2).
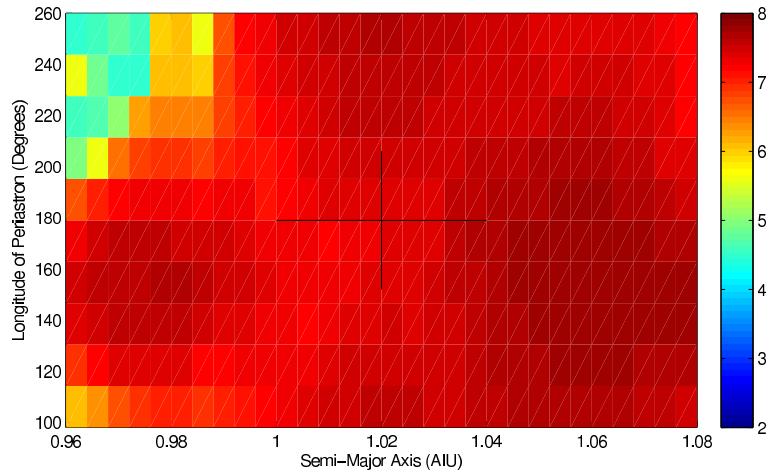
(a)
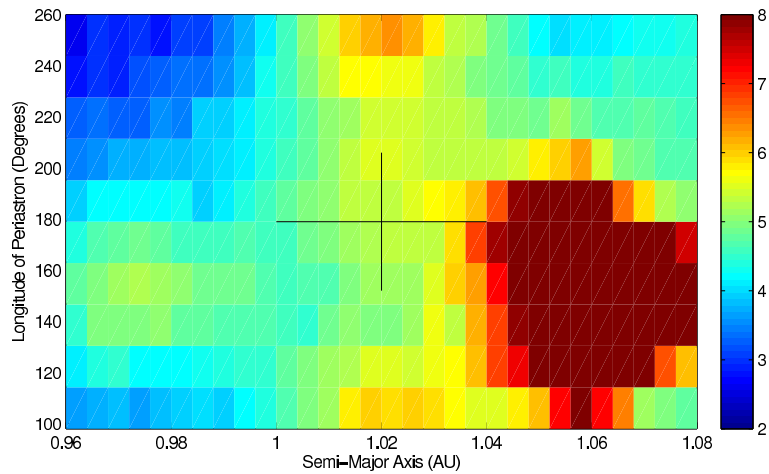
(b)

Figure 2.10: Results of our stability analysis for the HD 155358 planetary system in $a - \omega$ space. At each grid point, we have run 25 dynamic simulations with planet c at that point, with planet b remaining fixed at the configuration given in Table 2.2. The resulting intensity indicates the mean (a) or median (b) lifetime of the planet over those 25 runs in log years. Longer lifetimes indicate a more stable configuration. The crosshairs indicate our best-fit parameters as derived from the RV data (Table 2.2).

39

improbable.

It is apparent from close examination of Figure 2.9(b) (which shows the median stability as a function of semi-major axis and eccentricity) that the key determinant of the stability of the system (particularly for non-resonant orbits) is actually the periastron distance of planet c. The sculpted shape of the stability plot, outwards of $a \sim 0.98$ AU, is very similar to that observed for the proposed planets around the cataclysmic variable HU Aquarii [104, 235]. As was found in that work, the dividing line between unstable and stable orbits again seems to fall approximately five Hill radii beyond the orbit of the innermost planet. Any orbit for planet c that approaches the orbit of b more closely than this distance will be unstable on astronomically short timescales (aside from those protected from close encounters by the effects of the 2:1 mean motion resonance between the planets). On the other hand, orbits which keep the two planets sufficiently far apart tend to be dynamically stable. We note, too, that the sharp inner cut-off to this broad region of stability, at around 0.99 AU, corresponds to the apastron distance of the innermost planet plus five Hill radii. Once again, orbital solutions that allow the two planets to approach closer than five times the Hill radius of the inner planet destabilize on relatively short timescales.

The results of our dynamical simulations show that a large range of dynamically stable solutions exist within the 1σ errors on the orbit of HD 155358c. Given the breadth of the resonant feature apparent in Figure 3.5(a) (the mean lifetime as a function of a and e), it seems clear that all orbits within

1σ of the nominal best fit will be strongly influenced by that broad resonance. As such, it seems fair to conclude that these two planets are most likely trapped within their mutual 2:1 mean-motion resonance, although it is also apparent that non-resonant solutions also exist that satisfy both the dynamical and observational constraints. The stability restrictions are consistent with our orbital fit, but the parameters listed in Table 2.2 have not been modified to include the information obtained from the orbital simulations.

2.5.4 Habitability of Exomoons

Using the [Fe/H] and T_{eff} derived herein, an [α/Fe] of 0.32 [82], and an age of 10.7 Gyr [37], we have fit Yonsei-Yale isochrones [58] to HD 155358. With mass estimates ranging from $0.87 M_\odot$ [134] to $0.92 M_\odot$ [37], HD 155358 has a luminosity somewhere between $L_* = 1.14 L_\odot$ and $L_* = 1.67 L_\odot$. If we assume the location of the habitable zone scales as $\sqrt{L_*}$, then at an orbital separation of 1.06 AU, planet c lies within the habitable zone of its parent star (as defined by[119]). Typically, Jovian planets are not considered to be potential habitats for Earth-like life [135]. However, it has been suggested that such planets could host potentially habitable satellites (e.g. [181]), or even that they could dynamically capture planet-sized objects during their migration as

satellites or Trojan companions[f] (e.g. [214]). In fact, the presence of two giant planets on relatively close-in orbits may indirectly increase the water content on terrestrial satellites through radial mixing of planetesimals rich in ices [150], a key requirement for such objects to be considered habitable (e.g. [102]). Furthermore, any satellites sufficiently large to be considered habitable would also be subject to significant tidal heating from their host planet, which would likely act to increase their habitability when they lie towards the outer edge of Kasting's habitable zone (as they would have earlier in the life of the system). The induced tectonics would also potentially improve the habitability of any such moons (e.g. [102]).

Our dynamical analysis suggests that the two planets in the HD 155358 system are most likely trapped in mutual resonance. It might initially seem that such orbits would be variable on the long term, such that they would experience sufficiently large excursions as to render any satellites or Trojan companions uninhabitable. However, we know from our own Solar system

---

[f]Planetary Trojans are a particularly fascinating population of objects, trapped in 1:1 mean-motion resonance with their host planet. Typically, stable Trojans follow horseshoe-shaped paths that librate around either the leading- or trailing-Lagrange points in that planets orbit, located sixty degrees ahead and behind the planet (for a good illustration of such orbits, we direct the interested reader to [101]).

Within our Solar system, both Jupiter and Neptune host significant populations of Trojans that were captured during their migration (e.g. [145, 162]). For those planets, the captured Trojans are typically small, but there is nothing to prevent a giant planet from capturing an Earth-mass object as a Trojan during its migration. Once captured, and once the migration stops, such objects can be dynamically stable on timescales of billions of years (e.g. [103, 147]), even when moving on orbits of significantly different eccentricity and inclination to their host planet. Whilst the detection of such planets would no doubt be challenging (e.g. [77]), they remain an intriguing option in the search for habitable worlds.

that long term resonant captures can be maintained on timescales comparable to the age of the Solar system (e.g. the Neptune Trojans, [146]). As such, it is reasonable to assume that, if the planets are truly trapped in mutual resonance, they could have been on their current orbits for at least enough time for any moons or Trojans of planet c to be considered habitable. However, the current best-fit eccentricity for planet c is sufficiently high that it lies at the outer limit of the range in e that would allow for a habitable exomoon [214], which might limit the potential habitability of any exomoons in the system. That said, the one-sigma range of allowed orbits extends to relatively low eccentricities ($e = 0.06$), which is certainly compatible with potential habitability. As such, it is possible that such moons, if present, could be potential habitats for life.

2.6   Discussion

Of the planets discovered via the radial velocity method, only around 7 percent have $a \geq 3$ AU. The addition of the planets presented here therefore represent a significant contribution to that sample. As more such objects start to fall within the detection limits of RV surveys, our findings provide interesting comparison cases to begin to look for trends in the long-period gas giant population.

Continued monitoring of the HD 79498, HD 197037, and HD 220773 systems is crucial for refinement of planet formation and migration theories. The presence or absence of additional smaller planets will shape our understanding of the migrational history of these systems. [150], for example, predict

markedly different outcomes for the formation and water content of sub-giant planets after migration of a Jovian planet depending on whether or not gas drag plays a significant role in planetary migration.

Of the four stars presented herein, at least one–HD 155358–hosts multiple gas giant planets. Additionally, HD 197037 shows tentative evidence of a yet-undetected substellar companion at $a \sim 5.5$ AU. If the occurrence of multiple-Jupiter systems is as common as it appears in this very small sample, it would support the claim by [210] that the large population of free-floating planetary-mass objects within the Galaxy form in protoplanetary disks as planets. On the other hand, current RV results [232] indicate that multi-giant planet systems should actually be quite rare, at least inside of 2-3 AU. Understanding whether that result remains valid for planets further out, though, will rely heavily on detections of residual long-term trends for planets like HD 197037b.

The orbital evolution of the HD 155358 system is of particular interest, as it provides a comparison case for theoretical work exploring the formation and migration of the Jupiter-Saturn system (e.g. [216]). While Jupiter and Saturn appear to have crossed the 2:1 MMR and later separated, the HD 155358 giants remain locked in resonance, presumably for the entire ~ 10 Gyr lifetime of the system. Accounting for the difference in these final configurations most likely requires different initial architectures, disk masses, and encounter histories for the two systems.

While the stability simulations presented here offer some constraints

44

on the orbital configurations of the HD 155358 system, the true geometries of those planets' orbits will only be fully understood if their mutual inclinations are measured. Unfortunately, the HD 155358 planets will only be accessible to the next generation of astrometric instrumentation, as their predicted astrometric displacements are below the 0.2 mas precision limit of the HST Fine Guidance Sensor [168]. On the other hand, HD 220773b, which has a predicted displacement of 0.242 mas, might be an interesting astrometry target for FGS, both for the purpose of determining a true mass, and to search for outer companions to this distant planet.

The refined orbital parameters for HD 155358c places it, to zeroth order, within the habitable zone. While the planet itself is likely inhospitable to any Earthlike lifeforms, the possibility of habitable moons or Trojans make it an interesting datum for examining more exotic environments for biology [198]. Given the advanced age of the system, any intelligent life residing on planet c is potentially far more advanced than our own civilization. The technological advances accompanying such extended development may make interstellar broadcasts or beacons energetically and financially feasible, making HD 155358 an interesting target for SETI (e.g. [9, 10]).

Our results are somewhat atypical when viewed in the context of the metallicity-frequency correlation for giant planets (e.g. [76]). Only HD 79498 has significantly super-solar metallicity, while HD 197037 and HD 155358 qualify as metal-poor. In the case of HD 197037, its higher mass and earlier spectral type increase its likelihood of forming Jovian planets, at least somewhat off-

setting any metallicity effects [116]. HD 155358, on the other hand, remains a true anomaly despite the slightly higher [Fe/H] reported herein. While the sample presented here is obviously too small to make even tentative statements about the validity of observed correlations, it will be interesting to see whether gas giants continue to be found preferentially around metal-rich stars as long-term RV surveys begin to reveal a large number of Jupiter-mass planets. If the removal of the period bias on the giant planet census reveals a large population of Jovian planets around metal-poor stars, it will serve as strong evidence that at least some gas giants form through gravitational instability of the protoplanetary disk rather than core accretion [24]. Furthermore, the discovery of thick disk planets suggests a planet formation history essentially spanning the age of the Galaxy.

Table 2.3: Radial Velocities for HD 79498

BJD - 2450000	Radial Velocity (m/s)	Uncertainty (m/s)	S_{HK}
3038.86139200	-14.42	8.32	0.1823 ± 0.0247
3066.79412600	-24.59	4.67	0.1709 ± 0.0177
3073.81710000	-21.56	5.65	0.1598 ± 0.0202
3746.91651500	27.61	4.58	0.1532 ± 0.0242
3787.81423800	19.33	4.33	0.1592 ± 0.0195
3806.70783400	15.78	2.43	0.1584 ± 0.0203
3840.75580400	28.03	5.25	0.1848 ± 0.0238
3861.68232900	29.18	6.57	0.1535 ± 0.0187
4067.98581900	7.79	3.44	0.1435 ± 0.0210
4068.90695600	23.21	4.53	0.1607 ± 0.0214
4191.80349000	23.76	3.77	0.1617 ± 0.0220
4569.73532700	9.86	3.82	0.1748 ± 0.0216
4569.74801300	5.54	3.92	0.1701 ± 0.0212
4605.64036800	5.89	3.41	0.1759 ± 0.0235
4634.62414000	4.64	5.12	0.1701 ± 0.0209
4782.01348700	0.79	3.11	0.1590 ± 0.0212
4783.98080700	-4.54	4.65	0.1640 ± 0.0230
4821.93818500	-3.04	5.12	0.1705 ± 0.0249
4840.97668200	-10.65	4.49	0.1599 ± 0.0237
4868.91890100	-10.63	4.53	0.1651 ± 0.0212
4868.93042200	-5.90	4.35	0.1710 ± 0.0226
4868.94194000	-10.23	3.62	0.1693 ± 0.0225
4906.70221500	-9.93	3.16	0.1663 ± 0.0204
4906.71734700	-10.49	4.07	0.1578 ± 0.0197
4907.62242900	-4.23	4.12	0.1602 ± 0.0187
4907.63742600	-13.71	3.10	0.1629 ± 0.0187
4928.68528400	-11.02	4.05	0.1802 ± 0.0204
4928.70027200	-15.00	4.95	0.1845 ± 0.0191
4928.71526200	-7.46	4.88	0.1761 ± 0.0204
4931.63355900	-18.23	6.43	0.1698 ± 0.0194
4931.64625200	-14.05	4.44	0.1657 ± 0.0190
4931.65894600	-6.45	3.87	0.1693 ± 0.0210
4964.66292000	-16.12	5.03	0.1610 ± 0.0186
4986.64365700	-16.87	3.78	0.1659 ± 0.0199
5137.98754800	-33.34	5.93	0.1727 ± 0.0252
5152.96977000	-23.72	4.56	0.1580 ± 0.0212
5152.98476800	-28.36	1.92	0.1594 ± 0.0212

Table 2.3 cont'd.			
BJD - 2450000	Radial Velocity (m/s)	Uncertainty (m/s)	S_{HK}
5152.99976400	-34.83	3.19	0.1755 ± 0.0260
5153.98375300	-27.49	2.26	0.1751 ± 0.0235
5153.99875100	-24.33	6.65	0.1744 ± 0.0227
5154.01374700	-27.91	4.50	0.1941 ± 0.0244
5173.01441600	-28.77	3.36	0.1637 ± 0.0215
5222.85632500	-19.26	5.33	0.1604 ± 0.0231
5222.87135400	-9.87	5.73	0.1657 ± 0.0226
5254.79363200	-4.05	4.53	0.1638 ± 0.0211
5254.80862500	-9.12	3.76	0.1625 ± 0.0211
5254.82361900	1.41	1.30	0.1625 ± 0.0202
5278.74248800	9.95	3.47	0.1674 ± 0.0233
5290.64067500	7.71	3.50	0.1597 ± 0.0182
5311.71658900	24.55	5.50	0.2135 ± 0.0233
5314.69970700	10.85	4.08	0.2051 ± 0.0241
5347.65756900	23.91	3.41	0.1536 ± 0.0215
5468.97994600	12.33	3.61	0.1438 ± 0.0283
5493.95838700	18.82	3.93	0.1603 ± 0.0239
5523.92790400	16.50	4.50	0.1629 ± 0.0231
5527.90018100	16.64	3.61	0.1651 ± 0.0233
5528.98017000	14.76	2.61	0.1598 ± 0.0214
5548.88450200	24.70	3.61	0.1526 ± 0.0235
5583.86404700	21.17	2.35	0.1635 ± 0.0246
5615.70061600	7.11	4.07	0.1584 ± 0.0236
5632.72839900	20.16	4.44	0.1402 ± 0.0184
5645.82335600	15.88	4.48	0.1827 ± 0.0276
5667.76838200	24.85	2.11	0.1616 ± 0.0218
5671.67914300	22.60	3.44	0.1665 ± 0.0212
5699.62389400	24.99	2.69	0.1654 ± 0.0227

Table 2.4: Radial Velocities for HD 155358

BJD - 2450000	Radial Velocity (m/s)	Uncertainty (m/s)
2071.90483700	15.90	5.14
2075.88682700	20.05	4.94
2076.88985600	23.21	6.16
2091.84643500	34.24	3.14
2422.93714300	-5.59	4.38
3189.83913000	-22.21	7.08
3205.79562900	-8.55	3.01
3219.75321500	0.01	4.32

Table 2.4 cont'd.		
BJD - 2450000	Radial Velocity	Uncertainty
	(m/s)	(m/s)
3498.77697700	38.45	2.94
3507.95763400	35.30	7.35
3507.96287000	35.35	5.72
3511.95319500	34.61	3.07
3512.93931400	43.01	5.29
3590.73322900	-9.26	5.19
3601.70090300	12.52	5.64
3604.70193200	9.70	2.00
3606.70299700	0.19	6.58
3612.68403800	14.40	5.74
3625.64546400	32.49	6.59
3628.62430900	32.53	6.13
3629.61946400	27.18	9.73
3633.61627500	33.94	4.62
3755.04213400	-61.50	7.92
3758.04274400	-42.78	5.55
3765.03555800	-37.91	8.84
3769.02604800	-62.77	8.14
3774.02174300	-60.84	8.97
3779.97987100	-55.59	8.35
3805.93069400	-23.17	6.60
3808.89282200	-25.61	5.47
3866.96427700	37.27	3.26
3869.95498800	31.11	2.93
3881.94511600	35.50	3.67
3889.68235900	35.73	6.32
3894.67240300	34.58	3.73
3897.89540600	28.71	5.97
3898.68534400	33.44	6.64
3899.89225300	29.64	4.49
3902.65793200	25.22	4.23
3903.90645200	39.66	5.72
3904.66233800	36.68	3.76
3905.86023400	40.83	4.86
3907.62941500	27.22	3.36
3908.87691000	24.11	5.19
3910.63980200	33.87	5.72
3911.84525200	26.41	3.55
3912.63613800	26.48	4.33
3917.64144300	16.28	3.31

Table 2.4 cont'd.		
BJD - 2450000	Radial Velocity (m/s)	Uncertainty (m/s)
3924.81885900	21.80	6.37
3925.80799400	18.30	5.54
3926.82465700	8.51	3.52
3927.82203900	11.81	2.97
3936.79096100	-1.16	2.34
3937.79035200	-5.54	7.51
3937.80465200	7.17	6.49
3941.76239700	-4.15	4.90
3943.76691400	-9.60	2.65
3954.75689500	-14.66	4.44
3956.73476700	-12.62	5.02
3958.74755200	-10.15	3.92
3960.71484300	-5.65	3.64
3966.70814000	-7.53	4.04
3971.69798700	-11.28	3.98
3985.65146600	23.07	6.17
3988.63745600	2.12	4.94
3990.63945400	20.65	6.94
3993.64492500	15.75	8.30
4136.01098700	-51.82	7.94
4137.00571500	-53.22	7.28
4165.93375900	-65.36	4.93
4167.92406700	-55.67	6.97
4242.72348100	14.56	5.08
4252.92738200	28.95	3.17
4331.70165200	-0.03	5.67
4341.67683000	-7.91	6.11
4369.61238300	8.15	3.97
4503.00826800	3.28	7.75
4505.00883000	-14.65	6.71
4517.96440000	-40.82	4.73
4688.73045100	29.89	5.32
4742.59078800	-20.34	4.44
5018.84957500	11.69	6.21
5230.01528700	33.11	3.56
5261.94061600	21.80	3.57
5281.88078900	-5.74	6.49
5311.81103300	-43.71	8.13
5333.96546600	-58.91	4.25
5349.91269100	-45.15	7.05

Table 2.4 cont'd.		
BJD - 2450000	Radial Velocity (m/s)	Uncertainty (m/s)
5369.85529100	-17.54	4.71
5411.75132000	14.37	2.68
5441.66382200	32.94	4.27
5441.68951000	40.21	6.56
5455.63610500	23.60	5.33
5468.60493300	34.04	7.05
5598.01915300	44.73	10.12
5609.96969700	35.11	6.67
5635.90270500	30.45	3.11
5647.87224300	22.39	5.60
5654.85070000	19.53	6.12
5654.85347500	26.99	4.15
5670.79410300	-9.55	6.76
5670.79685700	-8.67	2.64
5685.78224300	-36.44	2.97
5685.78500500	-33.31	3.62
5697.73042500	-51.99	7.66
5697.73318400	-51.85	3.99
5709.69993000	-58.87	5.08
5709.70269600	-53.93	4.69
5721.89536400	-59.79	7.32
5721.89813000	-62.53	5.51
5733.64282800	-52.33	3.59
5733.64560600	-52.53	4.65
5745.83215500	-33.58	4.35
5745.83491700	-32.08	4.32
5757.80163500	-22.31	4.89
5757.80440100	-18.97	6.54
5769.76209100	-9.53	7.54
5769.76486400	-11.16	3.59
5782.71759900	2.27	6.58
5782.72037000	-0.97	5.78
5794.70209000	10.86	6.73
5794.70486500	15.27	5.42

Table 2.5: Radial Velocities for HD 197037

BJD - 2450000	Radial Velocity (m/s)	Uncertainty (m/s)	S_{HK}
1918.55952342	4.60	6.99	0.1506 ± 0.0207
2117.81076505	-14.85	6.37	0.1610 ± 0.0234
2141.79847525	-15.01	6.05	0.1629 ± 0.0244
2218.67152278	-5.63	6.26	0.1520 ± 0.0210
2451.93562208	26.73	5.60	0.1611 ± 0.0231
2471.88269604	18.07	6.37	0.1591 ± 0.0228
2493.79718560	20.89	7.15	0.1648 ± 0.0231
2538.74935239	27.04	8.62	0.1604 ± 0.0214
2576.61483724	23.72	6.90	0.1579 ± 0.0215
2598.60530888	24.87	6.41	0.1656 ± 0.0207
2600.63887515	27.60	6.16	0.1606 ± 0.0206
2619.60435179	14.33	6.20	0.1556 ± 0.0199
2620.57904934	25.72	6.30	0.1646 ± 0.0201
2805.90471501	10.70	6.85	0.1802 ± 0.0265
2839.84681367	-2.86	6.40	0.1646 ± 0.0242
2895.80593278	-5.91	6.95	0.1617 ± 0.0230
2930.69425024	4.31	6.31	0.1652 ± 0.0223
2960.60916112	-7.12	7.56	0.1678 ± 0.0204
3320.59580442	-13.35	10.17	0.1804 ± 0.0211
3563.95949295	7.98	8.18	0.1593 ± 0.0230
3630.71472969	1.69	8.58	0.1827 ± 0.0248
3630.87333165	-3.65	14.37	0.1866 ± 0.0227
3632.68024096	16.56	6.77	0.1641 ± 0.0229
3632.83643682	-2.79	8.61	0.1543 ± 0.0223
3633.63266139	18.63	7.49	0.1631 ± 0.0219
3633.81885619	15.61	7.83	0.1592 ± 0.0208
3634.65565355	15.49	7.93	0.1635 ± 0.0221
3635.68024320	14.26	7.62	0.1678 ± 0.0235
3636.66099343	23.03	8.64	0.1667 ± 0.0240
3655.70765286	21.04	7.03	0.1592 ± 0.0222
3690.65885729	-9.05	9.38	0.2181 ± 0.0265
3906.92067972	-7.81	6.56	0.1677 ± 0.0234
3930.81642848	-21.98	6.84	0.1657 ± 0.0234
3969.90052141	-9.32	7.53	0.1732 ± 0.0228
3985.77426805	-6.83	6.93	0.1674 ± 0.0231
4019.63256032	-4.18	8.86	0.1651 ± 0.0224
4020.80723692	-6.45	6.65	0.1603 ± 0.0215

Table 2.5 cont'd.			
BJD - 2450000	Radial Velocity (m/s)	Uncertainty (m/s)	S_{HK}
4068.66375417	9.06	6.96	0.1601 ± 0.0203
4309.85063550	-19.35	6.90	0.1770 ± 0.0252
4344.70987089	1.01	7.57	0.1680 ± 0.0244
4344.72024432	-23.29	7.32	0.1631 ± 0.0242
4344.73061543	-15.13	6.33	0.1695 ± 0.0251
4345.71065534	-4.07	7.42	0.1728 ± 0.0244
4345.71987193	-11.29	7.25	0.1677 ± 0.0240
4345.72908610	-3.99	7.69	0.1601 ± 0.0213
4346.70200957	-6.59	8.41	0.1670 ± 0.0230
4346.71122130	1.56	7.33	0.1670 ± 0.0224
4346.72043545	0.46	7.49	0.1655 ± 0.0229
4375.64708486	-11.15	7.87	0.1714 ± 0.0230
4375.65745814	-10.85	12.32	0.2151 ± 0.0265
4376.66244438	-8.84	7.66	0.1685 ± 0.0235
4376.67281521	-7.40	7.64	0.1679 ± 0.0234
4376.68318859	-11.25	7.20	0.1701 ± 0.0250
4401.57166865	-3.54	7.43	0.1528 ± 0.0223
4402.56562465	7.00	6.38	0.1625 ± 0.0219
4402.57542661	0.10	6.71	0.1592 ± 0.0218
4402.66299760	5.99	7.14	0.1614 ± 0.0229
4402.67279979	-7.23	7.22	0.1608 ± 0.0213
4403.55353945	-2.78	5.99	0.1535 ± 0.0191
4403.56276076	-7.91	6.89	0.1532 ± 0.0198
4403.66105457	2.66	7.38	0.1562 ± 0.0199
4403.67027553	-5.76	7.08	0.1525 ± 0.0192
4405.55611954	-3.48	7.97	0.1618 ± 0.0214
4405.56534582	-10.03	7.13	0.1655 ± 0.0231
4570.97352687	19.43	8.12	0.1701 ± 0.0243
4604.92111685	8.57	8.82	0.1820 ± 0.0264
4605.91057844	12.66	7.48	0.1732 ± 0.0255
4662.95425192	11.46	8.31	0.1771 ± 0.0251
4662.96610624	-1.38	8.21	0.1773 ± 0.0251
4663.81542937	19.18	9.20	0.1851 ± 0.0256
4663.85662433	2.50	7.23	0.1725 ± 0.0244
4663.88867894	4.10	6.74	0.1691 ± 0.0235
4663.90391404	10.16	6.00	0.1717 ± 0.0252
4665.78413890	11.48	7.78	0.1816 ± 0.0257
4665.79430438	-3.10	9.86	0.1812 ± 0.0252
4665.80583621	0.63	9.02	0.1786 ± 0.0242
4731.66600573	1.60	11.50	0.1734 ± 0.0230

Table 2.5 cont'd.			
BJD - 2450000	Radial Velocity (m/s)	Uncertainty (m/s)	S_{HK}
4731.67754085	0.72	7.35	0.1657 ± 0.0226
4731.68907100	-5.82	8.82	0.1795 ± 0.0236
4732.75396109	2.27	7.88	0.1682 ± 0.0242
4732.76548879	0.12	7.60	0.1667 ± 0.0223
4732.77701662	-2.03	6.90	0.1674 ± 0.0238
4733.69703238	9.44	8.14	0.1701 ± 0.0242
4733.70856019	-4.67	7.82	0.1677 ± 0.0235
4733.71697119	-7.09	9.14	0.1727 ± 0.0236
4747.77353788	4.25	5.98	0.1746 ± 0.0250
4781.65688110	7.76	6.41	0.1652 ± 0.0206
4816.61232656	10.29	8.72	0.1755 ± 0.0209
4986.92370887	-4.73	14.24	0.1887 ± 0.0262
5025.89140933	-37.17	8.23	0.1816 ± 0.0263
5048.87005530	-37.84	9.19	0.1823 ± 0.0239
5048.87535157	-12.18	9.07	0.1807 ± 0.0241
5075.87456767	-15.99	7.03	0.1695 ± 0.0230
5075.88610277	-13.42	8.76	0.1692 ± 0.0228
5100.78063288	-21.91	7.32	0.1673 ± 0.0212
5135.72812260	-27.54	8.80	0.1659 ± 0.0226
5172.58815669	-4.45	8.31	0.1728 ± 0.0219
5400.78427274	-10.86	6.31	0.1706 ± 0.0243
5435.78861255	-15.49	8.10	0.1714 ± 0.0246
5469.78414305	-13.65	7.30	0.1785 ± 0.0224
5492.76854834	-11.30	7.62	0.1627 ± 0.0222
5523.68425857	2.79	7.30	0.1601 ± 0.0208
5527.64465815	6.66	8.70	0.1742 ± 0.0234
5527.65392663	3.10	5.77	0.1669 ± 0.0223
5547.59458469	9.04	8.11	0.1649 ± 0.0249
5644.98896924	4.16	6.79	0.1519 ± 0.0239
5722.92872656	7.82	5.48	0.1523 ± 0.0216
5758.92483333	6.08	6.53	0.1721 ± 0.0260
5789.68097414	-0.49	6.97	0.1705 ± 0.0285
5791.86463193	13.74	8.20	0.1768 ± 0.0263
5792.79925378	-0.60	6.61	0.1742 ± 0.0253
5841.78442437	-8.29	7.41	0.1665 ± 0.0251
5842.79215631	-10.22	6.66	0.1649 ± 0.0281

Table 2.6: Radial Velocities for HD 220773

BJD - 2450000	Radial Velocity (m/s)	Uncertainty (m/s)
2479.859725	-0.4171	4.08
2480.838237	-13.5865	4.09
2486.820898	-11.3423	4.45
2487.830499	-16.1442	4.38
2948.718426	-10.1010	3.87
3185.902803	-24.8888	5.50
3267.686065	-22.1946	4.73
3542.934309	-35.1965	4.76
3604.768270	-26.1322	4.20
3901.952807	3.7467	3.70
3935.863371	-5.9660	4.19
3979.907141	-12.5221	4.13
4007.670760	1.0665	3.68
4014.657584	-0.4731	3.14
4015.639336	5.8017	4.02
4032.599555	14.5027	4.60
4044.722222	14.3386	4.10
4401.744726	12.0180	4.51
4428.675456	19.4405	3.78
4475.548221	14.3677	4.52
5114.635072	-11.1314	4.15
5140.721408	7.8337	3.75
5358.945550	4.7166	4.79
5358.947973	8.1944	4.58
5382.886175	-5.2398	3.81
5382.888643	-3.2236	4.03
5414.822196	-1.2009	3.47
5414.824720	-10.5412	3.58
5441.730451	-0.5391	3.39
5441.732880	-4.1901	3.75
5466.827877	-6.5113	4.33
5469.822406	-1.8755	3.72
5469.824889	-1.5983	3.69
5532.649379	-3.1531	4.21
5532.651798	8.9105	4.23
5547.609328	8.9497	3.68
5547.611809	2.8300	4.20
5724.945915	9.2505	3.56

Table 2.6 cont'd.		
BJD - 2450000	Radial Velocity (m/s)	Uncertainty (m/s)
5724.948402	-5.5916	3.73
5754.866046	-12.5525	4.50
5754.868528	0.3110	5.85
5790.949560	-2.0862	3.38
5790.952042	-3.9868	3.78

Chapter 3

Two Jupiters in a 3:2 Mean-Motion Resonance Around HD 204313

3.1 Background

HD 204313, a sun-like $V = 8$ star observable in both hemispheres, has been a target for multiple RV surveys. [199] announced the detection of the first member of the star's planetary system with the discovery of HD 204313b, a Jovian-class ($M \sin i \sim 4M_J$) planet on a long-period ($P \sim 5$ yr) orbit. More recently, the HARPS survey revealed an interior Neptune-mass planet with $P = 35$ days [158].

At [Fe/H] = 0.18 (as measured by [199]), HD 204313 follows the observed trend of gas giant hosts being generally metal-rich (e.g. [76]). Furthermore, planet c adds to the mounting evidence that Neptune- and lower-mass planets are extremely common around main-sequence stars [107, 158, 234, 236]. In many ways, HD 204313 represents a "typical" planetary system, according to current observations.

Since 1987, we have used the 2.7 m Harlan J. Smith Telescope at McDonald Observatory for a long-baseline RV planet survey [42]. An upgrade to our 2D coudé spectrograph in 1998 gave us access to the full optical wavelength

range of our I_2 absorption cell, enabling us to monitor hundreds of FGK stars with ~ 6 m/s precision over 7-13 years. One of the primary scientific objectives of the survey is to obtain a census of Jupiter analogs–giant planets in long period orbits (see [230, 233] for a complete discussion of Jupiter analogs and early detection limits from the McDonald Observatory RV survey). We have recently announced three giant planets in long-period orbits [189], demonstrating that we have the time baseline and sensitivity to detect long-period giants. In the core-accretion theory of giant planet formation [141, 179], surface-density enhancement by ices facilitates the formation of $\sim$10-15 $M_\oplus$ cores. The ice line, beyond which ices are present in the protoplanetary disk, has been estimated to lie at 1.6-1.8 AU in a minimum-mass solar nebula [138]. For the case of HD 204313, the inclusion of published CORALIE velocities from [199] gives us a total time baseline of 12 years, extending our sensitivity comfortably beyond the ice line, into the formation locations of gas giant planets. In this chapter, we present HD 204313d, another Jupiter analog exterior to planet b, and describe its orbital parameters and evolution.

3.2   Observations and Data Reduction

Our RV data for HD 204313 are all taken from the 2.7 m Smith telescope between July 2003 and June 2011, resulting in an 8-year time baseline. We use the Tull Coudé Spectrograph [217] with a 1.8 arcsecond slit, yielding a resolving power R = 60,000. Our RV measurement procedure and reduction code AUSTRAL is discussed in detail in [71]. In short, immediately before

starlight enters the slit, it passes through an I_2 absorption cell regulated at $50°$ C, which superimposes thousands of molecular absorption lines over the object spectra in the spectral region between 5000 and 6400 Å. Using these lines as a wavelength standard, we simultaneously model the time-variant instrumental profile and Doppler shift relative to an I_2-free template spectrum. The resulting RVs are corrected for the motion of the observatory around the solar system barycenter. We report our RV data for HD 204313 in Table 5.3.

3.3 Stellar Characterization

We seek to independently verify the stellar atmosphere parameters for HD 204313 derived by [199]. Using our I_2-free stellar template, we measure the equivalent widths of 61 Fe I lines and 17 Fe II lines. We feed these equivalent widths to the MOOG[a] local thermodynamic equilibrium (LTE) line analysis and spectral synthesis program [205]. By utilizing a grid of ATLAS9 model atmospheres [133], MOOG derives heavy-element abundances to match the measured equivalent widths. We then determine effective temperature T_{eff} by removing any trends in abundances versus excitation potential (assuming excitation equilibrium), and computes microturbulent velocity ξ by eliminating trends with reduced equivalent width ($\equiv W_\lambda/\lambda$). Stellar surface gravity is obtained by forcing the abundances measured with Fe I and Fe II lines to match (assuming ionization equilibrium). Our measured abundances are differential with respect to the sun. Using a solar port, we have taken a solar spectrum

---

[a]available at http://www.as.utexas.edu/∼chris/moog.html

Spectral Type	G5 V
V [126]	8.006 ± 0.014
$B - V$ [126]	0.695 ± 0.02
M_V	4.63 ± 0.03
Parallax [126]	21.06 ± 1.04 mas
Distance	47 ± 0.3 pc
T_{eff}	5760 ± 100 K
$\log g$	4.45 ± 0.12
[Fe/H]	0.24 ± 0.06
ξ	1.20 ± 0.15 km/s
Mass [37]	$1.02 M_\odot$
Age [37]	7.20 Gyr
$\log R'_{HK}$	-4.65 ± 0.03

Table 3.1: Stellar Properties for HD 204313

using the same instrumental setup used for our RV observations, and run the above analysis for the sun. For reference, we obtain values of $T_{eff} = 5780 \pm 70$ K, $\log g = 4.50 \pm 0.09$ dex, $\xi = 1.16 \pm 0.06$ km/s, and $\log \epsilon(\text{Fe}) = 7.52 \pm 0.05$ dex for the sun. Full details of our stellar analysis can be found in [31].

Our stellar parameters for HD 204313 are given in Table 5.1. For values our routine does not calculate, we include catalog values from [126] (Version 3) and [37]. Our computed values agree extremely well with those presented in [199]. Of particular interest is our measured [Fe/H] of 0.24 ± 0.06, which confirms the metal-rich nature of HD 204313.

3.4   Orbit Modeling

Over the 8-year period from July 2003 to June 2011, we have collected 36 RV points for HD 204313. Our data are plotted as a time series in Figure 3.1(a). The RMS scatter about the mean of these velocities is 40 m/s, with an average internal error of 5.21 m/s. When analyzed alone, our RVs show the high-amplitude ($K \sim 70$ m/s) signal expected as a result of HD 204313b, with a period around 5.5 years. We compute Keplerian orbital solutions using the GaussFit modeling program [113] and the SYSTEMIC console [160], finding excellent agreement between the one-planet solutions from both routines. However, a one-planet fit to our data gives a period more than 100 days longer than the period reported in [199], a discrepancy more than 3 times the combined 1σ uncertainties in the orbital period for the two models. Additionally, our fit includes a long-period linear trend. We note that [158] also find a period for planet b considerably longer than the originally published value.

We then compute a one-planet model using the CORALIE RVs as well as our own. The combined RV set includes 132 RVs taken over 10 years. The resulting parameters are closer to the previously published solution; we find a period of 2,000 days, with eccentricity 0.16 and a minimum mass of 4.36 Jupiter masses. However, this fit is still considerably discrepant from the [199] solution, and leaves a residual RMS scatter of 11.0 m/s, and a reduced $\chi^2 = 5.66$.

We have computed the fully generalized Lomb-Scargle periodogram [240] for the combined CORALIE-McDonald data set, and the residual RVs
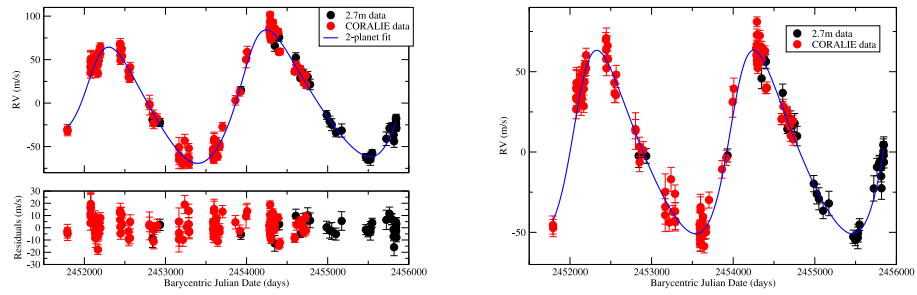
(a)

(b)
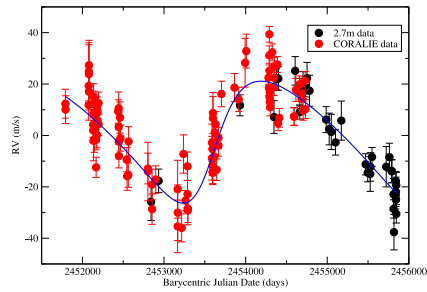
(c)

Figure 3.1: a. *Top*: Radial velocity data for HD 204313. Points in black are our 2.7m observations, while points in red are CORALIE observations from [199]. The best-fit orbit model is shown as a blue line. *Bottom*: Residuals to a two-planet fit. b. RVs after subtracting our fit to planet d from the velocities in (a). The blue line shows our Keplerian model for planet b. c. RVs after subtracting our fit to planet b from the velocities in (a). The blue line shows our Keplerian model for planet d.

around the one-planet fit. The resulting power spectrum is shown in Figure 3.2. The periodogram of the residual RVs shows significant peaks around 340 days, 395 days, and a broad peak between 2700 and 6700 days. We calculate a false-alarm probability (FAP) for these peaks using the method described in [209], and find a FAP of approximately 5×10^{-5} for the long-period peak, while the 395-day and 340-day peaks have FAPs of 4×10^{-4} and 1.5×10^{-3}, respectively.

We attempt to fit an additional planet to the residuals at each of the periods identified in the periodogram. Our fitting routine produces unsatisfactory solutions at the two shorter periods, but converges to a fit with an outer giant ($M \sin i = 1.68 M_J$) planet at 2831 days. The period of planet b in this solution is consistent with the original published result, although the eccentricity is higher than in a one-planet fit. The resultant two-planet fit is included in Figure 3.1(a), and we give residual plots of the individual planets in Figures 3.1(b) and 3.1(c). As with the one-planet solution, GaussFit and SYSTEMIC agree nicely on the orbital parameters and their uncertainties. The parameters of our final orbital model are listed in Table 5.2. The addition of planet d removes the need to include a linear slope. Although we attempted to fit an outer planet to each of the CORALIE and McDonald RV sets individually, our routines failed to converge for either set. Evidently, both data sets are required to achieve the time baseline needed to detect planet d, a fact reinforced by our periodogram analysis. When examining the residual RVs to our one-planet fit for each data set individually, we see only a monotonic
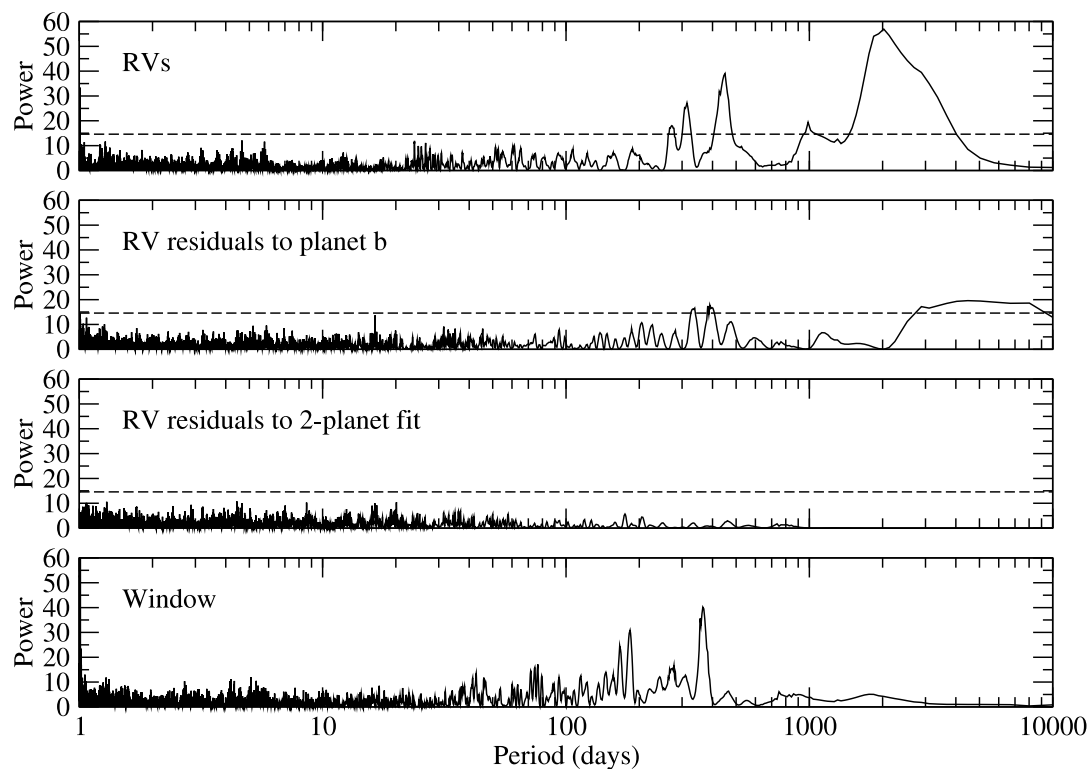
Figure 3.2: *From top*: [1] Generalized Lomb-Scargle periodogram for the combined CORALIE/McDonald RVs of HD 204313. [2] The same periodogram for the residual RVs after subtracting a one-planet fit. [3] Periodogram of the residual RVs after subtracting a two-planet fit. [4] Periodogram of our time sampling (the window function). The dashed lines indicate the approximate power level for a FAP of 0.01, computed from Equation 24 of [240].

Orbital Parameter	Planet b	Planet d
Period P (days)	1920.1 ± 25	2831.6 ± 150
Periastron Passage T_0 (BJD - 2 450 000)	2111.6 ± 28	6376.9 ± 176
RV Amplitude K (m/s)	57.0 ± 3	23.7 ± 4
Mean Anomaly M_0	$300° \pm 0.4°$	$137° \pm 2°$
Eccentricity e	0.23 ± 0.04	0.28 ± 0.09
Longitude of Periastron ω	$298° \pm 6°$	$247° \pm 16°$
Semimajor Axis a (AU)	3.04 ± 0.06	3.93 ± 0.14
Minimum Mass $M \sin i$ (M_J)	3.55 ± 0.2	1.68 ± 0.3
CORALIE RV offset (m/s)	-19.3	
2.7 m RV offset (m/s)	29.8	
RMS (m/s)	7.80	
Stellar "jitter" (m/s)	5.46	

Table 3.2: Two-planet orbital solution for the HD 204313 system

increase in power at long periods for the CORALIE data and insignificant power in the McDonald data. Only when the data are combined, and the total time baseline exceeds a full orbit of planet d, does the power spectrum show a clearly-defined peak around the period of that planet.

We note that we have not included planet c [158] in our analysis. With a reported RV amplitude of just 3.28 m/s, the signal of this short-period planet is below the sensitivity limit of our data and that of CORALIE. Indeed, our periodogram of the residuals to our two-planet solution (Figure 3.2) shows no additional signals. Furthermore, the inclusion of a third planet with the orbital elements published for planet c does not significantly change our orbital solution. However, the RMS (7.79 m/s) and reduced χ^2 (2.98) of our two-

planet model are still higher than we expect given the precision of the Tull spectrograph and the CORALIE data. While this is reflected in our model as a relatively high level of stellar "jitter" (5.46 m/s), our stellar activity analysis (see below) suggests HD 204313 should not be so active. Although it would be ideal to include the orbit of planet c in our model to verify this hypothesis, we are unable to do so because [158] include neither their measured RVs nor their complete orbital fit for the HD 204313 system. We nevertheless conclude that the additional scatter around our fit is most likely due to the unresolved planet c, and potentially additional low-mass companions. We refer to the outer planet as HD 204313d in acknowledgement of the inner Neptune-mass planet.

[68] report a companion star 6.2 arcseconds to the south of HD 204313, although they admit a significant probability of a chance alignment. At a distance of 47 pc, the angular separation indicates a minimum physical distance of 583 AU between the two objects. The companion is approximately 9 magnitudes fainter in the near infrared [68], and is therefore much less massive than HD 204313 if they are in fact bound. If we overestimate the mass of this object at $0.5 M_\odot$ and assume it is associated with HD 204313, the resulting radial velocity slope due to the companion is 0.28 m s^{-1} yr^{-1}, which is roughly equal to our 1σ uncertainty level of 0.2 m s^{-1} yr^{-1} for a slope in the combined data set. It is therefore safe to conclude that the second star is not influencing our modeling of the planetary system.

3.5 Stellar Activity and Line Bisector Analysis

While we do not anticipate that stellar activity should produce RV signals of the amplitudes of planets b and d, it is nevertheless important to understand how changes in the atmosphere of HD 204313 may influence our velocity measurements, particularly with the amount of scatter seen around our fit. We examine stellar activity simultaneously with RV through line bisector analysis of stellar lines outside the I_2 region and changes in the Ca H and K indices.

Changes in the stellar photosphere (starspots, etc.) may produce changes in the measured RVs. However, these processes will also alter the shapes of the individual stellar absorption lines. Following the method of [28], we calculate the bisector velocity span (BVS) for each of our spectra. The BVS is sensitive to these subtle changes in line shapes, and therefore a reliable indicator of activity the stellar photosphere.

Similarly, if stellar activity is producing RV signals, those signals should also appear in the Ca H and K indices. For each RV point in Table 5.3, we have computed the Mount Wilson S_{HK} index, which we list alongside the velocities. From [169] we use S_{HK} to derive $\log R'_{HK}$, the ratio of Ca H and K emission to the bolometric luminosity of the star. From $\log R'_{HK}$ we obtain a more general idea of the overall activity level of HD 204313.

All examinations show HD 204313 to be an extremely quiet star. The results of our activity analyses are shown in Figure 5.5. In Figure 3.3(a), we

plot BVS and S_{HK} versus our measured RVs and their residuals around the one-planet fit. In both cases, there is no significant correlation, suggesting photospheric activity is not influencing our velocities. Periodograms of S_{HK} and BVS (Figure 3.3(b)) show no periodicity for either index. Furthermore, we measure an RMS of only 17 m/s for the BVS, and $\log R'_{HK} = -4.65$. It is not surprising, then, that we see no signals or correlations in any of our activity indicators. With three planets now known, HD 204313 is rapidly becoming a rich planetary system. Its low activity level makes it an ideal candidate for follow-up observations to search for additional low-mass companions.

3.6 Dynamical Stability Analysis

A number of recent studies have highlighted the need for observational detections of multiple exoplanet systems to be supported by dynamical simulations that test whether the orbits of the proposed planets are dynamically feasible (e.g. [98, 104, 105, 235]). Such studies are particularly important when the planets in question appear to move on orbits close to mutual mean-motion resonance (e.g. [189]), an architecture that can yield either extreme stability or instability, depending on the precise orbits of the planets involved. In the case of HD 204313, the best-fit orbits for planets b and d suggest that they may well be trapped in mutual 3:2 mean-motion resonance (see Figure 3.4 for the orbital schematic). As such, we chose to perform a highly detailed dynamical study of the orbits of planets b and d to investigate whether the orbits that best fit the data are dynamically feasible.
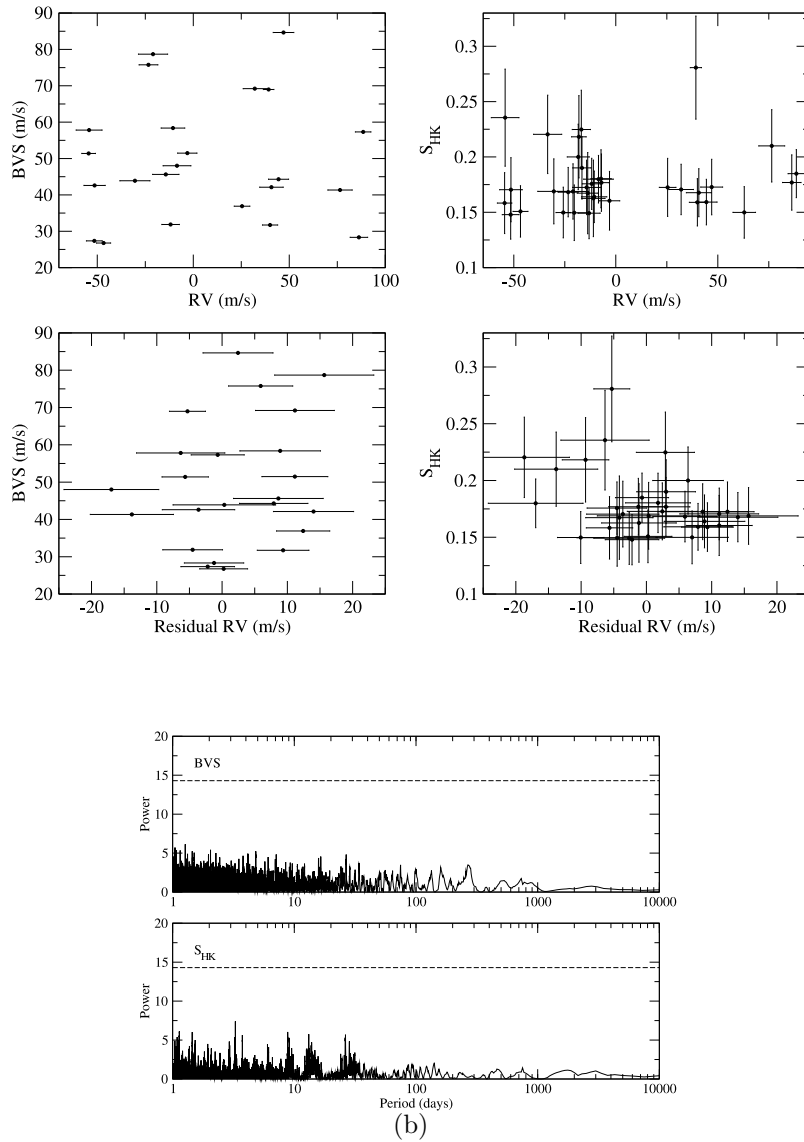
Figure 3.3: a. *Left*: BVS plotted against our measured RVs (*top*) and residual RVs to a one-planet fit (*bottom*) for HD 204313. *Right*: S_{HK} indices plotted against our measured RVs (*top*) and residual RVs to a one-planet fit (*bottom*) for HD 204313. b. Generalized Lomb-Scargle periodograms for the BVS (*top*) and S_{HK} indices (*bottom*) of our spectra for HD 204313. The dashed lines indicate the approximate power level for a FAP of 0.01.

69
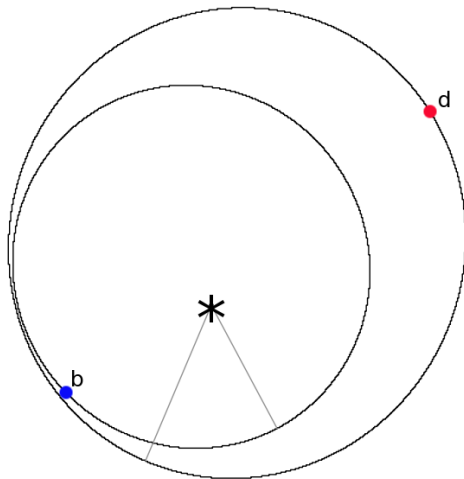
Figure 3.4: Face-on orbital diagram of the giant planets in the HD 204313 system. The ellipses shown are derived from the model in Table 5.2 (the open square in Figure 3.5), with the lines from the star pointing toward the periastron of each planet. The locations of planets b and d are adopted from the mean anomalies in Table 5.2.

Following earlier work [104, 155, 189], we used the *Hybrid* integrator within the n-body dynamics package MERCURY [39] to examine test systems in which the initial orbit of planet b was held fixed at the nominal best fit values (in this case, $a = 3.04$ AU, $e = 0.23$). The initial orbit of planet d was then systematically changed from one simulation to the next, such that scenarios were tested for orbits spanning the full $\pm 3\sigma$ error ranges in semi-major axis, eccentricity, longitude of periastron and mean anomaly. Such tests have already proven critical in confirming or rejecting planets thought to follow unusual orbits (e.g. [104, 235]), and allow the construction of detailed dynamical maps for the planetary system studied, in orbital element phase

space.

We examined 31 unique values of semi-major axis for planet d, ranging from 3.51 AU to 4.35 AU, inclusive, in even steps. For each of these 31 initial semi-major axes, we studied 31 values of orbital eccentricity, ranging across the full $\pm 3\sigma$ range ($e = 0.01 - 0.55$). For each of the resulting 961 a-e pairs, we considered 11 values of initial longitude of periastron (ω), and 5 values of initial mean anomaly (M_0), resulting in a total suite of 52,855 ($31 \times 31 \times 11 \times 5$) plausible architectures for the HD 204313 system.

In each of these simulations, the masses of the two planets studied were set to their minimum ($M \sin i$) values. The mass of planet b was therefore set to $3.55 M_J$, while that of planet d was set to $1.68 M_J$. To first order, the more massive the planets, the more strongly they will perturb one another, and so setting their masses to the minimum allows us to maximize the potential stability of the planetary system. In other words, we expect our resulting dynamical maps to show the maximal stability of the orbits tested. The dynamical evolution of the two planets was then followed for a period of 100 million years, or until one of the planets either collided with the central star, was transferred to an orbit that took it to a distance of at least 10 AU from the central star, or collided with the other planet. Collisions were modeled by assuming a density of 1.33 g cm^{-3}–equal to the average density of Jupiter–for each planet and computing a radius accordingly, so that our code registered a collision if an actual physical encounter occured. The time of such events was recorded, allowing us to construct a dynamical map of the planetary sys-

tem, shown in Figure 3.5(a). That figure shows the mean lifetime of the HD 204313b-d system as a function of the initial semi-major axis, a, and eccentricity, e, of planet d. Each individual initial a-e pair was tested a total of 55 times, each of which featured a different initial combination of ω-M_0. The lifetimes shown are the mean value of the 55 individual lifetimes obtained from those runs.

Aside from resonant solutions, the entire a-e phase space of allowed orbits for planet d is extremely unstable, with collisions between planets b and d often occurring within the first few hundred years of the simulations. It is also clear that, even within the resonance, some subset of the solutions are dynamically unstable (hence the reason the mean lifetime in the stable region is somewhat less than 10^8 years). At the highest eccentricities permitted for the orbit of planet d, no stable solutions exist, but there is a broad region of stability within the 1σ errors on the best-fit orbit. As can be seen in Figure 3.5(b), the stability of orbits in the vicinity of the 3:2 mutual mean-motion resonance between the planets is a strong function of the longitude of periastron ω for planet d (we note here that planet b's initial longitude of periastron was 298 degrees). Qualitatively, the strong ω dependence is reflective of the fact that the 3:2 resonance provides stability by ensuring planets b and d never simultaneously approach a true anomaly $\nu \sim 300°$, where their orbital paths allow very small separations. For configurations outside the stable $a - \omega$ space, the resonance becomes destructive. Once again, the stable region extends throughout the 1σ uncertainties on the best-fit orbit of planet

(a) (b)
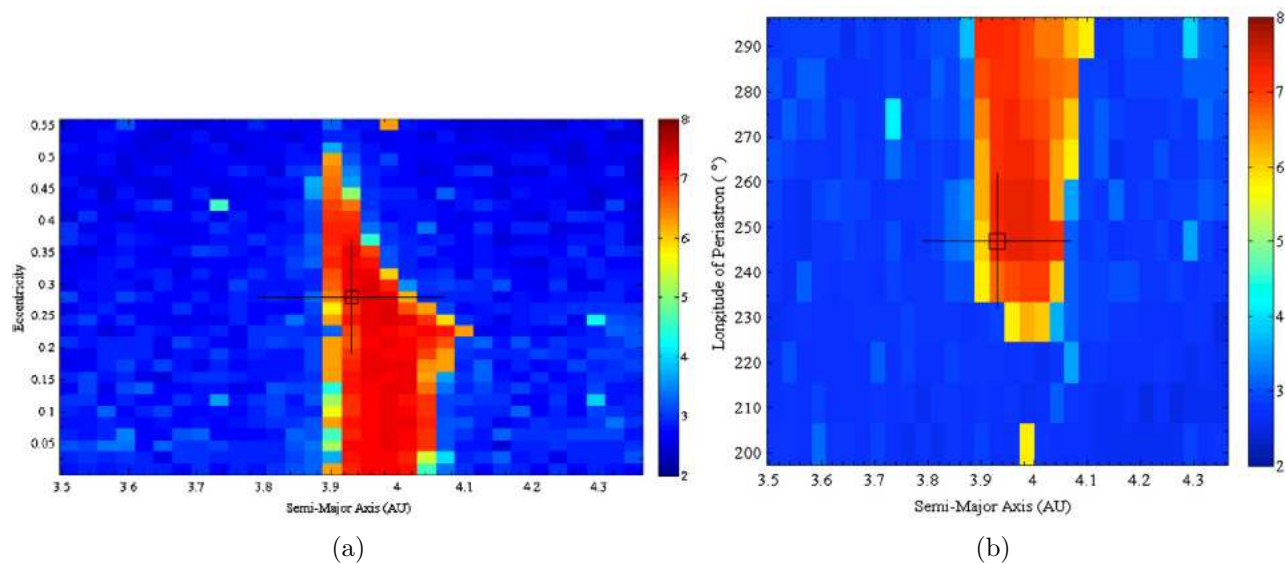
Figure 3.5: a: The mean dynamical lifetime of the HD 204313b-d planetary system, as a function of the initial semi-major axis (a) and eccentricity (e) of planet d. The lifetimes are shown on a logarithmic scale, ranging from 10^2 years (blue) to 10^8 years (red). The location of the nominal best-fit orbit for planet d is denoted by the open square, with the 1σ uncertainties shown by the solid lines radiating from that point. b: The mean lifetime of the HD 204313b-d system, as a function of the semi-major axis, a, and longitude of periastron, ω, of planet d's orbit. The lifetime shown at each location in a-ω space is the mean of 155 individual runs, which tested 31 different orbital eccentricities and 5 different mean anomalies for that particular a-ω combination.

d, with the location of the best-fit orbit lying close to the region of greatest stability.

Here again, our solution suffers from a lack of information regarding planet c. Fortunately, at $P = 35$ days and $M \sin i = 17 M_\oplus$, plausibility arguments suffice to rule out destabilizing interactions due to this inner planet. As demonstrated in [104], planets tend to be stable when separated by ~ 5 Hill radii. With planets b and c separated by nearly 12 Hill radii (measured from planet b), we expect little mutual influence. A similar argument is presented for KOI 961 [167]. Nevertheless, we have performed a small number of simulations in which we include a planet with $M = 17 M_\oplus$, $a = 0.21$ AU, and $e = 0.17$ [158] to the stable configurations nearest to our best-fit orbital solution. In all cases, the stability of the system is unaffected; while the exact values of a and e for the giant planets are slightly different at each time step when planet c is included, the periods over which the orbital parameters vary remain unchanged, and the long-term evolution is the same regardless of whether c is included. We therefore conclude that excluding planet c from our larger analysis does not significantly affect our results.

Taken in concert, the results shown in Figure 3.5 reveal that dynamically stable coplanar solutions for the orbit of planet d require that it be trapped in mutual mean-motion resonance with planet b. Given that the nominal best-fit orbit lies perfectly within the region spanned by that resonance, and that a significant fraction of the 1σ error ellipse for planet d is dynamically stable in both a-e and a-ω space, we find that our dynamical

results are broadly in support of the existence of planet d, and may even be used to more tightly constrain its orbit.

3.7   Discussion

With the addition of planet d, HD 204313 joins the growing list of stars hosting multiple gas giant planets. At G5 V spectral type and at virtually equal mass to the sun, having two planets with masses $\sim$ 2-4 times that of Jupiter makes HD 204313 somewhat of an outlier on the correlation between stellar mass and giant planet fraction/mass [116]. However, we confirm the star's super-solar metallicity measured by [199], thereby offsetting the slight discrepancy with stellar mass.

As of May 2012, there are 12 exoplanet systems in the exoplanets.org [238] database which contain giant planets believed to be in low-order resonances. However, only HD 45364 (3:2, [47]) and HD 200964 (4:3, [117]) host multiple gas giants in mean-motion resonances closer than 2:1. HD 204313 therefore joins a very small subset of the known planet systems. Furthermore, the minimum masses of planets b and d are considerably higher than either the HD 45364 or HD 200964 planets, making their continued stability even more remarkable. Interestingly, in addition to having the 3:2 resonance in common, HD 45364b/c and HD 204313b/d both have mass ratios close to the $\sim$ 3:1 Jupiter/Saturn mass ratio. These systems are thus valuable as a comparison to the Nice model [216] for the formation of the outer solar system. In particular, [8] invoke a 3:2 resonance between Jupiter and Saturn in simulations

which successfully reproduce the orbital configurations of the four outer solar system planets and the Kuiper belt.

The importance of 3:2 mean-motion resonances within the Solar system extends beyond the possible interactions between Jupiter and Saturn during the system's early evolution. Beyond the orbit of Neptune lie the Plutinos (named after the dwarf planet (134340) Pluto, the first known member). These objects, of which several hundred are currently known, are trapped within the 3:2 Neptunian mean-motion resonance. In Figure 3.6, we plot the Plutino distribution in *a-e* space. The Plutino population contains objects with a wide range of eccentricities and inclinations, with the most eccentric objects crossing the orbit of Neptune, and some moving on orbits that can range as close as halfway between the orbits of Uranus and Neptune. The inclinations of the Plutinos range from 0 degrees to over thirty degrees. This wide distribution of orbital elements has been used to decipher the migration history of Neptune - the idea being that, as that giant planet migrated outwards, objects were captured into the 3:2 mean-motion resonance and swept along with the planet, their orbits becoming ever more excited as they were carried along (e.g. [149]). As a result, the Plutinos nicely map the extent of the stable region of the 3:2 mean-motion resonance with Neptune. Though the stable Plutinos do not range to quite as extreme eccentricities as are supported for the orbit of HD204313d (as a result of the influence of Uranus on the evolution of the most eccentric members), it is striking that the region of stability occupied by the Plutinos is very similar to that obtained by our dynamical integrations, as can

be seen when comparing Figures 3.5(a) and 3.6. We note in passing that the Hilda family of main belt asteroids are trapped in 2:3 mean motion resonance with Jupiter, orbiting with periods of ~ 8 years. Despite their sometimes high orbital eccentricities (again up to, and in excess of, 0.3), these objects are protected from close encounters with the massive planet by the mean-motion resonance they occupy.
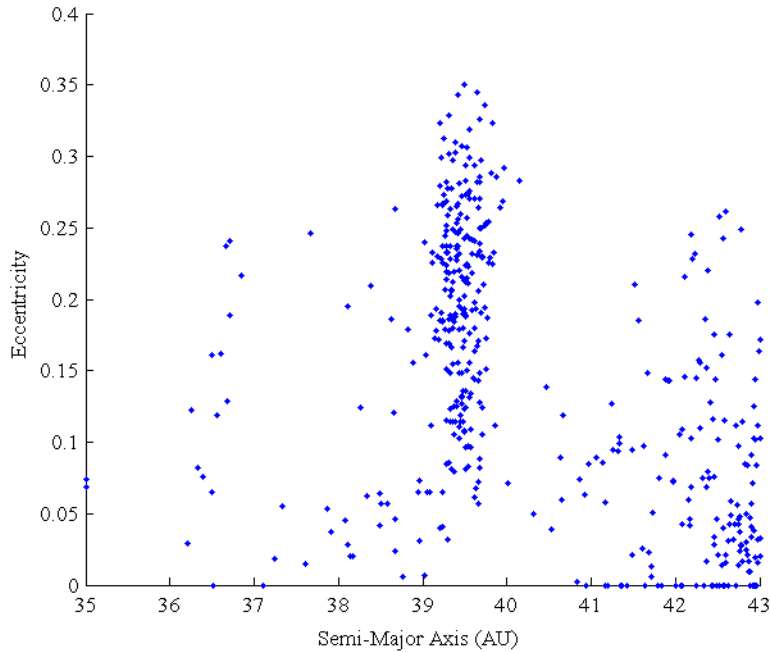
Figure 3.6: The distribution in a-e space of the population of trans-Neptunian objects between 35 and 43 AU. Note the concentration of objects just beyond 39 AU - the Plutinos, trapped in 3:2 mean-motion resonance with Neptune.

Unlike our recent results for the 2:1 mean-motion resonance in the HD 155358 system [189], our dynamical simulations for HD 204313 do not permit

77

coplanar orbits outside the 3:2 resonance. Evidently, such a small period ratio is only stable when protected by the resonance. Furthermore, the existence of unstable orbits within the permitted parameter space shows that location within a resonance is not a guarantee of stability. Finally, it is interesting that while for both HD 155358 and HU Aquarii [104, 235], the inner cutoff for stability in *a-e* space is equal to the inner planet's apastron distance plus five Hill radii, our stable solutions for HD 204313 allow planet d to have values of *a* much smaller than this value. Once again, such a conclusion is supported by our knowledge of our Solar system, in which resonant configurations ensure the stability of vast populations of objects on orbits that would otherwise be highly unstable. Prominent examples include the aforementioned Hildas (e.g. [80, 90]) and Plutinos [81, 149], along with the Jovian and Neptunian Trojans [106, 146, 162, 201]. In addition to the resonant exoplanets mentioned earlier, these populations reinforce the idea that such resonant scenarios are a common outcome from the planet formation process.

We note that the results of our stability analysis not only confirm the validity of our orbital model, but in fact place tighter constraints on the system's configuration than our fitting uncertainties alone. As long-term RV planet surveys such as ours become increasingly sensitive to systems with multiple long period companions, it is likely that additional systems with gas giants in close resonances will be discovered. Such dynamical simulations are therefore extremely valuable for understanding the true architecture of these systems, for which there may otherwise be considerable uncertainty as to the

orbital parameters.

It is important to note that our claim that planets b and d are trapped in mutual 3:2 mean-motion resonance is based on simulations that assumed that their orbits are coplanar. However, as can be seen from the examples of the Hildas and Plutinos within our own Solar system, resonant orbits can be dynamically stable for a wide range of mutual inclinations. It might instinctively seem that the coplanar case would actually be the least stable configuration, and therefore that mutually inclined orbits might allow a broader range of stable solutions. However, we note that in [104], the authors considered a wide range of orbital inclinations in an attempt to address the apparent instability of the proposed HU Aquarii planetary system, and found that increasing the mutual inclination of the planets in question did little to remedy their instability. That said, it would certainly be interesting, in future work, to examine the influence of the mutual inclination of the orbits of the planets of the HD204313 system. Fortunately, with predicted astrometric displacements of 0.432 mas and 0.264 mas for planets b and d, respectively, both planets should be accessible to astrometric measurements with the HST Fine Guidance Sensor [168]. Plus, the inclusion of inclination constraints would make HD 204313 a unique opportunity for comparison to the compact, multi-resonant planet systems discovered by the *Kepler* spacecraft [45, 100, 142]. If astrometry shows the HD 204313 planets to be coplanar, it would be strongly suggestive that similar migration mechanisms can result in systems as different as HD 204313 and the aforementioned *Kepler* planets. HD 204313 should therefore be considered a

high-priority target for current and future astrometric surveys.

Table 3.3: Radial Velocities for HD 204313

BJD - 2450000	Radial Velocity (m/s)	Uncertainty (m/s)	S_{MW}
2840.892291	-8.48	7.26	0.1799 ± 0.0215
2933.666733	-11.81	4.58	0.1757 ± 0.0231
3930.951397	25.41	4.08	0.1725 ± 0.0262
4347.740522	76.44	6.37	0.2100 ± 0.0327
4376.744143	88.50	4.07	0.1849 ± 0.0217
4401.617979	86.26	4.55	0.1769 ± 0.0250
4606.945812	62.97	5.54	0.1499 ± 0.0233
4663.924822	46.99	5.37	0.1728 ± 0.0251
4663.938000	39.25	2.76	0.2807 ± 0.0466
4703.749028	44.40	5.24	0.1592 ± 0.0206
4732.798800	40.00	3.96	0.1590 ± 0.0214
4752.702889	40.71	6.14	0.1677 ± 0.0217
4782.617353	32.02	6.04	0.1706 ± 0.0228
4986.953099	-3.09	5.05	0.1604 ± 0.0265
5023.896398	-10.58	6.18	0.1640 ± 0.0233
5049.798314	-14.30	6.87	0.1725 ± 0.0246
5101.700768	-23.34	4.92	0.1682 ± 0.0223
5172.538410	-20.96	7.60	0.1688 ± 0.0250
5470.683390	-51.54	4.11	0.1479 ± 0.0222
5496.568795	-54.50	3.56	0.1583 ± 0.0275
5526.556625	-54.25	6.77	0.2355 ± 0.0439
5529.556590	-51.40	5.55	0.1704 ± 0.0290
5548.544742	-46.72	3.67	0.1508 ± 0.0232
5722.947515	-30.38	7.86	0.1689 ± 0.0294
5761.927802	-18.40	5.41	0.2000 ± 0.0296
5790.814330	-16.89	4.45	0.2248 ± 0.0355
5791.852748	-16.59	4.50	0.1901 ± 0.0282
5811.740128	-20.36	6.16	0.1496 ± 0.0251
5812.750735	-25.75	3.56	0.1498 ± 0.0229
5817.780745	-33.40	6.91	0.2204 ± 0.0354
5838.671924	-13.10	5.43	0.1492 ± 0.0231
5840.686936	-7.06	3.68	0.1768 ± 0.0259
5841.664865	-10.98	5.72	0.1626 ± 0.0346
5842.697923	-13.76	5.16	0.1673 ± 0.0367
5845.589786	-7.23	4.97	0.1803 ± 0.0262
5846.724380	-18.09	3.57	0.2182 ± 0.0372

Chapter 4

M Dwarf Activity: The Hα Line

4.1 Background

The study of Hα activity for M dwarfs has provided a wealth of insight into the physics of low-mass stars. For young M stars with Hα emission lines (so-called "active" M dwarfs), stellar activity has been shown to be tightly coupled with rotation (e.g. [30, 187]). Furthermore, as these stars age and spin down, their Hα emission and variability decrease significantly, offering a diagnostic for distinguishing stellar populations of different ages [143, 228, 229].

Absorption line variability in inactive M dwarfs is often caused by periodic stellar activity cycles [32, 40, 87, 132, 241]. Because such cycles may appear in radial velocity (RV) measurements (as evidenced by correlation between RV and activity tracers such as Ca II H and K emission), potentially mimicking Keplerian planet signals [87, 111, 183], they are of particular interest to planet search surveys. As a somewhat happy coincidence, the long-term, multi-epoch spectral monitoring of stars conducted by RV surveys makes them uniquely sensitive to analogs of the 11-year solar cycle. These cycles may not appear in photometry if they manifest as variable heating of active chromospheric regions and not starspot modulation.

Identification and characterization of solar-type cycles will be instrumental in better understanding the solar magnetic dynamo [213, 238]. Since stellar cycles are reflective of a star's magnetic field strength and variability (e.g. [29]), internal structure ([170] and references therein), and long-term evolution [237], exploring activity across all spectral types is an excellent way to understand how fundamental stellar properties vary, and how stellar magnetic fields are generated and maintained.

In the Sun, the origin of the magnetic activity driving the observed 11-year cycle is believed to be the $\alpha\Omega$ dynamo maintained through differential rotation at the tachocline, the interface between the radiative and convective layers of the Sun. The prevalence of similar cycles for FGK stars [6] confirms that such dynamos are common amongst solar-type stars. However, the tachocline lies at increasing depths at later spectral types, disappearing altogether around $\sim$ M4 [38]. Thus, a direct comparison between the stellar activity levels and cyclic behavior of solar-type and lower-mass stars is essential to characterizing the effect of stellar mass on internal architecture and the resulting magnetic activity.

In this chapter, we present the first systematic analysis of stellar activity for the McDonald Observatory M Dwarf Planet Survey [72, 73]. While the long-term surveys at Mount Wilson [6] and HARPS [144] have already conducted similar studies for over 400 quiet FGK stars, analyses of M stars (e.g. [40, 87, 132]) are significantly lacking, with less than 50 total stars examined. With 93 stars included in this study, it is the largest such study to date for

inactive M stars, and represents a substantial addition to the total collection surveyed.

Here, we will use the flux in the Hα line as a tracer of stellar chromospheric activity. In areas of the stellar chromosphere where magnetic field lines influence the local convective behavior (so-called "active regions" or plages), Hα photons are emitted, resulting in an activity-dependent depth of the Hα absorption line. While this effect is more commonly observed in the calcium H and K lines, Hα is potentially a more suitable line for M stars because of their lack of flux near the calcium lines. Additionally, because Hα and Ca H and K are emitted from different depths in the chromosphere (and hence different distances from the tachocline), valuable information may be gained by comparing the results of M dwarf activity using both indices. Since Hα is a standard tracer of M dwarf activity, our measurements can easily be compared with previously published results.

The chapter is organized as follows. In Section 2, we describe how we acquired and reduced our data. We have identified a number of periodic Hα signals, which we discuss in Section 3. Additionally, we have computed the mean Hα flux levels of our targets, and include a detailed examination of how these average fluxes depend on stellar mass and metallicity. The broader implications of our results are discussed in Section 4, and we summarize our conclusions in Section 5.

4.2 Observations and Data Analysis

The McDonald Observatory Planet Search (e.g. [42, 189, 190]) has monitored nearby stars for RV variation induced by exoplanets with the Hobby-Eberly Telescope (HET; [185]) since 2001. During this period, we have also surveyed 100 M dwarfs to explore the frequency of planets around low-mass stars. Our 100 targets are specifically selected to have low activity based on a lack of X-ray emission from the *ROSAT* All-Sky Survey [110], and should therefore represent the old, quiet population of nearby M stars.

In order to better characterize our targets, we computed stellar masses using the [57] K-band mass-luminosity relation. Additionally, we calculate stellar metallicity using the [197] photometric metallicity calibration. We note that this calibration is largely consistent with earlier photometric metallicity estimates of [16] and [114], but is less susceptible to systematically over- or underestimating stellar [M/H]. Where available, we have also obtained spectral subtypes from the Orion Spiral Arm Catalogue [13]. In Figure 4.1, we show the distributions of these stellar properties for our sample.

After removing double-lined spectroscopic binaries (SB2s), the M dwarf survey has amassed 2933 high-resolution spectra of 93 stars as of July 2012. All of the 93 targets have been observed at high cadence for a brief amount of time (typically ~ 5 observations over one week) to explore short-period RV variability, and are observed at least once per season to ensure sensitivity to long-period signals. Stars with potentially interesting RV signals have been observed several times each season.
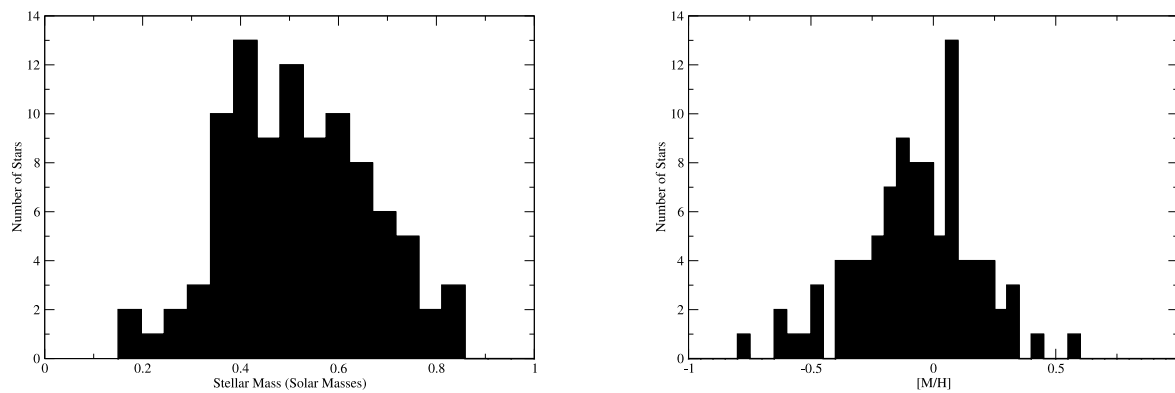
(a)
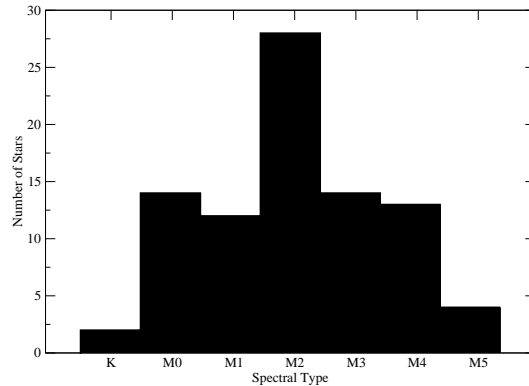
(c)

Figure 4.1: The McDonald Observatory M Dwarf Planet Search is a dedicated long-term survey of late-type stars in the Solar neighborhood. Here, we give histograms of the stellar masses, metallicities, and spectral subtypes of our targets.

Our HET M dwarf spectra are taken with the High Resolution Spectrograph (HRS; [218]). Nearly all the spectra are taken at a resolving power $R = 60,000$, with a small number of bright targets for which we observed at $R = 120,000$. We note that while our observations are taken with an I_2 absorption cell in front of the slit for the purpose of obtaining precise RVs, no I_2 absorption lines are present in the spectral region around Hα. Flat-fielding, bias subtraction, cosmic ray removal, and wavelength calibration are performed with standard IRAF[a] routines, and we have divided our spectra by the blaze function to normalize the continuum.

Although it is common practice for RV surveys to trace stellar activity with the Ca II H and K lines (S_{HK}, e.g. [111, 174, 189], those lines are not accessible to HRS. Instead, we examine the Hα line, which appears in absorption for our targets, but becomes increasingly filled in as chromospheric activity increases [86, 132]. Figure 4.2 shows the Hα absorption line for GJ 270 at times of high and low emission. In addition to the issue of availability, analyzing Hα reveals stellar behavior which will not necessarily appear in S_{HK} since Hα activity and Ca H and K activity do not always correlate, as shown in previous comparisons between tracers [41, 86, 196]. We measure this chromospheric Hα "filling in" with an index $I_{\mathrm{H}\alpha}$. Following [132], we define the index as

---

[a]IRAF is distributed by the National Optical Astronomy Observatories, which are operated by the Association of Universities for Research in Astronomy, Inc., under cooperative agreement with the National Science Foundation.
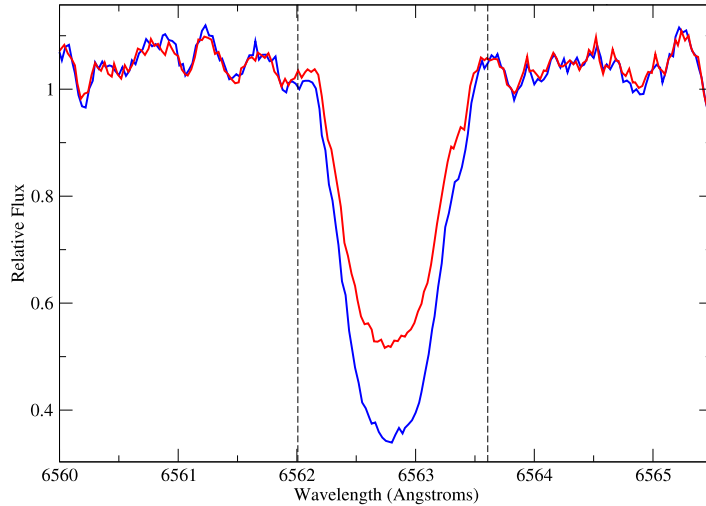
Figure 4.2: For quiet M stars, the Hα line traces stellar magnetic activity through the variable "filling in" of the absorption line with photons emitted from magnetically active regions of the chromosphere. Here, we show the Hα absorption line of GJ 270, in states of high (red) and low (blue) chromospheric emission. The dashed vertical lines indicate the 1.6 Å window in which the Hα flux is calculated.

$$I_{\mathrm{H}\alpha} = \frac{F_{\mathrm{H}\alpha}}{F_1 + F_2} \tag{4.1}$$

As in [86], we have taken $F_{\mathrm{H}\alpha}$ to be the sum of the flux in a band of width 1.6 Å centered on the Hα $\lambda 6562.828$ Å line. We find the line center with our fitted wavelength solution, making manual corrections for large stellar RV offsets where necessary. F_1 and F_2 are the sum of the fluxes in the reference bands $[-700 \text{ km s}^{-1}, -300 \text{ km s}^{-1}]$ (from the Hα line center) for band

1 and $[600 \text{ km s}^{-1}, 1000 \text{ km s}^{-1}]$ for band 2, as defined by [132]. To ensure any variation observed is in fact from stellar chromospheric activity and not instrumental effects, we also measured a similar index for the Ca I $\lambda6572.795$ Å line, where F_{CaI} is the sum of the flux from $[441.5 \text{ km s}^{-1}, 472.5 \text{ km s}^{-1}]$ around the Ca I line center, and using the same reference bands. Because the Ca I line should not be sensitive to stellar activity, the Ca I index serves as a control against which to verify Hα activity.

For each stellar line index, we calculated an error bar using a method analogous to the one employed for the Mount Wilson Ca II S_{HK} index we compute for our 2.7m spectra (e.g. [189]). Specifically, we multiplied the RMS in the continuum in the 0.5 Å adjacent to the Hα or Ca I line by $\sqrt{N}$, where N is the number of pixels in the line (i.e. $\sigma_{F_{\text{H}\alpha}} = \text{RMS}_{F_{\text{H}\alpha \pm 0.5}} \times \sqrt{N}$). Likewise, we multiplied the RMS scatter of each reference band by the square root of the number of pixels in the band, and added the errors in quadrature for the final line index. In equation form,

$$\left(\frac{\sigma_{I_{\text{H}\alpha}}}{I_{\text{H}\alpha}}\right)^2 = \left(\frac{\sigma_{F_{\text{H}\alpha}}}{F_{\text{H}\alpha}}\right)^2 + \left(\frac{\sqrt{\sigma_{F_1}^2 + \sigma_{F_2}^2}}{F_1 + F_2}\right)^2 \tag{4.2}$$

Rather than take the approach of [86] and bin our observations, we assign these error bars so as to accurately assess the quality of each spectrum, and to best make use of our more sparsely-sampled data sets, which nonetheless show significant activity.

4.3   Analysis

We see time-dependent stellar activity for a number of stars from our RV survey. In addition to detailing this behavior, we have also examined the time-averaged overall activity levels of our targets, and related those levels to other fundamental stellar properties. We present these results in separate subsections below.

4.3.1   Periodic Hα Activity

We began our analysis by searching the time series $I_{\mathrm{H}\alpha}$ measurements of each star for periodic activity. Since M dwarf stellar activity signals have been observed with periods as short as weeks or months (as is typical of rotation periods, e.g. [78, 132]) and as long as years [40, 87], we searched a broad range of frequencies. We search for periodicity using the fully generalized Lomb-Scargle periodogram [240] due to its ability to handle uneven time sampling and individually-weighted data points. In cases where our periodograms show significant power levels, we have estimated false alarm probabilities (FAPs) using three different methods. The first two computations, which we consider preliminary estimates, use Equation 24 of [240] and the method outlined in [209]. For the [240] FAP estimate, we normalize the periodogram assuming gaussian noise, so our false alarm probability for a peak of power P is

$$\mathrm{FAP} = 1 - [1 - (1 - \tfrac{2P}{N-1})^{\frac{N-3}{2}}]^{M},$$

where N is the number of data points and $M = \frac{\Delta f}{\delta f}$ is an estimate of the number of independent frequencies sampled. The FAP estimate of [209], which

90

compares the power of a periodogram peak to an expected distribution of power values based on Bayesian statistics, agrees well with the probabilistic calculation for our power spectra. Our final FAPs for periodic signals presented herein are calculated according to the bootstrap resampling technique of [131]. Briefly, the bootstrap FAP technique retains the time stamps of the original data set, then creates a series of fake data sets by assigning a random $I_{H\alpha}$ value (with replacement) from the set to each time stamp. The FAP is then taken as the percentage of resampled data sets which at any frequency give an equal or higher periodogram power value than the highest peak in the original data.

Because stellar activity is neither strictly periodic nor perfectly sinusoidal, and will experience stochastic behavior (flares, etc.) regardless of any regular cycles, the FAP required to confirm a $H\alpha$ activity cycle is somewhat higher than for a more rigidly periodic phenomenon such as a Keplerian planet orbit. Previous studies (e.g. [40]) have considered FAPs as high as 0.5. While we see many signals in our sample with a FAP in the 0.5-0.1 range, we do not present them here, pending confirmation either through more dense time sampling (for short-period signals) or a second activity tracer such as the Na I D feature (for low-amplitude signals). Here, we only claim detection of a periodic signal if it has a bootstrap FAP at or near the 0.01 level, with the exception of GJ 581 (FAP ~ 0.1), for which we offer a confirmation of a previously observed cycle (see below). This criterion is essentially equivalent to the one adopted by [32]. The periodograms for our confirmed activity cycles are shown in Figure 4.3, and the individual FAPs are discussed in later sections.
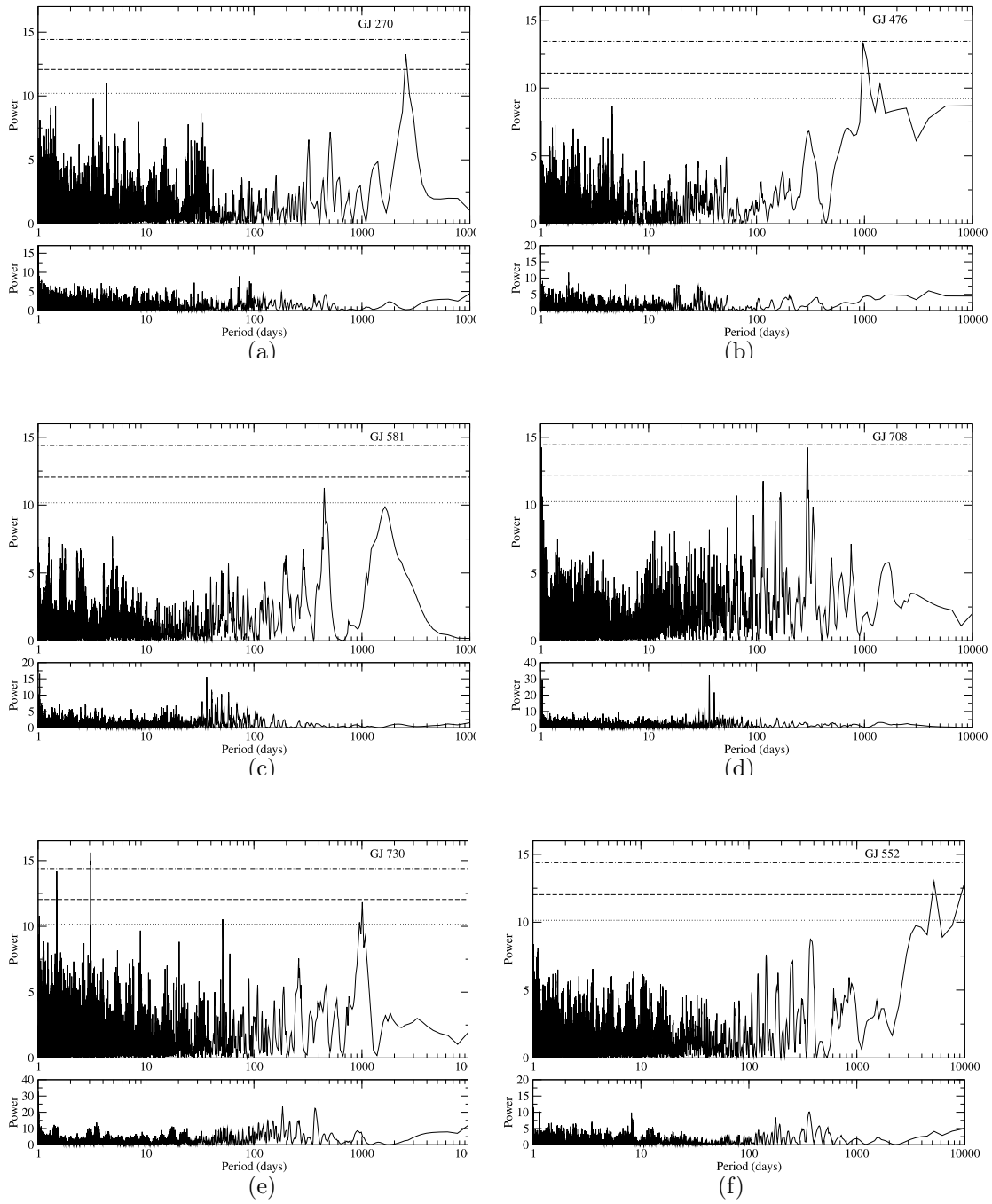
Figure 4.3: Periodograms for the six stellar activity cycles detected in our M dwarf sample. Below each periodogram is the power spectrum of our time sampling. The horizontal lines represent the power levels corresponding to a false alarm probability (FAP) of 0.5 (dotted line), 0.1 (dashed line), and 0.01(dash-dotted line), as calculated from Equation 24 of [240].

92

For each activity cycle, we have fit a sinusoid of the form $I_{\mathrm{H}\alpha}(t) = a_0 + a_1 \sin(\omega t + \phi)$, where $\omega = \frac{2\pi}{P}$, P is the period of the cycle, and a_0, a_1, and ϕ are free parameters to set the $I_{\mathrm{H}\alpha}$ zero point, amplitude, and phase, respectively. In Figure 4.4, we show the time-series $\mathrm{H}\alpha$ index of the six stars for which we observe periodic activity cycles and the fitted sine curves. Included with each plot is the time series of the Ca I index. We note that we have examined the periodograms of the Ca I index for each star in Figure 4.4, and do not see periodicity matching the signals seen in $\mathrm{H}\alpha$. Furthermore, the level of variation in Ca I is considerably lower than we see in $\mathrm{H}\alpha$, confirming that the cycles observed are in fact caused by stellar activity.

While we show sinusoidal fits to the activity cycles shown in Figure 4.4, it is clear from visual inspection that the cycles are not all perfectly sinusoidal in shape. Interestingly, the two most obviously non-sinusoidal signals–GJ 552 and GJ 630 (see below)–both exhibit gradual declines and rapid rises in $I_{\mathrm{H}\alpha}$. This behavior is reminiscent of the Waldmeier effect seen in the Sun, where higher-amplitude activity cycles are preceded by more rapid rises in activity (see, e.g. [35]). While the details of the Waldmeier effect are the subject of active research, its qualitative properties can be explained by the variable nonlinear feedback of hydrodynamic turbulence and small-scale magnetic fields on the large-scale stellar magnetic field [178]. If this is the case for our targets, we should expect to see varying shapes and durations of each cycle as we observe successive periods.

We find that in cases of non-sinusoidal $I_{\mathrm{H}\alpha}$ series, a better approach is

93
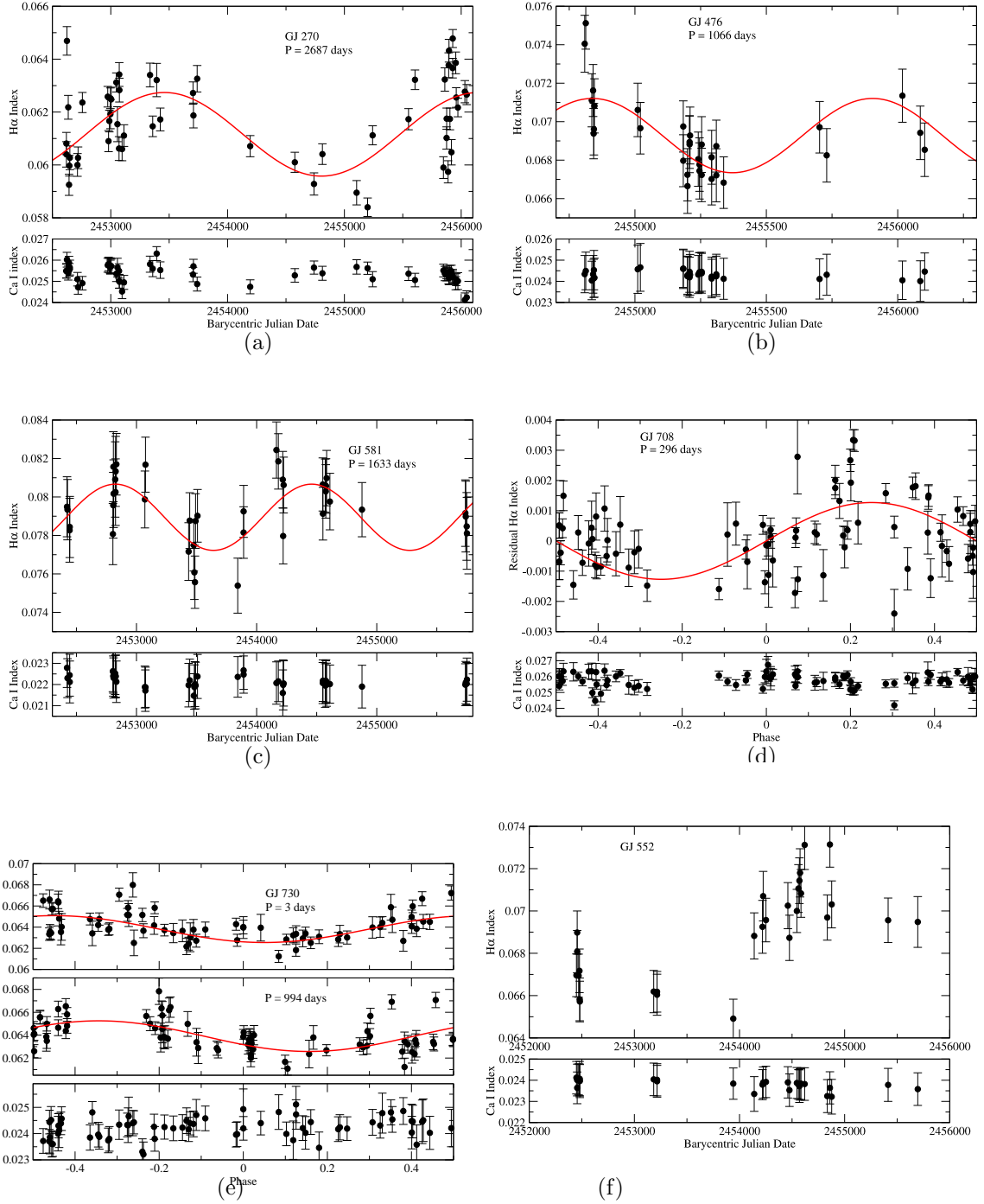
Figure 4.4: Hα activity cycles. Some data have been phase-folded for clarity. The red curves show our best fit to the data. We do not include a fit for GJ 552 because we cannot constrain its period. Below each Hα series is the corresponding Ca I index.

94

to fit a Fourier series. In Figure 4.5, we show the results of fitting three terms of the Fourier series

$$I_{\text{H}\alpha}(t) = a_0 + \sum_{i=1}^{n} a_i \sin(\omega_i t + \phi_i)$$

for two of the cycles presented in Figure 4.4. We set the initial guess for ω_1 equal to the frequency identified in the periodogram of each star's $I_{\text{H}\alpha}$ index. For both stars, the best-fit frequency of each successive term falls very close to twice the frequency of the previous term, leading us to conclude that we are likely observing harmonics of the initially-observed activity cycle. The drawback to fitting Fourier series is that each new term adds three free parameters to the fit. For targets without a large number of observations (e.g. GJ 552, Figure 4.5(b)), we quickly lose the ability to constrain the parameters of higher-order terms, leading to over-fitting as shown in the Figure.

Below, we discuss each observed activity signal in detail. Additionally, we have included the details of our fits to the data in Table 4.1.

4.3.1.1 GJ 270 and GJ 476

With periods ≥ 3 years, the $I_{\text{H}\alpha}$ signals of GJ 270, GJ 476, and GJ 581 (discussed below) could be considered the "stellar cycles" in our survey. Here, we see the advantage of utilizing the data set of an RV survey; the same observational strategy intended to reveal long-period giant planets gives us excellent coverage of very slow activity cycles, the durations of which have never been previously observed for M dwarf stars.

At $M_* = 0.68 M_\odot$, GJ 270 (M2) is among the more massive M dwarfs in
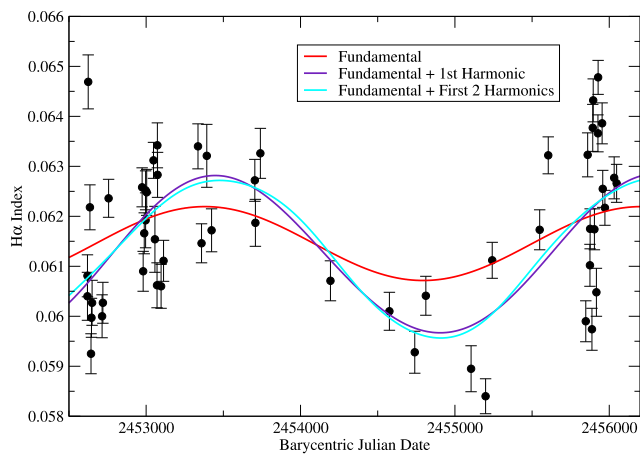
(a)
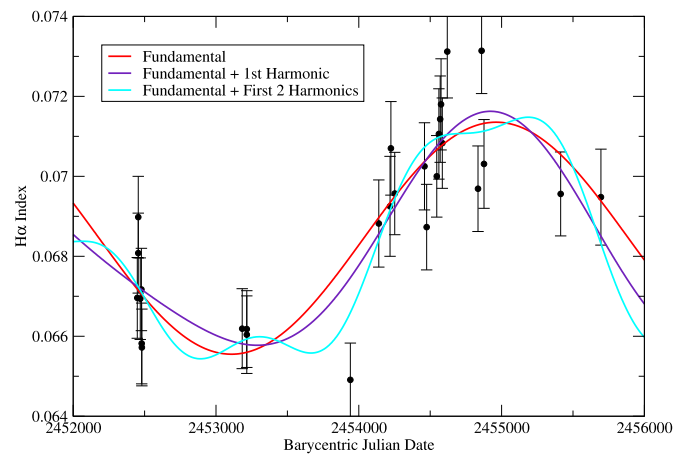
(b)

Figure 4.5: Here, we show the results of fitting Hα activity cycles with Fourier series instead of sine curves for a GJ 270 and b GJ 552. We see that our fits improve with the inclusion of higher-frequency harmonics, but that for few data points (as seen in b), we cannot constrain enough free parameters to justify adding a large number of terms.

our survey. As first reported in [73], we see evidence for a long-period binary companion in the RVs of GJ 270, but at present its period is longer than our observational time baseline. The $I_{H\alpha}$ time series, shown in Figure 4.4(a) shows clear cyclic variation, with a distinct peak in the corresponding periodogram (Figure 4.3(a)) at 2553 days. Our bootstrap analysis generated no false alarms in 10^4 trials, thus giving an upper limit on the FAP of 10^{-4}. We fit a sinusoidal model to this signal with a period of 2687 days and amplitude 0.00158 in $I_{H\alpha}$, the longest-period cycle for which we have observed a full period. We include our fit to the data in Figure 4.4(a).

[13] list GJ 476 as subtype M4, although with a mass estimate of $0.47 M_{\odot}$, it would be among the more massive M4 stars. In Figure 4.4(b), we show the $I_{H\alpha}$ time series, which again shows long-period variation. The power spectrum for GJ 476 peaks at 993 days, with a bootstrap FAP estimate again giving an upper limit of 10^{-4}. Our fitted sinusiod gives a final period of 1066 days. The cycle has an $I_{H\alpha}$ amplitude of 0.00193, the largest of the periodic signals presented herein.

4.3.1.2 GJ 581

We take particular note of GJ 581, both because of the considerable interest in its planetary system (e.g. [17, 157, 225]), and because our observed periodicity confirms the discovery of [87]. It is important to note that our periodogram analysis (Figure 4.3(c)) shows a peak at 448 days with higher power than the longer-period signal claimed in [87]. However, since the longer-

period peak leads to a marginally better fit–yielding an RMS of 0.00118 in $I_{\text{H}\alpha}$ versus 0.00123–we adopt the 1633-day peak as the true period. The 448-day peak disappears in the residuals to a 1633-day fit, indicating it is likely an alias of the fitted signal.

As seen in Figure 4.3, the 1633-day signal of GJ 581 appears at somewhat lower power in our periodogram analysis. In our bootstrap FAP analysis, our randomly-resampled $I_{\text{H}\alpha}$ indices produced higher power spectrum values in 1196 of 10^4 trials, for a FAP of 0.12. However, since our observed period is similar to the 1407-day period derived from the HARPS data, and because our observed $I_{\text{H}\alpha}$ maximum in December 2007/January 2008 matches the Hα maximum found by [86], we consider our detection valid despite having a FAP of ~ 0.1. It is especially remarkable that we observe the cycle in Hα, while [87] use the Na I D feature. Furthermore, the reversal of the minima/maxima between our Hα index and the HARPS Na I index confirms the anticorrelation between Hα and Na I for GJ 581 observed in the HARPS survey [86].

4.3.1.3   GJ 708

With a mass $M_* = 0.77 M_\odot$, GJ 708 is at the upper limit of where the [57] mass calibration is valid. While the Orion Spiral Arm Catalog lists it as spectral type M1, its mass indicates GJ 708 is most likely a late K dwarf. Our RV series shows a monotonic decreasing trend indicative of a binary companion, for which we are currently unable to estimate a period. In

many ways, then, GJ 708 is quite similar to GJ 270.

GJ 708 is unique among the objects presented here because it exhibits a long-term trend in Hα along with a periodic signal. We note that we have fitted and removed a linear slope from the $I_{\text{H}\alpha}$ series prior to creating the phase plot shown in Figure 4.4(d). Once removing the trend, the periodogram on the residual $I_{\text{H}\alpha}$ values (Figure 4.3(d)) shows significant power at 296 days, although we note that the peak appears regardless of whether the trend has been removed. In 10^4 bootstrap resamplings of the residual $I_{\text{H}\alpha}$ values for GJ 708, we observed 282 false alarms, for a FAP of 0.03 on the 296-day period. It is also important to point out that, while the period observed for GJ 708 is close to the 1 year alias, neither the periodogram of our time sampling (the window function) nor the Ca I periodogram showed periodicity near 296 days, eliminating the possibility that the observed signal is caused by our sampling.

The 296 day period of GJ 708's activity cycle is too long to be the rotation period of a typical old dwarf star (normally weeks or months), but is also somewhat short to be reminiscent of a long, solar-type cycle. On the other hand, it is quite similar to the $\sim$ 442 day period observed for the M dwarf Proxima Centauri [40]. It is possible, then, that these two stars represent the first examples of a new class of intermediate-duration activity cycle that occurs in low-mass stars. Alternatively, it may be the case that the linear trend we observe is the star's true "activity cycle," and that the 296-day signal is an intermediate-period cycle that exists alongside the longer signal. Such sub-cycles have been observed for the Sun (e.g. [212]), suggesting similar physics

99

may be at work here.

4.3.1.4 GJ 730

The periodogram for the time series $I_{H\alpha}$ of GJ 730 (Figure 4.3(e)) shows interesting peaks at 3.06 days and 993 days. While the longer periods of the other $I_{H\alpha}$ signals in this study make the longer period peak seem intuitively more likely to be the true signal, the 3-day signal continues to increase in power as we acquire additional data, while the 993-day peak remains constant. While many of our stars exhibit short-term variability, only GJ 730 displays a coherent signal of such statistical significance; our bootstrap FAP estimate gives an upper limit of 10^{-4} for the 3-day peak, making it much more significant than the long-period peak. We note that the 993-day peak is no longer present in the residuals around the 3-day fit, and also that the 3-day peak disappears from the residuals to a 993-day fit, giving further evidence to the two signals being aliases. Because it is possible for an alias to display stronger periodogram power than a true signal, and because the longer period is much more typical of stellar activity cycles, we will not make a definitive argument as to which is the true period. We include fits to both periods in Table 4.1, and show phase plots of both signals in Figure 4.4(e).

If the true period for GJ 730 is 3 days, it is by far the shortest periodicity presented herein. While 3 days could concievably be a rotation period for a very young, active star, it is almost certainly too short for a main-sequence M star, although we are unaware of any $v \sin i$ measurements which might

confirm or reject the rotation hypothesis. Hipparcos photometry [74] is not sampled densely enough to be sensitive to a 3-day period. At spectral type M2, with a mass of $0.62 M_\odot$ and [M/H] = 0.014, GJ 730 appears more or less typical of our sample, leaving no indication as to why such an unusually short periodicity should be present. Its average $I_{H\alpha}$ value of 0.064 is also close to the overall average for our targets, so the star is not especially active.

We note that 3 days is common for the periods of hot Jupiter planets. Previous results [177, 203] have shown evidence that hot Jupiters may induce star-planet interaction (SPI), with measurable periodicity in stellar activity tracers matching the period of the planet's orbit. Our RVs do not currently show evidence for planetary companions to GJ 730, and the RMS scatter of 7.4 m/s shows definitively that any hot Jupiter planet would need to be in an orbit which is highly inclined relative to the line of sight. While the inclination requirement in combination with the inherent paucity of hot Jupiters around M stars [73, 118] makes SPI an unlikely explanation for the 3-day activity signal observed for GJ 730, we present it as an interesting possibility.

On the other hand, if the ~ 1000 day signal is the true period, GJ 730 fits nicely with GJ 270, GJ 476, and GJ 581 as a star displaying solar-type activity cycles. Further study will be required to determine the nature of this star's periodic activity.

4.3.1.5 GJ 552

GJ 552 is an extreme example of non-sinusoidal behavior in Hα activity cycles, as evidenced by the sharp upturn in $I_{\text{H}\alpha}$ observed between July 2006 and April 2008. As mentioned previously, while we recognize the inadequacy of a sine wave fit, we do not have a sufficient number of observations to fit a long Fourier series. Furthermore, we see in Figure 4.5(b) that our different fits offer quite dissimilar estimates for the period of the cycle. While it is possible we have recorded close to a full period, some models result in a period far exceeding our observational time baseline. For this reason, while we believe the behavior seen in our Hα index is likely periodic, we do not claim a specific period, and do not include a model fit in Figure 4.4(f).

4.3.2 Long-Term Activity Trends

For a second subset of our target stars, we see long-term slopes or curvature in $I_{\text{H}\alpha}$, but are unable to confirm any periodicity for these objects because our observational time baseline is shorter than the duration of any periodic signals. We show the time-series $I_{\text{H}\alpha}$ data for these stars–GJ 16, GJ 521, GJ 96, GJ 3023, GJ 3801, GJ 611.3, and GJ 630–in Figure 4.6, along with the corresponding Ca I index. The details and statistics of our fitting are included in Table 4.1 as well. We separate the stars in Figure 4.6 into two groups: stars showing monotonic slopes, and objects for which we observe some curvature or turnaround.

102
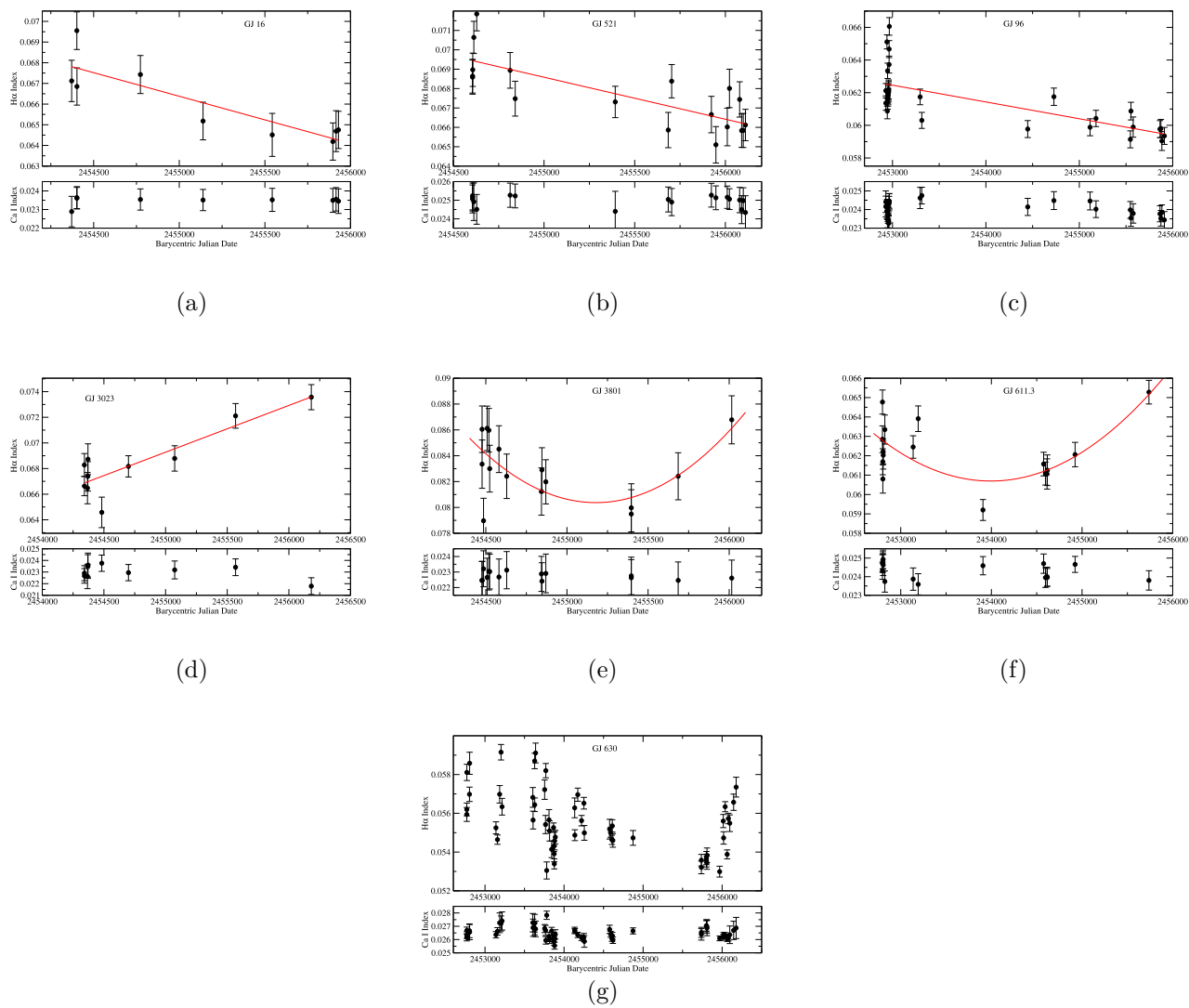
Figure 4.6: Stars with long-term linear trends or curvature in $I_{H\alpha}$ with our best fits (red).

4.3.2.1 GJ 16, GJ 521, GJ 96, and GJ 3023

GJ 16, GJ 521, GJ 96, and GJ 3023 all display a linear trend in $I_{H\alpha}$ over our entire observational time baseline. To ensure the statistical significance of these slopes, we perform a linear least-squares fit to each time series, and calculate the Pearson correlation coefficient. We include these fits in Figures 4.6(a)-4.6(d). In all four cases, the correlation coefficient indicates the relations are highly significant (with the probability of a null result $p << 0.01$).

4.3.2.2 GJ 3801, GJ 611.3, and GJ 630

GJ 3801, GJ 611.3, and GJ 630 all show significant variability, but are poorly fit by linear regression. For GJ 3801 and GJ 611.3, we have compared the quality of linear and quadratic fits with an F-test using

$$F_{\mathrm{poly}} = (N-3)(\chi^2_{\mathrm{slope}} - \chi^2_{\mathrm{poly}})/\chi^2_{\mathrm{poly}}$$

as described in [86]. Here, χ^2_{slope} is the chi-squared value of a straight-line fit, while χ^2_{poly} is the chi-squared of a quadratic fit. We find $P(F_{\mathrm{poly}}) = 0.04$ for GJ 3801 and $P(F_{\mathrm{poly}}) = 0.01$ for GJ 611.3, indicating the quadratic fits are a statistically significant improvement over straight-line models. Our fits are included in Figures 4.6(e)-4.6(f). In GJ 630, the recent dramatic upturn in $I_{H\alpha}$ looks very similar to that of GJ 552. If the Hα activity seen for GJ 630 does prove to be another highly non-sinusoidal periodic signal, its period will easily exceed 10 years, making it a direct analog to the 11-year solar cycle. Since the behavior of $I_{H\alpha}$ is approximately linear prior to this rapid upturn, we have not included a fit for GJ 630, pending future observations to more

accurately characterize the shape of the curve.

4.3.3 RV correlation

Among our motivations for examining the stellar activity of our targets was to evaluate to what level, if any, chromospheric variability influenced our RV measurements. To this end, we have searched for correlations between RV and $I_{H\alpha}$ for our entire sample. In cases where we see evidence for substellar companions (planets or brown dwarfs) in the RVs, we have subtracted those signals and examined the residual velocities.

Overall, we see little correlation between $I_{H\alpha}$ and RV. We find this result unsurprising for our data; [87] report correlations between stellar activity indicators and RV typically occur at or below the 5 m/s level. Such an effect will doubtless be significant for our sample following the HET/HRS upgrade, which will yield a throughput gain of approximately 2 magnitudes at our R = 60,000 setting, dramatically improving the RV precision for our faint M dwarf targets. However, with our current RV precision limited to $\sim$ 6 m/s for the majority of our sample, it is understandable that we see relatively few correlations between $I_{H\alpha}$ and RV. Furthermore, [144] observe a decrease in correlation between RV and R'_{HK} with decreasing T_{eff}, so it is likely we will see relatively fewer M stars with RV-Hα correlation regardless of precision.

On the other hand, we do see two examples–GJ 1170 and GJ 3801– for which RV is anticorrelated with $I_{H\alpha}$ at a level higher than 5 m/s. We show our measured RVs and the corresponding Hα indices for these stars in

Star	Period (days)	*Periodic Signals* Amplitude ($I_{H\alpha}$)	FAP
GJ 270	2687 ± 16	0.00158 ± 0.0003	$< 10^{-4}$
GJ 476	1066 ± 200	0.00193 ± 0.0005	$< 10^{-4}$
GJ 581	1633 ± 93	0.00172 ± 0.0003	0.12
GJ 708	296 ± 1	0.00127 ± 0.0002	0.03
GJ 730 (3-day fit)	3.06 ± 0.01	0.00128 ± 0.0002	$< 10^{-4}$
GJ 730 (994-day fit)	994 ± 40	0.00134 ± 0.0002	0.10
GJ 552	> 2000	$\cdots$	$< 10^{-4}$

	$I_{H\alpha}(t)$	*Linear Trends* r	$P(r)$
GJ 16	$5.7_{\pm 1} - 2.3_{\pm 0.5} \times 10^{-6}t$	-0.868	0.0012
GJ 521	$5.4_{\pm 1} - 2.2_{\pm 0.4} \times 10^{-6}t$	-0.783	6.1×10^{-5}
GJ 96	$2.6_{\pm 0.5} - 1.0_{\pm 0.2} \times 10^{-6}t$	-0.720	5.3×10^{-6}
GJ 3023	$-8.9_{\pm 2} - 3.6_{\pm 0.7} \times 10^{-6}t$	$+0.877$	4.3×10^{-4}

	$I_{H\alpha}(t)$	*Quadratic Trends* F_{poly}	$P(F_{\text{poly}})$
GJ 3801	$50000_{\pm 16000} - 0.04_{\pm 0.01}t + 8_{\pm 3} \times 10^{-9}t^2$	9.31	0.04
GJ 611.3	$9000_{\pm 2000} - 0.007_{\pm 0.002}t + 1.5_{\pm 0.4} \times 10^{-9}t^2$	12.4	0.01
GJ 630	Not Fit		

Table 4.1: Parameters of our fits to the $I_{H\alpha}$ time series discussed in Section 3. For the periodic fits, the FAP listed is taken from the results of our bootstrap resampling analyses. With the linear fits, we include the Pearson correlation coefficient r and the resulting probability of no correlation $P(r)$. Similarly, the quadratic trends include the results of our F-test, as detailed in Section 3.2.2. Our fits to $I_{H\alpha}(t)$ are given as a function of barycentric Julian date.

Figure 4.7. For GJ 1170, we derive a Pearson correlation coefficient of -0.48 for the relation between RV and $I_{H\alpha}$, yielding a probability $p = 0.005$ of no correlation. Similarly, for GJ 3801 the Pearson correlation coefficient is -0.51, indicating the probability of no correlation is just 0.03.

GJ 1170 is a particularly interesting case, as the Hα emission is reflected in the RVs, resulting in a signal which initially appeared to be a Keplerian planet orbit with RV amplitude $K \sim 20$ m/s. Assuming a stellar mass of $M_* = 0.52 M_\odot$, this signal corresponds to a planetary minimum mass of approximately 0.9 Jupiter masses. We therefore conclude that, while $I_{H\alpha}$ does not frequently correlate with RV for M dwarfs at a precision level higher than 5 m/s, there does exist a small subset of stars where Hα activity corresponds to large RV shifts. With such a small number of objects, though, we must concede the possibility that these stars actually have giant planets causing the observed RVs, and coincidentally exhibit activity cycles with periods similar to those of the planets (as with Jupiter and the solar cycle).

4.3.4 Stellar Activity Levels

In addition to examining time-series activity of individual stars, we have also considered the mean activity levels of our targets relative to the overall sample. To do so, we average our Hα index over all observations of a star.

Based on their observed positive correlation between time-averaged Hα index and $V - I$ color, [86] report that mean activity is a function of

107
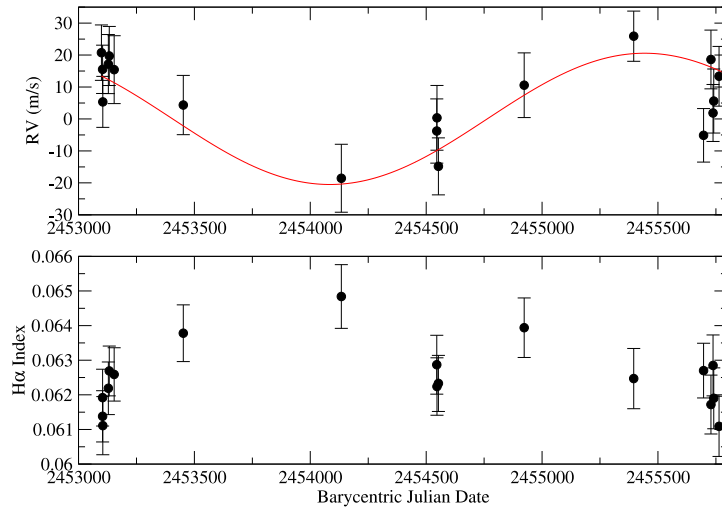
(a)
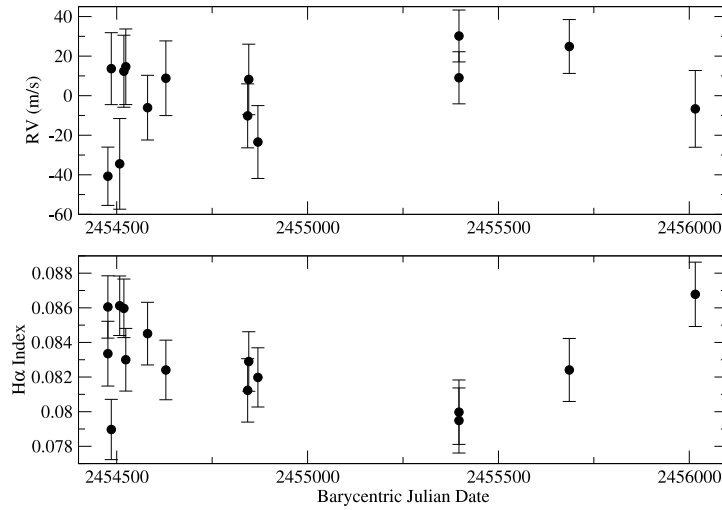
(b)

Figure 4.7: Radial velocity measurements (*Top*) and their corresponding
Hα indices (*Bottom*) for GJ 1170 (a) and GJ 3801 (b). The red curve over the
GJ 1170 RVs shows a Keplerian fit to the data. The RV variations appear to
be caused by stellar activity, as seen by the anticorrelation between RV and
$I_{\text{H}\alpha}$.

temperature. We attempted to confirm this correlation with our sample, but find considerably larger scatter than previously observed, as shown in Figure 4.8. While the relation holds relatively well within the $1.6 \leq V - I \leq 2.8$ color range covered by the [86] sample, it is much less suitable outside that regime. While we looked at mean $I_{\mathrm{H}\alpha}$ as a function of several color indices, we found that no color was a satisfactory tracer of Hα.

We considered the possibility that stellar mass might be a better predictor of mean Hα activity than temperature or color. In Figure 4.9(a), we show our time-averaged Hα index as a function of stellar mass. The resulting anticorrelation is obvious, and the scatter is greatly reduced from that of the color relations. It is apparent that Hα emission is much more tightly connected to mass than temperature. Performing a linear least squares fit to the data, we find the relation

$$\langle I_{\mathrm{H}\alpha} \rangle = 0.094 - 0.050 \frac{\mathrm{M}_*}{\mathrm{M}_\odot} \tag{4.3}$$

Our fit gives 1σ uncertainties of 0.003 on the slope and 0.001 on the intercept.

We explored the residuals to the fit above to determine whether additional dependencies exist. As before, we see no convincing correlation to any color index. On the other hand, stellar metallicity does appear to play a role. Figure 4.9(b) shows the residual Hα index after subtracting the Hα -M$_*$ relation. The resulting correlation is a clear indicator that stellar [M/H] is the primary contributor to the scatter around the mass-activity fit. Again

109
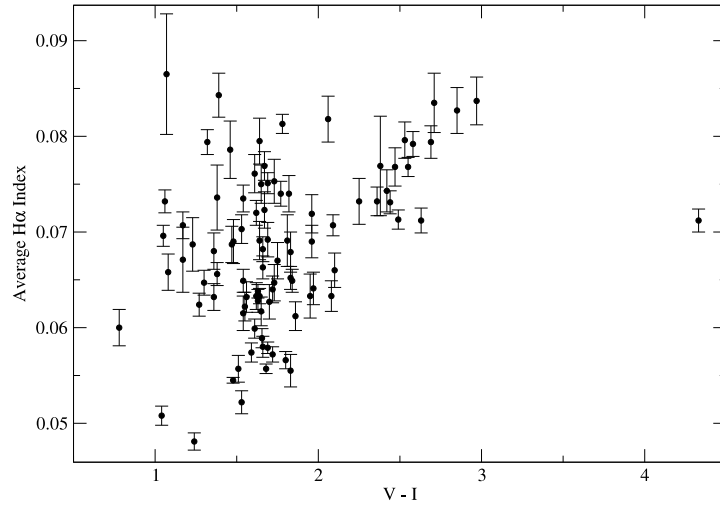
(a)
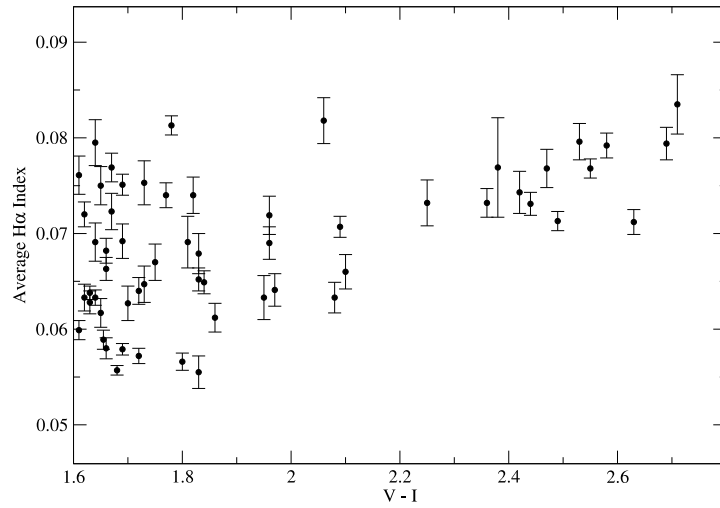
(b)

Figure 4.8: If stellar activity varies as a function of T_{eff}, the average Hα index should correlate with $V - I$ color. In a, we show our time-averaged $I_{\text{H}\alpha}$ as a function of $V - I$ for our entire sample. b shows the same data, but restricted to the same range in $V - I$ as covered by the [86] sample.

110
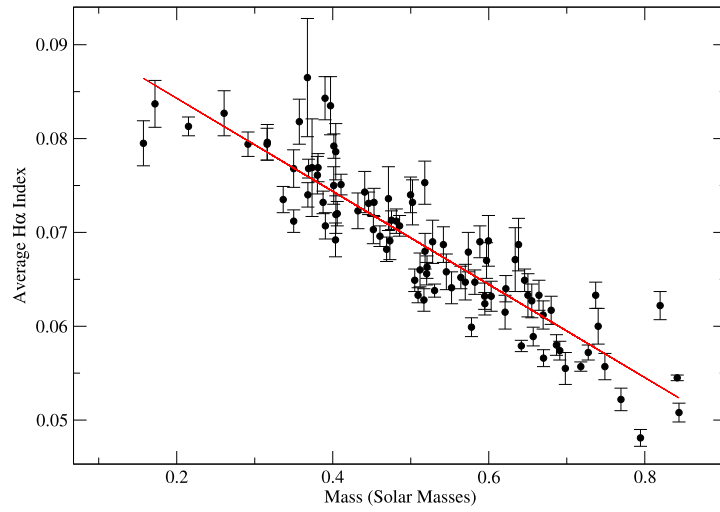
(a)
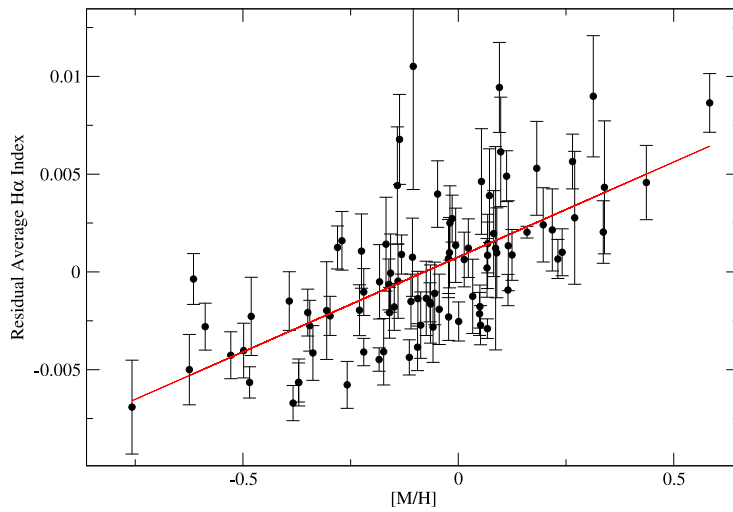
(b)

Figure 4.9: *a*. Time-averaged Hα index as a function of stellar mass for our sample. The red line shows our linear least squares fit to the data. In *b*, we give the residuals to the fit shown in *a*, plotted as a function of stellar metallicity. The red line shows our linear least-squares fit to the data.

performing a linear least-squares fit to our data, we find

$$\langle I_{H\alpha}\rangle_{\text{res}} = 7.6 \times 10^{-4} + 9.7 \times 10^{-3}[\text{M/H}] \tag{4.4}$$

with 1σ uncertainties of 10^{-3} on the slope and 3×10^{-4} on the intercept.

Before drawing conclusions as to the physical interpretation behind Figure 4.9, it is important to understand how the stellar continuum changes as a function of mass and metallicity. Since $I_{H\alpha}$ is normalized by the continuum adjacent to the Hα line, it is possible that the observed trends are due to changes in continuum flux rather than Hα emission. We considered this possibility by converting our Hα index to an equivalent width (EW) using a transformation basically identical to the one outlined in Appendix A of [241], then to the quantity $[L_{H\alpha}/L_{\text{bol}}]$, the logarithm of the luminosity in Hα, normalized by the star's bolometric luminosity. For this transformation, we used the method of [226], which calibrates the ratio of the continuum near Hα to the bolometric luminosity as a function of color for M dwarf stars. Briefly, we use the transformations

$$\text{EW}_{H\alpha} = \Delta\lambda_{H\alpha}(1 - \frac{2\Delta\lambda_C}{\lambda_{H\alpha}}I_{H\alpha}) \tag{4.5}$$

$$[L_{H\alpha}/L_{\text{bol}}] = \chi\text{EW}_{H\alpha} \tag{4.6}$$

Where $\lambda_C = 8.75$ Å is the width of each reference band used to compute $I_{H\alpha}$, $\lambda_{H\alpha} = 6562.808$ Å, $\Delta\lambda_{H\alpha} = 1.6$ Å is the width of the spectral window in
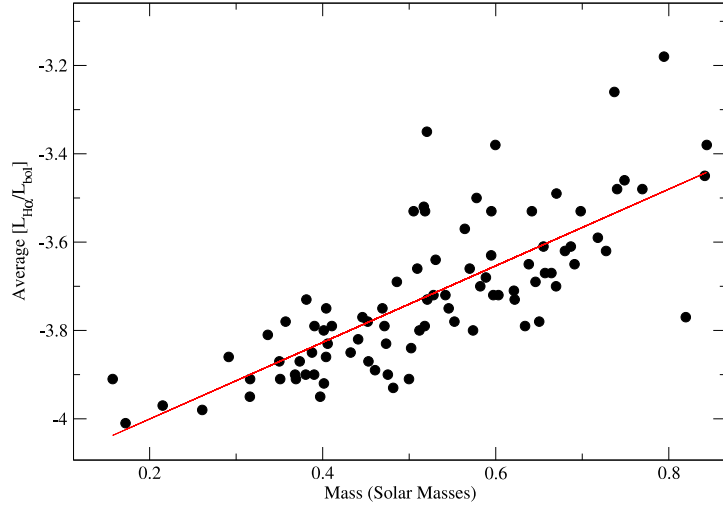
(a)
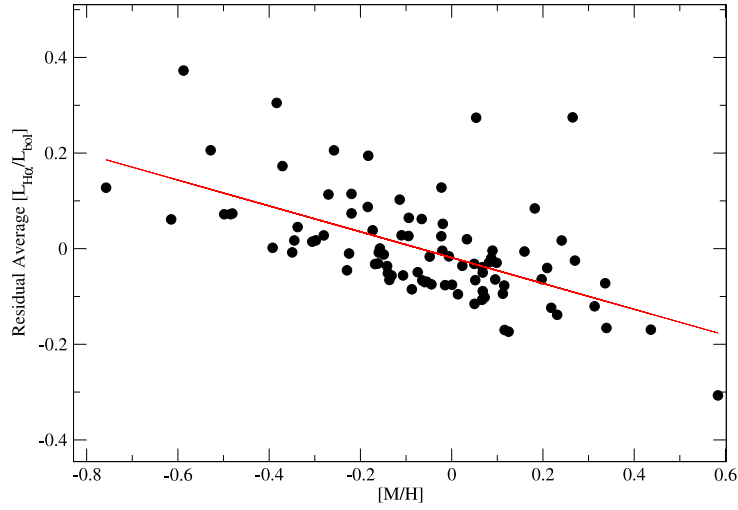
(b)

Figure 4.10: Because our Hα index is normalized to the nearby stellar continuum, variability in continuum flux as a function of stellar mass or T_{eff} may affect the interpretation of Figure 4.9. Here, we transform our $I_{H\alpha}$ values to $[L_{H\alpha}/L_{bol}]$ to remove the influence of the continuum. *a.* shows the time-averaged $[L_{H\alpha}/L_{bol}]$ as a function of stellar mass for our sample. *b.* again gives the residuals to the fit shown in *a*, plotted as a function of stellar metallicity. The red lines show our linear least-squares fits to the data.

which we sum the Hα flux, and χ is the luminosity scaling factor, calculated according to [226]. In Figure 4.10, we again show Hα emission as a function of stellar mass and metallicity, but measure Hα emission with $[L_{\mathrm{H}\alpha}/L_{\mathrm{bol}}]$ instead of $I_{\mathrm{H}\alpha}$.

Perhaps surprisingly, both of the trends seen in Figure 4.9 are reversed in Figure 4.10. Our fit to $[L_{\mathrm{H}\alpha}/L_{\mathrm{bol}}]$ as a function of stellar mass gives

$$\langle [L_{\mathrm{H}\alpha}/L_{\mathrm{bol}}]\rangle = -4.17 + 0.87\frac{\mathrm{M}_*}{\mathrm{M}_\odot} \tag{4.7}$$

with residuals anticorrelated with stellar metallicity. A linear least squares fit to Figure 4.10(b) yields

$$\langle [L_{\mathrm{H}\alpha}/L_{\mathrm{bol}}]\rangle_{\mathrm{res}} = -0.019 - 0.27[\mathrm{M/H}]. \tag{4.8}$$

Our 1σ uncertainties on the slopes and intercepts, respectively, are 0.08 and 0.04 for Equation 4.7, and 0.01 and 0.04 for Equation 4.8.

At first, the results of Equations 4.3-4.4 and 4.7-4.8 appear to present conflicting information regarding the dependence of stellar activity on mass and metallicity. However, we suggest a conceptually simple hypothesis consistent with all four relations. It has been firmly established that the stellar continuum near Hα varies along with bolometric luminosity [41, 93, 226]. According to the [41] $F_{\lambda 6605}$ versus $B - V$ relation, we expect the continuum around Hα to differ by up to a factor of 5 across the range of $B - V$ typical of our sample. Thus, since $[L_{\mathrm{H}\alpha}/L_{\mathrm{bol}}]$ spans a factor of ~ 4 over our sampled

114

range of stellar mass, we would expect a ~ 80 percent decrease in $I_{\mathrm{H}\alpha}$ over the same range (assuming $\Delta I_{\mathrm{H}\alpha} \sim \frac{\Delta L_{\mathrm{H}\alpha}}{\Delta F_{\lambda 6605}}$). The observed $I_{\mathrm{H}\alpha}$ decrease of ~ 60 percent is fully consistent with this expectation, considering the significant uncertainty in the Cincunegui relation at high $B - V$. We therefore conclude that chromospheric Hα emission is increasing with stellar mass, but the effect does not appear in our original Hα index because of the increasing continuum flux.

Understanding the metallicity dependence for Hα emission requires a similar deconstruction of stellar luminosity/continuum effects. When we subtract a linear fit to the $I_{\mathrm{H}\alpha}$ - M_* relation, the effects of the varying stellar continuum should be removed, suggesting higher-metallicity stars are more active. However, verifying this demands explaining the decrease in $[L_{\mathrm{H}\alpha}/L_{\mathrm{bol}}]$ with [M/H]. Previous observations of M dwarf activity have shown that more active stars are more luminous, possibly due to an increase in stellar radius [14]. Furthermore, stars with high [M/H] will be more luminous at a given $B - V$ or $V - K$ color than metal-poor stars due to line blanketing of blue light in the more metal-rich objects. Figures 4.9(b) and 4.10(b) are therefore consistent with the argument that metal-rich M dwarfs display higher Hα emission, but their increased activity and opacity in the blue cause L_{bol} to increase faster than $L_{\mathrm{H}\alpha}$, causing the negative slope seen in Figure 4.10(b).

Earlier studies of M dwarf activity (e.g. [30, 228]) emphasize the importance of considering the various subtypes of M stars, particularly around M4, where stars typically become fully convective. Figure 4.11 shows the time-

115
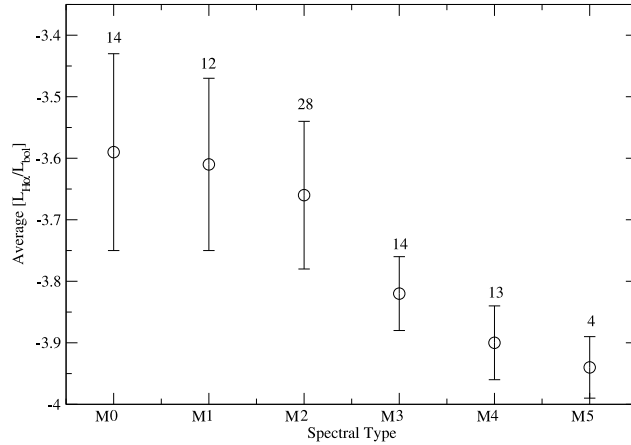
Figure 4.11: Activity levels of M stars has previously been shown to vary with spectral subtype. In this Figure, we have grouped our time-averaged $[L_{H\alpha}/L_{bol}]$ values as a function of spectral subtype for our sample. The error bars indicate the RMS scatter in each bin, and the numbers above each point give the number of stars in the bin.

averaged $[L_{H\alpha}/L_{bol}]$ values for objects of known subtype in our sample. In the Figure, the error bars represent the RMS scatter within a given bin, rather than measurement error. The decrease in $[L_{H\alpha}/L_{bol}]$ towards later types essentially reflects the observed mass dependence. However, we see more clearly in Figure 4.11 the tendency for more active bins to have more scatter as well.

4.4 Discussion

4.4.1 Stellar Cycles

Our observed stellar activity cycles indicate that even for an old, quiet stellar population, magnetic activity may appear at essentially any period. The

long-period subset of stars shown in Figure 4.4, particularly GJ 270 ($P \sim 7.5$ years), demonstrate stellar periodicity on the order of the 11-year solar cycle is far from unique; stars with cyclic activity of period > 1 year appear in at least 5% of our sample. In future work we will include additional tracers (e.g. the Na I D feature, see [60]), both to increase sensitivity to additional activity cycles, and to fully evaluate the impact of stellar variability on our RV survey. The addition of other tracer indices will almost surely increase the number of candidate signals among our targets.

While the periods of the stellar cycles observed in Figure 4.4 fall towards the low end of the period distribution found by [6] for solar-type stars, our results are entirely consistent with the Mount Wilson survey. While the Baliunas distribution peaks between $\sim 5 - 12$ years, there are a significant number of detections between 1 and 5 years. Furthermore, our observational time baseline, while extensive, is still too short to properly characterize stellar cycles with $P \geq 10$ years. It is quite likely that the six stars shown in Figure 4.6 are examples of partial detections of such periods. Clearly, it is essential that both the durations and number of targets be increased for M dwarf activity surveys for a proper comparison to FGK stars.

[144] find activity cycles with amplitude 0.04 or higher in R'_{HK} for $61 \pm 8\%$ of quiet FGK stars. At present, the percentage of M dwarfs with observed magnetic cycles is significantly lower. Using the Na I D feature, [87] find periodic signals for 5 of 27 M stars surveyed, for a rate of 19%. With 6 periodic signals found in 93 stars, our resulting "cyclic fraction" is even lower, at 6.5%.

If we assume the 7 stars for which we observe long-term trends are exhibiting activity cycles, our rate increases to 14%, which is more in agreement with the [87] value. It is possible that the difference in the periodic fractions is due to the relative sensitivites of the activity indices. Because the sodium feature is emitted deeper in the chromosphere than Hα, where the local density is higher, a change in the magnetic field should produce relatively more emission in sodium than hydrogen, making the amplitude of a given stellar cycle higher in the Na I index than in $I_{H\alpha}$. Our overall sample size, and the number of observed stellar cycles and trends in Hα will allow us to make a thorough comparison between the two indices in future work, as we will have a robust set of comparison cases to establish whether the Na I D feature is simply more sensitive to weaker signals, or in fact probes different stellar physics.

In any case, current data suggests M dwarfs are less likely to display measurable magnetic periodicity than earlier spectral types. A possible explanation for the discrepancy lies in the lack of a tachocline for many M stars. At a spectral subtype of M4 and below, stars become fully convective [38] and therefore do not possess a solar-type dynamo, which is driven by differential rotation between the radiative and convective layers. If the solar cycle and its analogs are driven by this dynamo, then we should expect to see only low-amplitude cycles or quasi-periodic oscillations for fully convective stars. Indeed, of the stars we identify as having cycles or trends, only GJ 476 and GJ 581 have spectral subtypes later than M3 according to [13]. Of those two, GJ 476 has an estimated mass of $0.47 M_\odot$, which is massive enough to have

a tachocline despite its listed type of M4, and the activity cycle of GJ 581 may be connected to its planetary system (see below). Furthermore, Figure 4.11 shows a distinct dropoff in $[L_{\mathrm{H}\alpha}/L_{\mathrm{bol}}]$ around spectral subtype M3-M4, suggesting the fully convective stars in our sample are characteristically less active. If continued study shows stellar activity cycles in M stars to be confined mainly to subtypes M0-M3, it will be an intriguing piece of evidence in favor of the tachocline dynamo as the origin of stellar magnetic cycles.

The period of the $I_{\mathrm{H}\alpha}$ cycle seen for GJ 270 is nearly equal to that of GJ 752 A [32], making it one of the two longest M dwarf activity cycles observed to date. It is worth noting that both of these stars are members of binary systems [32, 73]. Among the stars in Figures 4.4 and 4.6, we see evidence in our RVs for a brown-dwarf binary companion to GJ 708, and GJ 581 hosts a known multi-planet system. [163] have shown that M dwarfs with close binary companions display increased magnetic activity, and the SB2 GJ 375 has been shown to exhibit a long-period activity cycle in the Ca K index [61]. Likewise, [129] see tentative evidence of increasing Ca II emission for stars in known exoplanet systems. Interestingly, of the binary/planetary systems for which stellar cycles have been observed, none of the stellar activity periods match the companion orbital periods or their harmonics. Further study will be required to definitively establish or reject a physical connection between more distant/less massive substellar companions and stellar activity cycles, but it is worth noting that a number of our candidates exhibit both, as do those of previous studies.

4.4.2 Magnetic Activity and RV Planet Surveys

Aside from the obvious value to the study of low-mass stellar physics, the understanding of M dwarf activity cycles has important implications for RV planet surveys. It has been well established that periodic RV signals can be caused by stellar chromospheric variability, as traced by photometry or activity indicators such as Ca H and K [78, 183, 189]. While activity-induced RV signals are typically expected to have amplitudes of just a few m/s, Figure 4.7 shows that exceptionally large-amplitude effects will occasionally appear. In general, though, these results will be increasingly important as M dwarf RV surveys approach precisions of 1 m/s or less. GJ 581 stands as an excellent example. We notice a striking similarity between our periodogram of the GJ 581 Hα index (Figure 4.3(c)) and the periodogram of the residual RVs to a 4-planet fit shown in [224] (Figure 3, panel 5), particularly at the $\sim$ 450- and $\sim$ 1600-day peaks. The 433-day period of the unconfirmed planet f is very close to our observed alias at 448 days, as is the candidate 400-day planet identified in [91]. While fitting a Keplerian orbit to an activity-induced RV signal would essentially serve to correct the RVs for stellar activity, if the true period of GJ 581's $I_{\mathrm{H}\alpha}$ cycle is 1300-1600 days, then removing a 433-day orbit would lead to incorrect residuals, complicating the analysis of any additional planets. Clearly, any RV detection of low-mass planets around M dwarf stars should be accompanied by a careful analysis of the corresponding stellar activity indices.

4.4.3 Mean Activity Levels

Our results for the comparative activity levels between the stars in our sample are interesting in the context of previous surveys of more active M stars. Figure 4.11 shows essentially identical behavior to the findings of [227] (Figure 5) and [130] (Figure 7). We note a slight discrepancy from [163] (Figure 12), though, who do not see a decrease in $[L_{\mathrm{H}\alpha}/L_{\mathrm{bol}}]$ until spectral type M4. Whether this behavior extends to solar-type stars is somewhat unclear based on current results. [144] report that most G stars have $\log R'_{\mathrm{HK}}$ around -5, while stars of K type cluster around $\log R'_{\mathrm{HK}} \sim -4.7$, suggesting an inversion of the relation observed for M stars. These results could still be reconciled, since stellar bolometric luminosity increases at earlier spectral types, so some normalization may be required to properly understand how mean activity levels vary across the entire main sequence. Of course, it is known that Hα behaves differently from Ca H and K, especially for cool dwarfs such as those in our sample (e.g. [41]). A more harmonious result can be seen in [6], who plot mean $\log S_{\mathrm{HK}}$ against $(B-V)$ color for FGK stars, finding an increasing trend (and scatter) similar to Figure 4.8.

The data presented here are perhaps more compelling when shown as a function of stellar mass, though. Because our targets are pre-selected to be "quiet," and do not show Hα in emission, they should all be older than their "activity lifetime" [228]. Figure 4.10(a) seems to suggest that for these quiet stars, the dynamo responsible for driving the residual magnetic actvity following the spin-down phase is more effective in more massive stars, which

presumably are not fully convective. Again, it is possible that the presence of a more significant radiative zone in the interiors of the more massive stars leads to the generation of a solar-type magnetic dynamo at the interface of the convective and radiative layers, rather than the rotation-dominated magnetic activity of younger, highly active M dwarfs.

As explained above, our data indicate that metal-rich stars tend to be more active than average at a given stellar mass. One possible cause for this relation is that our measured [M/H] is–in a statistical sense–a tracer of age, and we are simply observing the previously-confirmed connection between stellar age and chromospheric variability (e.g. [14, 228]). To test this hypothesis, we have obtained space velocities for our sample from [13]. In Figure 4.12, we plot the mean galactic velocity dispersions of various metallicity bins in the UVW coordinates, excluding very high and low metallicities due to small numbers of stars. In general, we see that low-metallicity stars have higher velocity dispersions in all three coordinates, lending support to the proposal that the metal-rich stars in our sample are younger. Further evidence of the age-metallicity relationship is discussed in [228]. The fact that we see higher average $I_{H\alpha}$ values towards increasing [M/H] is therefore likely a reflection of the younger members of our sample being more active. Again, all of the stars discussed herein are old, and should have evolved past their early active stages. It is remarkable, then, that the effects of stellar age are still visible in the activity levels of these objects. It is worth pointing out that, while the UVW velocities suggest a spread in age among our objects, the probability

distributions of [186] indicate all of our targets are members of the Galactic thin disk with $\geq 99\%$ probability, so our observed mass and metallicity/age dependencies may or may not apply as cleanly to stars in the thick disk or halo.

The implications of this study are potentially encouraging for the prospects of current and future near-infrared (NIR) RV surveys for planets around late M stars. The old, low-mass stars which will make up the majority of the targets should have relatively low chromospheric activity levels, and will be less likely to exhibit activity cycles. Furthermore, we have shown that the stellar cycles which may be confused with planetary signals appear in Hα, which is much more likely to be accessible to a NIR spectrograph than Ca H and K. The CARMENES spectrograph [184], in particular, will be able to acquire Hα. Therefore, problematic signals may be properly identified and corrected. While the Habitable Zone Planet Finder on HET [148] will not have wavelength coverage at Hα, our results illustrate the necessity of identifying a suitable activity tracer in the NIR for RV surveys.

4.5   Conclusion

We have measured and analyzed time-series Hα emission for ~ 11 years of spectra for 93 low-mass stars. Our primary results may be summarized as follows:

(a)

(b)

(c)
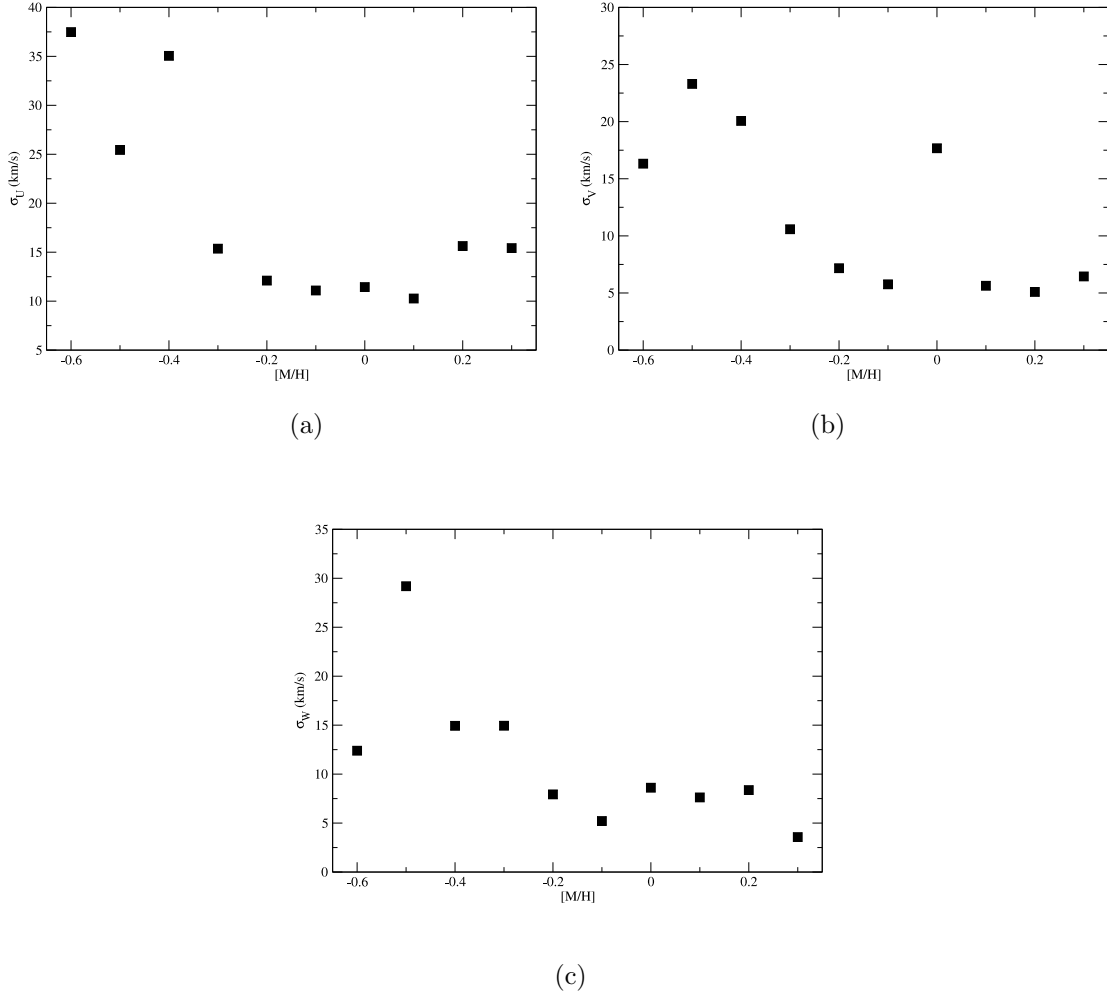
Figure 4.12: We investigate whether there is any indication that the more metal-poor stars in our sample are older than the metal-rich stars. Here, we plot galactocentric velocity dispersion in UVW coordinates as a function of stellar metallicity. Metal-poor stars tend to have higher velocity dispersions in all three coordinates, suggesting they are older, potentially explaining why our metal-poor targets exhibit lower mean $I_{\mathrm{H}\alpha}$ values.

1. We find strong periodic Hα variability for 6 stars in our sample, and long-term trends or curvature for 7 others. Among these, we confirm the discovery of the activity cycle for GJ 581 found by [87]. Our observed stellar cycles are analogous to those previously observed for FGK stars.

2. While activity-induced RV signals are relatively rare in our sample at its current precision level, we identify two stars–GJ 1170 and GJ 3801– for which our Hα index is anticorrelated with RV, indicating activity cycles causing RV variations of nearly 20 m/s. Additionally, we see evidence that the signal of the purported planet f in the GJ 581 system may in fact be caused by an alias of the $\sim$ 1600-day stellar activity cycle, further emphasizing the need to consider stellar RV modulation at the $\leq$ 3 m/s level of precision.

3. The mean Hα activity levels of our targets correlate with stellar mass. This result is qualitatively consistent with previous observations of both solar-type and low-mass stars, although the correlation has more often been expressed in terms of stellar temperature or color, rather than mass. We confirm that $[L_{H\alpha}/L_{bol}]$ decreases towards later stellar subtypes, a phenomenon that appears to hold true for M stars regardless of whether or not they are in the "active" phase. Lower $[L_{H\alpha}/L_{bol}]$ values and an apparent lack of observable stellar cycles for fully convective stars may be related to the absence of a tachocline for those stars.

4. In addition to the mass-activity relation, we see a metallicity dependence on average Hα emission. Lower average galacitc velocity dispersions indicate the more metal-rich stars in our survey are in fact younger. Even

125

though all the stars in our sample have aged beyond their "active" phase, it appears some residual age effect still contributes to their mean activity levels, and that the younger of our targets are still more active at a given stellar mass.

Chapter 5

Planet and Activity Signals in GJ 328

5.1 Background

The discovery of planets around nearby stars has become essentially routine, and exoplanets are now understood to be common around nearly every kind of star. Low-mass planets, in particular, appear to be virtually ubiquitous even for low-mass [108] and low-metallicity [33] stars, as shown in recent *Kepler* results. However, the one population of planets which remains sparse despite the recent explosion of exoplanet discoveries is gas giant planets in long-period orbits around low-mass stars.

The under-abundance of giant planets around low-mass stars is understood within the core accretion model as the result of less massive protoplanetary disks and longer dynamical timescales for such stars. As a result, protoplanetary cores fail to acquire enough material to undergo runaway accretion within the disk lifetime (e.g. [1, 137]). Giant planets do exist in both close (e.g. GJ 876b,c [56, 152, 153]) and distant (GJ 676Ab [79], GJ 832b [5]) orbits around M stars. Generally, though, gas giants ($M \sin i > 0.3 M_J$) are increasingly rare around lower-mass stars, particularly below $M_* = 0.85 M_\odot$ [115, 238]. In particular, close-in gas giants are exceedingly rare around M

stars [73, 167, 211], in agreement with the predictions of core accretion simulations. It is important to note, though, that to date there is not yet sufficient observational data to confirm predictions that low-mass stars are deficient in giant planets at *all* orbital radii. Since it is conceivable that planet formation through gravitational instability may contribute to the long-period Jovian population for M stars [23, 25, 26], it is essential to probe the space beyond ~ 1 AU around M dwarfs for exoplanets.

The early indications are that the early M dwarfs have detectable gas giant planets ($M \sin i$ greater than 0.8 Jupiter masses) on relatively short period orbits (semi-major axes less than 2.5 AU) with a frequency of about 5% [115]. However, gravitational microlensing searches have uncovered giant planets orbiting at greater distances at a rate consistent with a much higher frequency of giant planet companions to early M dwarfs, about 35% [89]. Microlensing has also detected a huge population of Jupiter-mass planets (about two per main sequence star) that are either unbound, or at distances of 10 AU or more from their host stars [210]. [182] showed that given the weak limits imposed by direct imaging surveys, most of these objects are likely to be bound to a star rather than to be free-floating. They suggest that Jupiter-mass planets are likely to be found in increasing numbers out to about 30 AU around M dwarfs. Evidently there is much remaining to be learned about the census of extrasolar giant planets.

The McDonald Observatory M dwarf exoplanet survey (see [72] for details, including selection criteria) is a long-term radial velocity (RV) sur-

vey of 100 M stars using the Hobby-Eberly Telescope. The survey has just finished its 12th year of operation, and has amassed approximately 3,000 high-precision RV measurements over that interval. We have previously established the paucity of hot Jupiters around M dwarfs [73], and now use the survey primarily to discover low-mass planets and long-period gas giants. Additionally, we are in the process of analyzing the long-term magnetic activity of our stellar targets [191].

In this chapter, we announce GJ 328b, a Jovian planet around a K/M dwarf at $a \sim 4.5$ AU. Although the star exhibits a solar-type activity cycle that shifts our measured RVs, we show that the signal of planet b is not caused by this behavior. Instead, when correcting for stellar activity, we see that the planet follows a more eccentric orbit than indicated by our model to the uncorrected velocities.

5.2 Stellar Properties of GJ 328

In Table 5.1, we list measured and derived stellar parameters for GJ 328. Because the absence of an optical continuum makes estimating these properties for low-mass stars difficult with spectral synthesis, we instead rely on photometric calibrations for several items in the table. We derive a mass of $M_* = 0.69 \pm 0.01 M_\odot$ using the [57] K-band mass-luminosity curve, and a metallicity $[\text{M/H}] = 0.00 \pm 0.15$ from the [197] color-magnitude relation.

With a mass of 0.69 solar masses and $T_{eff} = 3900 \pm 100$ K, GJ 328 lies at the boundary between spectral types K and M. Various catalogs classify

Parameter	Value	Reference
Spectral Type	M1 d	[126]
V	9.98 ± 0.04	[99]
$B - V$	1.32 ± 0.1	[99]
K	6.352 ± 0.026	[49]
M_V	8.50 ± 0.13	This Work
M_K	4.87 ± 0.06	This Work
Parallax	50.52 ± 1.90 mas	[221]
Distance	19.8 ± 0.8 pc	This Work
T_{eff}	3900 ± 100 K	[161]
[M/H]	0.00 ± 0.15	[197]
Mass	$0.69 \pm 0.05 M_\odot$	[57]
$[L_{H\alpha}/L_{bol}]$	-3.53 ± 0.01	[226]
R'_D	-4.91 ± 0.05	[61]

Table 5.1: Stellar Properties for GJ 328

the star between K7 [2] and M1 [126]. For our purposes, it suffices to say that GJ 328 is a "cool dwarf." We note that, using the Galactic UVW velocities of [13], the probability distributions of [186] indicate GJ 328 is a thin-disk star with greater than 99 percent confidence.

5.3   Data

Our primary data consist of 58 high-resolution spectra of GJ 328 taken with the High Resolution Spectrograph (HRS; [218]) on the 9.2m Hobby-Eberly Telescope (HET; [185]) at McDonald Observatory. The observations span the period between January 2003 and April 2013, for a total observational time baseline of 10 years. Our observations were taken using a 2.0 arcsecond

fiber imaged through a 0.5 arcsecond slit, for a resolving power $R = 60,000$. The queue-schedule system of HET (see [43] for details of our HET strategy) allows us to observe GJ 328 several times per season, resulting in quasi-unifom phase coverage for long-period planets. We perform routine wavelength calibration, bias subtraction, flat-fielding, and cosmic ray removal using standard IRAF[a] scripts.

In order to obtain high-precision velocities from our spectra, we place an absorption cell filled with molecular iodine (I_2) vapor in front of the slit. The cell is kept at constant temperature and pressure, which results in the superposition of thousands of stable absorption lines over our spectra from 5000-6400 Å. We have a high-S/N spectrum taken without the I_2 cell, which we deconvolve from the instrumental profile (IP) using the Maximum Entropy Method. This "template" spectrum serves as a baseline against which we model the time-variant IP and RV for each star $+ I_2$ template. The deconvolution and modeling for our spectra are handled by our RV extraction code AUSTRAL, the details of which are described in [71].

Our HET/HRS spectra are supplemented with 14 spectra from the Robert J. Tull Coudé spectrograph [217] on McDonald's 2.7m Harlan J. Smith Telescope (HJST). We have also acquired 4 spectra using the HIRES [223] spectrograph on the 10m Keck I telescope at Mauna Kea. These spectra

---

[a]IRAF is distributed by the National Optical Astronomy Observatories, which are operated by the Association of Universities for Research in Astronomy, Inc., under cooperative agreement with the National Science Foundation.

were taken during our Keck CoRoT RV follow-up observations [195] when the CoRoT field was unobservable. The HJST and Keck observations were also taken through I_2 absorption cells, at resolving powers 60,000 and 50,000, respectively. Again, RV extractions are performed with AUSTRAL.

We present all of our RV data in Table 5.3, and present them as a time series in Figure 5.1. The velocities have been corrected to remove the velocity of the observatory around the solar system barycenter at the time of observation.

5.4 RV Analysis

As seen in Figure 5.1, our velocities for GJ 328 show large deviations of an apparently periodic nature. The combined data set display an RMS scatter of 26.7 m/s with an average error of 6 m/s.

We began our analysis by computing the fully generalized Lomb-Scargle periodogram [240] for our data. The resulting power spectrum, shown in Figure 5.2, displays a broad, highly significant peak centered at $P = 3700$ days. We have also computed the window function, the periodogram of our time sampling. We note that our time sampling is not dense enough to avoid aliasing at very short ($P \sim 1$ day) periods, so our periodograms should be used with caution in the high-frequency regime.

In order to establish the reliability of our periodogram analysis, we compute a false alarm probability (FAP) using three different methods. The first
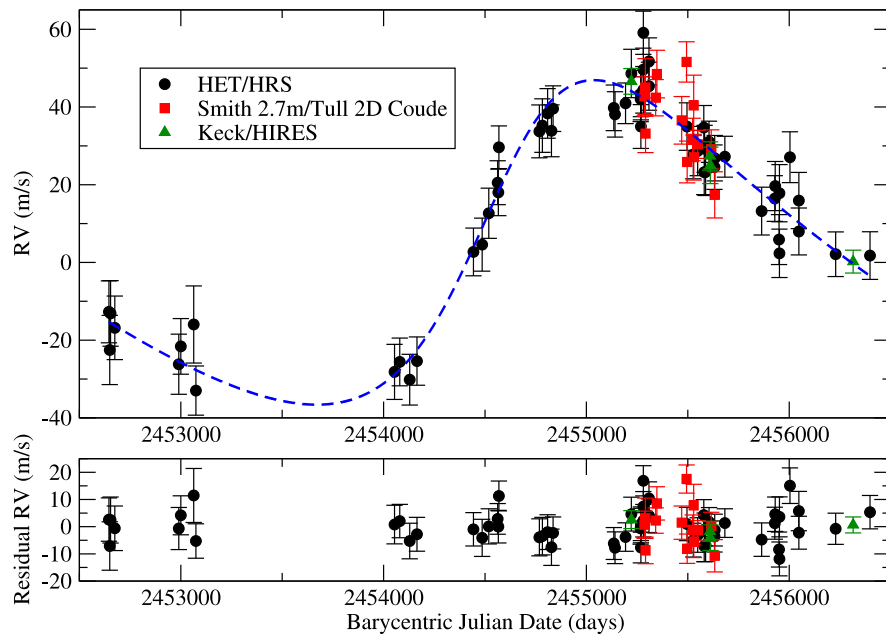
Figure 5.1: We present 10 years of radial velocity data for GJ 328. The RVs show a clear periodic signal, which we associate with a giant planet. Our Keplerian model to the data is shown as a dashed blue line.
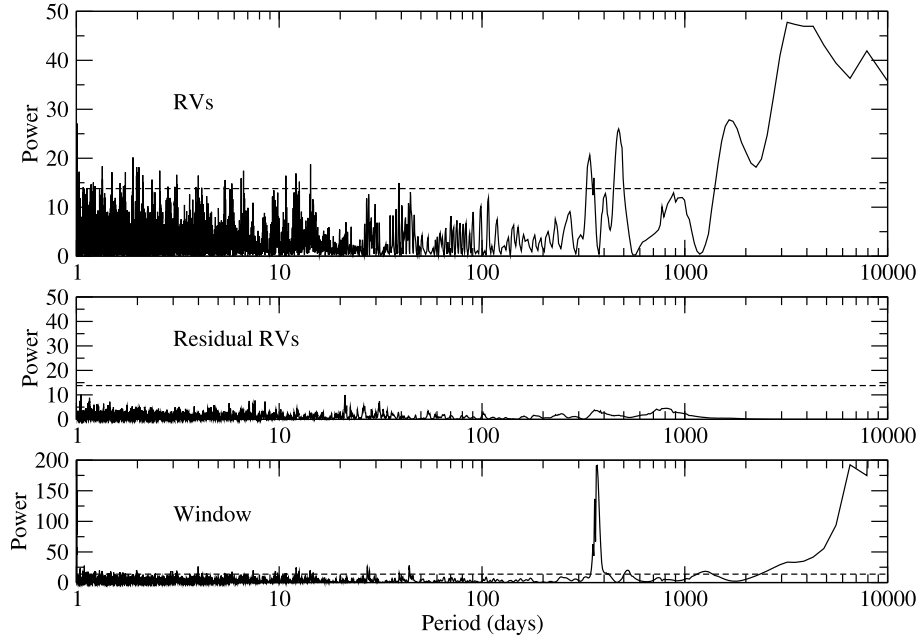
Figure 5.2: Fully generalized Lomb-Scargle periodograms for our RV data. The top panel shows the power spectrum for our combined RV data set with the strongest peak at $P \simeq 3500\text{d}$, while the middle panel gives the periodogram of the residuals to a one-planet fit, and the bottom shows the periodogram of our sampling pattern (the window function). The dashed horizontal lines represent the power level corresponding to a false alarm probability (FAP) of 0.01, as calculated from Equation 24 of [240]. We note that these FAP levels represent a preliminary estimate, and our formal FAP values are obtained through a bootstrap analysis, which we describe in Section 5.4.

134

method assumes the noise distribution in the data is Gaussian, and estimates the probability that a peak of power P_ω would arise at random from a sample of N points. The formula for this FAP is given in Equation 24 of [240], and we estimate M, the number of significant frequencies sampled as $\frac{\Delta f}{\partial f}$, where Δf is the range of frequencies in the periodogram and ∂f is the resolution of our computation. A second estimate, from [209], derives the FAP from the excess of power above an expected distribution of power values from Bayesian statistics. We consider both of these calculations to be preliminary estimates, and note that they agree with each other in all cases discussed herein. For the 3700-day peak in the RV power spectrum, we compute a preliminary FAP lower than our computational precision, approximately 1.0×10^{-14}.

To assign a formal FAP to the signal in Figure 5.2, we conducted a Monte Carlo bootstrap calculation as described in [131]. We retained the time stamps of the original data set, and assigned at random (with replacement) an RV value from the set to each time. We computed the periodogram of 10,000 such "fake" data sets, and took the FAP to be the percentage of those periodograms with a peak having greater power than the original power spectrum at any period. For the 3700-day signal, our bootstrap calculation produced no false positives in 10,000 trials, giving an upper limit to the FAP of 10^{-4}.

We begin with the assumption that the variability in the RVs is caused by a planetary companion. We model the orbit of the planet using both the GaussFit [113] and SYSTEMIC [160] software suites. The observed velocities are fit nicely with the Keplerian orbit of a giant planet. Our best-fit solution,

the parameters of which we list in Table 5.2, has a period $P = 4100$ days, which corresponds well with the peak in our periodogram when considering the breadth of the peak and the fact that our solution has a significant eccentricity $e = 0.29 \pm 0.04$. The signal, with an RV amplitude of 42 m/s, corresponds to a planet of minimum mass $M \sin i = 2.5 M_J$ at $a = 4.43$ AU. The planet, GJ 328b, is therefore a "cold Jupiter," a gas giant planet which remained at large orbital separation rather than migrating inward. We show our fit to the data in Figure 5.1, as well as the residual RVs after subtracting the model. Our model results in a reduced χ^2 of 1.12, with a residual RMS scatter of 6.0 m/s. We note that we see no additional signals in the periodogram of the residual RVs (middle panel, Figure 5.2).

5.5   Stellar Magnetic Activity

We are currently performing an in-depth analysis of stellar magnetic activity in the stars from our M dwarf RV survey (see [191] for full details). Because stellar activity can cause apparent RV shifts which may obscure [66] or imitate [183] a Keplerian planet signal, it is essential to consider activity indicators when analyzing RV data. Although it is not typical for the stellar magnetic behavior of old, quiet stars to create RV signals with magnitudes as large as seen for GJ 328, we have shown in the case of GJ 1170 that stellar activity can occasionally mimic the velocity signatures of giant planets [191]. We have therefore examined two spectroscopic tracers of stellar activity for GJ 328, and corrected the RV curve for its periodic stellar component.

Orbital Parameter	Value (Uncorrected for Stellar Activity)	Value (Corrected for Stellar Activity)
Period P (days)	4100 ± 170	4100 ± 300
Periastron Passage T_0 (BJD - 2 450 000)	4600 ± 70	4500 ± 100
RV Amplitude K (m/s)	42 ± 1.7	40 ± 2.0
Mean Anomaly M_0	$190° \pm 9°.0$	$200° \pm 9°.0$
Eccentricity e	0.29 ± 0.04	0.37 ± 0.05
Longitude of Periastron ω	$290° \pm 8°.0$	$290° \pm 3°.0$
Semimajor Axis a (AU)	4.4 ± 0.30	4.5 ± 0.20
Minimum Mass $M \sin i$ (M_J)	2.5 ± 0.10	2.3 ± 0.13
HET/HRS RV offset (m/s)	-18.0	-17.0
HJST/Tull RV offset (m/s)	-18.0	N/A
Keck/HIRES RV offset (m/s)	-7.2	N/A
RMS (m/s)	6.0	6.0

Table 5.2: Orbital solutions for GJ 328b, with and without corrections for stellar activity.

5.5.1 Stellar Activity Analysis

Because HRS does not acquire the Ca II H & K lines, we have examined the magnetic activity of GJ 328 using the Hα and Na I D ($\lambda_{D1} = 5895.92$ Å, $\lambda_{D2} = 5889.95$ Å) absorption lines from each RV spectrum. Briefly, as stellar activity creates magnetic hot spots in the chromosphere, emission of Hα and Na I photons is stimulated, filling in the observed absorption lines (see [191], Figure 2). As a control test, we have also analyzed the Ca I ($\lambda = 6572.795$ Å) line, which does not respond to stellar activity, and should therefore remain relatively constant.

We define $I_{H\alpha}$, our Hα index, according to [191], using a method analogous to the calculation of [132]. The index is simply a ratio of the flux in the 1.6 Å window centered on the Hα line relative to the nearby pseudocontinuum. The index can easily be transformed into an equivalent width, and to $[L_{H\alpha}/L_{bol}]$, the ratio of the Hα luminosity to the stellar bolometric luminosity (via [226]).

[86] suggest that the Na I D resonance lines may be a particularly sensitive indicator of magnetic activity in cool stars, particularly when the Ca II H&K lines are unavailable or lacking adequate flux. Here, we investigate the Na lines in our spectra. In Figure 5.3, we show the Na lines for the M dwarf GJ 213 in states of high and low emission.

We define an index I_D for the measured flux in the Na I D lines following the definition of [60]:
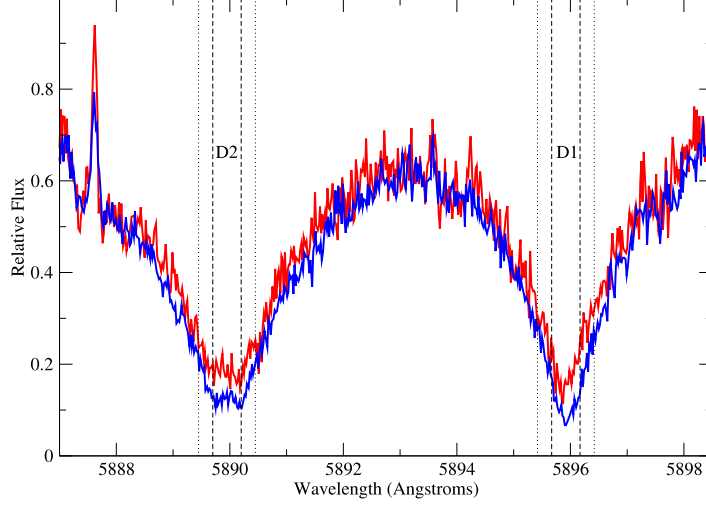
Figure 5.3: We trace the magnetic activity of old M stars through the variable "filling in" of the Na I D absorption doublet with photons emitted from magnetically active regions of the chromosphere. Here, we show the Na I D resonance lines for GJ 213, in states of high (red) and low (blue) chromospheric emission. The dashed and dotted vertical lines indicate the 0.5 Å and 1.0 Å windows, respectively, for which we calculate the I_D index.

$$I_D = \frac{F_{D1+D2}}{F_c} \tag{5.1}$$

In our formulation, F_{D1+D2} is the average combined flux contained in the 1 Å windows surrounding each line center.

As for our Hα index, the I_D index is normalized to the local pseudocontinuum F_c. However, because the Na lines sit within a large molecular band

139

in M stars, the spectral windows containing pseudocontinuum are much more separated from the line cores than they are for the Hα line. [60] choose a 10-Å window centered at $\lambda = 5805$ Å and a 20-Å window centered on $\lambda = 6090$ Å. For our HRS configuration, the redder of these windows falls on a separate CCD chip from the Na lines and the blue pseudocontinuum region. Because this red CCD was replaced in 2006, we chose not to introduce potential systematic errors in our time series analysis by including the red window in our computation of F_c. Instead, we define F_c as the average flux of the 10 highest points in the window centered at 5805 Å. We have verified that for data using the same red CCD, the resulting I_D values are identical except for a constant offset.

We note that although [86] report stronger correlation between their Na I D and Ca H & K indices when using 0.5 Å windows for I_D, we have retained the 1 Å windows in order to compute R'_D, the temperature-independent ratio of Na I D luminosity to bolometric luminosity [60]. Figure 5.3 shows each of the two windows superimposed over the sodium lines. We note that when using the 0.5 Å windows we see essentially identical stellar magnetic behavior for GJ 328, but at lower signal-to-noise.

GJ 328 has a mean $[L_{H\alpha}/L_{bol}]$ of -3.53, which is typical for a quiet star of comparable mass [191]. We show our time series $I_{H\alpha}$ data in the top panel of Figure 5.4. To evaluate any periodic activity, we have computed a generalized Lomb-Scargle periodogram for $I_{H\alpha}$ (Figure 5.5, top). We see no evidence in Hα for periodic behavior that might appear as a Keplerian signal in our RV

data. Furthermore, Figure 5.6 shows our measured RVs as a function of $I_{H\alpha}$. We find no correlation between the values, and therefore conclude there is no evidence in the Hα activity of GJ 328 that the observed planetary signal is caused by stellar activity.

Our analysis of the sodium D features requires more careful scrutiny in the context of interpreting the RV measurements. We present our Na I D measurements in the middle panel of Figure 5.4. The periodogram (middle panel, Figure 5.5) shows a strong peak at 2006 days with a preliminary FAP of 0.006. Our bootstrap false alarm routine produced no false alarms in 10^4 trials, yielding an upper-limit final FAP of 10^{-4}. We consider this a highly significant detection for a stellar cycle, which may not be strictly periodic, and which may also be subject to stochastic activity in addition to cyclic behavior. We fit a sinusoid of the form $I_D(t) = a_0 + a_1 \sin(\omega t + \phi)$ to the data, where $\omega = \frac{2\pi}{P}$, P is the period of the cycle, and a_0, a_1, and ϕ are free parameters to set the I_D zero point, amplitude, and phase, respectively. Our final fitted period is 2013 days, in good agreement with the periodogram peak, and has an amplitude of 0.0104 (7.2%) in I_D. The fit to the curve is shown in Figure 5.4.

Given the presence of a stellar activity cycle for GJ 328, it is especially important to verify the observed exoplanet signature is not produced by this stellar magnetic behavior. The right panel of Figure 5.6 shows our RVs as a function of I_D. A Pearson correlation test yields a correlation coefficient of 0.41 which, for a sample size of 58 data points, indicates a probability $p = 0.0007$ of

141
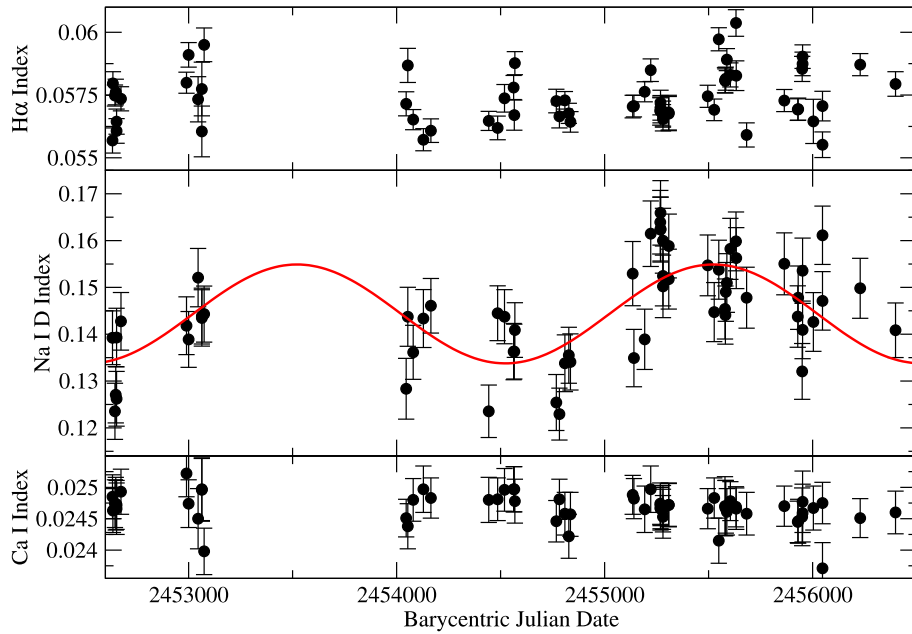
Figure 5.4: We monitor the stellar magnetic activity of GJ 328 through the variable depths of activity-sensitive absorption lines. Here, we show our Hα (top) and Na I D (middle) indices at the time of each RV observation. For the sodium index, we detect a periodic activity cycle with a period of 2000 days, shown in red. The Ca I index (bottom) is insensitive to stellar activity, and serves as a control measurement.
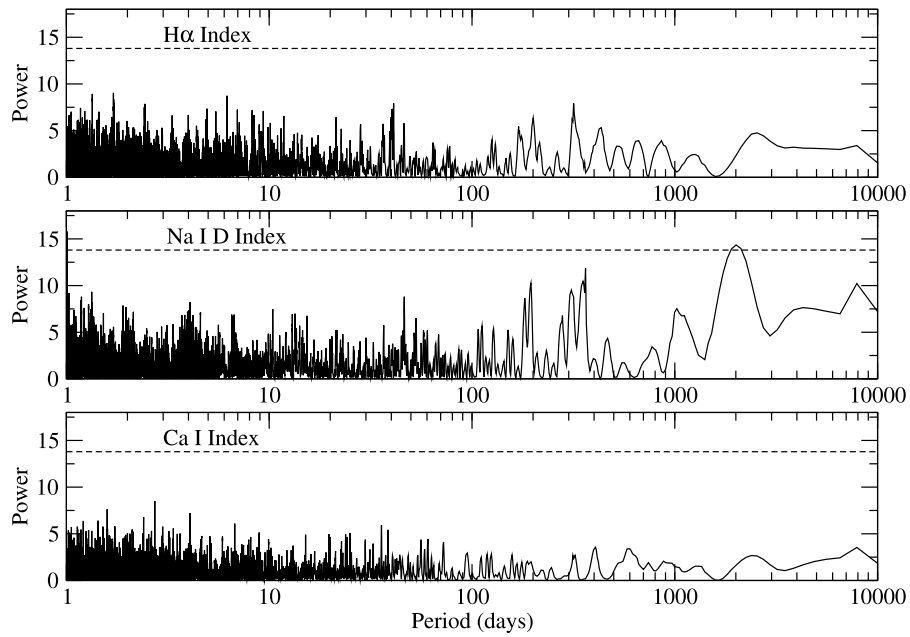
Figure 5.5: Fully generalized Lomb-Scargle periodograms for the stellar activity indices shown in Figure 5.4. The dashed horizontal lines represent the power level corresponding to a false alarm probability (FAP) of 0.01, as calculated from Equation 24 of [240]. We note that these FAP levels represent a preliminary estimate, and our formal FAP values are obtained through a bootstrap analysis, which we describe in Section 5.4.
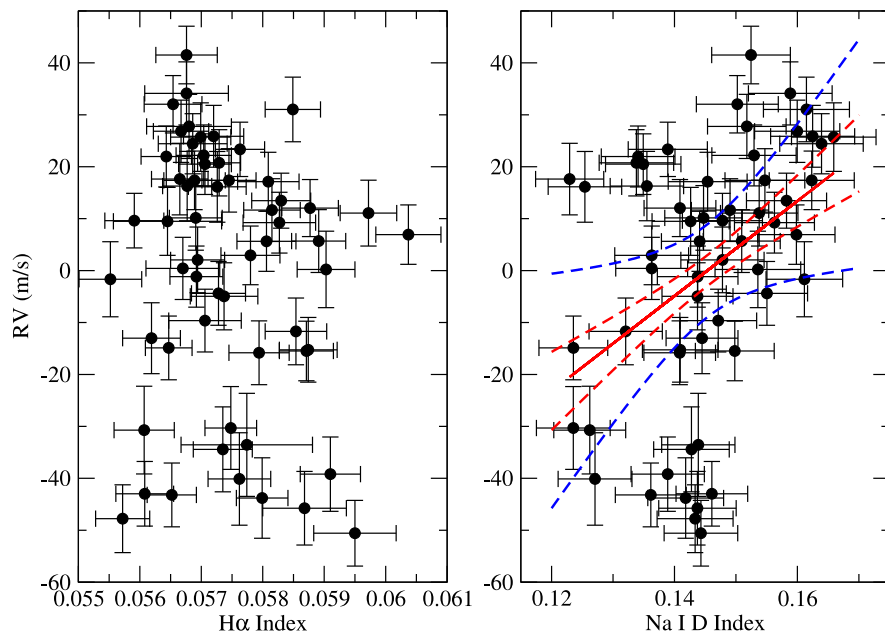
Figure 5.6: To evaluate the influence of stellar activity on our RV measurements, we plot our HET/HRS RV measurements as a function of $I_{H\alpha}$ (left) and I_D (right). We find that our RVs are correlated with I_D at a statistically significant level. Our best linear least-squares fit to the relation is shown as a solid red line. The dashed curves indicate our 1σ (red) and 3σ (blue) error bounds on the fit. Note that the planetary signal has not been removed from these data.

no correlation. Evidently, then, our measured velocities include a component from the star itself. Performing a standard linear least squares fit to the data, we find a relation

$$\mathrm{RV(m/s)} = -133 + 9.15 \times (I_\mathrm{D}/0.01) \tag{5.2}$$

with 1σ errors of 40 m/s on the intercept and 2.7 $\frac{\mathrm{m/s}}{I_D/0.01}$ on the slope.

While we wish to verify the observed exoplanet signal is not caused by stellar activity, it is equally important to confirm that the I_D-RV correlation is not in fact created by the planet signal. Since the periods of the planet and the cycle are near the 2:1 ratio, it could be the case we are simply seeing the first harmonic of the planet's period. However, if the observed correlation were simply due to the high/low extremes of the exoplanet signal coincidentally occurring during periods of high/low stellar activity, we should expect to see a similar effect in Hα. Since we do not, we conclude the correlation seen in Figure 5.6 is truly due to stellar activity shifting the stellar absorption lines.

5.5.2 Stellar Activity Correction

To investigate the effect of stellar activity on our velocity measurements, and its possible consequences for the existence of the planet, we subtracted the fit shown in Equation 5.2 from our HRS RVs. We adopt a linear model because it fits within the physical interpretation that the RV-activity dependence is the result of convective redshift. The process is described fully in [132], who observe a similar dependence for Barnard's star (= GJ 699) on

145

the Hα line. Briefly, the outward convective motion of gas at the stellar photosphere typically produces a net blueshift of the measured absorption lines. During periods of high stellar activity (increasing chromospheric emission and yielding higher I_D values), regions of magnetic plage will suppress the local convection, resulting in a perceived redshift (i.e. a positive RV, hence the positive slope in Figure 5.6). We therefore expect the convective redshift to increase roughly linearly as the stellar magnetic activity increases.
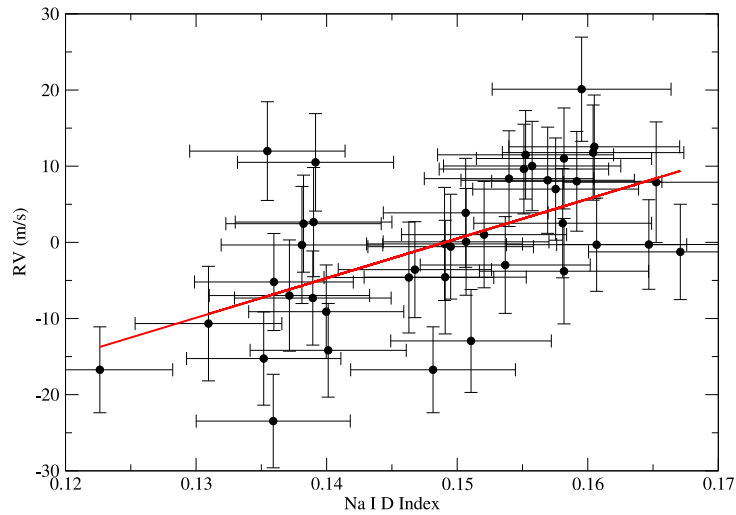
Figure 5.7: RV as a function of I_D for GJ 184, another M0 star in our M dwarf survey. As for GJ 328 and GJ 699, RV increases at higher stellar activity. We interpret this phenomenon as resulting from magnetic plage suppressing local photospheric convection during periods of higher activity. Our best linear least-squares fit to the data is shown as a red line.

To illustrate the effect of convective redshift in a simpler case, we show

in Figure 5.7 our measured RVs for GJ 184 versus I_{D}. GJ 184, another M0 dwarf in our survey, has no known exoplanets, thereby eliminating the large scatter created by the presence of a giant planet in the velocity data. We see again that RV increases as a function of sodium emission, and the relation is nicely approximated as linear. In the case of GJ 184, we find a linear dependence of $\mathrm{RV(m/s)} = -77 + 5.20 \times (I_{\mathrm{D}}/0.01)$, the slope of similar order to that found for GJ 328.

The "corrected" RVs for GJ 328 are shown in Figure 5.8; from inspection, it is clear that a large signal is still present after removing the activity correlation. A periodogram of the de-trended data again shows a strong peak at 3500 days, with a bootstrap FAP less than 10^{-4}. Performing a Keplerian fit to the corrected velocities yields orbital parameters largely consistent with those of our original fit, although the eccentricity increases from its original value of 0.29 to 0.44.

We wish to verify that the observed correlation between RV and I_{D} is a result of the stellar activity cycle identified herein. To do so, we subtracted our orbital fit to the activity-corrected RVs from the uncorrected velocities (Figure 5.8, middle panel). A periodogram of the residuals reveals another strong peak at 1830 days, with a bootstrap FAP again falling below 10^{-4}. Fitting a circular orbit to the residuals (so as to preserve the assumption of a sinusoidal fit to the activity cycle), we find a period of 1870 days with mean anomaly $M_0 = 163°$. The fit has an RV amplitude of 8.7 m/s. We show the residual velocities and the associated fit in the bottom panel of Figure 5.8. Re-
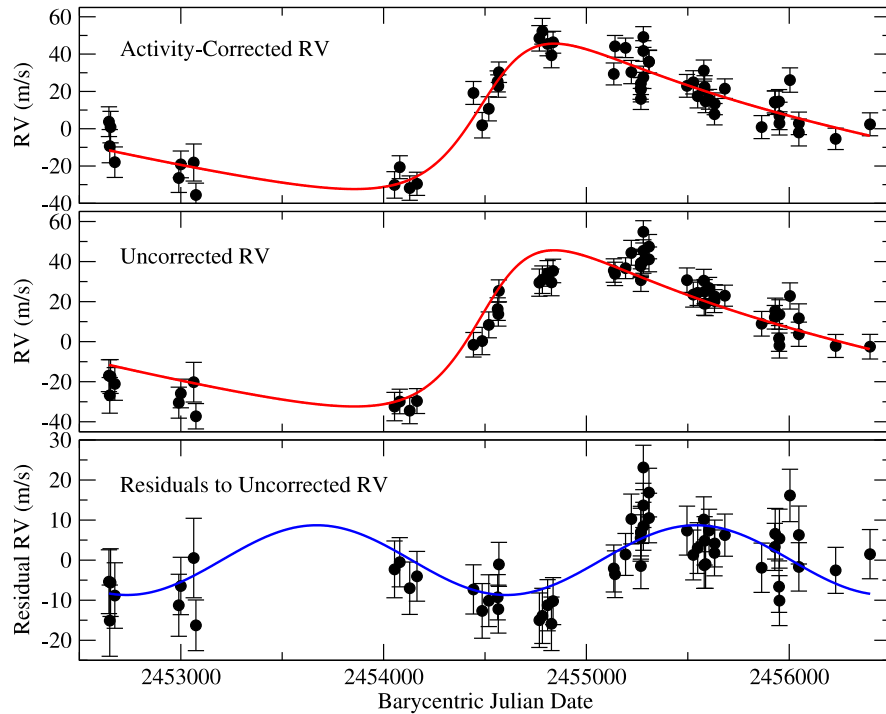
Figure 5.8: Upon subtracting the relation in Equation 5.2 from our HET/HRS RVs, we obtain the corrected velocities shown in the top panel. We perform a Keplerian fit to these RVs, shown in red. When subtracting this fit from the uncorrected RVs (middle panel), we recover an 1865-day signal in the residual velocities (bottom). The period and phase of this signal (fit shown in blue) are consistent with the activity cycle observed for the Na I D features.

turning to our time-series I_D data, we performed a second sinusiodal fit, with the period and phase fixed to match the residual RV signal. This fit yields an RMS scatter of 0.00822 in I_D , compared to 0.00796 for the 2013-day fit. Performing an F-test to compare the fits, we find a probability $P = 0.79$ that the fits are equally valid. Therefore, our observed 1870-day RV signal is statistically consistent with the activity cycle present in the sodium D features. Furthermore, upon applying the planetary fit obtained from the "corrected" velocities (shown in Figure 5.8) to the uncorrected RVs, the Pearson correlation coefficient between the resulting residual RVs and I_D increases to 0.66, corresponding to a probability $p < 10^{-8}$ of no correlation. Based on these tests, we conclude that the correlation between RV and I_D is the result of apparent stellar velocity shifts caused by the periodic activity cycle of GJ 328.

Properly correcting for the influence of stellar activity on our RVs is problematic. Due to the presence of planet b's signal, there is a high amount of scatter in the RV-versus-I_D relation, which leads to large uncertainties in Equation 5.2. It is therefore not wise to assume that the "corrected" velocities shown in Figure 5.8 are properly adjusted. It is also not possible to perform a two-signal fit with the period and phase of the activity cycle fixed. Given our current data set, the eccentric signal of planet b and the sinusoidal activity cycle can be easily modeled as a single, mildly eccentric Keplerian. Therefore, any two-signal fit where the amplitude of the activity cycle is allowed to vary will result in an amplitude of zero for the cycle. While such a model is preferable statistically, it does not account for the additional information contained

in the I_D data.

Because of the difficulties listed above, we have elected to take a conservative approach in modeling the system based on our current data. From the slope of Equation 5.2 and the amplitude of the I_D cycle, we expect the RV amplitude of the stellar cycle to be between 6.7 and 11.9 m/s. We have therefore fixed the RV amplitude for the stellar cycle to 6.7 m/s, which we consider the minimum possible given our analysis. Also, rather than retain the 1870-day period for the cycle, we have fixed its period and phase to the 2013-day solution found for the I_D data, since we expect that data to be free of any influence from planet b's signal. Using these assumptions for the stellar cycle, we subtracted the stellar activity signal from our HRS RVs and re-modeled the orbit of planet b. Our final "corrected" model is given alongside the uncorrected model in Table 5.2, and we show the model, decomposed into the stellar and planetary components, in Figure 5.9.

We note that for this conservative treatment of the stellar activity, the orbital parameters typically only differ by approximately 1σ. It is perhaps more interesting to examine *how* the orbit of planet b changes as the activity cycle's RV amplitude increases, rather than to what magnitude. Most notably, the planet's eccentricity continues to increase as we assign higher amplitudes to the stellar RV contribution. In general, we can say confidently that because of the activity-induced component to our measured RVs, planet b is more eccentric–and consequently less massive–than implied by a simple single-Keplerian fit to the uncorrected velocities.

150
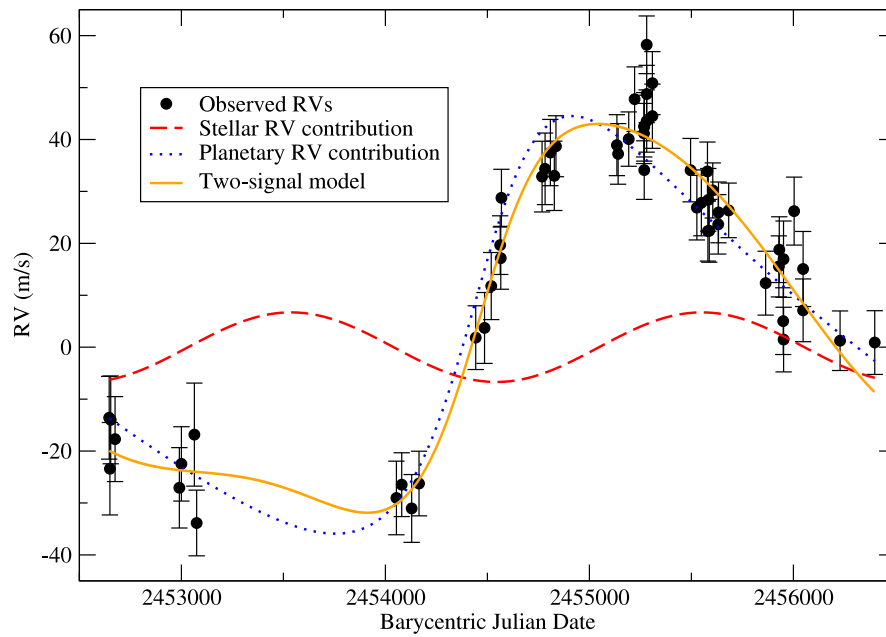
Figure 5.9: HET/HRS RVs for GJ 328, showing our two-signal model derived from the RV and I_D data. The solid orange curve indicates the model to the data, while the dashed red and dotted blue curves show the individual RV contributions from the stellar magnetic cycle and planet b, respectively.

5.6   Discussion

GJ 328b joins the rapidly growing list of long-period giant planets emerging as the McDonald Observatory exoplanet survey approaches a decade of semi-constant monitoring on many of its targets [189, 190]. Such discoveries illustrate the importance of the long-term RV surveys in obtaining a complete census of the Galactic planet population. Transit surveys such as *Kepler* [18] will not operate long enough to find planets in Jupiter-like orbits, and imaging programs are currently unable to observe planets at $a < 10$ AU. While microlensing (e.g. [89]) is sensitive to Jupiter analogs, the possibility of detailed characterization for both the star and planet are extremely limited.

The large mass and orbital separation of GJ 328b offer the potential of further study via astrometry or imaging. Adopting our activity-corrected orbital fit, we calculate an amplitude $\alpha \sin i = 0.70$ mas for the astrometric motion of GJ 328. Such motion is well within the detection limits of the Fine Guidance Sensor on HST [168]. However, the long orbital period likely makes an astrometric campaign prohibitively expensive. Similarly, the sky-projected separation of the planet is approximately 220 mas, slightly more than half the 368-mas separation of HR 8799e [154], which might be resolvable for an M star. Unlike HR 8799, though, the lack of X-ray emission [110] or rotational line broadening indicates GJ 328 is an old star, and the planet will therefore be cold. The resulting lack of thermal emission from the planet should render direct imaging impossible for current instruments.

On the other hand, whereas all of our previously published long-period

giant planets have been found around solar-type stars, GJ 328b is unique in that it orbits a red dwarf star. It is currently the most massive and most distant planet found to orbit a low-mass star[b]. Along with GJ 832b [5], it is one of only two M dwarf planets with $P > 10$ years. While theoretical analyses predicting a deficit of giant planets at small orbital radii around M stars have been thoroughly confirmed by observation [73], further study is required to determine whether GJ 832 and GJ 328 are anomalies, or whether the Jovian population of low-mass stars is more similar to their FGK counterparts at larger separation. Interestingly, both stars fail to show super-Solar metal content; using the [197] calibration, GJ 832 has [M/H] = -0.24, while GJ 328 is roughly solar at [M/H] = 0.00. These metallicities may be considered low in light of the well-established metallicity-frequency relation for giant planets [76], which is generally seen as strong evidence of planet formation via core accretion. Considering both planets fall within the range of semi-major axes where [25] shows gas giants can quickly form via gravitational instability around M dwarfs, the lack of metal excess could be seen as evidence that these planets formed via direct gravitational collapse. Such a claim would be strengthened with the discovery of additional Jupiter analogs around "metal-poor" M dwarfs.

Regardless of the formation mechanism, it appears that low-mass stars can form giant planets even without a highly abundant supply of heavy ele-

---

[b]Excluding planets found via gravitational microlensing, due to the large uncertainties in stellar and orbital parameters.

ments. This seems to rule out the possibility that our survey found no close-in gas giants around M dwarfs because our targets are biased towards metal-poor stars [73]. The relatively low frequency of Jovian planets inside 1 AU around low-mass stars must therefore either reflect an overall underabundance of large planets relative to FGK stars, or point towards a mechanism preventing inward planetary migration for cool stars.

The presence of a long-period ($P \sim 5$ years) solar-type cycle in GJ 328 adds further evidence that activity cycles are commonplace amongst red dwarf stars (e.g. [32, 87, 191]). GJ 328's relatively high mass for an M star is consistent with the current understanding that stars massive enough to maintain a radiative inner envelope–and thus a tachocline–are likely to exhibit activity cycles, while fully convective stars will not (see [191] and references therein). This trend seems to point to the ubiquity of the tachocline-driven magnetic dynamo for maintaining solar-like magnetic activity in old main-sequence stars. As the period of the activity cycle is too long to be the result of spot modulation via stellar rotation, we conclude we are observing cycles in the mean granulation pattern on the stellar surface. The resulting effect on RV must therefore be due to variations in the percentage of the chromosphere covered by cells of hot gas, convecting upward and creating a net blueshift.

The appearance of GJ 328's activity cycle in the Na I D resonance lines and not in Hα reaffirms the conclusions of [60] and [86] that I_{D} is the most sensitive tracer of stellar activity in low-mass stars for spectrographs which do not acquire Ca II H&K. We are in the process of investigating I_{D} variability for

our entire M dwarf data set, and will soon have a more quantitative comparison between the $I_{\rm D}$ and $I_{\rm H\alpha}$ tracers.

While it is not common for stellar magnetic activity to create an RV signal with $K > 8$ m/s, we have previously identified two such stars within our M dwarf sample [191], suggesting such behavior is not highly unusual. Unfortunately, our time sampling for GJ 328 prevents us from obtaining a fully quantitative two-signal model for our RVs. However, our current data set still provides some insight as to what effect stellar activity has on our derived properties for planet b. The positive correlation between RV and $I_{\rm D}$ (Figure 5.6) ensures that RV should change in phase with $I_{\rm D}$, rather than the two quantities being a half cycle out of phase. As a result, the "true" orbit of planet b will always be more eccentric than implied by a single-Keplerian fit to our data for any amplitude of the activity cycle. Because more eccentric orbits have higher RV amplitudes at fixed a, the planet must also be less massive than found in our uncorrected fit. Still, the difficulty inherent in separating stellar and planetary RV signals even for a planet with $K > 40$ m/s illustrates the need to exercise a great deal of caution when considering planets with RV amplitudes comparable to (or smaller than) signals caused by stellar activity (e.g. [66]). We see also that period commensurability between stellar and planetary signals need not automatically disqualify an RV signal as an exoplanet, as the periods of the planet and cycle for GJ 328 are near 2:1. In the case of the Sun (activity cycle period $\simeq 11$ years) and Jupiter ($P = 12$ years), the periods of planets and activity cycles may be very close to

1:1 commensurability. A planetary signal need not be disregarded because RV measurements correlate with activity indices, or because the stellar activity displays periodic behavior. In such cases, though, it is doubly important to include a thorough analysis of stellar magnetic behavior before accepting any planetary solution.

5.7 Conclusions

We have discovered a "cold Jupiter" planet orbiting approximately 4 AU from the late K/early M star GJ 328. Like many old dwarfs, GJ 328 exhibits a long-period magnetic cycle, which we see in the variability of the Na I D lines. We have shown that this activity cycle influences our measured RVs. Although we are unable to make a statistically robust two-signal model that accounts for both the stellar and planetary velocity contributions, we show that the fit to planet b must become more eccentric as the RV amplitude of the stellar cycle increases.

Table 5.3: Radial Velocities and Stellar Activity Indices for GJ 328

BJD - 2450000	Radial Velocity (m/s)	Uncertainty (m/s)	$I_{\mathrm{H}\alpha}$	I_{D}
HET/HRS Velocities				
2645.81037607	-30.31	7.97	0.05748 ± 0.00042	0.12353 ± 0.00600
2649.79770587	-40.13	8.90	0.05762 ± 0.00051	0.12707 ± 0.00601
2653.79836840	-30.72	8.45	0.05644 ± 0.00050	0.13929 ± 0.00625
2674.73658463	-34.43	8.18	0.05735 ± 0.00048	0.14276 ± 0.00615
2989.98128744	-43.80	7.74	0.05799 ± 0.00042	0.14182 ± 0.00617
2999.96108900	-39.20	7.16	0.05910 ± 0.00049	0.13889 ± 0.00596
3063.78296966	-33.56	9.92	0.05774 ± 0.00107	0.14387 ± 0.00596
3074.76013011	-50.58	6.33	0.05950 ± 0.00067	0.14430 ± 0.00599
4053.95303460	-45.76	7.09	0.05868 ± 0.00068	0.14373 ± 0.00630
4079.87702463	-43.20	6.14	0.05652 ± 0.00040	0.13614 ± 0.00577
4128.87683185	-47.78	6.53	0.05572 ± 0.00044	0.14335 ± 0.00618
4164.77031060	-42.98	6.22	0.05608 ± 0.00047	0.14608 ± 0.00583
4442.99734598	-14.89	6.14	0.05647 ± 0.00038	0.12354 ± 0.00560
4485.88562946	-13.02	6.83	0.05619 ± 0.00047	0.14448 ± 0.00585
4518.68369633	-4.95	6.46	0.05737 ± 0.00055	0.14374 ± 0.00578
4562.66614754	2.93	5.65	0.05780 ± 0.00048	0.13629 ± 0.00601
4565.65834052	0.42	5.99	0.05670 ± 0.00060	0.13629 ± 0.00585
4568.66504682	12.04	5.49	0.05877 ± 0.00046	0.14089 ± 0.00584
4767.99308233	16.13	6.81	0.05726 ± 0.00047	0.12542 ± 0.00598
4782.95101189	17.62	6.89	0.05665 ± 0.00046	0.12294 ± 0.00554
4808.89548004	20.75	6.38	0.05729 ± 0.00035	0.13380 ± 0.00606
4827.84051511	16.28	6.68	0.05677 ± 0.00040	0.13551 ± 0.00598
4835.92477666	21.97	5.87	0.05643 ± 0.00041	0.13408 ± 0.00600
5134.99081805	22.18	5.87	0.05704 ± 0.00045	0.15294 ± 0.00686
5140.96822648	20.50	5.84	0.05706 ± 0.00043	0.13491 ± 0.00613
5192.95380323	23.35	5.23	0.05763 ± 0.00040	0.13891 ± 0.00644
5221.76209389	31.03	6.22	0.05849 ± 0.00045	0.16147 ± 0.00700
5267.63490551	24.43	5.79	0.05686 ± 0.00056	0.16392 ± 0.00679
5268.75910493	25.86	5.95	0.05720 ± 0.00049	0.16248 ± 0.00684
5268.76694488	17.38	5.64	0.05689 ± 0.00050	0.16233 ± 0.00692
5268.77478240	25.70	6.60	0.05699 ± 0.00049	0.16592 ± 0.00688
5280.70816761	41.51	5.55	0.05676 ± 0.00050	0.15245 ± 0.00640
5280.71600501	32.03	5.52	0.05654 ± 0.00047	0.15022 ± 0.00667
5280.72383987	26.83	5.99	0.05667 ± 0.00045	0.15997 ± 0.00693
5308.63116619	34.12	6.07	0.05676 ± 0.00068	0.15884 ± 0.00681
5308.63906025	27.76	6.18	0.05680 ± 0.00069	0.15177 ± 0.00639

Table 5.3 cont'd.				
BJD - 2450000	Radial Velocity (m/s)	Uncertainty (m/s)	$I_{H\alpha}$	I_D
5496.00271940	17.37	6.11	0.05745 ± 0.00044	0.15471 ± 0.00649
5526.92170976	10.15	6.22	0.05691 ± 0.00043	0.14472 ± 0.00631
5548.87054184	11.07	6.34	0.05972 ± 0.00046	0.15378 ± 0.00630
5578.88402982	17.12	5.66	0.05809 ± 0.00050	0.14539 ± 0.00642
5580.88847924	5.64	5.78	0.05806 ± 0.00048	0.14409 ± 0.00622
5582.89142512	11.65	6.04	0.05815 ± 0.00046	0.14904 ± 0.00629
5587.75750742	5.68	6.05	0.05891 ± 0.00044	0.15094 ± 0.00627
5604.70581615	13.46	5.30	0.05830 ± 0.00048	0.15823 ± 0.00652
5631.63868921	6.93	5.72	0.06037 ± 0.00053	0.15983 ± 0.00628
5632.74633132	9.23	5.85	0.05827 ± 0.00059	0.15626 ± 0.00651
5682.61355140	9.62	5.26	0.05591 ± 0.00048	0.14780 ± 0.00651
5864.00738743	-4.39	6.15	0.05728 ± 0.00044	0.15504 ± 0.00661
5928.82773310	-1.16	5.88	0.05692 ± 0.00043	0.14377 ± 0.00656
5930.81296731	2.06	6.33	0.05694 ± 0.00044	0.14780 ± 0.00677
5949.88927832	-11.71	6.43	0.05854 ± 0.00050	0.13206 ± 0.00596
5951.75489283	0.22	7.36	0.05903 ± 0.00047	0.15357 ± 0.00697
5951.87637749	-15.26	6.23	0.05874 ± 0.00047	0.14093 ± 0.00615
6003.73677125	9.48	6.54	0.05645 ± 0.00088	0.14262 ± 0.00627
6047.61554908	-1.67	7.23	0.05552 ± 0.00051	0.16113 ± 0.00623
6047.62618002	-9.63	6.04	0.05706 ± 0.00059	0.14712 ± 0.00625
6228.99908594	-15.48	5.74	0.05871 ± 0.00044	0.14981 ± 0.00641
6398.63806982	-15.83	6.14	0.05794 ± 0.00049	0.14085 ± 0.00583
Keck/HIRES Velocities				
5222.10054500	21.80	3.31	$\cdots$	$\cdots$
5609.85679500	2.59	3.66	$\cdots$	$\cdots$
5611.02903000	0.19	4.69	$\cdots$	$\cdots$
6315.04761800	-24.58	2.94	$\cdots$	$\cdots$
HJST/Tull Velocities				
5286.67118600	6.90	5.03	$\cdots$	$\cdots$
5290.69557300	9.18	7.41	$\cdots$	$\cdots$
5291.68657100	-2.69	4.89	$\cdots$	$\cdots$
5341.63611800	6.55	4.67	$\cdots$	$\cdots$
5347.63440000	12.63	6.12	$\cdots$	$\cdots$
5469.98876500	0.72	6.12	$\cdots$	$\cdots$
5493.97635400	15.75	5.18	$\cdots$	$\cdots$
5496.98315600	-10.00	5.38	$\cdots$	$\cdots$
5523.96230100	-4.21	5.47	$\cdots$	$\cdots$
5528.96290100	4.57	7.77	$\cdots$	$\cdots$
5529.94187300	-8.76	5.89	$\cdots$	$\cdots$
5548.90295700	-5.46	3.61	$\cdots$	$\cdots$

Table 5.3 cont'd.				
BJD - 2450000	Radial Velocity (m/s)	Uncertainty (m/s)	$I_{H\alpha}$	I_D
5615.71883100	-6.75	5.02	$\cdots$	$\cdots$
5632.69279200	-18.46	5.95	$\cdots$	$\cdots$

Chapter 6

Conclusion

As exoplanet surveys have matured–both in time and technology–the planetary systems discovered have begun to more closely resemble our own solar system. While other projects, particularly the *Kepler* mission, have revealed that low-mass planets such as exist in the inner solar system are extremely common, the work presented herein further completes the concept of the exoplanet *system* by providing examples of comparisons to the gas giants in the outer solar system. As the time baseline for the McDonald RV survey is extended, it is likely these planets will represent the "tip of the iceberg," being just the first examples of a large population of gaseous planets on wide orbits.

As with the compact systems of low-mass planets identified by *Kepler*, my work reveals multiple instances of stars hosting multiple planets. In both cases, the planets follow orbits packed closely enough to result in gravitational interactions between the planets. The dynamical analyses presented in Chapters 2 and 3 reveal the value and importance of verifying the stability of proposed exoplanet discoveries. In a practical sense, stability integrations can help confirm the planetary nature of RV signals, and may even improve the

determination of orbital parameters (as seen for HD 204313). Scientifically, understanding the dynamics of multi-planet systems can offer insight into the general processes of planetary formation and migration, and offer clues as to how individual systems have evolved.

Looking forward, the newfound knowledge that low-mass planets–including those in the habitable zones of their host stars–are extremely common presents the imperative to locate these "Earthlike" planets around nearby stars so as to facilitate detailed follow-up observations. A significant obstacle to doing so with RV is characterizing and correcting RV signals produced by stellar magnetic activity. My analysis of Hα activity for our M dwarf survey represents the largest study to date of the magnetic behavior of old, low-mass stars. While the Hα line appears to be of limited use for correcting stellar activity above the 5 m/s precision level, the characterization of M dwarf activity seen in Hα will doubtless be extremely valuable for predicting and identifying the occurrence of stellar activity in future RV surveys.

While my investigation of the Na I lines is still ongoing, the example of GJ 328 is encouraging for the prospect of using the lines to correct stellar activity. Of course, it is also a reminder of the importance of such analysis. With an activity cycle of RV amplitude 6 m/s or more, identifying Earth-mass planets with RV amplitudes at or below 1 m/s is impossible without proper activity corrections. GJ 328 therefore represents an important first case–a relatively simple scenario in which the planetary RV signal is much larger than that of the magnetic activity, thereby eliminating any ambiguity

caused by planet and activity signals of comparable magnitudes. The work presented here should therefore motivate further study, particularly refining the technique for simultaneously modeling activity and planetary RV signals.

Appendices

Appendix A

Introduction: Chemical Evolution in Spiral Galaxies

The macroscopic properties of galaxies result from a complex assortment of physical processes taking place over virtually the entire history of the universe. In order to isolate and understand the impact of one of these processes, it is often necessary to assemble large data sets using a large number of galaxies in order to confidently detect subtle effects underneath large scatter.

In most cases, a galaxy's evolution is driven both by internal processes and environmental influences. For galaxies in clusters, though, the local environment becomes an increasingly dominant factor in shaping their morphologies, chemical contents, star formation rates, and sizes. The denser environment leads to an increase in galaxy-galaxy encounters (both direct mergers and tidal interactions), as well as interaction between a galaxy's interstellar gas (interstellar medium, or ISM) and the hot, sparse gas belonging to the cluster itself (intercluster medium, or ICM). As the closest large cluster of galaxies, the Virgo cluster serves as an important laboratory for understanding how the cluster environment shapes its member galaxies. However, as Virgo is among the most massive of the nearby clusters, it is important to in-

vestigate to what extent smaller clusters drive similar evolution, and to verify the observed results do not also occur for field galaxies. A relevant example is the Pegasus I cluster, which is both less massive than Virgo ([188] and references therein) and most likely younger, with most of its members just now falling into the cluster's gravitational potential [222]. [139] found that, as in Virgo, spiral galaxies in Pegasus were deficient in interstellar H I gas, probably due to tidal interactions between galaxies, ram pressure from the ICM on the ISM, and a lack of infall from pure-H I clouds. Later, [194] confirmed Pegasus spirals exhibiting H I deficiency also experienced suppressed star formation.

An under-abundance of pure hydrogen gas can have an effect on the average heavy-element content in the ISM of a spiral galaxy. As H I content decreases, the heavy-element yield of massive stars represents a proportionally larger amount of the total gas content of the galaxy. [204] confirmed this is the case for hydrogen-deficient spirals in Virgo, finding that a subset of central, highly-depleted galaxies display systematically higher metal content (as measured by the ratio of oxygen to hydrogen, $\log(O/H)$) than H I-normal galaxies at the outskirts of the cluster. As part of my dissertation work, I leveraged the excellent H I data of [139]'s Pegasus analysis and the integral-field capabilities of the George Mitchell Spectrograph (previously VIRUS-P, [97]) to test whether a similar abundance offset exists for Pegasus. As shown in Appendix B, a marginally significant offset does exist between the hydrogen-deficient and non-deficient control spirals, but when considering the combined Virgo-Pegasus data set, it becomes apparent that the relationship between H I

165

content and nebular metallicity is actually a continuous trend rather than a discrete separation.

With the understanding that H I abundance and gas-phase metallicity is a gradual progression from H I rich/metal poor to H I deficient/metal rich, it is interesting to reconsider whether the phenomenon is strictly a cluster effect, or if it extends to spirals in the field as well. While a dense cluster environment certainly contributes to creating highly H I-poor spirals, modest deficiencies are observed in the field as well. Rather than mount an observationally-expensive campaign to survey hundreds of galaxies with the Mitchell Spectrograph, though, I found a suitably large catalog of galaxy spectra in [165], containing dozens of cluster and field spirals for which 21cm H I data was also available in the literature [59]. The results of this experiment are detailed in Appendix C. When considering the larger sample of galaxies, the observed trend between H I deficiency (DEF) and log(O/H) from the Virgo/Pegasus galaxies is confirmed for the entire set of cluster spirals. More surprisingly, the field galaxies obey a similar relation. This result was predicted by the cosmological hydrodynamical simulations of [52], and can be interpreted as the result of a galaxy's natural pattern for growth and star formation. As a spiral galaxy acquires mass through mergers with gas-rich, metal poor dwarf galaxies or clouds and subsequently forms stars which return heavy elements to the ISM, it moves sporadically between the high-DEF/high-metal, low-DEF/low-metal stages. Although cluster environments may force galaxies away from equilibrium towards a permanent H I-poor, metal-rich state, cluster

membership does not appear to be a prerequisite for a galaxy following the DEF-log(O/H) correlation.

Appendix B

Chemical Abundances in Spiral Galaxies of the Pegasus I Cluster

B.1 Background

The effect of environment on galaxy evolution has long been a subject of intense research and debate (see review articles by [22, 95] for a comprehensive discussion). Known environmental effects include tidal encounters and mergers, altered morphologies, and stripping of gas from disks. A natural question is whether the cluster environment has significant effects of the chemical evolution of galaxies. This topic has received increasing attention in the last few years. [204] explore the effect of environment on chemical evolution for spirals in the Virgo cluster. Examining H II region spectra from 9 Virgo spirals, they find the three most H I deficient objects to have O/H abundances 0.3-0.5 dex higher than their gas-normal counterparts. They suggest that the abundance differential results in part from a lack of infall of metal-poor gas into the spirals in the cluster core. [64] fit photoionization models to the Virgo data, confirming the abundance excess for O/H and N/O. Other studies, involving large-scale spectroscopic surveys [46, 70, 242], see a qualitatively similar galactic metallicity dependence on local galaxy density or gas fraction. [242] analyze a sample of 800 galaxies in the HyperLeda catalog, concluding gas-

poor galaxies display higher heavy-element content for a given stellar mass. [175] examine abundances of dwarf and spiral galaxies in the Hercules cluster, finding higher abundances in dwarf galaxies located in relatively dense environments.

While these results suggest a significant impact of cluster environment on chemical evolution, the number of detailed studies for individual clusters is small. This chapter presents, for the Pegasus I cluster, a study analogous to the [204] analysis of the Virgo cluster. Pegasus I (hereafter referred to as Pegasus) is a low-density, low velocity dispersion cluster of redshift ~ 3900 km/s in the foreground of the Pisces-Perseus supercluster. It displays weak X-ray emission, primarily concentrated around the two central ellipticals, without additional substructure ([36], Figure 1) Full details of the cluster's location and member galaxies can be found in [139], including a comparison to Virgo in their Table 4. A comprehensive comparison of the properties of the Pegasus galaxies to other nearby clusters is presented in [207].

Because the density of Pegasus is so low, the classical ram pressure stripping effect should not cause significant gas loss in the disks of member spirals. Furthermore, [222] conclude that the cluster is in the early stages of gravitational collapse, which suggests that any environment-driven evolution should be in an early phase as well. Nevertheless, [139] demonstrate that the Pegasus spirals are in fact experiencing H I loss as they fall into the cluster, suggesting mechanisms other than the classic ram pressure effect [92] may be at work. In a follow-up study, [194] find that star formation in Pegasus galaxies

is suppressed with higher H I deficiency. Given that the cluster environment has already caused noticeable changes in the gas content and star formation of these galaxies, one might expect changes in nebular abundance as well. Using the VIRUS-P integral-field spectrograph [97] on the 2.7m Harlan J Smith Telescope at McDonald Observatory, we have obtained spectra for six Pegasus spirals. From the H II region spectra, we calculate radial O/H profiles, and examine the extent to which a metallicity offset can be seen between the gas-poor and gas-normal spirals. We compare our results to those of [204], noting the difference in environments of Virgo and Pegasus. We discuss the possible causes of the offset for Pegasus, and the potential implications for environment-driven chemical evolution in Virgo and other clusters.

B.2   Sample and Observations

B.2.1   Target Galaxy Selection

Our targets were selected from among the Pegasus spirals analyzed for H I content in [139]. The sample was chosen so as to cover a wide range of values for DEF, the overall galactic H I deficiency value. As described in [139], DEF measures an offset between a galaxy's H I content (measured from 21 cm radio emission) and an expectation value based on field galaxies of similar luminosity and morphological type, with increasingly positive values indicating higher gas deficiency. A value of DEF ~ 0.3 indicates H I is deficient by a factor of two, and is considered the threshold at which a galaxy is considered definitively H I deficient.

The nature of our observations placed further constraints on our target selection. In order to obtain adequate radial coverage of our sample, we selected spirals with a sufficient number of bright H II regions, as determined from the H α images obtained in [194]. This requirement limited somewhat the highest DEF values we could explore, since, as discussed in [194], the prominence of H II regions is severely truncated at large DEF. Additionally, we observed the most face-on objects to minimize inclination and reddening effects. We note that in the optical images of our target galaxies, we see no nearby companions, tidal tails, or other morphological peculiarities. Furthermore, the galaxies are not listed as having morphological abnormalities in the literature, and do not have close neighbors in the cluster map of [139] (Figure 8). We therefore conclude that our targets are not members of interacting pairs. However, NGC 7643 is approximately 200 kpc away from UGC 12562, the possible effects of which will be addressed in the discussion.

Table B.1 lists the names, coordinates, inclination-corrected circular velocities, absolute B magnitudes, and effective/isophotal radii of the six spirals observed in this study [173, 194]. Of these, IC 5309, NGC 7518, and NGC 7643 serve as our hydrogen-deficient sample. The other three objects–NGC 7591, NGC 7529, and IC 1474–have either normal or high H I content, and serve as the control sample. For all galaxy data, we assume a cosmology with $H_0 = 73.0$ km s^{-1} Mpc^{-1}, $\Omega_m = 0.27$, $\Omega_\Lambda = 0.73$.

Target Galaxies

Galaxy	R.A.	Decl.	V_C (km/s)	M_B	R_e	R_{iso}
IC 1474	23:12:51.2	+05:48:23	138.3	-19.72	14.	34.
NGC 7518	23:13:12.8	+06:19:18	35.6	-19.81	22.	43.
NGC 7529	23:14:03.2	+08:59:33	173.2	-19.60	11.	29.
NGC 7591	23:18:16.2	+06:35:09	211.2	-21.29	14.	62.
IC 5309	23:19:11.7	+08:06:34	139.4	-20.26	19.	56.
NGC 7643	23:22:50.4	+11:59:20	172.2	-20.09	20.	43.

Table B.1: Target galaxies, their coordinates (J2000.0), inclination-corrected circular velocities, absolute B magnitudes, effective radii (R_e), and isophotal radii (R_{iso}). Radii are given in arcseconds.

B.2.2 Observations

Our data were obtained during observing runs from 16-20 September 2009 and 14-15 August 2010. For each galaxy, we observed a three-dither pattern in order to ensure full coverage of the disk with VIRUS-P's fiber field. Figure B.1 shows the narrowband H α images of our targets from Rose et al. (2010) and the fiber maps of the three VIRUS-P dithers for our pointings. Note the relatively small radii at which H II region emission ceases for our H I deficient sample relative to the control galaxies.

Wherever possible, we have obtained spectra of our sample using two wavelength settings on the VIRUS-P spectrograph. The "blue" setting covers approximately 3600-5600 Å, while the "red" setting covers approximately 4600-6900 Å. The resulting spectral coverage includes emission lines for [O II], [O III], H α, H β, [N II], and [S II]. Furthermore, H β is available in both

(a) IC 5309   (b) NGC 7643   (c) NGC 7518

(d) NGC 7529   (e) NGC 7591   (f) IC 1474
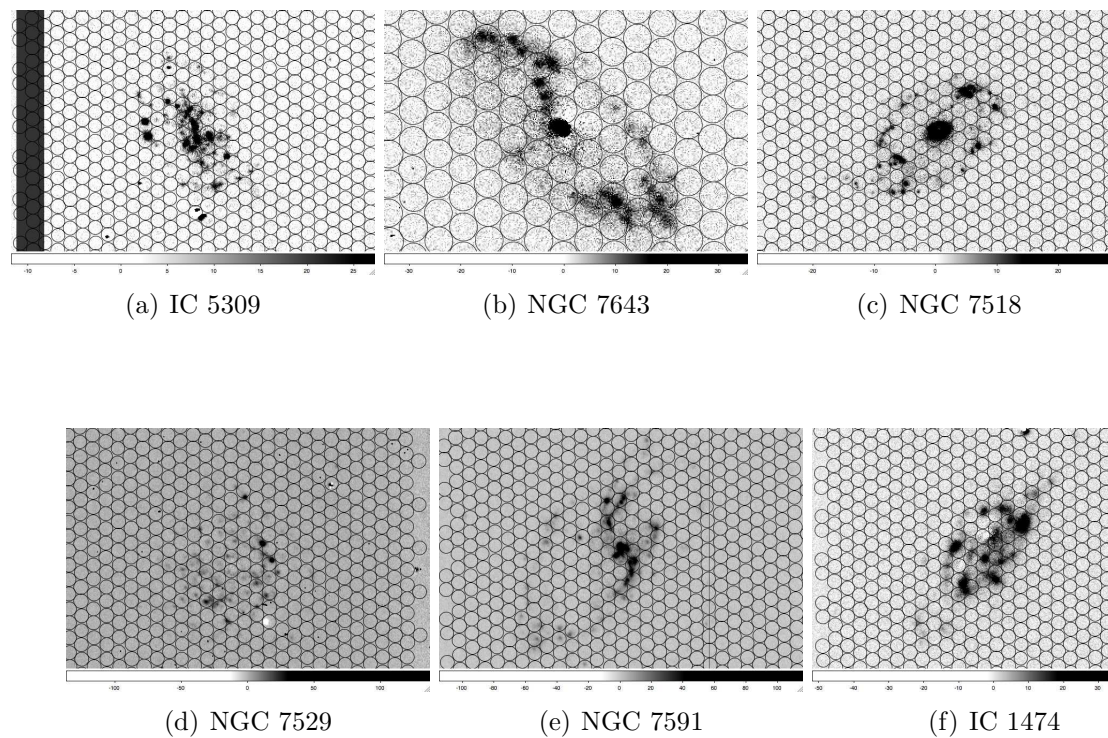
Figure B.1: H α images of Pegasus I cluster spirals included in our sample. The first row (a-c) shows our hydrogen-deficient targets, while the second row (d-f) presents our gas-normal control set. The black circles indicate the locations of the 4-arcsecond diameter VIRUS-P fibers, and the arrows are each 30 arcseconds in length.

settings as a normalization value. In each wavelength setup, we exposed for 1 hour on each dither, for a maximum of 6 hours of exposure on each galaxy. Our targets fit easily on VIRUS-P's 3.5 arcmin^2 field of view, so multiple pointings were not required. For every galaxy in our sample, we have a complete set of dithers on the "red" wavelength setting, and we have at least one dither in the "blue" setting for every galaxy except IC 1474. Our treatment for H II regions without blue data will be discussed in subsequent sections.

B.3   Data Reduction

For each pointing on a galaxy, we acquired spectra from 256 fibers. From these, we have selected those fibers which fall on H II regions using the H α images taken in [194]. As seen in Figure B.1, the 4 arcsecond fiber diameter is a good match to the typical angular diameter of H II regions in the Pegasus cluster, so in most cases the spectrum of an individual H II region is contained within a single fiber. Therefore, the spectra from multiple dithers have not been combined, with the single exception of the H II region labeled (+6.0,-10.2) in IC 1474.

Figure B.2 shows a typical H II region spectrum for a Pegasus spiral. Basic reduction steps such as bias subtraction, flat fielding, and wavelength calibration were done using the VACCINE software suite for VIRUS-P [97]. Wavelength calibration (accurate to at least 0.5 Å) is achieved through observation of NeCd (for the "red" setting) or HgCd ("blue" setting) emission lamps, while twilight sky spectra are used to correct uneven pixel response

174
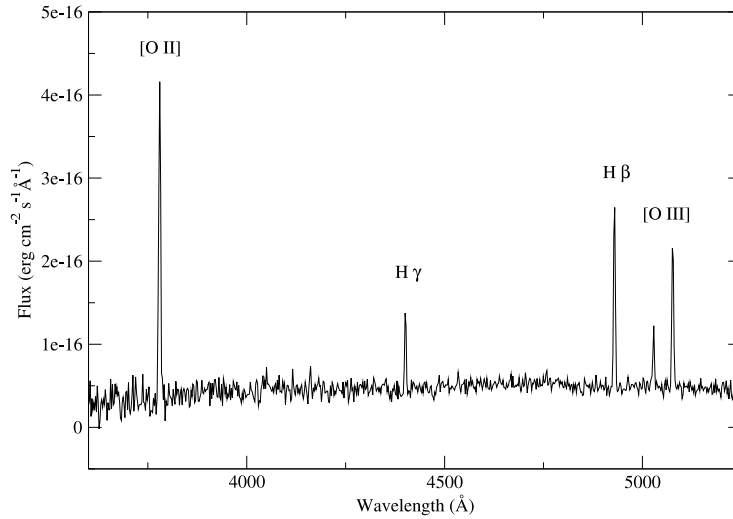
Figure B.2: Example H II region spectrum from VIRUS-P. This fiber was taken on the "blue" wavelength setting. The H II region shown here is from NGC 7529, and is labeled (-1.6, -6.1) in Table B.4.

across the CCD. Each night we also observed at least one white dwarf standard using a six-dither pattern to completely cover the stellar PSF, which we use for flux calibration. We then measured the emission lines using the splot task in IRAF[a]. Following [204], the error bars quoted for our line fluxes are obtained by multiplying the RMS of the continuum adjacent to each line by the line width. Tables B.4 (blue) and B.5 (red) contain the measured emission-line

---

[a]IRAF is distributed by the National Optical Astronomy Observatories, which are operated by the Association of Universities for Research in Astronomy, Inc., under cooperative agreement with the National Science Foundation.

fluxes for our sample, corrected for reddening and stellar absorption, normalized to H $\beta = 100$.

B.3.1 Correction for Balmer Absorption

Following the method of [204], among others, we have added a constant 2 Å EW correction to all Balmer lines in each H II region spectrum to account for underlying stellar absorption. Our correction follows Equation 3 of [127]. This adjustment eliminates a strong dependence of the Hα/Hβ ratio on the EW of H β apparent in our line fluxes before this correction.

B.3.2 Reddening Correction

For each H II region examined, we determined the reddening coefficent c from the H α/H β ratio in the "red" spectrum. Fluxes were corrected to the "case B" limit for H I recombination lines, namely H α/H $\beta = 2.86$, using the $R = 5.5$ extinction curve, $f(\lambda)$, from [171]. For each H II region, we determine the reddening constant $c = (f_{H\alpha} - f_{H\beta})^{-1} \log(I_{H\alpha}/2.86 I_{H\beta})$, which we include in Table B.5. Two H II regions have small negative reddening constants, possibly resulting from errors in the line fluxes or in the stellar absorption correction.

B.3.3 Abundance Determination

As with similar studies of extragalactic H II region abundances (e.g. [204, 239]), we use $\log(O/H)$ as a proxy for the total heavy-element abun-

dance. For the individual H II regions in Table B.4, we determine the overall oxygen abundance using the empirical strong-line emission calibration of [239]. We choose to use the oxygen lines from the "blue" grating setup for consistency (the [O II] and [O III] lines come from the same spectrum), and so that the weak [O III] lines will fall on the red end of the CCD which, as can be seen from the error bars in Tables B.4 and B.5, tends to be less noisy. The [239] O/H calibration is based on the quantity $R_{23} \equiv$ ([O II] + [O III])/H β. For an illustration of the behavior of R_{23} as a function of $\log(O/H)$, see Figure 1 of [159]. For $\log(O/H) > -4.0$, as nebular abundance increases, the greater efficiency of collisional cooling in the fine structure lines lowers the gas temperature, thereby weakening the optical [O II] and [O III] lines. In addition, the ionization drops with increasing abundance, because of effects on the temperature and spectrum of the ionizing stars; and this makes the decrease in [O III] with increasing O/H particularly strong. While R_{23} is degenerate in $\log(O/H)$, the turnaround occurs at very low metallicity ($\log(O/H) \sim -4.0$). Were the oxygen emission decreasing as a result of lower abundance rather than lower temperatures, we would anticipate the [N II] emission, which also traces nebular metallicity, to be low as well. The [N II] emission lines (Table B.5) are sufficiently strong in all H II regions considered here that we can safely assume abundances high enough that R_{23} should decrease monotonically with $\log(O/H)$. In Figure B.3(a), we plot $12 + \log(O/H)$ for each H II region versus its galactocentric radius (as measured by R/R_e). H II regions for which we did not obtain blue spectra are omitted due to a lack of [O II] data.

177
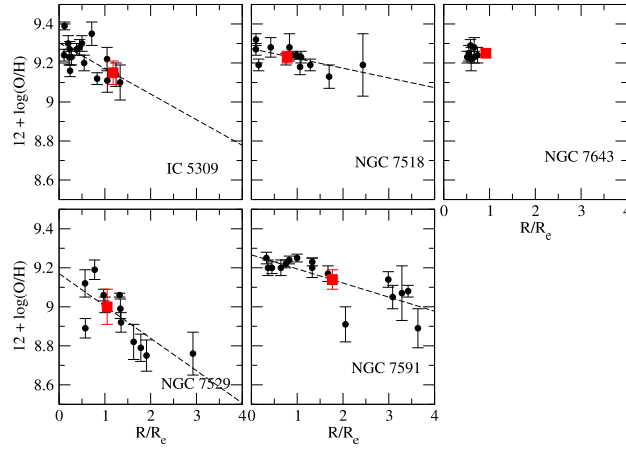
(a)
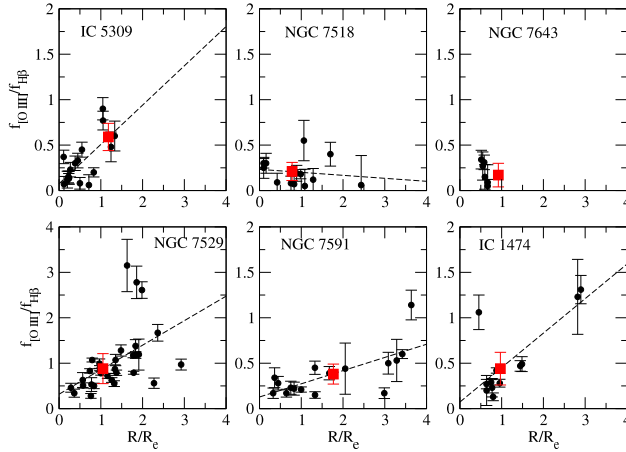
(b)

Figure B.3: Radial plots of [a] $12 + \log(\text{O/H})$ and [b] $f_{[OIII]}/f_{H\beta}$ for H II regions in our sample. H I deficient galaxies are shown in the top row, while H I normal galaxies are shown on the bottom row. The dashed lines are our best-fit linear gradients, and the red boxes indicate the mean galactic values. The mean values are plotted at $0.4\ R_{iso}$, which is where we evaluate the galactic metallicity.

Determining the global nebular abundances for the Pegasus spirals requires some care. As is evident from Figure B.3(a), radial truncation of H II region emission as a result of gas stripping limits our radial coverage of the H I deficient spirals relative to the control sample. Comparing averages over all H II regions would therefore introduce a bias, given the typical presence of a radial abundance gradient (see, e.g. [84, 122, 239]). A better alternative is to use the metallicity at some characteristic radius. [239] compare several choices for such a fiducial radius, and conclude that 0.4 of the isophotal radius, R_{iso} (the radius for which the R-band surface brightness is equal to 25 magnitudes per square arcsecond), is both reflective of the global O/H content and relatively immune to contamination effects. Because we have few H II regions at 0.4 R_{iso}, we fit a linear least squares slope for 12 + log(O/H) versus R/R_e for all H II regions shown in Figure B.3(a). The mean oxygen abundance for each galaxy is then taken to be the value of this fit at 0.4 R_{iso}, with uncertainties derived from the errors of the fitted slopes and intercepts. For all of our galaxies, we use the values of R_e and R_{iso} listed in [194]. In the case of NGC 7643, for which the H II regions span only a small range of radius, we simply take a weighted average over all values of 12 + log(O/H), and adopt the average scatter around the mean as our uncertainty. As seen in Figure B.3, our measured H II regions for NGC 7643 are close enough to $0.4R_{iso}$, and the fitted gradients are shallow enough that this average should be a reasonable estimate. In Table B.2, we give the resulting galactic mean abundances and gradients for our sample.

(1) Galaxy	(2) DEF	(3) Mean $f_{[OIII]}/f_{H\beta}$	(4) Mean 12 + log(O/H)	(5) (O/H) Gradient (dex/R_e)
IC 5309	0.29	0.59 ± 0.15	9.15 ± 0.06	-0.13 ± 0.04
NGC 7518	0.27	0.21 ± 0.10	9.23 ± 0.03	-0.05 ± 0.02
NGC 7643	0.65	0.17 ± 0.13	9.25 ± 0.02	$\cdots$
IC 1474	-0.05	0.44 ± 0.18	$\cdots$	$\cdots$
NGC 7529	-0.08	0.88 ± 0.33	9.00 ± 0.09	-0.17 ± 0.05
NGC 7591	-0.25	0.38 ± 0.11	9.14 ± 0.05	-0.07 ± 0.02

Table B.2: Mean oxygen data for our targets.

As a consistency check, and to include the H II regions for which we do not have [O II] lines, we examine the [O III] lines separately. Figure B.3(b) shows the [O III]/H β flux for each H II region versus galactocentric radius. For the sake of uniformity, all flux ratios plotted in Figure B.3(b) are taken from the "red" grating setting. Recall that the [O II] + [O III] flux increases with decreasing metallicity, hence the inverted slopes between Figures B.3(a) and B.3(b). Using the same method as described above for the mean abundance, we evaluate the mean [O III]/H β for each galaxy, which we include in Table B.2. We plot the mean galactic oxygen measurements against DEF in Figures B.4(a)-B.4(b). From inspection of Figures B.3(b) and B.4(b), there is considerably higher scatter and uncertainty for the [O III]-only data. Furthermore, since the [O III] flux is dependent on the ionization state of the gas as well as the metallicity, we do not include any H II regions without [O II] data in our analysis.

B.4   Analysis

Inspection of Figure B.3(a) shows considerable overlap in the metallicities of the central H II regions between the gas-deficient and gas-normal galaxies in the Pegasus cluster. However, Figure B.4(a) shows a significant trend of increasing mean log(O/H) with DEF. Allowance for the higher mass of NGC 7591 (see below) strengthens this conclusion.

We see from the mean galactic log(O/H) values that our sample is divided into the expected H I deficient/metal rich and H I normal/metal poor groups for 4 of the 5 objects for which we can determine abundances. However, NGC 7591 bears discussion as it only marginally conforms. This object is more than a magnitude brighter than the other galaxies considered, and its circular velocity is the highest of our sample (see Table B.1). [239] establish metallicity dependences on V_C and M_B–both of which are tracers of mass–for spiral galaxies. Several more recent studies (e.g. [75, 164, 215]) have confirmed the observational and theoretical veracity of the so-called "mass-metallicity relationship" (MZR). From Figure 10 of [239], we see that average galactic O/H varies significantly with these properties. Given the higher mass indicated by M_B and V_C, the MZR appears to be a likely reason for the otherwise anomalously high O/H content of NGC 7591 for its value of DEF. Indeed, similar scatter can be seen for the Virgo cluster, with NGC 4501 (DEF = 0.55) having a higher abundance (log(O/H) = 9.32) than the fainter, more gas-poor NGC 4689 (DEF = 0.90, log(O/H) = 9.28) [85, 204]. We therefore conclude that the relatively high log(O/H) observed for NGC 7591 does not contradict
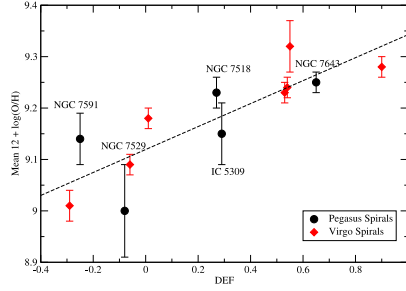
(a)
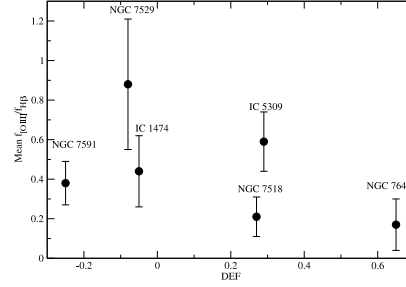
(b)
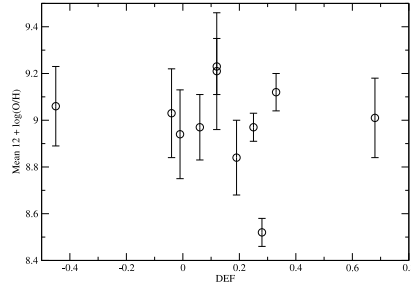
(c)

Figure B.4: [a]: Mean galactic values of $12 + \log(O/H)$ for Pegasus (black circles) and Virgo (red diamonds) spirals as a function of H I deficiency (DEF). The dashed line indicates our linear least-squares fit to the data. [b]: Mean galactic $f_{[OIII]}/f_{H\beta}$ for Pegasus spirals as a function of DEF. [c]: Mean galactic values of $12 + \log(O/H)$ for unbarred field spirals from [239].

182

the correlation between H I content and nebular abundance observed for the other galaxies.

It is also interesting to consider the abundances of the Pegasus galaxies in comparison to field galaxies. Figure B.5 plots the mean $12 + \log(O/H)$ for our sample along with a group of unbarred field spirals from [239]. We see that, as a whole, the cluster galaxies all fall towards the higher-metallicity end of the plot, and the H I deficient members are among the most metal rich. For comparison, Figure 6a of [204] shows the same field galaxies alongside Virgo spirals. In the case of Virgo, the most H I deficient galaxies are clearly more metal rich than the field, but only slightly more so than our sample.

Taking our H I deficient sample as a whole, we find an average of 9.24 ± 0.02 for the galactic mean $12 + \log(O/H)$, compared to 9.11 ± 0.05 for the H I normal controls (excluding IC 1474). The resultant metallicity offset between H I deficient and H I normal spirals is then 0.13 ± 0.07 dex. While this offset is admittedly marginal at 2σ, and considerably lower than the 0.3 dex offset claimed for Virgo, a more careful comparison of the two samples shows the metallicity enhancement of the clusters to be more similar than these averages suggest.

While the environments (IGM density, spiral fraction, velocity dispersion) of the Pegasus cluster differ significantly from Virgo, the individual spirals examined herein represent a very similar population to the Virgo galaxies analyzed in [204]. As shown in Tables B.1 and B.3, the two samples cover a similar range in V_C and M_B, indicating comparable galactic masses and re-
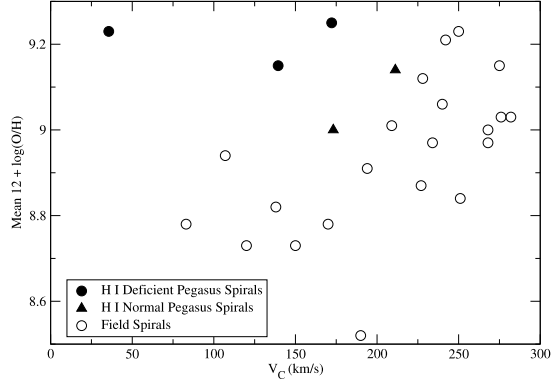
(a)
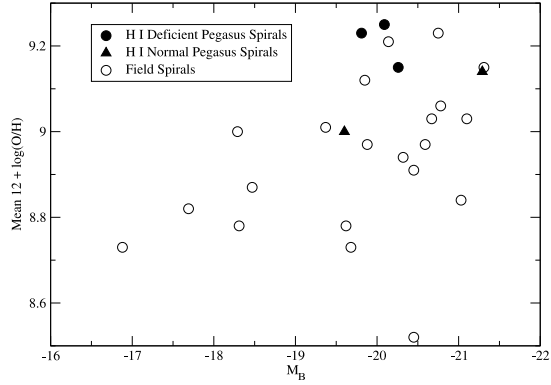
(b)

Figure B.5: Mean galactic 12 + log(O/H) as a function of [a] inclination-corrected circular velocity and [b] absolute blue magnitude for gas-deficient Pegasus spirals (filled circles), gas-normal Pegaus spirals (filled triangles), and a sample of unbarred field spirals from [239] (open circles).

cent star formation histories. Furthermore, our targets were selected from the Pegasus surveys of [139] and [194] which selected spirals of similar morphologies to the Virgo spirals to enable comparison between the clusters. We may therefore compare our results to those of [204], but doing so requires attention to how our characterization of the H I deficiency compares to that used by Skillman et al.

Interestingly, the 0.13 dex difference between mean (O/H) values for our "H deficient" and "H normal" groups is approximately the same as the offsets between the hydrogen "deficient" and "intermediate" and between the "intermediate" and "normal" groups of Virgo galaxies found in [204]. A closer examination of their galaxy selection shows that the similarity between these offsets is not coincidental. [85] compute DEF values for Virgo galaxies, allowing us to compare the gas content of the two samples directly. While the Virgo cluster contains many more galaxies with very high values of DEF (and therefore presumably higher abundances) than Pegasus, only one galaxy (NGC 4689) in the [204] sample has a higher DEF (0.90) than Pegasus' NGC 7643. We plot the abundances of the seven Virgo spirals from the [204] survey with DEF values measured by [85] (Table B.3) alongside those of Pegasus in Figure B.4(a); the two samples have a great deal of overlap in metallicity-DEF space. Apparently, we are sampling a range of DEF for Pegasus in which our "gas-normal" group is analogous to the "intermediate" Virgo galaxies, with the "deficient" groups being similar for both clusters. Our metallicity offset is therefore consistent with what we know of the abundance - DEF correlation

185

Deficiency Group	Galaxy	V_C (km/s)	M_B	DEF	12 + log(O/H)
Virgo Cluster					
H I Normal	NGC 4303	216	-21.13	-0.06	9.09 ± 0.02
	NGC 4651	250	-20.18	...	8.99 ± 0.06
	NGC 4713	137	-19.10	...	8.84 ± 0.03
Intermediate	NGC 4254	250	-20.95	0.01	9.18 ± 0.02
	NGC 4321	201	-21.29	0.53	9.23 ± 0.02
	NGC 4654	198	-20.71	-0.29	9.01 ± 0.03
H I Deficient	NGC 4501	278	-21.57	0.55	9.32 ± 0.05
	NGC 4571	165	-19.43	0.54	9.24 ± 0.02
	NGC 4689	185	-19.86	0.90	9.28 ± 0.02
Field Galaxies from [239]					
N/A	NGC 628	107	-20.32	-0.01	8.94 ± 0.19
	NGC 2903	228	-19.85	0.33	9.12 ± 0.08
	NGC 3521	268	-19.88	0.06	8.97 ± 0.14
	NGC 4258	234	-20.59	0.25	8.97 ± 0.06
	NGC 4736	209	-19.37	0.68	9.01 ± 0.17
	NGC 5033	251	-21.03	0.19	8.84 ± 0.16
	NGC 5055	242	-20.14	0.12	9.21 ± 0.25
	NGC 5194	250	-20.75	0.12	9.23 ± 0.12
	NGC 5457	190	-20.45	0.28	8.52 ± 0.06
	NGC 6946	240	-20.78	-0.45	9.06 ± 0.17
	NGC 7331	282	-21.10	-0.04	9.03 ± 0.19

Table B.3: Inclination-corrected circular velocities, absolute B magnitudes, H I deficiencies, and abundances for spiral galaxies in the Virgo cluster and in the field.

in Virgo. For the Virgo spirals plotted in Figure B.4(a), the H I deficient galaxies (as defined by having DEF > 0.3) have an average $12 + \log(O/H)$ of 9.25 ± 0.03, while the H I normal (DEF < 0.3) spirals have an average $12 + \log(O/H) = 9.11 \pm 0.06$. This offset, 0.14 ± 0.09, is neither larger nor more significant than the offset for our Pegasus sample. Evidently, the larger metallicity offset observed for Virgo is not a result of sampling more stripped, metal-rich galaxies, but from choosing a more remote, gas-rich control sample. Figure 1 of [204] shows that two of the three H I normal Virgo galaxies examined–NGC 4651 and NGC4713–are so far from the cluster center as to essentially be field galaxies. Indeed, neither of these objects appears in the Virgo Cluster Catalog (VCC; [12]), hence their absence in the [85] H I survey. As expected based on the observed correlation, they display very low oxygen content $(12 + \log(O/H) < 9.00)$, contributing to the 0.3 dex metallicity offset for Virgo. We conclude, then, that the process of nebular metallicity enhancement observed in the Virgo cluster has occurred to a similar degree in Pegasus at fixed DEF.

When evaluating galactic H I deficiency quantitiatively with DEF rather than the more qualitative groupings of [204], it becomes apparent that evaluating the influence of the cluster environment on galactic metallicity with an offset between hydrogen-poor and hydrogen-normal groups can be misleading. As each sample is likely to have a different range of DEF values, as seen for our sample compared to Virgo, such a bimodal separation leads to ambiguous conclusions. A better solution is to examine the correlation between
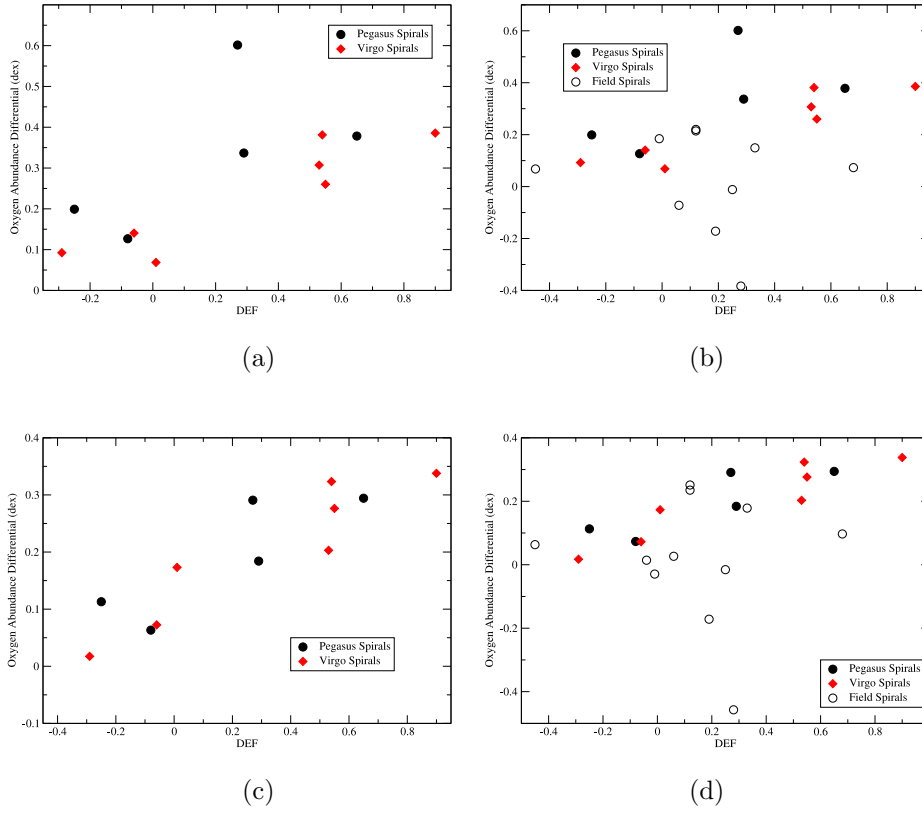
Figure B.6: [a,c]: log(O/H) differential (measured - expected) versus DEF for Pegasus (black circles) and Virgo (red diamonds) spirals. Expectation values are based on the log(O/H)-V_C (a) and log(O/H)-M_B (c) correlations presented in [239]. [b,d]: Same as [a,c], but with the addition of the Zaritsky field spirals.

log(O/H) and DEF, which more accurately describes the continuous progression towards higher metallicities with increasing H I deficiency. From Figure B.4(a), we see a strong correlation in log(O/H) versus DEF for the combined Pegasus-Virgo sample. Performing a linear least-squares fit to the trend, we derive the relation $12 + \log(O/H) = 9.120 + 0.223 \times DEF$, with uncertainties of 0.045 $dex_{(O/H)}/dex_{DEF}$ on the slope and 0.02 $dex_{(O/H)}$ on the intercept. The resulting Pearson correlation coefficient to the data is 0.84. Thus, while the metallicity offsets of the samples above and below $DEF = 0.3$ are only significant at the $\sim 2\sigma$ level, we find a slope in metallicity-DEF space that approaches a 5σ confidence level.

While we see that H I deficiency affects the overall nebular metallicity of cluster spirals, it is important to disentangle this process from the secular effects of galaxy mass. In order to examine the metallicity-DEF correlation independently of the mass-metallicity relationship, we consider the differential (O/H) offset between a galaxy and expectation values based on its V_C and M_B. We adopt V_C as our primary tracer of a galaxy's mass since, as mentioned in [239], it is distance-independent, unbiased by recent star formation, and more tightly correlated with galactic metallicity. However, we include our analysis in terms of M_B for the sake of completeness. Fitting a linear trend to the abundance versus circular velocity plot for the [239] field sample shown in Figure B.5(a), we derive a galaxy's expected oxygen abundance as

$$12 + \log(O/H) = 8.5652 + 0.35582 \times V_C/(200 km/s).$$

Similarly, from Figure B.5(b), we derive

$$12 + \log(\text{O/H}) = 7.7633 - 0.059358 \times M_B.$$

Figure B.6 shows the offsets in log(O/H) (measured - expected) versus DEF for the galaxies presented in Figure B.4. The comparison to expectation values effectively removes the scatter introduced by the MZR, and the resulting correlation is obvious. For the combined set of Pegasus and Virgo spirals (excluding NGC 7518, which has a V_C of 36 km/s, far lower than any of the other galaxies examined here), the Pearson correlation coefficient reaches 0.86 after removal of the (O/H)-V_C trend. If we instead remove the (O/H)-M_B trend, the correlation coefficient for the two samples is 0.90. From this analysis, we conclude that, as expected, at least some of the scatter around the DEF-(O/H) correlation in Figure B.4(a) is due to the MZR.

It is important to note that while we see effects of the MZR in our sample, the observed metallicity offsets are not primarily driven by galaxy mass. This would be particularly likely if the H I deficient galaxies were systematically more massive than the H I normal sample. If this were the case, we would expect to see a correlation between DEF and V_C. To test this possibility, we plot DEF versus V_C in Figure B.7. We observe no correlation for Pegasus or Virgo spirals, thus ruling out a mass offset between hydrogen normal/poor spirals. We can therefore conclude that H I deficiency is driving metallicity augmentation independently of galaxy mass.

The observed correlation between heavy element content and DEF observed for Pegasus and Virgo galaxies might suggest that these objects' metallicity offsets are caused entirely by H I deficiency, and are independent of

190
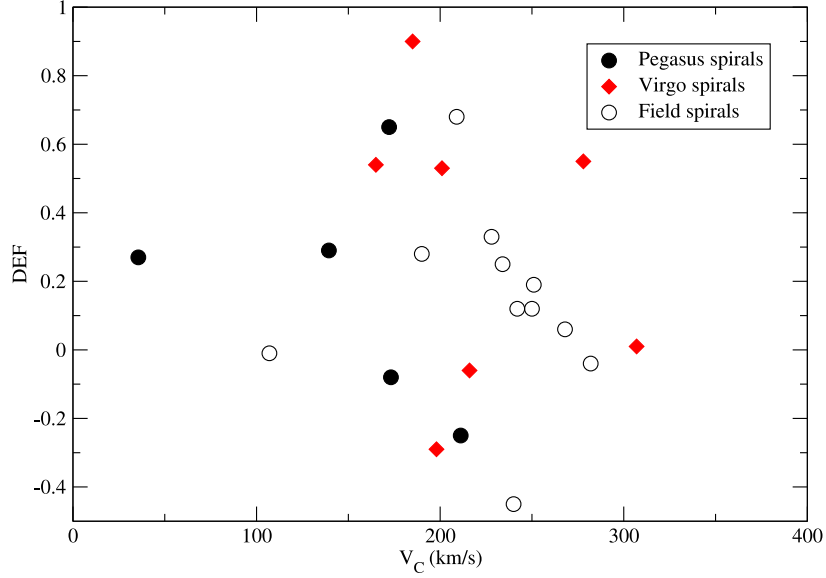
Figure B.7: H I deficiency parameter DEF as a function of V_C for Pegasus (filled circles), Virgo (diamonds), and field (open circles) spirals.

cluster membership. However, a comparison to field spirals refutes that notion. In Figures B.4(c) and B.6, we have plotted the mean $12 + \log(O/H)$ against DEF for field galaxies from [239]. Our values of DEF for the field galaxies–which we include in Table B.3–are adopted from [83]. We see that, unlike for the cluster spirals, the abundances for field galaxies are completely uncorrelated with DEF. The Pearson correlation test confirms what visual inspection suggests; the (O/H)-DEF correlation coefficient for the field sample is -0.16. While the measured metallicities for the field sample have a lower

191

precision than our sample or the Virgo sample, it appears very tentatively that heavy element content is only dependent on H I deficiency if a galaxy has lost its H I through cluster-driven mechanisms, as opposed to field objects that have always been gas-poor. However, further study of both field and cluster spirals will be required to properly evaluate how the (O/H)-DEF correlation changes for different environments. In particular, it will be essential to obtain abundances for a larger sample of field spirals with DEF > 0.3 to facilitate a more meaningful comparison to Pegasus and Virgo.

B.5   Discussion

The physical cause of the observed metallicity offset for cluster galaxies has been the subject of some debate. The typical model for gas-phase chemical evolution in an isolated galaxy is a variant of the "simple model" (e.g. [172]). The simple model treats a galaxy as a "closed box" of hydrogen gas, which grows progressively more metal-rich through stellar recycling according to $Z = -y \ln\mu$, where Z is the total metallicity, μ is the gas fraction, and y is the yield of metals from massive stars. This model is easily modified to account for the infall of primordial gas. As mentioned before, the inflow of unprocessed gas should be terminated when a galaxy falls into the hot ICM, resulting in a metal enrichment pattern that more closely parallels the pure simple model (as in [96], for example). [204] explore the possibility that infall cutoff explains the enhanced metal abundance of the core Virgo spirals. Their chemical evolution models with and without infall demonstrate that infall sup-

pression can create a metallicity increase of 0.15 dex–a significant fraction of the Virgo offset, but not sufficient to account for the entire effect. In the case of Pegasus, though, 0.15 dex is adequate to produce the observed enrichment. One possibility, then, is that as a galaxy first falls into a cluster environment, infall cutoff is the primary external driver of chemical evolution, producing a metallicity transition akin to the H I normal-intermediate shift seen for Virgo. As galaxies continue to fall through the ICM and experience increasingly more H I stripping, additional processes associated with the more extreme H I deficiencies observed become important, resulting in the elevated abundances seen for the "deficient" spirals.

A second mechanism proposed to drive metal enhancement requires the elimination of radial inflows of metal-poor gas. As described in [202], if the galactic H I disk is truncated at a radius interior to the stellar disk, then the inward transport of low-metallicity gas from the exterior of the galaxy is inhibited, preventing the dilution of metals in the galactic interior. Without this dilution, the abundance gradients typically seen for field galaxies tend to flatten out, leading to high characteristic metallicities. The H α emission of Pegasus spirals is clearly truncated inside the stellar disks for H I deficient members [194]. Furthermore, the flattened metallicity gradients predicted for inflow cutoff by [202] are precisely what we observe for our targets. If the radial inflow effect is comparably important as infall cutoff for Virgo, the same may be true for the Pegasus cluster.

Our results add to a growing number of studies demonstrating evidence

for environmental influences on galactic chemical evolution. [215] use strong-line calibrations for integrated spectra (which are reflective of a galaxy's mean metallicity, see [166]) of SDSS galaxies to determine $12 + \log(O/H)$. [46] analyze these abundances, finding a strong dependence on local galaxy density (as defined by nearest-neighbor analysis), particularly for objects in group/cluster environments. Similarly, [70] use nebular abundances from SDSS galaxies in [124] to demonstrate a metallicity-galaxy density relationship, although they claim the effect depends only on local density, not cluster membership. However, using the local galaxy density alone has its limits, as very close galaxy pairs induce inflow of metal-poor gas through tidal interactions, leading to *lower* characteristic abundances than isolated field galaxies [69, 125]. These results bear particular significance for NGC 7643, which is within ~ 200 kpc from UGC 12562 [139]. While this separation is too large by an order of magnitude for tidal interactions to lower the metallicity of NGC 7643 [125], it is possible that "galaxy harassment" has contributed to that galaxy's high DEF, and therefore elevated (O/H) abundance.

The metallicity dependence on gas content is confirmed by [242], who cross-correlate the galaxies in [215] with H I data in the HyperLeda catalog, and find that gas-poor galaxies tend to be metal rich. While our study rejects a dependence on H I content for the metallicities of field galaxies, we note that the [242] galaxy selection does not account for cluster membership, so their observed correlation may be driven by galaxies in clusters.

The importance of environment for galactic metallicity has not been

194

unanimously accepted. [164] examine the [215] data and find a metallicity correlation with local density that is much weaker than those claimed in [46] and [70]. [164] concede, however, that local environment can drive chemical evolution at least in the cores of dense clusters. In a study more similar to our own, [175] compute oxygen content from spatially-resolved long-slit spectroscopy of star-forming galaxies in the Hercules cluster. While they do observe a local density dependence for the metallicity of dwarf galaxies, they claim no environmental effect for major spiral galaxies. We note two caveats here, though. First, they do not quantify hydrogen deficiency, making comparisons to Pegasus or Virgo difficult. Additionaly, they have much lower spatial resolution than we have for Pegasus, and they treat the cores and disks of giant spirals as separate objects, making them insensitive to the kind of metallicity offset we extract from the galactic abundance gradients. We therefore do not consider the [175] study to be contradictory to ours. Overall, the evidence indicates that dense environments like those found in galaxy clusters have a significant influence on the abundance patterns of their member galaxies.

As with Virgo, the heavy element abundance differential for Pegasus is considerably larger than the aforementioned statistical samples of SDSS galaxies. The combined set of data for these two clusters appears to explain why. It seems that, while considering cluster/group membership alone will reveal a small metallcity offset, the primary importance of the cluster is to drive H I stripping and infall cutoff, which ultimately leads to proportionally higher heavy element content. To date, [204] and this study are the only

195

analyses to scrutinize the complementary processes of H I removal and metallicity enhancement as codependent effects of cluster-driven galaxy evolution. The additions of NGC 7518 and IC 5309 to the metallicity-DEF relationship (Figure B.4a) are particularly interesting, as they fill a previously unsampled intermediate range in DEF, showing the correlation to be continuous rather than bimodal. We emphasize that future metallicity surveys of additional clusters should pay careful attention to H I content, as we believe it to be essential to understanding the full influence of a cluster on the properties of its member galaxies.

B.6   Summary

We have presented integral-field spectroscopy of six galaxies in the Pegasus I cluster, a young, low-density cluster. We analyze the spectra of H II regions in these galaxies with the aid of a calibration of the [O II] and [O III] emission-line intensities to determine gas-phase heavy element abundance. Combining these results with published H I data, we examine the abundances as a function of H I deficiency, the possible result of ISM-ICM interactions. When we account for the effects of the galactic mass-metallicity relationship, we find that oxygen abundance correlates well with the hydrogen deficiency parameter DEF for the Pegasus galaxies. The hydrogen-deficient members of our sample show, on average, higher values of $\log(\mathrm{O/H})$ at the 0.15 dex level, which is consistent with Virgo spirals of similar gas deficiency. Our results agree qualitatively with a number of recent publications indicat-

ing intimate connections between a galaxy's heavy element content, hydrogen deficiency, and the density of its local environment.

Table B.4: Corrected emission line fluxes for H II region spectra using the VIRUS-P blue setup.

H II region position (arcsec from center)	[O II] $\lambda3726 + \lambda3729$	H γ	Hβ	[O III] $\lambda4959$	[O III] $\lambda5007$	R/R_e
IC 5309						
-3.6, +0.0	97 ± 4	≤ 3	100 ± 5	7 ± 4	16 ± 4	0.109
-1.9, +2.2	12 ± 8	≤ 5	100 ± 5	≤ 5	11 ± 5	0.118
+1.7, -2.0	58 ± 6	≤ 5	100 ± 5	≤ 3	16 ± 6	0.199
-0.1, -4.0	104 ± 9	≤ 7	100 ± 6	≤ 6	17 ± 5	0.222
-0.1, +4.2	67 ± 6	≤ 6	100 ± 6	15 ± 4	14 ± 9	0.233
-5.6, -1.9	145 ± 7	47 ± 8	100 ± 5	11 ± 4	23 ± 4	0.240
+3.7, -0.1	118 ± 8	≤ 6	100 ± 5	≤ 6	7 ± 5	0.270
-5.3, +6.2	72 ± 5	49 ± 5	100 ± 4	11 ± 4	15 ± 4	0.384
-3.4, +8.3	76 ± 7	57 ± 5	100 ± 6	≤ 4	11 ± 3	0.449
+7.1, -4.1	65 ± 6	47 ± 4	100 ± 4	≤ 5	8 ± 4	0.500
-1.7,+10.4	133 ± 10	40 ± 6	100 ± 6	8 ± 6	12 ± 5	0.547
-7.0,+12.4	41 ± 10	≤ 13	100 ± 6	≤ 6	8 ± 6	0.714
+5.0,-14.4	194 ± 7	38 ± 6	100 ± 4	8 ± 3	12 ± 5	0.831
-8.6,+18.6	103 ± 12	≤ 11	100 ± 9	≤ 9	22 ± 9	1.048
+12.3,-14.5	175 ± 14	47 ± 7	100 ± 8	16 ± 5	30 ± 6	1.054
-16.0,+18.7	147 ± 13	23 ± 7	100 ± 8	≤ 5	42 ± 5	1.244
-12.3,+22.9	151 ± 19	≤ 11	100 ± 10	37 ± 10	41 ± 7	1.333
NGC 7518						
-3.6, +0.1	78 ± 3	44 ± 5	100 ± 4	3 ± 4	14 ± 4	0.098
-1.6, +2.2	48 ± 4	36 ± 3	100 ± 4	4 ± 3	14 ± 3	0.100
+1.3, -2.0	125 ± 4	52 ± 6	100 ± 6	7 ± 3	25 ± 3	0.158
-10.8, +0.1	73 ± 8	42 ± 4	100 ± 7	≤ 6	11 ± 6	0.423
-14.3,+10.6	97 ± 5	45 ± 3	100 ± 4	≤ 4	25 ± 3	0.754
-18.6, +6.4	69 ± 13	≤ 12	100 ± 10	≤ 8	16 ± 7	0.830
+16.2, -8.4	95 ± 5	48 ± 4	100 ± 3	≤ 3	15 ± 3	0.890
-19.2,+12.6	103 ± 3	53 ± 2	100 ± 2	≤ 2	11 ± 2	0.987
+16.8,-14.6	142 ± 8	≤ 7	100 ± 6	≤ 7	15 ± 7	1.063
-23.7, +8.7	103 ± 7	43 ± 4	100 ± 4	4 ± 3	17 ± 4	1.085
+21.4,-16.6	131 ± 6	36 ± 5	100 ± 4	≤ 4	17 ± 4	1.285
+33.6,-12.8	173 ± 13	29 ± 7	100 ± 8	5 ± 7	28 ± 5	1.698
+48.6,-19.1	138 ± 34	≤ 25	100 ± 22	≤ 22	13 ± 23	2.435
NGC 7643						
-1.7,-10.1	109 ± 6	45 ± 4	100 ± 4	4 ± 3	11 ± 3	0.512
-7.0, +8.4	85 ± 7	≤ 6	100 ± 6	6 ± 5	21 ± 5	0.547
+5.6,-10.2	79 ± 5	38 ± 3	100 ± 4	≤ 3	5 ± 2	0.583

Table B.4 cont'd.						
H II region position	[O II] $\lambda3726 + \lambda3729$	H γ	Hβ	[O III] $\lambda4959$	[O III] $\lambda5007$	R/R_e
-5.9,+10.4	128 ± 10	≤ 15	100 ± 11	≤ 10	6 ± 6	0.598
-4.8,+12.4	86 ± 9	≤ 7	100 ± 7	2 ± 6	5 ± 5	0.664
+4.8,-12.4	118 ± 6	≤ 6	100 ± 5	≤ 5	8 ± 4	0.664
+3.7,-14.3	105 ± 9	≤ 7	100 ± 7	≤ 6	10 ± 5	0.738
NGC 7529						
+1.3, +6.1	180 ± 13	≤ 8	100 ± 9	10 ± 6	29 ± 7	0.567
-1.6, -6.1	323 ± 6	43 ± 3	100 ± 4	21 ± 3	67 ± 3	0.574
-5.9, +6.2	138 ± 14	≤ 8	100 ± 7	4 ± 4	17 ± 6	0.777
+10.7, -0.2	211 ± 6	≤ 4	100 ± 3	11 ± 3	45 ± 3	0.974
-11.0, +0.2	232 ± 6	47 ± 3	100 ± 4	17 ± 3	61 ± 3	1.001
-13.1, +6.3	200 ± 3	49 ± 2	100 ± 1	16 ± 1	51 ± 1	1.322
+7.9, -12.4	242 ± 6	55 ± 4	100 ± 5	20 ± 4	67 ± 3	1.338
-8.2, +12.4	263 ± 9	82 ± 5	100 ± 4	42 ± 5	79 ± 6	1.353
+17.9, -0.3	353 ± 13	38 ± 6	100 ± 6	23 ± 5	97 ± 7	1.629
+15.1, -12.5	428 ± 8	56 ± 4	100 ± 5	14 ± 5	56 ± 5	1.785
+20.0, -6.4	449 ± 10	42 ± 5	100 ± 5	22 ± 5	58 ± 5	1.910
+29.6, -12.7	359 ± 16	≤ 9	100 ± 7	38 ± 7	127 ± 7	2.924
NGC 7591						
-0.8, -4.0	88 ± 6	≤ 5	100 ± 6	≤ 4	19 ± 4	0.328
-3.6, +0.0	113 ± 11	≤ 10	100 ± 6	4 ± 3	31 ± 5	0.362
+2.9, +6.1	135 ± 7	51 ± 3	100 ± 4	≤ 3	10 ± 3	0.447
-2.1, +8.3	129 ± 10	≤ 8	100 ± 5	6 ± 4	11 ± 6	0.645
-8.8, +2.3	102 ± 4	36 ± 4	100 ± 4	6 ± 2	25 ± 4	0.750
+7.0,-10.2	91 ± 4	51 ± 5	100 ± 4	10 ± 3	18 ± 3	0.828
-5.0,+12.4	94 ± 5	30 ± 3	100 ± 2	≤ 2	14 ± 2	0.998
+20.0, +1.9	123 ± 13	≤ 7	100 ± 6	7 ± 5	16 ± 6	1.328
-10.1,+14.6	100 ± 4	35 ± 3	100 ± 3	9 ± 2	15 ± 3	1.330
-12.7,+18.6	143 ± 9	30 ± 5	100 ± 5	8 ± 4	27 ± 6	1.672
+35.0,-25.1	171 ± 9	≤ 5	100 ± 4	≤ 4	20 ± 4	2.990
+30.1, -2.4	272 ± 12	38 ± 8	100 ± 7	29 ± 9	97 ± 9	2.054
-28.5,+31.1	228 ± 11	52 ± 6	100 ± 6	13 ± 7	32 ± 7	3.085
+33.3,-33.2	186 ± 28	≤ 13	100 ± 15	13 ± 11	63 ± 11	3.287
+42.2,-25.2	214 ± 6	33 ± 3	100 ± 3	2 ± 3	33 ± 3	3.421
+41.5,-19.0	323 ± 14	38 ± 7	100 ± 8	≤ 8	66 ± 8	3.636

199

Table B.5: Corrected emission line fluxes for H II region spectra using the VIRUS-P red setup. Normalized to Hβ = 100, and reddening corrected so Hα = 286.

H II region (" from center)	[O III] λ4959	[O III] λ5007	[N II] λ6548	[N II] λ6583	[S II] λ6716	[S II] λ6731	R/R_e	c
IC 5309								
-3.6, +0.0	8 ± 5	29 ± 5	30 ± 6	90 ± 5	27 ± 8	28 ± 8	0.109	0.94
-1.9, +2.2	≤ 6	7 ± 6	259 ± 4	965 ± 4	578 ± 4	452 ± 4	0.118	0.73
+1.7, -2.0	≤ 6	12 ± 7	20 ± 8	90 ± 7	29 ± 8	24 ± 6	0.199	1.00
-0.1, -4.0	4 ± 4	11 ± 5	22 ± 4	86 ± 4	29 ± 4	26 ± 5	0.222	0.88
-0.1, +4.2	3 ± 4	10 ± 4	27 ± 10	88 ± 9	31 ± 12	27 ± 12	0.233	1.32
-5.6, -1.9	2 ± 5	12 ± 5	18 ± 5	76 ± 4	41 ± 6	28 ± 5	0.240	0.80
+3.7, -0.1	4 ± 5	19 ± 6	25 ± 8	95 ± 7	31 ± 7	35 ± 7	0.270	1.07
-5.3, +6.2	4 ± 5	26 ± 6	24 ± 6	94 ± 5	34 ± 6	23 ± 6	0.384	0.78
-3.4, +8.3	7 ± 6	26 ± 5	27 ± 6	99 ± 4	36 ± 7	25 ± 8	0.449	0.87
+7.1, -4.1	≤ 4	8 ± 5	22 ± 5	106 ± 5	48 ± 4	30 ± 7	0.500	0.67
-1.7,+10.4	12 ± 5	33 ± 6	21 ± 9	70 ± 6	42 ± 8	45 ± 11	0.547	0.55
-7.0,+12.4	≤ 7	6 ± 9	22 ± 13	91 ± 11	54 ± 11	48 ± 12	0.714	0.55
+5.0,-14.4	1 ± 3	19 ± 4	19 ± 6	77 ± 5	53 ± 4	41 ± 7	0.831	0.43
-8.6,+18.6	41 ± 7	49 ± 7	23 ± 11	90 ± 13	45 ± 17	29 ± 17	1.048	0.58
+12.3,-14.5	13 ± 6	64 ± 7	16 ± 9	82 ± 11	49 ± 10	54 ± 17	1.054	0.75
-16.0,+18.7	10 ± 12	38 ± 10	51 ± 13	84 ± 13	55 ± 13	108 ± 17	1.244	0.34
-12.3,+22.9	10 ± 10	50 ± 10	19 ± 17	49 ± 11	48 ± 13	67 ± 22	1.333	0.51
NGC 7518								
-3.6, +0.1	9 ± 3	21 ± 4	30 ± 5	117 ± 3	33 ± 3	26 ± 4	0.098	0.90
-1.6, +2.2	≤ 7	25 ± 9	29 ± 7	133 ± 7	64 ± 6	53 ± 6	0.100	0.29
+1.3, -2.0	≤ 8	30 ± 7	31 ± 11	121 ± 11	31 ± 13	26 ± 17	0.158	1.75
-10.8, +0.1	≤ 6	9 ± 8	25 ± 6	113 ± 7	30 ± 8	2 ± 12	0.423	0.53
-14.3,+10.6	≤ 6	8 ± 5	25 ± 6	92 ± 11	18 ± 10	19 ± 7	0.754	1.38
-18.6, +6.4	≤ 7	7 ± 8	23 ± 11	98 ± 8	48 ± 9	30 ± 15	0.830	0.38
+16.2, -8.4	≤ 5	19 ± 7	26 ± 10	90 ± 10	23 ± 9	25 ± 11	0.890	1.45
-19.2,+12.6	4 ± 4	14 ± 3	37 ± 3	104 ± 4	29 ± 3	18 ± 7	0.987	0.87
+16.8,-14.6	36 ± 15	19 ± 15	13 ± 14	128 ± 14	60 ± 17	38 ± 32	1.063	1.07
-23.7, +8.7	≤ 14	5 ± 12	23 ± 11	84 ± 14	19 ± 17	10 ± 11	1.085	1.15
+21.4,-16.6	≤ 7	12 ± 10	38 ± 9	116 ± 9	52 ± 13	56 ± 16	1.285	0.61
+33.6,-12.8	18 ± 9	22 ± 9	29 ± 12	104 ± 10	49 ± 8	37 ± 10	1.698	0.54
+48.6,-19.1	≤ 23	6 ± 23	17 ± 45	114 ± 38	≤ 47	67 ± 47	2.435	1.06
NGC 7643								
-1.7,-10.1	8 ± 8	26 ± 6	28 ± 9	103 ± 10	39 ± 8	31 ± 6	0.512	0.86

Table B.5 cont'd.								
H II	[O III]	[O III]	[N II]	[N II]	[S II]	[S II]	R/R_e	c
region	λ4959	λ5007	λ6548	λ6583	λ6716	λ6731		
-7.0, +8.4	$\leq$ 8	27 $\pm$ 13	45 $\pm$ 13	124 $\pm$ 11	51 $\pm$ 15	25 $\pm$ 18	0.547	0.65
+5.6,-10.2	5 $\pm$ 5	26 $\pm$ 6	32 $\pm$ 7	115 $\pm$ 5	38 $\pm$ 8	35 $\pm$ 7	0.583	0.61
-5.9,+10.4	$\leq$ 10	15 $\pm$ 9	27 $\pm$ 7	127 $\pm$ 8	37 $\pm$ 7	48 $\pm$ 10	0.598	0.75
-4.8,+12.4	$\leq$ 16	9 $\pm$ 11	69 $\pm$ 16	165 $\pm$ 14	74 $\pm$ 11	37 $\pm$ 15	0.664	-0.15
+4.8,-12.4	$\leq$ 6	5 $\pm$ 4	32 $\pm$ 6	113 $\pm$ 4	46 $\pm$ 3	43 $\pm$ 5	0.664	0.31
+3.7,-14.3	$\leq$ 4	$\leq$ 6	32 $\pm$ 7	107 $\pm$ 6	39 $\pm$ 8	49 $\pm$ 12	0.738	0.68
IC 1474								
+3.3, +6.1	13 $\pm$ 10	93 $\pm$ 10	32 $\pm$ 10	97 $\pm$ 13	45 $\pm$ 10	55 $\pm$ 20	0.454	0.58
-1.6, +8.4	$\leq$ 4	27 $\pm$ 3	35 $\pm$ 5	106 $\pm$ 4	47 $\pm$ 4	35 $\pm$ 4	0.639	0.60
-6.4, +4.3	$\leq$ 13	20 $\pm$ 10	31 $\pm$ 15	107 $\pm$ 14	47 $\pm$ 12	30 $\pm$ 18	0.640	1.40
-8.7, +2.3	4 $\pm$ 2	25 $\pm$ 2	28 $\pm$ 2	99 $\pm$ 1	48 $\pm$ 1	34 $\pm$ 2	0.748	0.73
+8.4, -8.3	$\leq$ 7	23 $\pm$ 7	16 $\pm$ 13	107 $\pm$ 12	30 $\pm$ 12	28 $\pm$ 12	0.771	1.12
+6.0,-10.2	$\leq$ 3	13 $\pm$ 3	22 $\pm$ 4	89 $\pm$ 3	37 $\pm$ 3	29 $\pm$ 4	0.796	0.78
+13.0, -4.2	8 $\pm$ 2	34 $\pm$ 2	27 $\pm$ 2	90 $\pm$ 1	51 $\pm$ 2	38 $\pm$ 2	0.877	0.65
-8.8, +8.5	5 $\pm$ 3	23 $\pm$ 3	33 $\pm$ 2	100 $\pm$ 2	43 $\pm$ 2	33 $\pm$ 3	0.954	0.63
+15.6,-14.5	9 $\pm$ 4	38 $\pm$ 4	25 $\pm$ 6	97 $\pm$ 4	45 $\pm$ 4	24 $\pm$ 6	1.446	0.71
+18.0,-12.6	8 $\pm$ 6	41 $\pm$ 5	25 $\pm$ 7	92 $\pm$ 6	51 $\pm$ 6	36 $\pm$ 12	1.486	0.81
+30.3,-27.0	23 $\pm$ 22	100 $\pm$ 22	39 $\pm$ 23	58 $\pm$ 17	24 $\pm$ 24	17 $\pm$ 24	2.821	0.75
+35.0,-22.9	29 $\pm$ 6	102 $\pm$ 6	30 $\pm$ 10	87 $\pm$ 5	33 $\pm$ 8	25 $\pm$ 16	2.897	0.75
NGC 7529								
-2.2, +2.2	15 $\pm$ 7	31 $\pm$ 6	28 $\pm$ 6	102 $\pm$ 4	50 $\pm$ 3	35 $\pm$ 14	0.285	0.34
+0.1, -4.0	5 $\pm$ 6	29 $\pm$ 6	25 $\pm$ 5	110 $\pm$ 6	76 $\pm$ 5	47 $\pm$ 9	0.364	0.42
+1.3, +6.1	16 $\pm$ 10	47 $\pm$ 10	23 $\pm$ 7	89 $\pm$ 9	82 $\pm$ 14	75 $\pm$ 14	0.567	0.39
-1.6, -6.1	11 $\pm$ 4	40 $\pm$ 4	22 $\pm$ 4	87 $\pm$ 4	54 $\pm$ 4	51 $\pm$ 5	0.574	0.53
-7.1, -3.9	21 $\pm$ 3	62 $\pm$ 3	23 $\pm$ 3	90 $\pm$ 4	51 $\pm$ 3	44 $\pm$ 2	0.737	0.34
+7.3, -4.1	$\leq$ 3	28 $\pm$ 4	31 $\pm$ 3	90 $\pm$ 4	68 $\pm$ 5	49 $\pm$ 9	0.762	0.41
-5.9, +6.2	22 $\pm$ 11	31 $\pm$ 9	23 $\pm$ 8	118 $\pm$ 12	55 $\pm$ 10	44 $\pm$ 10	0.777	0.70
-3.3, -8.1	24 $\pm$ 2	83 $\pm$ 2	18 $\pm$ 3	70 $\pm$ 3	57 $\pm$ 2	42 $\pm$ 3	0.794	0.31
+9.0, -2.1	17 $\pm$ 4	33 $\pm$ 4	29 $\pm$ 5	88 $\pm$ 4	58 $\pm$ 5	35 $\pm$ 5	0.837	0.35
-2.7,+10.3	26 $\pm$ 6	73 $\pm$ 6	10 $\pm$ 3	76 $\pm$ 5	60 $\pm$ 7	39 $\pm$ 16	0.968	0.07
+10.7, -0.2	23 $\pm$ 3	66 $\pm$ 4	21 $\pm$ 3	71 $\pm$ 3	67 $\pm$ 6	54 $\pm$ 5	0.974	0.43
-11.0, +0.2	21 $\pm$ 2	57 $\pm$ 3	19 $\pm$ 1	80 $\pm$ 2	47 $\pm$ 3	42 $\pm$ 3	1.001	0.61
-12.7, -1.8	11 $\pm$ 3	61 $\pm$ 4	25 $\pm$ 4	67 $\pm$ 4	56 $\pm$ 4	44 $\pm$ 12	1.162	0.16
+9.4,-10.2	16 $\pm$ 4	47 $\pm$ 2	24 $\pm$ 3	94 $\pm$ 4	60 $\pm$ 3	36 $\pm$ 2	1.261	0.35
-13.1, +6.3	6 $\pm$ 4	49 $\pm$ 4	25 $\pm$ 3	82 $\pm$ 4	56 $\pm$ 4	51 $\pm$ 5	1.322	0.68
+7.9, -12.4	14 $\pm$ 6	73 $\pm$ 5	24 $\pm$ 7	75 $\pm$ 5	71 $\pm$ 8	69 $\pm$ 10	1.338	0.43
-8.2, +12.4	21 $\pm$ 8	86 $\pm$ 7	24 $\pm$ 9	86 $\pm$ 9	64 $\pm$ 9	44 $\pm$ 11	1.353	0.53
+14.5, -4.2	21 $\pm$ 3	58 $\pm$ 3	21 $\pm$ 3	83 $\pm$ 3	80 $\pm$ 5	62 $\pm$ 5	1.373	0.39
+16.2, -2.2	30 $\pm$ 6	98 $\pm$ 6	20 $\pm$ 8	64 $\pm$ 8	64 $\pm$ 6	36 $\pm$ 12	1.483	0.36
+17.9, -0.3	87 $\pm$ 15	228 $\pm$ 15	29 $\pm$ 7	76 $\pm$ 13	56 $\pm$ 20	28 $\pm$ 17	1.629	0.73

H II	[O III]	[O III]	[N II]	[N II]	[S II]	[S II]	R/R_e	c
region	λ4959	λ5007	λ6548	λ6583	λ6716	λ6731		
+16.6,-10.3	23 ± 3	94 ± 2	25 ± 1	82 ± 2	59 ± 3	38 ± 7	1.776	0.51
+15.1, -12.5	20 ± 1	59 ± 2	26 ± 2	77 ± 2	49 ± 1	33 ± 3	1.785	0.36
-13.9,+14.6	38 ± 7	100 ± 7	32 ± 4	65 ± 6	77 ± 8	45 ± 17	1.832	0.22
+18.4, -8.4	21 ± 4	97 ± 4	18 ± 5	82 ± 5	64 ± 6	30 ± 11	1.835	0.27
+1.2,-20.4	72 ± 9	206 ± 9	≤ 12	26 ± 8	49 ± 8	61 ± 25	1.858	-0.09
+20.0, -6.4	≤ 20	119 ± 16	≤ 21	65 ± 21	71 ± 21	48 ± 59	1.910	1.33
-21.5, -3.7	72 ± 9	189 ± 9	≤ 7	24 ± 7	52 ± 10	20 ± 14	1.985	0.17
+18.8,-16.5	9 ± 7	47 ± 8	25 ± 10	73 ± 7	82 ± 8	36 ± 10	2.274	0.43
+23.8,-10.4	29 ± 10	138 ± 10	17 ± 5	76 ± 9	51 ± 9	37 ± 19	2.362	0.47
+29.6, -12.7	16 ± 7	81 ± 7	24 ± 7	46 ± 7	93 ± 12	33 ± 15	2.924	0.31
NGC 7591								
-0.8, -4.0	4 ± 4	13 ± 4	30 ± 2	112 ± 3	27 ± 4	16 ± 4	0.328	0.78
-3.6, +0.0	7 ± 8	27 ± 7	41 ± 9	252 ± 5	40 ± 4	30 ± 8	0.362	0.58
+2.9, +6.1	6 ± 5	22 ± 5	24 ± 3	106 ± 5	43 ± 5	33 ± 20	0.447	1.21
-2.1, +8.3	≤ 3	17 ± 3	25 ± 3	96 ± 3	36 ± 3	25 ± 6	0.645	1.32
-8.8, +2.3	≤ 5	23 ± 5	29 ± 6	125 ± 5	42 ± 4	29 ± 11	0.750	0.83
+7.0,-10.2	≤ 5	22 ± 5	26 ± 2	98 ± 5	32 ± 5	22 ± 17	0.828	1.32
-5.0,+12.4	≤ 2	21 ± 2	29 ± 2	99 ± 2	35 ± 2	24 ± 7	0.998	1.30
+20.0, +1.9	9 ± 5	36 ± 5	28 ± 6	89 ± 6	43 ± 6	22 ± 6	1.328	1.03
-10.1,+14.6	≤ 2	15 ± 3	26 ± 1	90 ± 2	38 ± 2	27 ± 10	1.330	1.12
-12.7,+18.6	12 ± 5	27 ± 5	28 ± 3	104 ± 5	55 ± 7	29 ± 17	1.672	1.18
+30.1, -2.4	≤ 19	44 ± 19	≤ 25	116 ± 25	77 ± 19	22 ± 19	2.054	0.15
+35.0,-25.1	≤ 3	17 ± 5	31 ± 5	96 ± 6	47 ± 6	29 ± 16	2.990	1.16
-28.5,+31.1	≤ 8	50 ± 8	18 ± 6	95 ± 6	48 ± 8	27 ± 17	3.085	0.43
+33.3,-33.2	≤ 17	53 ± 13	57 ± 22	94 ± 23	133 ± 17	12 ± 29	3.287	0.25
+42.2,-25.2	16 ± 3	44 ± 3	24 ± 5	91 ± 5	61 ± 5	35 ± 11	3.421	0.79
+41.5,-19.0	12 ± 9	102 ± 9	27 ± 8	75 ± 12	70 ± 12	42 ± 24	3.636	1.41

Table B.5 cont'd.

Appendix C

Hydrogen Content and Metallicity in Field Spiral Galaxies

C.1 Background

The relationship between galactic H I content and other properties of giant spiral galaxies is a well-documented phenomenon. Most notably, star formation (e.g. [123, 194]) and gas-phase metal abundance ([70, 204, 242], among others) are known to be intimately connected to a galaxy's overall H I mass. Many observational studies of the H I-metallicity relation interpret the phenomenon as a consequence of environment-driven evolution (namely ram pressure gas stripping or infall cutoff) through either cluster membership [176, 204] or local overdensity [46, 70]. On the other hand, cosmological hydrodynamical simulations (e.g. [52]) predict a dependence of galactic metallicity on H I content for galaxies in the field as well.

In [188], we took the approach of the [204] analysis of Virgo, examining a single galaxy cluster–Pegasus I–to evaluate the effect of H I content on mean galactic metallicity for giant spirals. Rather than bifurcate our sample into "gas-rich" and "gas-poor," as had been done for Virgo, we quantified H I content using the DEF parameter described in [206], and considered galac-

tic abundances as a function of this quantity. In the case of Pegasus I, DEF proved to be an excellent predictor of galactic $\log(O/H)$. Furthermore, the Virgo galaxies from the [204] study agreed nicely with the $\log(O/H)$-DEF correlation despite the dramatically different properties (density, number of galaxies, velocity dispersion) of the two clusters.

The most significant limitation of the observed relation between $\log(O/H)$ and DEF is the small number of galaxies for which the dependence has been tested. Between the Virgo and Pegasus I clusters, only 12 cluster galaxies were included in the [188] paper. Furthermore, while we included a small number of field spirals from the [239] sample, the number of objects and the precision of their associated $\log(O/H)$ measurements made it impossible to conclude whether our observed correlation extended to galaxies in the field. In this chapter, we remedy both of these shortcomings by utilizing galaxy-integrated spectra of 60 giant spirals (35 cluster, 25 field) from the [165] catalog. Here, we show that the abundances of these galaxies confirm the dependence of galactic $\log(O/H)$ on DEF for cluster spirals, and that field spirals are subject to a similar relation, in agreement with cosmological hydrodynamical simulations.

C.2   Data

To expand on the results of [204] and ([188], hereafter Paper I), we sought to obtain H I and metallicity measures for a large number of galaxies in a wide range of environments. Because our H I deficiency parameter DEF requires accurate 21 cm H I fluxes and morphological types, we were confined

to relatively nearby galaxies. Also, since accurate $\log(O/H)$ determinations for spiral galaxies are dependent on spectra covering the entire galactic disk, very large surveys such as SDSS are unsuitable, as nearby spirals do not fit within a single fiber.

We found a suitable sample of objects in the [165] catalog of long-slit galactic spectra. The catalog contains emission-line spectra for 417 galaxies. While Paper I and other similar studies determine galactic nebular metallicities by fitting abundance gradients to spatially resolved H II region spectra, [166] show that the integrated spectra from these long-slit observations yield equivalent $\log(O/H)$ values. Taking advantage of their result, we derived galactic abundances from this catalog. First, though, we selected the galaxies suitable for our $\log(O/H)$/DEF analysis according to the following criteria:

I. We selected only objects for which H I 21cm flux measurements, optical diameters, and T-types exist in the Third Reference Catalog of Bright Galaxies (RC3; [59]).

II. We eliminated any objects without significant detections of the [O II]λ3727 or H β emission lines.

III. We selected only massive spirals, with T-types between 0 and 8. Additionally, we eliminated any objects known to be in interacting or merging pairs because of the difficulty of assigning morphological types to these galaxies, and because of the known metallicity dilution effects [69, 125] for interacting pairs. Galaxies known to be in groups (not clusters) have also been

eliminated due to their relatively limited number.

After selecting for the above requirements, we are left with a sample of 60 spiral galaxies. For these objects, we first calculated the H I deficiency parameter DEF [88]. We computed DEF following [206], who define the quantity as

$$\mathrm{DEF} = \log M_{\mathrm{H\ I},exp} - \log M_{\mathrm{H\ I}}$$

where $M_{\mathrm{H\ I},exp}$ is an expectation value for a galaxy's H I mass based on its optical diameter and morphological type. Since DEF is an underabundance relative to the expectation, more positive values represent lower H I content.

As in Paper I, we used oxygen as a proxy for a galaxy's heavy-element abundance, and used the strong-line R_{23} calibration for the [O II] and [O III] emission lines. To facilitate direct comparison to Paper I, we have again used the [239] R_{23} calibration to compute $12 + \log(O/H)$. Our error bars are obtained from standard propagation of the uncertainties given for the [165] emission lines.

We categorized our galaxies as cluster, group, or field members using the associations listed in HyperLeda [173]. In cases where HyperLeda did not offer this information, we consulted the SIMBAD and SDSS SkyServer Object Explorer databases, and references therein. If a galaxy was not listed as a group or cluster member in any available literature or database, we considered it a field galaxy.

In Table C.1, we list the names, DEFs, 12+log(O/H) values, and, where

applicable, host clusters of the galaxies examined in this study. For cluster members, we have also included approximate sky-projected separations ρ_C from the cluster center, using the coordinates and redshifts of cluster centers from [4], assuming $H_0 = 72 \,\mathrm{km\,s^{-1}\,Mpc^{-1}}$. The Table is separated into cluster and field populations, as they will be presented in the following section.

C.3 Analysis

As in Paper I, we are interested in the dependence of $\log(O/H)$ on DEF for the galaxies in Table C.1. In order to evaluate any functional dependence, it is important that our sample cover a satisfactory dynamical range in DEF. In Figure C.1, we show a histogram of DEF for the galaxies studied herein. For comparison, we also indicate the DEFs sampled in Paper I. We see that these objects cover a broad range of H I deficiency, and include significantly more very high- and low-DEF galaxies than the targets of Paper I and [204]. We note that, while there are members of both cluster and field samples with very low DEFs, there are considerably more cluster galaxies with positive DEF values. This is consistent with the results of [207] and [139], among others, who show that the cluster environment drives galactic H I depletion.

In order to properly understand the influence of H I content on galactic heavy-element abundance, we must first correct for the mass-metallicity relationship (MZR; [215, 239]). To ensure easy comparison to Paper I, we have again removed the effect of the MZR by using inclination-corrected circular velocity as a proxy for galactic mass, and subtracting the $\log(O/H)$ versus v_C
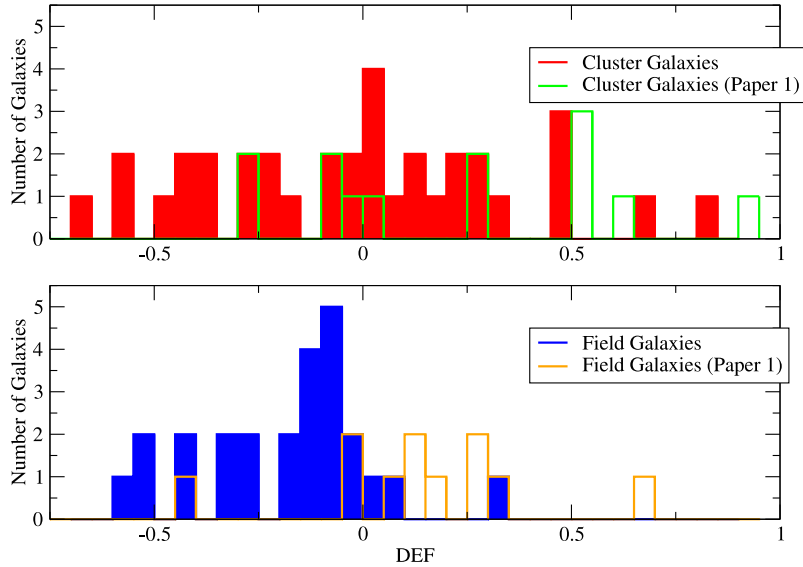
Figure C.1: Distributions of the H I deficiency parameter DEF for our cluster (top) and field (bottom) selections of galaxies from the [165] catalog. The open bins show the DEF distributions from Paper I.

fit derived in Paper I:

$$12 + \log(\text{O/H}) = 8.57 + 0.356 \times V_C/(200 \text{ km/s}).$$

We plot the residual $\log(O/H)$ differential for each galaxy in Figure C.2. In order to ensure that our results are not dependent on our MZR correction, we also present the same data, corrected by instead subtracting the $\log(O/H)$ versus M_B relation from Paper I:

$$12 + \log(\text{O/H}) = 8.95 - 0.0594 \times (M_B + 20).$$

208

Note that we show our M_B-corrected data as a consistency check, and base all of our formal conclusions on the v_C-based MZR correction. This is because, as mentioned in Paper I and [239], v_C is independent of distance and unbiased by recent star formation.

Because Paper I showed a clear correlation between oxygen content and DEF for cluster galaxies, but was unable to confirm or reject that correlation for galaxies in the field, we examine the cluster and field galaxies separately.

C.3.1 Cluster Galaxies

Considering first the subset of cluster galaxies (Figure C.2(a)), we see that the greatly increased number of objects contains a considerable amount of scatter in comparison to the Virgo/Pegasus sample of Paper I (Figure 6 in that paper). Evaluating the dependence of $\log(O/H)$ on DEF therefore requires a careful statistical analysis.

As mentioned in the previous section, uncertainties on galactic $\log(O/H)$ are obtained in a straightforward manner from the errors on the line fluxes. However, understanding the uncertainty on DEF is considerably more complicated. Because the calcluation of DEF relies on T-type and optical diameter in addition to 21 cm flux, uncertainties in all of those parameters contribute to the overall error budget. Additionally, since DEF is calibrated to a finite sample of field galaxies [206], the calculation of expected H I mass is not exact. Rather than assign individual errors to each object, we chose instead to adopt a uniform error $\sigma_{\mathrm{DEF}} = 0.15$ for all galaxies, based on the recommendation of [139],
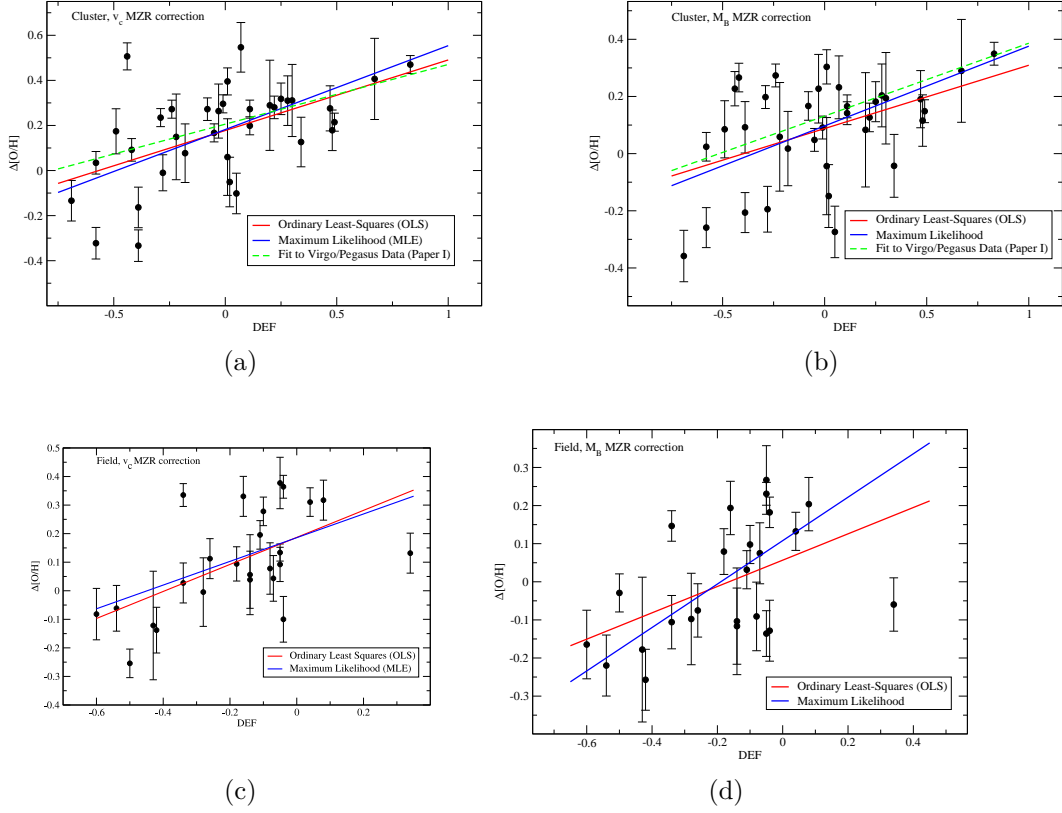
Figure C.2: Residual $\log(O/H)$ after subtracting the mass-metallicity relationship (MZR) for our selected galaxies, plotted as a function of DEF. Our sample is separated into [a,b] cluster and [c,d] field galaxies. Plots on the left [a,c] have been corrected for the MZR using circular velocity, while plots on the right [b,d] use absolute blue magnitude instead (see text for details). For each subset of galaxies, we have included linear fits according to ordinary least squares (red) and maximum likelihood (blue). For the cluster galaxies, we have also included our ordinary least squares fit to the Virgo/Pegasus data from Paper I (dashed green line).

who estimate a "cosmic scatter" of 0.15 in DEF. Our derived dependencies on DEF will therefore have relatively conservative error estimates, since purely statistical error calculations would result in smaller uncertainties.

We began our analysis with a standard linear regression on the cluster subset. Although we experimented with a number of weighting schemes, because the uncertainties in our data only differ in the estimates of $\log(O/H)$, which does not by itself dominate the error budget, each of our weighted fits resulted in unreasonably small errors on the resulting slopes and intercepts. For this reason, all least-squares fits presented herein are computed with equal weights for all data points. With an ordinary least squares (OLS) fit, our model is

$$\log(O/H)_{res} = 0.18_{\pm 0.03} + 0.31_{\pm 0.08} \times \text{DEF} \qquad (C.1)$$

where $\log(O/H)_{res}$ is the measured abundance after subtracting our MZR fit.

Because our fitted slope is only $\sim 3\sigma$ away from zero, we also performed a Pearson correlation test on the data in our cluster sample to confirm the statistical significance of the relation between $\log(O/H)$ and DEF. The correlation coefficient for the cluster galaxies is 0.55. For a sample size of 35 galaxies, this coefficient indicates the probability of no correlation is just 0.0006. We see, then, that there is a significant correlation between $\log(O/H)$ and DEF, and the slope of the relation is consistent with that found in Paper I.

To obtain a better estimate of the actual functional relationship be-

211

tween $\log(O/H)$ and DEF, we have performed a more statistically rigorous linear fit to the data using the maximum likelihood (MLE) method outlined by [121]. The code works by creating a likelihood function for the true distribution of regression parameters, based on the observed data and errors. The regression coefficients and errors are estimated by performing Bayesian inference using 10,000 MCMC samples of the parameter space, where each chain performs a random walk through the parameter space (using a Gibbs sampler), eventually converging on the posterior distribution. The values of the slope and intercept to which each chain converges represents a single random draw from the posterior distribution. Fitting a gaussian to the resulting distribution of slopes, and extracting the mean and FWHM, the resulting "mean fit" to the cluster subset becomes

$$\log(O/H)_{res} = 0.18_{\pm 0.15} + 0.37_{\pm 0.15} \times \text{DEF} \tag{C.2}$$

We have included both of the fits above in Figure C.2(a). Since the MLE routine allowed us to include uncertainties on both DEF and $\log(O/H)$, we adopt the MLE fit as our final model. However, it is worth pointing out the agreement between the OLS and MLE fits for the cluster subset, suggesting OLS is actually adequate in this case.

When considering our sample using the M_B-based MZR, we find results consistent with our primary MZR correction. We obtain slopes of 0.31 ± 0.08 (OLS) and 0.28 ± 0.13 (MLE), which agree with the fits above.

In addition to being internally consistent, our fits to the $\log(O/H)$ versus DEF relation, also agree with our fits to the Virgo and Pegasus spirals derived in Paper I. For comparison, we have included these fits in Figures C.2(a) and C.2(b).

C.3.2 Field Galaxies

Having recovered the $\log(O/H)$ versus DEF relationship discovered in Paper I, we revisited the question of whether the same dependence exists for galaxies in the field. Our field galaxy sample is plotted in Figure C.2(c). Again, there is plenty of scatter, but a positive trend is visible. We again performed a Pearson correlation test to the field sample, acquiring a correlation coefficient of 0.58. For 25 galaxies, our correlation coefficient gives the probability of no correlation at $P = 0.0024$. Our OLS model for the field subset gives

$$\log(O/H)_{res} = 0.19_{\pm 0.04} + 0.47_{\pm 0.14} \times \text{DEF} \qquad \text{(C.3)}$$

To properly quantify the relationship using our errors on DEF, we again calculate the MLE fit, giving a final model

$$\log(O/H)_{res} = 0.19_{\pm 0.09} + 0.41_{\pm 0.14} \times \text{DEF} \qquad \text{(C.4)}$$

We note that the OLS and MLE fits for field galaxies all agree to within 1σ regardless of which MZR correction we use. However, it is worth noting that the MLE fit to the M_B-corrected data (Figure C.2(d) results in a very steep

slope of 0.57 ± 0.4. We find that when we exclude NGC 4605, which is very metal-poor for its DEF value (0.34), the OLS fit also displays a much higher slope. Since our v_C MZR correction places NGC 4605 in better agreement with the observed trend, we do not exclude it as an outlier.

Since the [165] selection of spiral galaxies is not a volume-limited sample, it is prudent to consider whether our observed trends in $\log(O/H)$ versus DEF could be produced by an observational bias. The RC3 catalog is essentially complete for galaxies with optical diameters greater than 1 arcminute and total B magnitudes brigher than 15.5. Although the surface brightness cutoff may lead to the omission of some edge-on spirals, such a bias should not have a significant influence on our result, as the uncertainty in morphological type and increase in interstellar reddening complicate the determinations of DEF and $\log(O/H)$, respectively. In Paper I, we intentionally avoided edge-on spirals for this reason.

As for the [165] selection, which is described in [166] while it is neither blind nor complete, the galaxies included cover a wide range in M_B, $B - V$, and morphological type. We therefore expect a representative sampling of different galaxy masses, star formation histories, and dust content.

In order for a bias to create such an effect, we would somehow have to systematically exclude H I-rich galaxies with high metallicity and/or H I-poor galaxies with low metallicities. We believe both possibilities are very unlikely. Galaxies with low DEF (high H I content) should produce strong 21 cm radiation, and will also likely have relatively high specific star formation

rates (e.g. [194]), leading to strong H β lines. Therefore, low-DEF galaxies should not be excluded from our selection at any metallicity, according to our criteria listed in the previous section. As for high DEF/low metallicity spirals, their low metal content should lead to strong nebular emission lines via higher temperatures, ensuring their inclusion from the [165] catalog. Furthermore, even our highest-DEF galaxies represent 21 cm detections well above the 100σ level, so we are not excluding any high-DEF galaxies due to nondetections of H I emission. We are therefore confident that our result is not due to an observational bias, despite the fact that our sample was not specifically chosen to be completely unbiased.

C.4 Discussion

C.4.1 Comparison to Previous Observations

The slope of the DEF-log(O/H) relation for cluster galaxies (0.37 ± 0.15) remains in good agreement with the slope derived in Paper I (0.26 ± 0.1) upon increasing the number of galaxies in our sample by a factor of 3. While the scatter around the fit in Figure C.2(a) is higher than seen in the Virgo and Pegasus samples, it is important to consider the differences between the galaxies examined in the two studies. The Virgo and Pegasus galaxies selected by [204] and Paper I were chosen for their abundance of bright individual H II regions, and were also all nearly face-on. Furthermore, the Virgo/Pegasus galaxies were all very similar in mass and luminosity. In this larger sample, there is certainly scatter introduced by inclination effects, ambiguous morphological

types, and imperfect mass correction which was largely inconsequential in the smaller, more homogeneous earlier data sets. In this sense, the Virgo/Pegasus galaxies can be interpreted as the "ideal case," and our analysis of the [165] sample extends the preliminary results to a much broader group of objects.

Considering most studies of the interrelation between galactic gas content and metallicity (e.g. [70, 176, 204]) have examined H I deficiency in the context of cluster environment or local galactic density, it is somewhat surprising to find that the observed metallicity dependence extends to field galaxies. In fact, our measured slope for the field subset is actually higher than for the cluster galaxies, although it is doubtful that difference is significant. While the distributions of the slopes in our Monte Carlo resamplings are different, given the uncertainties on our fits, we are not confident that the difference in the observed slopes is significant over the range of DEF explored here. We therefore conclude that, within the uncertainties, the $\log(O/H)$ versus DEF relation applies generally to any non-interacting massive spiral galaxy in a similar way, regardless of environment.

C.4.2 Comparison to Hydrodynamic Models

Modern cosmological hydrodynamic simulations can predict the neutral hydrogen and oxygen content for representative samples of galaxies. Here we compare our DEF-$\log(O/H)_{res}$ results to the simulations of [52]. Since these simulations have a box length of $48\ h^{-1}$ Mpc on a side that does not contain any cluster-sized objects, their simulated sample is most appropriately compared

to our field sample. Similar to [52], we have excluded any galaxies with stellar masses lower than $M_* = 2 \times 10^9 M_\odot$. While the sample does not include morphological data, the masses, star formation rates, and gas fractions of our simulated galaxies are a good match to the selection of [165], who note in [166] that their observed galaxies are largely late-type (Sbc and later) spirals.

In these models, we compute the deviations in metal and H I content at a given *specific star formation rate* (sSFR≡ SFR/M_*). This is different than our treatment of the observations, where DEF is defined based on the expected HI content of galaxies with similar morphology and size. Unfortunately, these simulations lack the resolution to predict these parameters, and hence we must choose a proxy from among the available model-predicted quantities. We choose sSFR because [194] showed that DEF is most tightly correlated with sSFR, as opposed to SFR or M_* alone. To verify this approach is qualitatively valid, we have examined 19 spiral galaxies with measured sSFRs from [109]. Taking T-types, 21cm fluxes, and optical diameters from HyperLeda, we computed DEF via the [206] formulae. We then estimated H I deficiency by correcting for a trend in $M_{\rm H\,I}$ versus sSFR, and adopting DEF as the vertical offset from this trend. We show a comparison between the two estimates of DEF in Figure C.3. Performing a linear fit to the data, we find a slope of 0.87 ± 0.19, but also a vertical offset of 0.36 ± 0.09, indicating a systematic difference between the two calculations. Therefore, while we are confident that the two estimates of DEF reflect qualitatively similar trends, the offset prevents us from directly equating the simulations and our data.
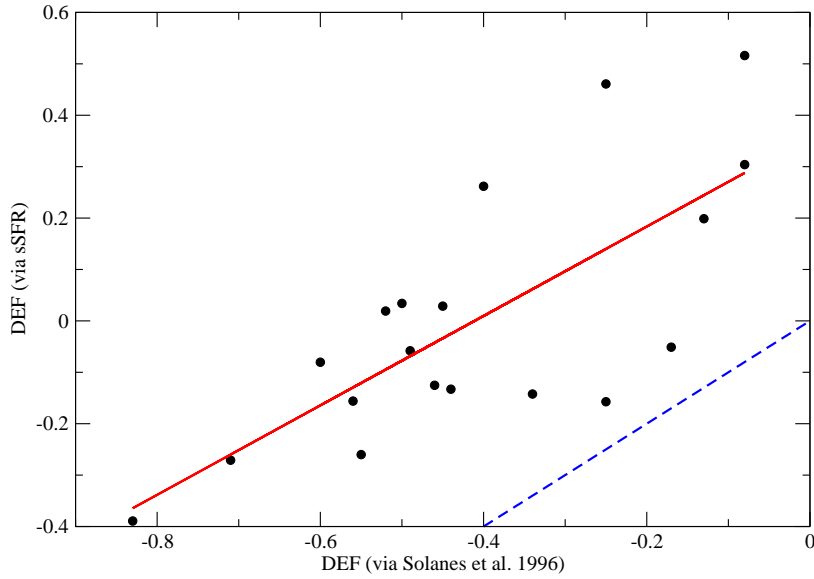
Figure C.3: We compare DEF as measured by the [206] method and by using our estimate relative to a given sSFR. The red line gives the best fit to the data, while the dotted blue line indicates the line $y = x$.

Figure C.4 shows the correlation between DEF and $\log(O/H)_{res}$ from the momentum-driven wind scaling simulation of [52], defined relative to the mean at a given sSFR. The galaxy metallicities are computed as described in [52], while the H I mass accounts for self-shielding and conversion to molecular hydrogen as described in [54], broadly following [180] and [65]. The green line shows the best-fit power law to these points, which follows the relation DEF$= 0.07 + 0.43 \times [O/H]_{res}$. Also shown in the Figure is the best linear fit to the constant wind model (red line, see [52] for details on the constant wind model).

The predicted slope is close to that observed (0.41), and the results
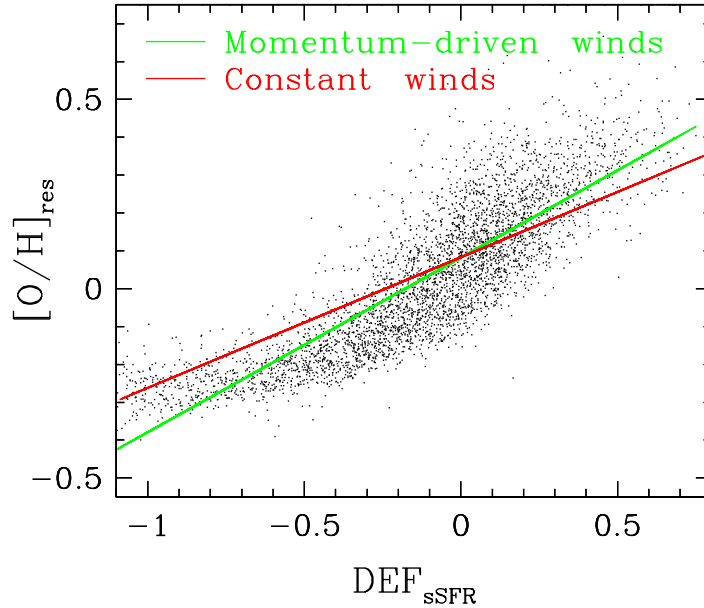
Figure C.4: Residual [O/H] as a function of DEF for galaxies from our hydro-dynamical simulation. The green line gives our best fit to the relation, while the red line represents the best fit to the same galaxies with a constant wind model (see text). We note that DEF in this figure is computed relative to a "normal" H I content at fixed sSFR to account for a lack of morphological information in our simulations.

display a similar amount of scatter around the fit. The predicted amplitude is slightly low, but likely within uncertainties given the different way in which DEF is computed between the models and the data. We note that had we chosen stellar mass rather than sSFR about which to measure our deviations, the predicted slope would be shallower, namely 0.27, but still within 1σ of that observed. Hence *the trend in DEF vs. $[O/H]_{res}$ appears to be a relatively robust prediction of hierarchical galaxy formation simulations, regardless of the details of feedback.*

Why do these hierarchical models predict such a trend? The physical origin can be explained by appealing to the equilibrium model of galaxy evolution [53]. In this scenario, galaxies live in a slowly-evolving balance between accretion, outflows, and star formation. This results in preferred equilibrium relations for the main physical properties of galaxies, such as tight relations between stellar mass, star formation rate [50], metallicity [75], and H I content [180].

Galaxies are perturbed off these equilibrium relations owing to the stochasticity in accretion (e.g. mergers), which governs the scatter around these relations [75]. Consider a galaxy undergoing a merger with a smaller system. Its metallicity will go down because the smaller system will tend to have lower metallicity. However, its H I content will rise since smaller systems tend to be more H I-rich. Hence deviations towards low metallicity will be correlated with deviations towards high H I content. The converse can also happen, where a galaxy experiences a lull in accretion (or a dimunition owing to it becoming a satellite in a larger halo), in which case it will consume its available gas reservoir, increase its metallicity, and lower its H I content. It is straightforward to see that such perturbations will produce a trend in DEF vs. $[O/H]_{res}$ that is qualitatively as observed. Furthermore, the fact that an upward trend exists regardless of wind model indicates the behavior does not arise as the result of an outflow effect, but rather it appears because of inflow stochasticity, which is independent of outflows.

We attribute the slope of the DEF vs. $[O/H]_{res}$ relation in the simu-

lations primarily to three physical phenomena: First, it reflects the characteristic spectrum of mergers and smooth accretion that drive perturbations off the equilibrium relations. Second, it reflects the tendency of minor mergers to enrich spirals with metal-poor gas, decreasing the global nebular metallicity. Finally, it reflects the trend of H I richness vs. sSFR, which analogously sets the typical deviation in H I content when a giant spiral merges with a gas-rich dwarf.

The agreement between the models and the data suggests that the simulations are properly capturing these phenomena. As shown in [52], this model produces roughly the correct mass-metallicity relation. In [54] we show that it also broadly matches the observed mass-H I richness relation. The spectrum of mergers is set by the underlying cosmology, which is assumed to be WMAP7-concordant. Given that all the individual pieces in the model agree with data, it is perhaps not surprising that the DEF vs. $[O/H]_{res}$ is also reproduced. Also, since the constant and momentum-driven wind models yield qualitatively similar trends (Figure C.4) for metallicity and H I richness, it is also not surprising that our simulation results are not strongly sensitive to the assumed feedback model.

We see that this scenario for what sets the H I deficiency in galaxies offers a mechanism to produce the $\log(O/H)$-DEF relation separate from traditional scenarios that have posited that it arises from environmentally-driven processes such as ram pressure stripping (e.g. [92]). Naively, such scenarios would predict that the trends would be stronger in clusters, but our observa-

tions suggest that the trend of DEF vs. $[O/H]_{res}$ is similar in the field. In the simulations, environment does not play a large role (except for satellite galaxies; [51]). Instead, DEF is simply set by the stochastic nature of hierarchical accretion, and galaxies' response to such stochasticity generically yields the observed trend in DEF vs. $[O/H]_{res}$. We caution that these simulations only produce field galaxies, so environmental processes may still play a major role in extreme environments such as clusters. But the success of these models suggests that at least for typical field galaxies, it is not necessary to appeal to environmental processes in order to understand the behavior of $[O/H]_{res}$ vs. DEF. Evidently, changes to a galaxy's nebular metallicity caused by varying H I content are to some degree insensitive to the specific physical processes (i.e. infall, minor mergers, ram-pressure stripping) responsible for regulating H I richness.

C.5   Conclusion

Using the spectral library of [165], we have conducted an expanded investigation into the influence of H I abundance on galactic nebular metallicity analogous to the analysis of [188] for the Pegasus cluster. We have compared these results to predictions based on cosmological hydrodynamical simulations. Our conclusions can be summarized in three main results:

1. For galaxies in clusters, we recover the previously observed trend of increasing $\log(O/H)$ with decreasing H I content.

2. For galaxies in the field, $\log(O/H)$ is similarly dependent on H I de-

ficiency.

3. Our hydrodynamical simulations for field galaxies predict a metallicity-DEF correlation similar to that observed. We interpret this result as the product of a galaxy's natural "excursions" between H I-rich/metal-poor and H I-poor/metal-rich in response to stochastic fluctuations in the inflow rate. These departures from equilibrium with respect to the mass-metallicity relation can occur in any environment, and do not require cluster membership or enhanced local galaxy density.

Table C.1: Galaxy data from [165]. DEF has been computed according to [206], and $12 + \log(O/H)$ is calibrated using the method outlined in [239]. v_C values are taken from the HyperLeda database, and are corrected for inclination. Where appropriate, UGCl cluster listings have been replaced with their more familiar names according to [4].

Galaxy Name	DEF	$12 + \log(O/H)$	v_C	Cluster	ρ_C (kpc)
		Cluster Galaxies			
NGC 0660	-0.22	8.97 ± 0.19	140.82	UGCl 029	1650
UGC 01281	0.30	8.97 ± 0.16	50.11	UGCl 032	2340
UGC 01385	-0.29	9.21 ± 0.04	227.69	Abell 262	513
NGC 0784	0.34	8.77 ± 0.11	41.31	UGCl 032	3700
NGC 0877	-0.58	9.09 ± 0.05	272.82	UGCl 035	2090
NGC 0976	-0.39	9.12 ± 0.09	400.9	UGCl 038	6840
NGC 0972	0.22	9.11 ± 0.05	145.99	UGCl 038	3640
NGC 1003	-0.28	8.73 ± 0.08	95.49	Perseus	6580
NGC 1058	-0.44	9.10 ± 0.06	13.27	Perseus	6750
NGC 1087	-0.01	9.08 ± 0.04	120.27	UGCl 043	937
NGC 1345	-0.18	8.82 ± 0.13	97.19	Eridanus	369
NGC 2893	0.01	9.16 ± 0.06	109.36	UGCl 148	505
NGC 3079	0.02	8.89 ± 0.11	208.39	UGCl 163	22100
NGC 3310	-0.39	8.75 ± 0.07	288.38	UGCl 163	9170
NGC 3353	0.05	8.57 ± 0.09	57.16	UGCl 189	167
NGC 3504	0.49	9.13 ± 0.04	194.09	Abell 1185	1590
UGC 06665	-0.69	8.64 ± 0.09	114.58	UGCl 231	3660
NGC 3913	0.20	8.92 ± 0.20	34.07	UGCl 229	3260
NGC 3953	0.47	9.23 ± 0.10	215.86	UGCl 229	9490
NGC 3972	0.67	9.18 ± 0.18	114.36	UGCl 229	3830
NGC 3982	0.11	9.11 ± 0.04	191.83	UGCl 229	4290
NGC 4062	0.28	9.13 ± 0.11	140.47	UGCl 263	8531
NGC 4085	0.11	9.07 ± 0.04	127.84	UGCl 229	14600
NGC 4088	-0.08	9.14 ± 0.05	167.29	UGCl 229	14200
NGC 4102	0.48	9.03 ± 0.09	158.14	UGCl 229	10100
NGC 4136	0.01	8.81 ± 0.17	101.3	UGCl 263	3880
NGC 4157	-0.03	9.17 ± 0.12	188.89	UGCl 229	15000
NGC 4288	-0.45	8.76 ± 0.10	114.37	UGCl 265	388
NGC 4389	0.83	9.21 ± 0.04	95.47	UGCl 265	47.1
NGC 4414	-0.24	9.23 ± 0.04	217.83	UGCl 267	19.2
NGC 5014	0.25	9.04 ± 0.07	85.29	UGCl 281	2530

Table C.1 cont'd.					
Galaxy Name	DEF	$12 + \log(O/H)$	v_C	Cluster	ρ_C (kpc)
NGC 6052	-0.58	8.77 ± 0.07	293.49	Hercules	4620
NGC 7518	0.07	9.18 ± 0.11	35.61	Pegasus	2590
NGC 7591	-0.49	9.12 ± 0.10	211.21	Pegasus	2480
NGC 7625	-0.42	9.17 ± 0.05	285.57	UGCl 486	1880
NGC 7678	-0.05	9.09 ± 0.04	198.3	Abell 2657	13100
		Field Galaxies			
NGC 0095	-0.34	8.96 ± 0.07	203.78		
NGC 0157	-0.34	9.18 ± 0.04	154.42		
NGC 0278	-0.05	9.16 ± 0.03	256.28		
NGC 0922	-0.42	8.75 ± 0.08	178.59		
NGC 1421	-0.26	8.97 ± 0.07	161.59		
NGC 2139	-0.54	8.75 ± 0.08	135.61		
NGC 2782	-0.05	8.87 ± 0.06	116.73		
NGC 2903	0.08	9.22 ± 0.07	186.95		
NGC 3049	-0.05	9.13 ± 0.09	102.61		
NGC 3198	-0.14	8.88 ± 0.14	142.51		
NGC 3274	-0.60	8.63 ± 0.09	79.62		
NGC 3344	-0.07	9.01 ± 0.08	222.87		
NGC 3521	-0.18	9.10 ± 0.06	244.92		
NGC 3600	-0.28	8.72 ± 0.12	86.9		
NGC 4384	-0.10	9.03 ± 0.05	102.29		
NGC 4455	-0.14	8.71 ± 0.10	56.98		
NGC 4605	0.34	8.81 ± 0.07	60.87		
NGC 4670	-0.04	8.72 ± 0.08	140.4		
NGC 5104	-0.43	8.81 ± 0.19	203.18		
NGC 6207	-0.11	8.97 ± 0.05	114.83		
NGC 7137	-0.04	9.12 ± 0.04	104.46		
NGC 7620	-0.50	9.07 ± 0.05	423.69		
NGC 7624	-0.16	9.21 ± 0.07	173.88		
NGC 7640	-0.08	8.84 ± 0.09	107.92		
NGC 7742	0.04	9.08 ± 0.05	112.06		

Bibliography

[1] Alibert, Y., Mordasini, C., & Benz, W. 2011, *Astronomy & Astrophysics*, 526, A63

[2] Anderson, E., & Francis, C. 2012, *Astronomy Letters*, 38, 331

[3] Baglin, A. 2003, *Advances in Space Research*, 31, 345

[4] Baiesi-Pillastrini, G. C., Palumbo, G. G. C., & Vettolani, G. 1984, *Astronomy & Astrophysics Supplements*, 56, 363

[5] Bailey, J., Butler, R. P., Tinney, C. G., et al. 2009, *The Astrophysical Journal*, 690, 743

[6] Baliunas, S. L., Donahue, R. A., Soon, W. H. et al. 1995, *The Astrophysical Journal*, 438, 269

[7] Batalha, N. M., Rowe, J. F., Bryson, S. T., et al. 2013, *The Astrophysical Journal Supplements*, 204, 24

[8] Batygin, K., Brown, M. E., & Betts, H. 2012, *The Astrophysical Journal Letters*, 744, 3

[9] Benford, G., Benford, J., & Benford, D. 2010, *Astrobiology*, 10, 491

[10] Benford, J., Benford, G., & Benford, D. 2010, *Astrobiology*, 10, 475

[11] Benz, W., Mordasini, C., Alibert, Y., & Naef, D. 2008, *Physica Scripta Volume T*, 130, 014022

[12] Binggeli, B., Sandage, A., & Tammann, G. A. 1985, *The Astronomical Journal*, 90, 1681

[13] Bobylev, V. V.,Bajkova, A. T., & Gontcharov, G. A. 2006, *Astronomical and Astrophysical Transactions*, 25, 143

[14] Bochanski, J. J., Hawley, S. L., & West, A. A. 2011, *The Astronomical Journal*, 141, 98

[15] Bonnarel, F., Fernique, P., Bienaymé, O., et al. 2000, *Astronomy & Astrophysics Supplements*, 143, 33

[16] Bonfils, X., Delfosse, X., Udry, S. et al. 2005a, *Astronomy & Astrophysics*, 442, 635

[17] Bonfils, X., Forveille, T., Delfosse, X. et al. 2005b, *Astronomy & Astrophysics*, 443, L15

[18] Borucki, W. J., Koch, D., Basri, G., et al. 2010, *Science*, 327, 977

[19] Borucki, W. J., Koch, D. G., Basri, G., et al. 2011, *The Astrophysical Journal*, 736, 19

[20] Borucki, W. J., Koch, D. G., Batalha, N., et al. 2012, *The Astrophysical Journal*, 745, 120

[21] Borucki, W. J., Agol, E., Fressin, F., et al. 2013, *Science*, 340, 587

[22] Boselli, A., & Gavazzi, G. 2006, *Publications of the Astronomical Society of the Pacific*, 118, 517

[23] Boss, A. P. 1998, *The Astrophysical Journal*, 503, 923

[24] Boss, A. P. 2002, *The Astrophysical Journal Letters*, 567, 149

[25] Boss, A. P. 2006, *The Astrophysical Journal*, 643, 501

[26] Boss, A. P. 2011, *The Astrophysical Journal*, 731, 74

[27] Bromley, B. C. & Kenyon, S. J. 2011, *The Astrophysical Journal*, 731, 101

[28] Brown, K. I. T., Gray, D. F., & Baliunas, S. L. 2008, *The Astrophysical Journal*, 679, 1531

[29] Brown, B. P., Miesch, M. S., Browning, M. K. et al. 2011, *The Astrophysical Journal*, 731, 69

[30] Browning, M. K., Basri, G., Marcy, G. W., West, A. A. & Zhang, J. 2010, *The Astronomical Journal*, 139, 504

[31] Brugamyer, E., Dodson-Robinson, S. E., Cochran, W. D., & Sneden, C. 2011, *The Astrophysical Journal*, 738, 97

[32] Buccino, A. P., Díaz, R. F., Luoni, M. L., Abrevaya, X. C., & Mauas, P. J. D. 2011, *The Astronomical Journal*, 141, 34

[33] Buchhave, L. A., Latham, D. W., Johansen, A., et al. 2012, *Nature*, 486, 375

[34] Butler, R. P., Marcy, G. W., Williams, E., et al. 1996, *Publications of the Astronomical Society of the Pacific*, 108, 500

[35] Cameron, R. & Schüssler, M. 2008, *The Astrophysical Journal*, 685, 1291

[36] Canizares, C. R., Donahue, M. E., Trinchieri, G., Stewart, G. C., & McGlynn, T. A. 1986, *The Astrophysical Journal*, 304, 312

[37] Casagrande, L., Schönrich, R., Asplund, M., et al. 2011, *Astronomy & Astrophysics*, 530, A138

[38] Chabrier, G. & Baraffe, I. 1997, *Astronomy & Astrophysics*, 327, 1039

[39] Chambers, J. E. 1999, *Monthly Notices of the Royal Astronomical Society*, 304, 793

[40] Cincunegui, C., Díaz, R. F., & Mauas, P. J. D. 2007, *Astronomy & Astrophysics*, 461, 1107

[41] Cincunegui, C., Díaz, R. F., & Mauas, P. J. D. 2007, *Astronomy & Astrophysics*, 469, 309

[42] Cochran, W. D. & Hatzes, A. P. 1993, *ASP Conference Series*, 36, 267

[43] Cochran, W. D., Endl, M., McArthur, B., et al. 2004, *The Astrophysical Journal Letters*, 611, L133

[44] Cochran, W. D., Endl, M., Wittenmyer, R. A., & Bean, J. L. 2007, *The Astrophysical Journal*, 665, 1407

[45] Cochran, W. D., Fabrycky, D. C., Torres, G. et al. 2011, *The Astrophysical Journal Supplements*, 197, 7

[46] Cooper, M. C., Tremonti, C. A., Newman, J. A., & Zabludoff, A. I. 2008, *Monthly Notices of the Royal Astronomical Society*, 390, 245

[47] Correia, A. C. M., Couetdic, J., Laskar, J. et al. 2009, *Astronomy & Astrophysics*, 496, 521

[48] Cumming, A., Butler, R. P., Marcy, G. W., et al. 2008, *Publications of the Astronomical Society of the Pacific*, 120, 531

[49] Cutri, R. M., Skrutskie, M. F., van Dyk, S., et al. 2003, VizieR Online Data Catalog, 2246, 0

[50] Davé, R. 2008, *Monthly Notices of the Royal Astronomical Society*, 385, 147

[51] Davé, R., Oppenheimer, B. D., & Finlator, K. 2011, *Monthly Notices of the Royal Astronomical Society*, 415, 11

[52] Davé, R., Finlator, K., & Oppenheimer, B. D. 2011, *Monthly Notices of the Royal Astronomical Society*, 416, 1354

[53] Davé, R., Finlator, K. & Oppenheimer, B. D. 2012, *Monthly Notices of the Royal Astronomical Society*, 421, 98

[54] Davé, R., Katz, N., Oppenheimer, B. D., Kollmeier, J. A., & Weinberg, D. H. 2013, arXiv:1302.3631

[55] Del Popolo, A., Ercan, N., & Yeşilyurt, I. S. 2005, *Astronomy & Astrophysics*, 436, 363

[56] Delfosse, X., Forveille, T., Mayor, M., et al. 1998, *Astronomy & Astrophysics*, 338, L67

[57] Delfosse, X., Forveille, T., Ségransan, D. et al. 2000, *Astronomy & Astrophysics*, 364, 217

[58] Demarque, P., Woo, J.-H., Kim, Y.-C., & Yi, S. K. 2004, *The Astrophysical Journal Supplements*, 155, 667

[59] de Vaucouleurs, G., de Vaucouleurs, A., Corwin, H. G., Jr., et al. 1991, Third Reference Catalogue of Bright Galaxies. Volume I: Explanations and references. Volume II: Data for galaxies between 0^h and 12^h. Volume III: Data for galaxies between 12^h and 24^h., by de Vaucouleurs, G.; de Vaucouleurs, A.; Corwin, H. G., Jr.; Buta, R. J.; Paturel, G.; Fouqué, P.. Springer, New York, NY (USA), 1991, 2091 p., ISBN 0-387-97552-7, Price US\$ 198.00. ISBN 3-540-97552-7, Price DM 448.00. ISBN 0-387-97549-7 (Vol. I), ISBN 0-387-97550-0 (Vol. II), ISBN 0-387-97551-9 (Vol. III).

[60] Díaz, R. F., Cincunegui, C., & Mauas, P. J. D. 2007, *Monthly Notices of the Royal Astronomical Society*, 378, 1007

[61] Díaz, R. F., González, J. F., Cincunegui, C., & Mauas, P. J. D. 2007, *Astronomy & Astrophysics*, 474, 345

[62] Dodson-Robinson, S. E., Willacy, K., Bodenheimer, P., Turner, N. J., & Beichman, C. A. 2009, *Icarus*, 200, 672

[63] Dommanget, J., & Nys, O. 2002, VizieR Online Data Catalog, 1274, 0

[64] Dors, O. L., Jr., & Copetti, M. V. F. 2006, *Astronomy & Astrophysics*, 452, 473

[65] Duffy, A. R., Kay, S. T., Battye, R. A. et al. 2012, *Monthly Notices of the Royal Astronomical Society*, 420, 2799

[66] Dumusque, X., Pepe, F., Lovis, C., et al. 2012, *Nature*, 491, 207

[67] Ecuvillon, A., Israelian, G., Pont, F., Santos, N. C., & Mayor, M. 2007, *Astronomy & Astrophysics*, 461, 171

[68] Eggenberger, A., Udry, S., Chauvin, G. et al. 2007, *Astronomy & Astrophysics*, 474, 273

[69] Ellison, S. L., Patton, D. R., Simard, L., & McConnachie, A. W. 2008, *The Astronomical Journal*, 135, 1877

[70] Ellison, S. L., Simard, L., Cowan, N. B., et al. 2009, *Monthly Notices of the Royal Astronomical Society*, 396, 1257

[71] Endl, M., Kürster, M., & Els, S. 2000, *Astronomy & Astrophysics*, 362, 585

[72] Endl, M., Cochran, W. D., Tull, R. G., & MacQueen, P. 2003, *The Astronomical Journal*, 126, 3099

[73] Endl, M., Cochran, W. D., Kürster, M. et al. 2006, *The Astrophysical Journal*, 649, 436

[74] ESA 1997, *The Hipparcos and Tycho Catalogues* (ESA SP-1200) (Noordwijk: ESA)

[75] Finlator, K., & Davé, R. 2008, *Monthly Notices of the Royal Astronomical Society*, 385, 2181

[76] Fischer, D. A. & Valenti, J. 2005, *The Astrophysical Journal*, 622, 1102

[77] Ford, E. B., & Holman, M. J. 2007, *The Astrophysical Journal Letters*, 664, L51

[78] Forveille, T., Bonfils, X., Delfosse, X. et al. 2009, *Astronomy & Astrophysics*, 493, 645

[79] Forveille, T., Bonfils, X., Lo Curto, G., et al. 2011, *Astronomy & Astrophysics*, 526, A141

[80] Franklin, F, Lecar, M., & Murison, M. 1993, *The Astronomical Journal*, 105, 2336

[81] Friedland, L. 2001, *The Astrophysical Journal*, 547, 75

[82] Fuhrmann, K. & Bernkopf, J. 2008, *Monthly Notices of the Royal Astronomical Society*, 384, 1563

[83] Fumagalli, M., Krumholz, M. R., Prochaska, J. X., Gavazzi, G., & Boselli, A. 2009, *The Astrophysical Journal*, 697, 1811

[84] Garnett, D. R., Shields, G. A., Skillman, E. D., Sagan, S. P., & Dufour, R. J. 1997, *The Astrophysical Journal*, 489, 63

[85] Gavazzi, G., Boselli, A., van Driel, W., & O'Neil, K. 2005, *Astronomy & Astrophysics*, 429, 439

[86] Gomes da Silva, J., Santos, N. C., Bonfils, X. et al. 2011, *Astronomy & Astrophysics*, 534A, 30

[87] Gomes da Silva, J., Santos, N. C., Bonfils, X. et al. 2012, *Astronomy & Astrophysics*, 541A, 9

[88] Giovanelli, R., & Haynes, M. P. 1985, *The Astrophysical Journal*, 292, 404

[89] Gould, A., Dong, S., Gaudi, B. S., et al. 2010, *The Astrophysical Journal*, 720, 1073

[90] Grav, T., Mainzer, A. K., Bauer, J. et al. 2012, *The Astrophysical Journal*, 744, 197

[91] Gregory, P. C. 2011, *Monthly Notices of the Royal Astronomical Society*, 415, 2523

[92] Gunn, J. E., & Gott, J. R., III 1972, *The Astrophysical Journal*, 176, 1

[93] Hall, J. C. 1996, *Publications of the Astronomical Society of the Pacific*, 108, 313

[94] Hatzes, A. P. 2013, *The Astrophysical Journal*, 770, 133

[95] Haynes, M. P., Giovanelli, R., & Chincarini, G. L. 1984, *Annual Review of Astronomy & Astrophysics*, 22, 445

[96] Henry, R. B. C., Pagel, B. E. J., & Chincarini, G. L. 1994, *Monthly Notices of the Royal Astronomical Society*, 266, 421

[97] Hill, G. J., MacQueen, P. J., Smith, M. P., et al. 2008, *SPIE Proceedings*, 7014

[98] Hinse, T. C., Lee, J. W., Goździewski, K., et al. 2012, *Monthly Notices of the Royal Astronomical Society*, 420, 3609

[99] Høg, E., Fabricius, C., Makarov, V. V., et al. 2000, *Astronomy & Astrophysics*, 355, L27

[100] Holman, M. J., Fabrycky, D. C., Ragozzine, D. et al. 2010, *Science*, 330, 51

[101] Horner, J., & Wyn Evans, N. 2006, *Monthly Notices of the Royal Astronomical Society*, 367, L20

[102] Horner, J., & Jones, B. W. 2010, *International Journal of Astrobiology*, 9, 273

[103] Horner, J., & Lykawka, P. S. 2010, *Monthly Notices of the Royal Astronomical Society*, 405, 49

[104] Horner, J., Marshall, J. P., Wittenmyer, R. A., & Tinney, C. G. 2011, *Monthly Notices of the Royal Astronomical Society*, 416, L11

[105] Horner, J., Wittenmyer, R. A., Marshall, J. P., Tinney, C. G., Butters, O. W., 2012a, *Proceedings of the 11th Annual Australian Space Science Conference*, in press

[106] Horner, J., Müller, T. G., & Lykawka, P. S. 2012b, *Monthly Notices of the Royal Astronomical Society*, 423, 2587

[107] Howard, A. W., Marcy, G. W., Johnson, J. A. et al. 2010, *Science*, 330, 653

[108] Howard, A. W., Marcy, G. W., Bryson, S. T., et al. 2012, *The Astrophysical Journal Supplements*, 201, 15

[109] Howell, J. H., Armus, L., Mazzarella, J. M., et al. 2010, *The Astrophysical Journal*, 715, 572

[110] Hünsch, M., Schmitt, J. H. M. M., Sterzik, M. F., & Voges, W. 1999, *Astronomy & Astrophysics Supplements*, 135, 319

[111] Isaacson, H. & Fischer, D. 2010, *The Astrophysical Journal*, 725, 875

[112] Isobe, T., Feigelson, E. D., Akritas, M. G., & Babu, G. J. 1990, *The Astrophysical Journal*, 364, 104

[113] Jefferys, W. H. et al. 1988, *Celestial Mechanics*, 41, 39

[114] Johnson, J. A. & Apps, K. 2009, *The Astrophysical Journal*, 699, 933

[115] Johnson, J. A., Aller, K. M., Howard, A. W., & Crepp, J. R. 2010, *Publications of the Astronomical Society of the Pacific*, 122, 905

[116] Johnson, J. A., Clanton, C., Howard, A. W., et al. 2011a, *The Astrophysical Journal Supplements*, 197, 26

[117] Johnson, J. A., Payne, M., Howard, A. W. et al. 2011b, *The Astronomical Journal*, 141, 16

[118] Johnson, J. A., Gazak, J. Z., Apps, K. et al. 2012, *The Astronomical Journal*, 143, 111

[119] Kasting, J. F., Whitmire, D. P., & Reynolds, R. T. 1993, *Icarus*, 101, 108

[120] Katz, B., Dong, S., & Malhotra, R. 2011, *Physical Review Letters*, 107, 181101

[121] Kelly, B. C. 2007, *The Astrophysical Journal*, 665, 1489

[122] Kennicutt, R. C., Oey, M. S., Zaritsky, D., & Huchra, J. P. 1993, *Revista Mexicana de Astronomia y Astrofisica*, 27, 21

[123] Kennicutt, R. C., Jr. 1998, *The Astrophysical Journal*, 498, 541

[124] Kewley, L. J., & Dopita, M. A. 2002, *The Astrophysical Journal Supplements*, 142, 35

[125] Kewley, L. J., Geller, M. J., & Barton, E. J. 2006, *The Astronomical Journal*, 131, 2004

[126] Kharchenko, N. V., & Roeser, S. 2009, VizieR Online Data Catalog, 1280, 0

[127] Kong, X., Cheng, F. Z., Weiss, A., & Charlot, S. 2002, *Astronomy & Astrophysics*, 396, 503

[128] Kozai, Y. 1962, *The Astronomical Journal*, 67, 591

[129] Krejčová, T. & Budaj, J. 2012, *Astronomy & Astrophysics*, 540, A82

[130] Kruse, E. A., Berger, E., Knapp, G. R. et al. 2010, *The Astrophysical Journal*, 722, 1352

[131] Kürster, M., Schmitt, J. H. M. M., Cutispoto, G., & Dennerl, K. 1997, *Astronomy & Astrophysics*, 320, 831

[132] Kürster, M., Endl, M., Rouesnel, F. et al. 2003, *Astronomy & Astrophysics*, 403, 1077

[133] Kurucz, R. 1993, ATLAS9 Stellar Atmosphere Programs and 2 km/s grid. Kurucz CD-ROM No. 13 (Cambridge: Smithsonian Astrophys. Obs.)

[134] Lambert, D. L., Heath, J. E., & Edvardsson, B. 1991, *Monthly Notices of the Royal Astronomical Society*, 253, 610

[135] Lammer, H., Bredehöft, J. H., Coustenis, A., et al. 2009, *The Astronomy & Astrophysics Review*, 17, 181

[136] Latham, D. W., Stefanik, R. P., Mazeh, T., Mayor, M., & Burki, G. 1989, *Nature*, 339, 38

[137] Laughlin, G., Bodenheimer, P., & Adams, F. C. 2004, *The Astrophysical Journal Letters*, 612, L73

[138] Lecar, M., Podolak, M., Sasselov, D., & Chiang, E. 2006, *The Astrophysical Journal*, 640, 1115

[139] Levy, L., Rose, J. A., van Gorkom, J. H., & Chaboyer, B. 2007, *The Astronomical Journal*, 133, 1104

[140] Lidov, M. L. 1962, *Planetary and Space Science*, 9, 719

[141] Lissauer, J. J. 1995, *Icarus*, 114, 217

[142] Lissauer, J. J., Fabrycky, D. C., Ford, E. B. et al. 2011, *Nature*, 470, 53

[143] López-Santiago, J., Montes, D., Gálvez-Ortiz, M. C. et al. 2010, *Astronomy & Astrophysics*, 514, A97

[144] Lovis, C., Dumusque, X., Santos, N. C. et al. 2011, arXiv:1107.5325v1

[145] Lykawka, P. S., Horner, J., Jones, B. W., & Mukai, T. 2009, *Monthly Notices of the Royal Astronomical Society*, 398, 1715

[146] Lykawka, P. S., & Horner, J. 2010, *Monthly Notices of the Royal Astronomical Society*, 405, 1375

[147] Lykawka, P. S., Horner, J., Jones, B. W., & Mukai, T. 2011, *Monthly Notices of the Royal Astronomical Society*, 412, 537

[148] Mahadevan, S., Ramsey, L., Bender, C., et al. 2012, *SPIE Proceedings*, 8446

[149] Malhotra, R. 1995, *The Astronomical Journal*, 110, 420

[150] Mandell, A. M., Raymond, S. N., & Sigurdsson, S. 2007, *The Astrophysical Journal*, 660, 823

[151] Mann, A. W., Gaidos, E., & Gaudi, B. S. 2010, *The Astrophysical Journal*, 719, 1454

[152] Marcy, G. W., Butler, R. P., Vogt, S. S., Fischer, D., & Lissauer, J. J. 1998, *The Astrophysical Journal Letters*, 505, L147

[153] Marcy, G. W., Butler, R. P., Fischer, D., et al. 2001, *The Astrophysical Journal*, 556, 296

[154] Marois, C., Zuckerman, B., Konopacky, Q. M., Macintosh, B., & Barman, T. 2010, *Nature*, 468, 1080

240

[155] Marshall, J., Horner, J., & Carter, A. 2010, *International Journal of Astrobiology*, 9, 259

[156] Mayor, M. & Queloz, D. 1995, *Nature*, 378, 355

[157] Mayor, M., Bonfils, X., Forveille, T. et al. 2009, *Astronomy & Astrophysics*, 507, 487

[158] Mayor, M., Marmier, M., Lovis, C. et al. 2011, arXiv: 1109.2497v1

[159] McGaugh, S. S. 1991, *The Astrophysical Journal*, 380, 140

[160] Meschiari, S., Wolf, A. S., Rivera, E., et al. 2009, *Publications of the Astronomical Society of the Pacific*, 121, 1016

[161] Morales, J. C., Ribas, I., & Jordi, C. 2008, *Astronomy & Astrophysics*, 478, 507

[162] Morbidelli, A., Levison, H. F., Tsiganis, K., & Gomes, R. 2005, *Nature*, 435, 462

[163] Morgan, D. P., West, A. A., Garcés, A. et al. 2012, arXiv:1205.6806v2

[164] Mouhcine, M., Baldry, I. K., & Bamford, S. P. 2007, *Monthly Notices of the Royal Astronomical Society*, 382, 801

[165] Moustakas, J. & Kennicutt, R. C., Jr. 2006, *The Astrophysical Journal Supplements*, 164, 81

[166] Moustakas, J. & Kennicutt, R. C., Jr. 2006, *The Astrophysical Journal*, 651, 155

[167] Muirhead, P. S., Johnson, J. A., Apps, K. et al. 2012, *The Astrophysical Journal*, 747, 144.

[168] Nelan, E. et al. 2010, "Fine Guidance Sensor Instrument Handbook," Version 18.0, (Baltimore: STScI)

[169] Noyes, R. W., Hartmann, L. W., Baliunas, S. L., Duncan, D. K., & Vaughan, A. H. 1984, *The Astrophysical Journal*, 279, 763

[170] Ossendrijver, M. 2003, *Astronomy & Astrophysics*Rev., 11, 287

[171] Osterbrock, D. E., & Ferland, G. J. 2006, *Astrophysics of gaseous nebulae and active galactic nuclei*, 2nd. ed. by D.E. Osterbrock and G.J. Ferland. Sausalito, CA: University

[172] Pagel, B. E. J., & Patchett, B. E. 1975, *Monthly Notices of the Royal Astronomical Society*, 172, 13

[173] Paturel, G., Petit, C., Prugniel, P., et al. 2003, *Astronomy & Astrophysics*, 412, 45

[174] Paulson, D. B., Cochran, W. D., & Hatzes, A. P. 2004, *The Astronomical Journal*, 127, 3579

[175] Petropoulou, V., Vílchez, J., Iglesias-Páramo, J., et al. 2011, *The Astrophysical Journal*, 734, 32

[176] Petropoulou, V., Vílchez, J., & Iglesias-Páramo, J. 2012, *The Astrophysical Journal*, 749, 133

[177] Pillitteri, I., Günther, H. M., Wolk, S. J., Kashyap, V. L., & Cohen, O. 2011, *The Astrophysical Journal*, 741, 18

[178] Pipin, V. V. & Kosovichev, A. G. 2011, *The Astrophysical Journal*, 741, 1

[179] Pollack, J. B., Hubickyj, O., Bodenheimer, P., Lissauer, J. J., Podolak, M., & Greenzweig, Y. 1996, *Icarus*, 124, 62

[180] Popping, A., Davé, R., Braun, R. & Oppenheimer, B. D. 2009, *Astronomy & Astrophysics*, 504, 15

[181] Porter, S. B. & Grundy, W. M. 2011, *The Astrophysical Journal Letters*, 736, 14

[182] Quanz, S. P., Lafrenière, D., Meyer, M. R., Reggiani, M. M., & Buenzli, E. 2012, *Astronomy & Astrophysics*, 541, A133

[183] Queloz, D., Henry, G. W., Sivan, J. P., et al. 2001, *Astronomy & Astrophysics*, 379, 279

[184] Quirrenbach, A., Amado, P. J., Caballero, J. A. et al. 2011, *Proceedings of the International Astronomical Union*, 276, 545

[185] Ramsey, L. W., Adams, M. T., Barnes, T. G., et al. 1998, *SPIE Proceedings*, 3352, 34

[186] Reddy, B. E., Lambert, D. L., & Prieto, C. A. 2006, *Monthly Notices of the Royal Astronomical Society*, 367, 1329

[187] Reiners, A., Joshi, N., & Goldman, B. 2012, *The Astronomical Journal*, 143, 93

[188] Robertson, P., Shields, G. A., & Blanc, G. A. 2012a, *The Astrophysical Journal*, 748, 48

[189] Robertson, P., Endl, M., Cochran, W. D. et al. 2012b, *The Astrophysical Journal*, 749, 39

[190] Robertson, P., Horner, J., Wittenmyer, R. A. et al. 2012c, *The Astrophysical Journal*, 754, 50

[191] Robertson, P., Endl, M., Cochran, W. D., & Dodson-Robinson, S. E. 2013a, *The Astrophysical Journal*, 764, 3

[192] Robertson, P., Shields, G. A., Davé, R., Blanc, G. A., & Wright, A. 2013b, *The Astrophysical Journal*, 773, 4

[193] Robertson, P., Endl, M., Cochran, W. D., MacQueen, P. J., & Boss, A. P. 2013, arXiv:1307.7640

[194] Rose, J. A., Robertson, P., Miner, J., & Levy, L. 2010, *The Astronomical Journal*, 139, 765

[195] Santerne, A., Endl, M., Hatzes, A., et al. 2011, European Physical Journal Web of Conferences, 11, 2001

244

[196] Santos, N. C., Gomes da Silva, J., Lovis, C., & Melo, C. 2010, *Astronomy & Astrophysics*, 511, A54

[197] Schlaufman, K. C. & Laughlin, G. 2010, *Astronomy & Astrophysics*, 519A, 105

[198] Schulze-Makuch, D., Méndez, A., Fairén, A. G., et al. 2011, *Astrobiology*, 11, 1041

[199] Ségransan, D., Udry, S., Mayor, M. et al. 2010, *Astronomy & Astrophysics*, 511, A45

[200] Setiawan, J., Klement, R. J., Henning, T., et al. 2010, *Science*, 330, 1642

[201] Sheppard, S. S. & Trujillo, C. A. 2006, *Science*, 313, 511

[202] Shields, G. A., Skillman, E. D., & Kennicutt, R. C., Jr. 1991, *The Astrophysical Journal*, 371, 82

[203] Shkolnik, E., Bohlender, D. A., Walker, G. A., & Collier Cameron, A. 2008, *The Astrophysical Journal*, 676, 628

[204] Skillman, E. D., Kennicutt, R. C., Jr., Shields, G. A., & Zaritsky, D. 1996, *The Astrophysical Journal*, 462, 147

[205] Sneden, C. A. 1973, Ph.D. thesis, Univ. of Texas at Austin

[206] Solanes, J. M., Giovanelli, R., & Haynes, M. P. 1996, *The Astrophysical Journal*, 461, 609

[207] Solanes, J. M., Manrique, A., García-Gómez, C., et al. 2001, *The Astrophysical Journal*, 548, 97

[208] Steffen, J. H., Fabrycky, D. C., Agol, E., et al. 2013, *Monthly Notices of the Royal Astronomical Society*, 428, 1077

[209] Sturrock, P. A. & Scargle, J. D. 2010, *The Astrophysical Journal*, 718, 527

[210] Sumi, T., Kamiya, K., Bennett, D. P., et al. 2011, *Nature*, 473, 349

[211] Swift, J. J., Johnson, J. A., Morton, T. D., et al. 2013, *The Astrophysical Journal*, 764, 105

[212] Tan, B., & Cheng, Z. 2012, *Astrophysics & Space Science*, 382

[213] Thompson, M. J., Christensen-Dalsgaard, J., Miesch, M. S. & Toomre, J. 2003, *Annual Review of Astronomy & Astrophysics*, 2003, 599

[214] Tinney, C. G., Wittenmyer, R. A., Butler, R. P., et al. 2011, *The Astrophysical Journal*, 732, 31

[215] Tremonti, C. A., Heckman, T. M., Kauffmann, G., et al. 2004, *The Astrophysical Journal*, 613, 898

[216] Tsiganis, K., Gomes, R., Morbidelli, A., & Levison, H. F. 2005, *Nature*, 435, 459

[217] Tull, R. G. et al. 1995, *Publications of the Astronomical Society of the Pacific*, 107, 251

[218] Tull, R. G. et al. 1998, *SPIE Proceedings*, 3355, 387

[219] Udry, S. & Santos, N. C. 2007, *Annual Review of Astronomy & Astrophysics*, 45, 397

[220] Valenti, J. A., Butler, R. P., & Marcy, G. W. 1995, *Publications of the Astronomical Society of the Pacific*, 107, 966

[221] van Leeuwen, F. 2007, *Astronomy & Astrophysics*, 474, 653

[222] Vigroux, L., Boulade, O., & Rose, J. A. 1989, *The Astronomical Journal*, 98, 2044

[223] Vogt, S. S., Allen, S. L., Bigelow, B. C., et al. 1994, *SPIE Proceedings*, 2198, 362

[224] Vogt, S. S., Butler, R. P., Rivera, E. J. et al. 2010, *The Astrophysical Journal*, 723, 954

[225] Vogt, S. S., Butler, R. P., & Haghighipour, N. 2012, arXiv:1207.4515

[226] Walkowicz, L. M., Hawley, S. L., & West, A. A. 2004, *Publications of the Astronomical Society of the Pacific*, 116, 1105

[227] West, A. A., Hawley, S. L., Walkowicz, L. M. et al. 2004, *The Astronomical Journal*, 128, 426

[228] West, A. A., Hawley, S. L., Bochanski, J. J. et al. 2008, *The Astronomical Journal*, 135, 785

[229] West, A. A., Hawley, S. L., Bochanski, J. J., Covey, K. R., & Burgasser, A. J. 2009, *Proceedings of the International Astronomical Union*, 258, 327

[230] Wittenmyer, R. A., Endl, M., Cochran, W. D., Hatzes, A. P., Walker, G. A. H., Yang, S. L. S., & Paulson, D. B. 2006, *The Astronomical Journal*, 132, 177

[231] Wittenmyer, R. A., Endl, M., Cochran, W. D., & Levison, H. F. 2007, *The Astronomical Journal*, 134, 1276

[232] Wittenmyer, R. A., Endl, M., Cochran, W. D., Levison, H. F., & Henry, G. W. 2009, *The Astrophysical Journal Supplements*, 182, 97

[233] Wittenmyer, R. A., Tinney, C. G., O'Toole, S. J., et al. 2011a, *The Astrophysical Journal*, 727, 102

[234] Wittenmyer, R. A., Tinney, C. G., Butler, R. P., et al. 2011b, *The Astrophysical Journal*, 738, 81

[235] Wittenmyer, R. A., Horner, J., Marshall, J. P., Butters, O. W., & Tinney, C. G. 2012, *Monthly Notices of the Royal Astronomical Society*, 419, 3258

[236] Wolfgang, A. & Laughlin, G. 2011, arXiv: 1108.5842v1

[237] Wright, J. T. 2004, *The Astronomical Journal*, 128, 1273

[238] Wright, J. T., Fakhouri, O., Marcy, G. W., et al. 2011, *Publications of the Astronomical Society of the Pacific*, 123, 412

[239] Zaritsky, D., Kennicutt, R. C., Jr., & Huchra, J. P. 1994, *The Astrophysical Journal*, 420, 87

[240] Zechmeister, M. & Kürster, M. 2009, *Astronomy & Astrophysics*, 496, 577

[241] Zechmeister, M., Kürster, M., & Endl, M. 2009, *Astronomy & Astrophysics*, 505, 859

[242] Zhang, W., Li, C., Kauffmann, G., et al. 2009, *Monthly Notices of the Royal Astronomical Society*, 397, 1243

Vita

Paul Montgomery Robertson was born November 1, 1985 to William and Blair Robertson. He grew up in Morganton, North Carolina, and attended the University of North Carolina at Chapel Hill from 2004-2008. Upon completing Bachelor's degrees in Physics and Mathematics, he moved to Austin to pursue a PhD in astronomy at the University of Texas. In 2010, he married his wife, Emily Bartlett, with whom he has lived in Austin until presently.

Permanent address: 713 E 45th Street
                    Austin, Texas 78751

This dissertation was typeset with LaTeX[†] by the author.

[†]LaTeX is a document preparation system developed by Leslie Lamport as a special version of Donald Knuth's TeX Program.